Single-Phase Fluid Flow and Heat Transfer in Microtubes

Von der Fakultät Maschinenbau der Universität Stuttgart
zur Erlangung der Würde eines Doktoringenieurs (Dr.-Ing.)
genehmigte Abhandlung

vorgelegt von
Stephen John McPhail
aus Johannesburg, Südafrika

Hauptberichter:	Prof. Dr.-Ing. habil. M. Groll
Mitberichter:	Prof. Dr.-Ing. habil. H. Müller-Steinhagen
Mitberichter:	Prof. G.P. Celata, Ph.D.

Tag der Einreichung: 5. Februar 2007
Tag der mündlichen Prüfung: 16. Mai 2008

Institut für Kernenergetik und Energiesysteme der Universität Stuttgart

2008

Many hundred large volumes have been published upon this controversy: but the books of the Big-Endians have been long-forbidden, and the whole party rendered incapable by law of holding employments. During the course of these troubles, the Emperors of Blefuscu did frequently expostulate by their ambassadors, accusing us of making a schism in religion, by offending against a fundamental doctrine of our great prophet Lustrog, in the fifty-fourth chapter of the Brundecral *(which is their Alcoran). This, however, is thought to be a mere strain upon the text: for the words are these;* That all true believers shall break their eggs at the convenient end: *and which is the convenient end, seems, in my humble opinion, to be left to every man's conscience, or at least in the power of the chief magistrate to determine.*

J. Swift (Gulliver's Travels)

ABSTRACT

The current experimental investigation focuses on the single-phase flow characteristics inside microtubes, both in adiabatic conditions as with heat input. In the literature, contrasting effects concerning pressure drop and heat transfer are reported that are tied to miniaturization of the flow passage. That is why a systematic variation of conditions has been carried out to evaluate the possible occurrence of anomalies tied to the increased viscous deformation, rarefaction and pressure drop in microchannels. It has been verified that miniaturization of the test section brings about considerable difficulties through altered *peripheral* conditions: measuring equipment, material thickness and total fluid volume do not scale to the same degree as the characteristic dimension of the system (*i.e.* the inner diameter of the studied microtube). This can have a substantial effect on the experimental output and accuracy.

The findings of this investigation have led to the conclusion that no anomalous phenomena occur solely through reduction of the flow passage down to 30 μm inner diameter. The friction factor for laminar liquid flow in tubes is in agreement with the classic correlation of Hagen-Poiseuille. Up to shear rates of 10^6 s^{-1} and a relative roughness of 1%, no alterations could be measured, as also with degassed water flow over a hydrophobic surface. In compressible flow, even a ten-fold pressure drop between inlet and outlet did not evidence significant deviations from the incompressible flow relation for friction. This points to a near-reversible process of expansion under these conditions. No rarefaction effects could be detected in the experiments carried out.

In microchannels, the liquid shear rate at the wall is very great, causing irreversible heat production which increases the bulk fluid temperature of the flow. This increase is known as viscous dissipation and is tied directly to the friction at the wall. A derivation is provided, with experimental validation, that shows how the friction factor can be expressed in terms of this temperature rise only.

Adding heat input to the microtubes showed that the effect of incongruous scaling can be very disturbing. In laminar flow, a distinct reduction was observed in the heat transfer efficacy of thick-walled glass microtubes compared to thin walled stainless steel tubes of the same *inner* diameter. The large thermal resistance of the former compared to the small volume of flow causes the heat put in to select preferential paths (through peripheral attachments to the test section), thereby not reaching the fluid-wall interface completely, falsifying the assumed experimental conditions. Otherwise, a strong heat transfer improvement was observed in the thermal development region, recommending the use of *short* microchannels in single-phase heat exchanging applications, providing the added benefit of reduced head loss. In turbulent flow, no significant deviations were found with respect to the predictions of the – conventional – Gnielinski correlation for the heat transfer coefficient.

ZUSAMMENFASSUNG

Die in dieser Arbeit beschriebenen experimentellen Untersuchungen befassen sich mit einphasigen adiabatischen und diabatischen Strömungen in Mikrorohren. In der Literatur sind widersprüchliche Ergebnisse bezüglich der Auswirkung eines verkleinerten Strömungsquerschnitts veröffentlicht worden. Daher wurden Untersuchungen unter systematisch veränderten Randbedingungen durchgeführt, um das mögliche Auftreten von Anomalien im Zusammenhang mit erhöhter viskoser Strömungsdeformation , Strömungsverdünnung und Druckabfall in Mikrokanälen zu beurteilen.
Die Verkleinerung einer Teststrecke verursacht erhebliche Probleme aufgrund der veränderten äußeren Bedingungen. Zum Beispiel sind die Dimensionen der eingesetzten Messgeräte, die Materialstärken und die Fluidvolumina nicht im selben Maße skalierbar wie die charakteristische Dimension der Teststrecke, d.h. der Innendurchmesser des Mikrokanals. Dies kann substantielle Auswirkungen auf die experimentellen Ergebnisse und deren Genauigkeit haben.

Die Ergebnisse dieser Arbeit haben zu der Schlußfolgerung geführt, daß bis zu einem Innendurchmesser von 30 μm keine ungewöhnlichen Phänomene nur aufgrund der Verringerung des Strömungsquerschnitts auftreten. Der Reibungsfaktor bei laminarer Fluidströmung stimmt mit der klassische Korrelation von Hagen-Poiseuille überein. Dies gilt bis zu Schergeschwindigkeiten von 10^6 s^{-1} und einer relativen Rauhigkeit von 1%, sowie bei Strömung von entgastem Wasser über eine hydrophobe Oberfläche. Kompressible Gasströmungen, sogar mit einem Druckabfall im Bereich einer 10er Potenz zwischen Ein- und Ausgang, zeigen keine signifikanten Abweichungen von Ergebnissen der Rohrreibungsgleichung für inkompressible Strömung. Dies deutet auf einen quasi-reversiblen Expansionvorgang unter diesen Bedingungen hin. In den durchgeführten Versuchen konnte keine Strömungsverdünnung beobachtet werden.

In Mikrokanälen ist die Schergeschwindigkeit von Flüssigkeiten an der Wand sehr hoch, was eine irreversible Wärmeproduktion verursacht und zu einer Erhöhung der Flüssigkeitstemperatur führt. Dieser Temperaturanstieg wird als viskose Dissipation bezeichnet und steht in direktem Zusammenhang mit der Wandreibung. Es wurde abgeleitet und experimentell validiert wie die Rohrreibungszahl allein bezogen auf diese Temperaturerhöhung ausgedrückt werden kann.

Die Zufuhr von Wärme in Mikrokanäle hat gezeigt, daß eine unverhältnismäßige Skalierung sehr störend sein kann. Bei laminaren Strömungen wurde in dickwandigen Glasrohren, im Vergleich mit dünnwandige Edelstahlrohren mit gleichem Innendurchmesser, eine deutliche Verringerung der Wärmeübertragungeffizienz festgestellt. Bei Ersteren wird die eingebrachte Wärme zu einem guten Teil durch periphere Anschlüsse an der Teststrecke abgeleitet, wodurch nicht die gesamte Wärmemenge an der Heizwand-Fluidgrenzfläche zur Verfügung steht; damit werden die Versuchsbedingungen verfälscht. Andererseits wurde eine starke Verbesserung der Wärmeübertragung in der thermischen Einlaufstrecke beobachtet. Daher empfiehlt sich der Einsatz von kurzen Mikrokanälen für einphasige Wärmeübertragungsanwendungen, was zusätzlich auch den auftretenden Druckabfall reduziert. Bei turbulenter Strömung wurden keine signifikanten Abweichungen von der konventionellen Gnielinski-Korrelation zur Bestimmung des Wärmeübergangskoeffizienten gefunden.

ACKNOWLEDGMENTS

What would this path of life we're bound upon be without milestones? A pleasant walk, one could maintain, seeing as our destination is given. Or would the lack of direction make us aimlessly lost in an undifferentiated environment, stuck on an island of possibility, in a forest of entropy? Though we would probably not – like the allegorical donkey between two equal heaps of oats – starve, not being able to choose, for sure the lack of highlights would make us little dull boys.

This, then, shall be a milestone. And like all milestones, they cannot be reached or even conceived without the help of others who have gone before us or have backed us along the way.

My gratitude goes out to Prof. Manfred Groll and Dr. Gian Piero Celata for having created the opportunity for me to seal this stage of my voyage with the work that is in front of you. I thank Prof. Groll for the genuine attention and frank criticism with which my Thesis was surveyed and thanks to which it has obtained its present form. Words fall short at the continuous moral, material and mental support and at the confidence with which Dr. Celata provided me in the past four years.

Thanks to Dr. Zummo for having given me the wings to fly between the lab and the data analysis desk. A true researcher, his organization will never keep up with the prolificacy of his ideas, so that his office already half-encompasses the world. Forza Roma sempre. Thanks to Dr. Mertz for his selfless practical help in the suspense-laden moments of submission. The Kurzfassung is dedicated to him.

Gratitude and best wishes to my comrades in the HMTMIC project, young researchers now professionals (and a little bit less young): Ewelina Sobierska, Claudi Martín-Callizo, Lorenzo Consolini, Rémi Révellin, Frederik Lundell, Marko Matkovic, Enrico Stalio, Stefano Dall'Olio. The acknowledgments of us all go out to the European Union for making us a present of this fantastic experience – long may our continent prosper.

Silence and rise at the mentioning of a truly great scientist: Prof. Gian Luca Morini, thanks to whom the most successful chapter in this Treatise could be conceived. It is hard to say whether his knowledge of fluid-dynamic theory or his exquisite personality is the greater; suffice it to state that true intelligence always has an open face and a candid heart. Greetings also to Dr. Marco Lorenzini, polyglot competitor, and gratitude for his critical comments on our colleagues and superiors – no-one may rest on his laurels – and for the Short Course in Toulouse on European Medieval History.

Back in Rome, and a hearty salute goes out to the priceless ITFD staff: thanks to Anna (behind every great man there has to be a great woman), thanks to Luca Simonetti (open source of course) and respect to those who keep up the good name of scientific research, against all of modern society's thankless frenzy: Andrea Mariani, Francesco D'Annibale, Gino Boccardi, Massimo Furrer.

Grateful acknowledgment is due to Emanuele Serra (SEM pics), Luigi Nardi (capillaries) and Maurizio Diamanti (turbomolecular vacuum pump). This study not have been possible without their expertise and their willingness to share it. Similarly, many thanks to my dear undergraduates! High-flyers by now, I had the privilege to guide and coax them through the final stage of their university education, often gleaning fresh insights and vigour from their efforts. Their contribution to this work has been material, as I hope mine was to theirs: Lucia Tesfagabir, Valerio Marconi, Armando Bianco.

Un ringraziamento speciale ai tecnici, coloro che – ma solo con le buone! – mettono in opera le alte concezioni di noialtri scienziati: Alberto (per avermi insegnato a lavorare con precisione), Antonio (un onore all'apprendistato), Mariano (bracconiere di ogni tipo e misura d'attrezzo), Vaniero (vetusto progettista che non dice se non fa) e ammirazione, inoltre, per Michele Sica, animo gentile con le mani d'oro: quando il mondo ti tradisce, c'è sempre la musica che ti accoglie.

A pari passo con la carriera deve sempre starci lo sviluppo interiore, per cui ricomincio da capo quando ringrazio i seguenti personaggi.

Luca Saraceno, vero fratello e compagno di sventure nel nostro esilio volontario ai confini della città eterna; ingegnere, cuoco, poeta, pianista, atleta, strategista, e oltretutto Siciliano – ma gli voglio bene lo stesso.

Mariano – er duca – l'insegnante che mi mancava; senza prezzo le lezioni impartite nell'ufficio, nella cantina, nel campo. Insostituibili le dosi di sgrassante per avviare le giornate, lo scambio di storie e di risate. Smetterò di essergli grato quando avrà finito casa…

Elio – il nuovo San Francesco – immancabile fornitore, compagno nel gradire, tesoro di sapienza popolare e perenne ottimista – malgrado se stesso.

Grazie a tutti gli altri Eneidi, precari e non, che hanno fatto sì che andare al lavoro portava sempre l'incognita di un sipario che si alza: Erika (per gli effetti cardiaci), Luca C., Daniele, Alessandro, Walter, Marcons, Alvaro, Chiaretta, Arianna, Giada, Cinzia, Chiara Z. (Certosa x sempre), e naturalmente la sezione calcio. Fuori dall'Enea filo da torcere per farci belle treccine colorate me l'han dato la Kiara (Regina Nera), Noemi (la psicopolemica), Laura (anima e Tango).

To conclude, love and respect goes out to my family members: first of all – this time – to the Rome connection, Vera and Valerie. Thanks to Jozé & Henk and my aunties from Holland, Oma, the Fays for their Mediterranean spirit. All my love to my best friend and little sister Susy. Incessant thanks to Mum & Dad for sticking it out and being marvellous – everything I do is ultimately their responsibility…

And a big hug and kiss to Nonna, to whom this work is entirely dedicated.

Enjoy.

February, 2007.

CONTENTS

1

INTRODUCTION

The technological development of Society is the most apparent manifestation of its evolution. Since Man invented the use of tools to strengthen his arm and lengthen his reach, he has steadily been gaining hold of the world around him; first by taking up arms against the inclemencies of his surroundings, arriving lately at large-scale manipulation of his environment and fellow-beings. This expansion of material power, which received its greatest boosts during the Industrial Revolution and the advent of the Information Era, but is still increasing, has brought about massive changes in the way society functions, in the relationships among and the identity of its constituents, and in its requirements of the world's resources. Economy of primary materials, efficiency of space, reduced consumption and higher specific performance are the criteria which new applications have to satisfy in order for our technocracy to remain sustainable. Where a maximization of these precepts coincides with market predominance, the ideal product has been conceived. Unfortunately, conflict between these driving forces is the rule and only rarely is the balance tipped in favour of long-term benefits. However, the game is on, and the field of play comprises a myriad of appliances, over the entire scale of productivity: from bulbs to pacemakers, from microchips to combustion engines, from farming to construction, from low-level programming to product flow logistics.

Dictated by this ever-increasing demand for (space-)efficient equipment of ever-increasing power, made possible by new manufacturing techniques of highest precision, and provided with opportunities for commercial prevalence, miniaturization of appliances has proved to be a valuable solution and has become the scene of highly fertile activity.

1.1 Working at microscale

Partly because of the technological challenge, partly because of stark necessity, there has been an increasing movement towards a miniaturization of appliances in the last decade. In all technical fields solutions are sought that encumber as little as possible without compromising on performance: in medical diagnostics, environmental sample analysis, military defence, consumer electronics, biomedical appliances, chemical reactors and heat management a constant research for quicker response times and portable devices has driven the field of microtechnology to impressive levels. In many applications it has been found that *many small* active components are more productive than *few large* ones, which is also in keeping with the growing trend towards modular design.

As a rule of thumb all devices with characteristic dimensions between 1 μm and 1 mm are called micro-devices. Generally, these micro-systems can be subdivided into three categories:

- *MEMS*: Micro-Electro-Mechanical Systems (*e.g.* air bag acceleration sensors, HD readers, *etc*.)
- *MOEMS*: Micro-Opto-Electro-Mechanical Systems (*e.g.* micro-collimators, micro-endoscopes, *etc*.)

- *MFDs*: Micro-Flow Devices (*e.g.* micro heat exchangers, micro-pumps, micro-mixers *etc*.), of which a large fraction are united in *μTAS*: Micro Total Analysis Systems or lab-on-a-chip systems.

In this Thesis the concepts behind MFDs – without the chemical aspect – are the focus of study. MFDs function through the heat and mass transfer, by diffusion and convection, of a working fluid that acts out its particular properties most efficiently in high surface-to-volume enclosures, maximizing the area of exchange: microchannels. Current research in this field is exploring different applications which intimately involve the dynamics of fluids, single-phase and two-phase forced convective heat transfer and new potential applications are continuously being proposed. The performance of these appliances relies heavily on the design of the channels where the process takes place, as a narrow line of trade-offs has to be walked between effective heat and mass transfer and unacceptably high flow resistance.

These applications would remain in the realm of fiction however if manufacturing technologies didn't keep up the pace as well. Those particularly apt for microscopic fabrication are:

- *Micromechanical machining*: fabrication that relies on the mechanical formation of micro-geometries; examples are diamond cutters, lasers, pullers, *etc.*
- *Photolithographic-based processes*: chemical etching techniques, successfully used on silicon wafers, a widespread material in the micro-electronics industry.
- *X-ray micromachining*: this technology uses electromagnetic radiation; the most widely applied example is LIGA (*"Lithographie-Galvanoformung-Abformung"*)
- *Surface micro-machining*: incision of one or more layers of differing properties deposited on a base (frequently silicon).

Photolithographic processes are particularly indicated for silicon wafers; this technology, born in the electronic field, is fairly mature. The cross-sectional shapes that can be obtained for microchannels realized with this technique are limited though. In fact, the microchannels produced by chemical etching directly on silicon wafers have a cross-sectional shape that depends on a variety of factors such as the crystallographic nature of the silicon used. When a photolithographic-based process is employed, one can obtain microchannels having a cross-section fixed by the orientation of the silicon crystal planes; for example, the microchannels etched in <100> or in <110> silicon by using a KOH solution have a trapezoidal cross-section (with an apex angle of 54.74° imposed by the crystallographic morphology of the <100> silicon) or a rectangular cross-section, respectively. Since this technique is widely diffused, in literature there are many experimental results obtained for microchannels having a trapezoidal, triangular, rectangular and double-trapezoidal (hexagonal) cross-section. On the contrary, with the other techniques it is possible to realize miniaturized channels having – theoretically – any shape of cross-section.

Microchannels with a circular cross-section are called microtubes or micropipes. These have the advantage of being axial-symmetrical (and therefore easier to characterize), fairly uncomplicated in their manufacture (a brief description of the pulling process is given in paragraph 4.1.1.1), and relatively strong – mechanically speaking, for a given size of flow passage – in comparison with their bulk. These are the main reasons for the adoption of this geometry in this study, focused on a reduction to the essentials of microchannel heat and mass transfer.

In practical applications usually angular cross-sections will be preferred, because of their increased proportion of wetted area to fluid volume and – importantly – because the agglomeration of microchannels for a given, say, heat transfer requirement is more easily realised by machining many grooves on a flat surface, rather than bundling together many microtubes. The disadvantage of the machined ducts on a surface, is that they have to be closed by a cover plate, which never

guarantees perfect (uniform and clean) adherence and thereby distorts the idealised geometry of the channels, or in the worst case can cause leakage or transverse migration of the working fluid.

One of the most important applications of miniature heat sinks, heat exchangers and coolers is the cooling of computer CPUs. For many years there has been a relentless increase in the cooling requirements of microelectronics as the demand for more powerful, sophisticated microchips has led to a dramatic increase in component densities on chips. Intel's first processor, the 4004, debuted in 1971 and consisted of 2,300 transistors. Compare that to the 230 million transistors found in today's Pentium Extreme Edition 840: that's an increase by a factor of 100,000!

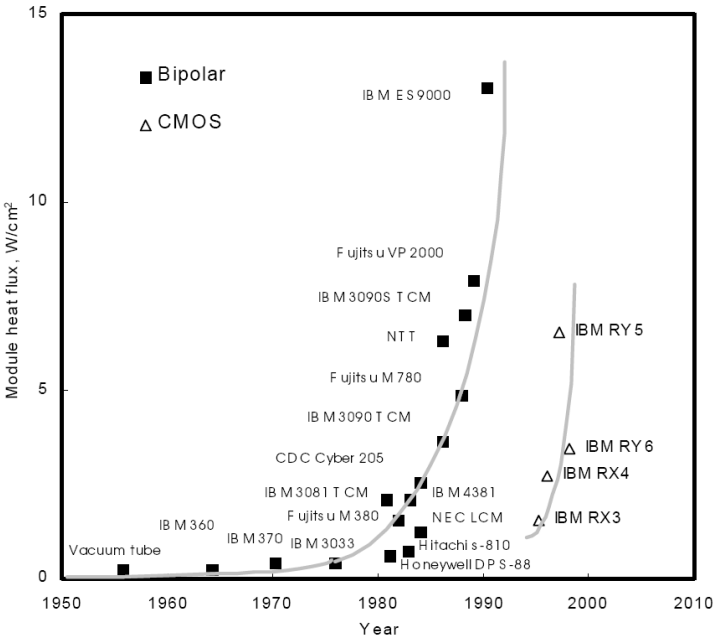

Fig. 1.1: *CPU module heat fluxes in the past years* [1]

The increased density of active components on CPUs causes a concentrated generation of heat that needs to be removed for the processor to be kept below its maximum operating temperature of 70 or 80°C. In 2004 peak heat fluxes of around 160 W/cm^2 were the norm [1]. Traditional cooling approaches, consisting typically of external air-cooled heat sinks, are increasingly falling short in meeting the thermal management challenges of emerging electronic systems: air cooling is believed to be limited to about 50 W/cm^2. That is why increased attention is being directed to liquid-cooled heat removal units: microchannels seem to be a promising solution.

More possibilities of application of MFDs are touched upon in the business activity survey in Chapter 3, section 3.2.

1.2 Objectives of this Thesis

Proper understanding of microscale transport phenomena is fundamental for the designer of microfluidic devices. For this reason, many studies have been conducted to analyse the behaviour of convective flow through microchannels, which up to now have led, however, only to an agglomeration of disparate conclusions (see the literature survey, section 3.1). To provide convincing measurements to establish some sort of base note in the melisma of publicised data is the motivation for this Thesis. The objective hereby is to select a few key arguments for study and elaboration, conducting an as accurate as possible train of experiments with a critical observation of the reliability of the obtained results.

This work will only cover single-phase flow and heat transfer, since this argument will prove to be challenging and multi-faceted enough without pretending to incorporate phase-changing phenomena as well. Various single-phase effects peculiar to microscale have been hypothesised in the recent past, and at the end of this investigation, a clearer picture is hoped to have been conveyed as to the veracity of such statements, or the conditions under which a particular behaviour may be expected. Thus, after verification of incompressible fluid behaviour in simple, smooth microtubes, the effects will be studied of various wall surface conditions (rough and hydrophobic) and of compressibility of the fluid. Then, the very marked viscous dissipation effects that result in extremely narrow passages will be qualified and quantified. Eventually, flow behaviour where uniform heat input is applied at the microtube walls will be put under scrutiny, taking into account also peripheral effects that the miniaturization of the test section implies.

The treatise will be built up as follows. In Chapter 2, the theoretical concepts behind single-phase fluid flow and heat transfer in pipes will be explained, with a separate section dedicated to those aspects of the physical model that may be altered or accentuated when the system under consideration is below a certain dimension. This will lead us to come up with some sort of definition of microchannels, by the exclusion of unsatisfying hypotheses.

A survey of the open literature that deals with the arguments proposed is presented in Chapter 3, divided in reviews of single-phase fluid flow and single-phase heat transfer in microducts. Also, a brief overview is given of company activity on the global market, to establish what the state-of the-art in the consumer catalogues is as regards microfluidic products.

The experimental facilities and methodologies are set out in Chapter 4. In-depth description will be provided of the test sections, measurement techniques and instrumentation utilised in the gathering of data, as well as a thorough analysis of the experimental uncertainty.

The heart of the Thesis is Chapter 5, where the results of extensive test runs and the data of many measurements will be presented, discussed and analysed, according to the theoretical precepts put forward in Chapter 2. The discussion of the results will be centred around the 4 distinguished campaigns of experiments that were carried out: liquid flow in microtubes, gas flow in microtubes, viscous dissipation in microtubes and single-phase heat transfer in microtubes.

Finally, the conclusions will be summarized in Chapter 6, providing some recommendations for future work on the topic.

2

THEORETICAL BACKGROUND

In this chapter the fundamental concepts behind the physics of flow and heat transfer will be set out. The basic equations that describe a physical system are explained in section 2.1, applied subsequently to the particular situation of fluid flow in pipes (section 2.2) and heat transfer in pipes (section 2.3). In section 2.4 will be investigated what difficulties are to be expected when we transpose our physical analysis from the conventional scale to applications of microscopic characteristic length. This will lead us to the discussion on what actually defines a "micro" channel in section 2.5.

2.1 Basic equations

Though one cannot be confident of premises offered as ready-made conclusions, it is undoable to start at the very beginning of the mathematical formulation of physical laws. To maintain the upward drive of science, and Knowledge in general, one has to build upon the blocks that form the tower below us, and make reference to the fact that it still stands as a justification for its growth. For those who are interested in the construction methods that have brought us to this point, textbooks will provide satisfaction [*e.g.* 2-5], unless one wants to attempt to re-elevate the same tower on one's own efforts. In other words, the fundamental principles of fluid-dynamic and heat transfer theory will be presented in summarized form, and applied directly to the problem in hand.

2.1.1 Conservation of mass

Since a system is, by definition, an arbitrary collection of matter of fixed identity, it must be composed of the same quantity of matter at all times (assuming that the velocities involved are much smaller than the speed of light). The mass, m, of the system must be constant:

$$\left.\frac{dm}{dt}\right)_{system} = 0 \tag{2.1}$$

Transcribing the *system* formulation to a *control volume* (*CV*) formulation yields:

$$\left.\frac{dm}{dt}\right)_{system} = \frac{\partial}{\partial t}\int_{CV}\rho dV + \int_{CS}\rho\vec{u}\cdot d\vec{A} \quad (=0) \tag{2.2}$$

The first term in equation (2.2) on the right-hand side (r.h.s.) represents the rate of change of mass within the control volume; the second term represents the net rate of mass flux through the

control surface (*CS*), where ρ is the fluid density, and $\vec{u}$ is the vectorial velocity measured relative to the unit control surface $d\vec{A}$. Conservation of mass requires that the sum of these terms be zero.

This is the general formulation for a *macroscopic* control volume. In the case that a concentration, temperature or any particles-related quantity (in this particular case it would be the density) can not be assumed to be uniform over the control volume, it is not practical to formulate the macroscopic, integral balance. One could resort to microscopic or differential formulation, which is equivalent to observing a control volume of infinitesimal dimensions $dV = dx.dy.dz$, where dx, dy and dz approach zero. Mathematically, this boils down to omitting the integral sign and dividing by dV. The equation for conservation of mass, or continuity equation, using 3 equivalent mathematical notations, thus becomes:

$$\frac{\partial \rho}{\partial t} + \frac{\partial \rho u_x}{\partial x} + \frac{\partial \rho u_y}{\partial y} + \frac{\partial \rho u_z}{\partial z} \equiv \frac{\partial \rho}{\partial t} + \frac{\partial \rho u_i}{\partial x_i} \equiv \frac{D\rho}{Dt} + \rho \frac{\partial u_i}{\partial x_i} = 0 \tag{2.3}$$

In steady flow, time derivatives cancel out; furthermore, for an incompressible fluid, density is constant, so that all partial differentiations of ρ yield zero and equation (2.3) can be simplified to, in vector notation:

$$\nabla \cdot \vec{u} = 0 \tag{2.4}$$

This means that in whichever way the system boundary deforms and moves, what goes in must come out.

2.1.2 Conservation of momentum

For a system moving relative to an inertial reference frame, Newton's second law states that the time rate of change of linear momentum of the system is always equal to the sum of all external forces acting on the system:

$$\left.\frac{d\vec{I}}{dt}\right)_{system} = \vec{F} \tag{2.5}$$

The resultant force $\vec{F}$ acting on the system is composed of surface (pressure, tension, etc., summarized in a tensor τ_{ij}) and body forces (in particular gravity, $\vec{g}$), so that transcribing equation (2.5) to control volume formulation yields:

$$\frac{\partial}{\partial t}\int_{CV} \vec{u}\rho dV + \int_{CS} \vec{u}\rho\vec{u}\cdot d\vec{A} = \int_{CV} \rho\vec{g}dV + \int_{CS} \tau_{ij}\cdot\vec{n}dA \tag{2.6}$$

where the left-hand side (l.h.s.) is the time derivative of linear momentum elaborated in terms of the mass-velocity product.

The tensor of surface tensions τ_{ij} includes both normal and tangential forces and is complex in its elaboration, therefore outside of the scope of this thesis. Basically, it is composed of the thermodynamic pressure, p, and the viscosity stress, which is dependent on the velocity gradient and the coefficient of viscosity μ; although it is a matrix, *qualitatively* it can be described as:

$$\tau_{ij} \approx -p\delta_{ij} + \mu\frac{\partial u}{\partial x} \tag{2.7}$$

where δ_{ij} is the Kronecker delta, which sifts all operations on p so that they have effect normal to the elemental surface only. The (approximated) viscous stress term contains all tangential components.

If the fluid is assumed to be Newtonian, incompressible and to have constant thermophysical properties, some simplifications can be applied. Under these conditions, equation (2.6) – converted from integral to differential formulation (omitting the integral sign and dividing by dV) – reduces to:

$$\rho\left(\frac{\partial u_i}{\partial t} + u_j\frac{\partial u_i}{\partial x_j}\right) = \rho g_i - \frac{\partial p}{\partial x_i} + \mu\frac{\partial^2 u_i}{\partial {x_j}^2} \tag{2.8}$$

which is the reduced form of the *Navier-Stokes* equations[1].

It should be noted that expressing this equation explicitly in x, y, and z coordinates yields 3 separate equations, one for each ordinate. In the case of steady-state, the first term on the l.h.s. cancels out and the vector notation becomes:

$$\rho(\vec{u}\cdot\nabla)\vec{u} = \rho\vec{g} - \nabla p + \mu\nabla^2\vec{u} \tag{2.9}$$

2.1.3 Conservation of energy

The first law of thermodynamics states that energy cannot be created nor destroyed, which is a reformulation of the principle of conservation of energy. Within a system therefore, the balance of energy is closed as follows:

$$\left.\frac{dE}{dt}\right)_{system} = q - w \tag{2.10}$$

where the rate of heat transfer q is positive when heat is added to the system from the surroundings; the rate of work w is positive when work is done by the system on its surroundings. The rate of work term is composed of the surface and body forces as defined in the previous sub-section, acting along the path of the system per unit time. If we assume the gravitational work to be negligible (which is true for a horizontally oriented system, and in any case a good approximation for pressure-dominated flow), the work *acted on* the system w can be expressed as:

$$w = -\int_{CV}\tau_{ij}\frac{\partial u_i}{\partial x_j}dV \tag{2.11}$$

The heat flow term is equally divisible in body and surface components:

$$q = \int_{CV}\rho q_m\,dV + \int_{CS} -q_i''n_i\,dA \tag{2.12}$$

[1] Although reduced, this is a *precise* form of the Navier-Stokes equations: the tensor τ_{ij} is defined in approximate form for clarity, but the complete form was used in the derivation of equation (2.8).

where q_m are the internal heat sources per unit mass and q''_i is the heat flux entering the system at the surface along the normal (which is directed outwards, explaining the negative sign). The rate of change of the energy term in equation (2.9) can be expressed in terms of temperature change along the particle's path (using the *material derivative*) through use of the thermal capacity c_p and the density ρ. Substituting the equations, reverting to differential notation and combining terms, the following balance results:

$$\rho c_p \frac{DT}{Dt} = \tau_{ij} \frac{\partial u_i}{\partial x_j} - \frac{\partial q''_i}{\partial x_i} + \rho q_m \tag{2.13}$$

If we write out the tension tensor in its pressure part and its viscous part (see equation (2.7)), this becomes:

$$\rho c_p \frac{DT}{Dt} = -p\delta_{ij} \frac{\partial u_i}{\partial x_j} + \mu \frac{\partial^2 u_i}{\partial x_j{}^2} - \frac{\partial q''_i}{\partial x_i} + \rho q_m \tag{2.14}$$

Thanks to the property of the Kronecker delta the first term on the r.h.s. can be rewritten:

$$-p\delta_{ij} \frac{\partial u_i}{\partial x_j} = -p \frac{\partial u_i}{\partial x_i}$$

and – for incompressible flow – eliminated, by virtue of the continuity equation (2.4).

As we consider the flow to be stationary, the time derivatives equal zero. Furthermore, the heat flux term can be transcribed in temperature variables using Fourier's conduction law[2]. We have thus managed to reduce the conservation of energy equation to the following vectorial form:

$$\rho c_p \vec{u} \cdot \nabla T = \mu \left[\nabla \vec{u} \cdot \nabla \vec{u} \right] + k \nabla^2 T + \rho q_m \tag{2.15}$$

2.1.4 Equation of state

Equations of state are relations among intensive thermodynamic properties. In the discussion of compressible fluids, behaviour of the *density* is of particular interest, which is described for an *ideal gas* by:

$$\rho = \frac{pM_{mol}}{RT} \tag{2.16}$$

where M_{mol} is the molar mass of the gas in question and R is the universal gas constant, 8.314 J/mol.K. T and p are the gas temperature and pressure, respectively. The departure of a real gas from such ideal behaviour can be evaluated from the compressibility factor Z, which determines to

[2] This empirical law defines the thermal conductivity k of a material, which is the proportionality constant that links the heat transfer rate per unit area q'' with the temperature gradient in the direction of the heat flow: $q'' = -k \frac{\partial T}{\partial x}$. The minus sign represents the second law of thermodynamics that states that heat must flow downhill on the temperature scale. Differentiation of the law with respect to x, yields the analogy that is used and can be found in equation (2.15).

which degree the above equation is valid: the closer to 1 this factor, the more ideal the behaviour of the gas.

Table 2.1: *Compressibility factor Z for different gases at different pressures at 20°C*

Pressure (psi)[3]	Oxygen	Nitrogen	Helium	Air
100	0.995	0.998	1.004	0.997
500	0.977	0.993	1.018	0.990
1000	0.959	0.994	1.036	0.986
1500	0.947	1.001	1.054	0.990
2000	0.941	1.014	1.071	0.999
2500	0.941	1.032	1.088	1.013
3000	0.947	1.054	1.104	1.032
3500	0.957	1.080	1.120	1.054
4000	0.972	1.107	1.136	1.079

The gas that was utilised in the experiments discussed in this Thesis was Helium. As can be seen from Table 2.1, with good approximation this gas can be considered ideal, which simplifies to a large degree the elaboration of the equations to be discussed in sub-section 2.2.2. The molar mass of Helium is 4.003 g/mol.

The density is therefore dependent on the quotient of pressure and temperature. Since the temperature of the gas will practically remain invariant for flow in an adiabatic channel, the density can be said to be linearly dependent on the pressure, which decreases along the channel due to wall friction. This means that, in order for the mass flow to remain constant at each cross-section, the flow has to be accelerated. But before looking at this complication, let us observe the behaviour of flow in a pipe of an incompressible fluid.

[3] 1 PSI = 6.89×10^{-2} bar

2.2 Physics of flow in pipes

Focusing on flow in pipes, the fluid-dynamics can be analysed axial-symmetrically. The problem becomes essentially one-dimensional and with the assumption of steady-state flow the equations in the previous section are abundantly simplified. For radial characterization, necessary to investigate the velocity profile, it is convenient to work in cylindrical coordinates. Ultimately, it is aimed to introduce the *friction factor*, primarily in laminar flow, which is one of the main parameters that are object of research in this Thesis. First, incompressible flow in circular ducts will be considered, then the effect of fluid compressibility will be tackled.

2.2.1 Incompressible flow

Consider a horizontal tube of constant diameter through which steady-state, incompressible, fully developed flow takes place. The fluid velocity in this case is constant, both in time as in axial direction. Because there is no horizontal component of the gravity force, and by virtue of equation (2.4), the integral momentum equation (2.6) is reduced to:

$$0 = \int_{CS} \tau_{ij} \cdot \vec{n} d\vec{A} \tag{2.17}$$

To describe a horizontal axisymmetric steady flow, the notation of this equation can be simplified. The tension tensor τ_{ij}, which contains both normal and tangential forces on the surface of a control volume, can be derived observing a differential control volume inside the pipe, figure 2.1.

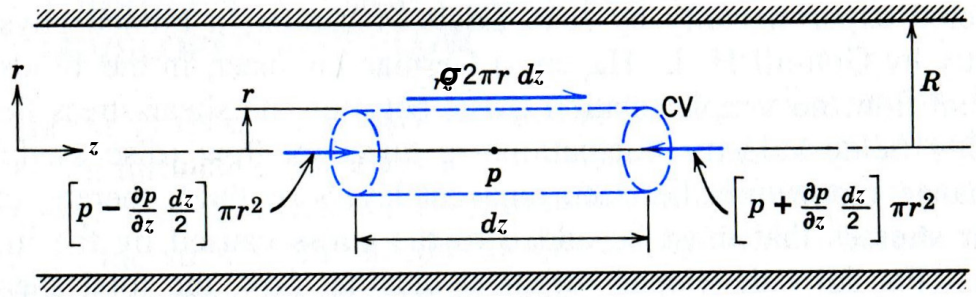

Fig. 2.1: *Control volume analysis of tension distribution*

The pressure at the centre of the element is p; the pressure at each end is obtained from a Taylor series expansion of p about the centre of the element. The shear force σ_{rz} acts on the circumferential surface of the element. The direction has been assumed such that the shear stress is positive. Summing up the balance of forces of this simple situation:

$$\int_{CS} \tau_{ij} \cdot \vec{n} d\vec{A} = \left(p - \frac{\partial p}{\partial z} \frac{dz}{2} \right) \pi r^2 - \left(p + \frac{\partial p}{\partial z} \frac{dz}{2} \right) \pi r^2 + \sigma_{rz} 2\pi r dz = 0 \tag{2.18}$$

or

$$-\frac{\partial p}{\partial z} dz \pi r^2 + \sigma_{rz} 2\pi r dz = 0 \tag{2.19}$$

so that

$$\sigma_{rz} = \frac{r}{2}\frac{\partial p}{\partial z} \tag{2.20}$$

Thus we can see that the shear stress σ_{rz} in the fluid varies linearly across the pipe, from zero at the centreline to a maximum at the pipe wall. If we denote the shear stress at the wall as σ_R, equation (2.20) shows that at the inner surface of the pipe (action = - reaction):

$$\sigma_R = -\left[\sigma_{rz}\right]_{r=R} = -\frac{R}{2}\frac{\partial p}{\partial z} \tag{2.21}$$

Equation (2.21) relates the wall shear stress to the axial pressure gradient. The momentum equation was used to derive it, but no assumption was made about a relation between the shear stress and the velocity field. Consequently, equation (2.21) is applicable to both laminar and turbulent fully developed pipe flow.

If it were possible to relate the shear stress field to the mean velocity field, we could determine analytically the pressure drop over a length of pipe for fully developed flow. In the case of laminar flow of a Newtonian fluid, such a relation exists:

$$\sigma_{rz} = \mu\frac{du}{dr} \tag{2.22}$$

Since the fluid velocity at the pipe wall must be zero for non-slip flow, there is a boundary condition to resolve the first-order differential equation that results, and the velocity profile in laminar fully developed flow can be obtained combining equations (2.20-22):

$$u = -\frac{R^2}{4\mu}\left(\frac{\partial p}{\partial z}\right)\left[1-\left(\frac{r}{R}\right)^2\right] \tag{2.23}$$

At the centerline ($r = 0$) the velocity will be:

$$u_c = -\frac{R^2}{4\mu}\left(\frac{\partial p}{\partial z}\right) \tag{2.24}$$

so that the velocity distribution at each cross-section has the well-known parabolic shape:

$$\frac{u}{u_c} = 1-\frac{r^2}{R^2} \tag{2.25}$$

which is also known as the Poiseuille velocity profile.

We can obtain the volumetric flow rate $\dot{V}$ by integrating equation (2.23) over the circular cross-section (from $r = 0$ to $r = R$); this enables us subsequently to calculate the *average* velocity of the bulk fluid, U. Furthermore, for an incompressible fluid in fully developed flow, the pressure gradient is constant, or, the pressure drop between inlet and outlet of the pipe is linear. Carrying out these mathematical operations allows us to determine *analytically* the pressure drop Δp over a length of tube L:

$$\frac{dp}{dz} = \frac{\Delta p}{L} = \frac{128 \mu \dot{V}}{\pi d^4} = 32 \frac{\mu U}{d^2} \tag{2.26}$$

where d is the pipe (inner) diameter. Dividing the equation by the specific kinetic energy $\frac{1}{2}\rho U^2$:

$$\frac{2\Delta p}{\rho U^2} = 64 \frac{L}{d} \frac{\mu}{\rho U d} \tag{2.27}$$

so that

$$\Delta p = \left(\frac{64}{Re} \right) \frac{L}{d} \frac{\rho U^2}{2} = f \frac{L}{d} \frac{\rho U^2}{2} \tag{2.28}$$

Thus, we have derived the analytical expression for the *friction factor, f,* for laminar flow in a pipe. The relation between pressure drop and volumetric flow, equation (2.26), was first discovered experimentally by Jean Louis Poiseuille [6] and independently by G.H.L. Hagen around the middle of the 19th century. The definition of the friction factor as in equation (2.28) is thanks to Darcy and Weisbach, but its dependency on 64/*Re* is called the Hagen-Poiseuille law. Finally, the constant in the numerator that defines the friction factor, is dependent on the channel cross-sectional shape, and is called the Poiseuille constant, *Po*.

Of course, the tidy solution presented above, is only possible thanks to the known relation of equation (2.22): for turbulent or compressible flow such a relation does not exist, or is implicit and not so straightforward to resolve. For turbulent flow, empirical correlations exist that describe the friction factor:

$$f = \frac{0.3164}{Re^{0.25}} \qquad \text{(Blasius)}$$

$$f = 0.25 \left[\log \left(\frac{e/d}{3.7} + \frac{2.51}{Re\sqrt{f}} \right) \right]^{-2} \qquad \text{(Colebrook)}$$

It can be noticed that the Colebrook correlation, apart from being transcendental and therefore only resolvable through iteration, has introduced the wall roughness, *e*, as an influential parameter. In the derivation of the friction factor for laminar flow, no dependence of surface roughness appeared – and experiments confirm that it is a function of Reynolds number only – but in turbulent flow the velocity profile becomes fuller and the size of the viscous sublayer near the wall decreases. As roughness elements begin to poke through this layer, they start to have an effect, and the friction factor becomes a function of both the Reynolds number *and* the relative roughness *e/d*.

It is interesting to note that the pressure drop in a pipe, equation (2.26), is dependent on the *fourth* power of the inner diameter. Thus, if this parameter is reduced, a very strong effect will be noticed in the head loss along the tube, which will increase to very high values. If we transcribe equation (2.28) in terms of *directly measurable* quantities only, we can see that the friction factor even has a *fifth* power dependence on the inner diameter value:

$$f = \frac{\pi^2}{8} \frac{\Delta p}{L} \frac{\rho d^5}{\Gamma^2} \tag{2.29}$$

where Γ is the mass flow in kg/s. This also means that even small imperfections in the measurement of the diameter will have a large effect on the determination of the friction factor – see paragraph 4.3.1.1.

2.2.2 Compressible flow

As is stated in Perry's Chemical Engineer's Handbook [7]: "A common error is to assume that compressibility effects are always negligible when the Mach number is small. The proper assessment of whether compressibility is important should be based on relative density changes, not on Mach number."

The high pressure drops involved in microscopic flow cause, in the case of gas being the working fluid, large variations of density in the duct – as equation (2.16) orders – even at *low speeds* ($Ma < 0.3$). The change in density as the gas loses pressure causes a change of the fluid bulk velocity, and thus also of the velocity profile. This means that the momentum equation (2.6) retains the unknown convective term on the l.h.s. (we still assume the duct to be horizontal):

$$\int_{CS} \vec{u}\rho\vec{u}\cdot d\vec{A} = \int_{CS} \tau_{ij}\cdot\vec{n}dA \tag{2.30}$$

which simplifies, assuming now a uniform cross-sectional velocity profile, to give:

$$\rho U\Omega dU = -\sigma_R \Pi dz - \Omega dp \tag{2.31}$$

where Ω is the cross-sectional area of the pipe ($\pi d^2/4$) and Π is the wetted perimeter (πd). Unfortunately, the expression for σ_{rz} in equation (2.22) is no longer explicit because of the dependence of the velocity u on the axial co-ordinate z (assuming μ constant). Equation (2.20) becomes statically indeterminate, and no univocal expression for the pressure drop can be obtained. To bypass this problem, the pressure gradient is taken from equations (2.26) and (2.28), and σ_R is calculated with equation (2.20), so that the momentum equation for compressible flow in a horizontal pipe becomes [8]:

$$\rho U dU + \rho U^2 \frac{f}{2d} dz + dp = 0 \tag{2.32}$$

So, to solve the indeterminate set of conservation equations, an equation strictly only valid for *incompressible* flow is adopted to describe also the case of *compressible* flow. This is assumed to be valid where subsonic velocities are concerned (an assumption, however, which is based on experience with conventionally-sized pipes, where frictional pressure drop is almost negligible for low-viscosity gas flow). The equations of continuity and energy can then take compressibility into account, so that the solution of the indeterminate problem amalgamates physically sound conclusions with an approximation that was intended originally for different conditions.

Let us proceed to isolate the friction factor in equation (2.32) for subsequent experimental verification. In the case of *isothermal* flow, the equation of state (2.16), differentiated, reduces to:

$$\frac{dp}{p} = \frac{d\rho}{\rho} \tag{2.33}$$

Also, the continuity equation dictates that $\rho U = G$ = constant (where G is the mass flux per unit area), which differentially means:

$$\frac{dU}{U}+\frac{d\rho}{\rho}=0 \tag{2.34}$$

Combining equations (2.16), (2.33) and (2.34), and rearranging, equation (2.32) can be shown to become:

$$-\frac{dp}{p}+\frac{f}{2d}dz+\frac{pdp}{G^2R_MT}=0 \tag{2.35}$$

Finally, integrating this expression from (z, p) = (0, P_{in}) to (L, P_{out}), the description of the friction factor is obtained:

$$f\frac{L}{d}=\frac{P_{in}{}^2-P_{out}{}^2}{R_MTG^2}-2ln\left(\frac{P_{in}}{P_{out}}\right) \tag{2.36}$$

For frictional *adiabatic* flow, the temperature term is added to the differentiated equation of state for an ideal gas:

$$\frac{dp}{p}=\frac{d\rho}{\rho}+\frac{dT}{T} \tag{2.37}$$

The solution of the momentum equation is now not so straightforward: it is expounded step-by-step in [2]. Eventually, the following expression for f is got to [9]:

$$f\frac{L}{D}=\frac{P_{in}{}^2}{R_MT_{in}G^2}\left(1-\frac{P_{out}{}^2T_{in}}{P_{in}{}^2T_{out}}\right)+\frac{\gamma+1}{2\gamma}ln\left(\frac{T_{in}}{T_{out}}\cdot\frac{2P_{out}{}^2\gamma+(\gamma-1)R_MT_{out}G^2}{2P_{in}{}^2\gamma+(\gamma-1)R_MT_{in}G^2}\right) \tag{2.38}$$

In these equations, the pressures P_{in} and P_{out} represent the net values of the static pressure at inlet and outlet of the channel section L under consideration, γ is the proportion of specific heats, R_M the specific universal gas constant: R/M_{mol}.

2.3 Physics of heat transfer in pipes

In studying the physics of heat transfer, one aims to predict the energy transfer that takes place between material bodies as a result of temperature difference. There are three modes of heat transfer: conduction, convection and radiation, which know of myriad examples in the phenomenological world. In this section we shall directly focus on the application of the physical principles of these modes on a cylindrical geometry through which a heated fluid is flowing exchanging energy with its surroundings. For further detail, the reader is referred to [3].

2.3.1 Convection – the heat transfer coefficient

Convection heat transfer is a superposition of a fluid-dynamic situation with heat that is exchanged at its boundaries due to the constant refreshing of the materials at the interface. The static problem of, for example, the cooling of a hot steel bar in a pool of water is only a problem of conduction. If the bar is placed in a flowing stream, the heat transfer that takes place is stimulated and is governed by the principles of convection.

Let us now look at the problem in hand: consider the tube-flow system with heat input schematized in figure 2.2. (See also the derivation of velocity profile for laminar flow in sub-section 2.2.1.)

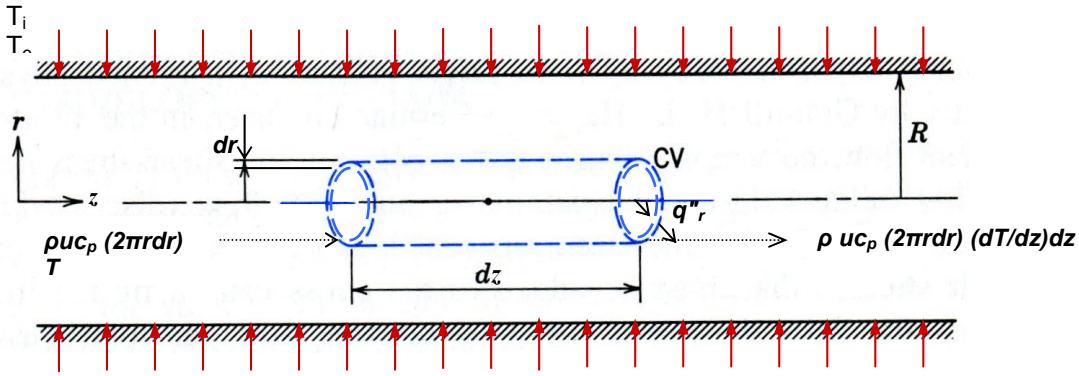

Fig. 2.2: *Annular control volume analysis of heat balance in diabatic tube flow*

Assuming there is a constant heat flux at the wall q''_w, the heat balance is (in cylindrical co-ordinates – see equation (2.51) – and neglecting second-order differentials):

$$r\rho c_p u \frac{\partial T}{\partial z} dz dr = k_f \left(\frac{\partial T}{\partial r} + r \frac{\partial^2 T}{\partial r^2} \right) dz dr \tag{2.39}$$

since the radial heat flow conducted into and out of the element can be transcribed with Fourier's conduction law (see footnote 2, with k_f the conductivity of the fluid). The l.h.s. of equation (2.39) represents the convective term of heat transported through the element, which must find equilibrium with the heat put into the element through conduction (r.h.s.). The equation may be rewritten as:

$$\frac{1}{ur} \frac{\partial}{\partial r} \left(r \frac{\partial T}{\partial r} \right) = \frac{\rho c_p}{k_f} \frac{\partial T}{\partial z} \tag{2.40}$$

Constant heat flux boundary condition

If the heat flux at the wall is constant, and assuming constant thermophysical properties, the average fluid temperature must increase linearly along the axis. Also, the temperature profiles will be similar at all cross-sections and axial-symmetrical. Applying these boundary conditions to the differential equation and inserting the laminar velocity profile for u (equation (2.25)), allows us to obtain the description of the temperature profile in terms of the centerline fluid temperature T_c:

$$T - T_c = \frac{\rho c_p}{k_f}\frac{\partial T}{\partial z}\frac{u_c R^2}{4}\left[\left(\frac{r}{R}\right)^2 - \frac{1}{4}\left(\frac{r}{R}\right)^4\right] \tag{2.41}$$

For most tube- or channel-flow heat transfer problems the topic of central interest is the total energy transferred to the fluid in either an elemental length of the tube or over the entire channel length. At any z position, the temperature that is indicative of the total energy of the flow is an integrated mass-energy temperature over the entire flow area: we refer to this temperature as the fluid *bulk* – or *mixing cup* – temperature, T_b, which is calculated from the temperature profile of equation (2.41) as follows:

$$T_b = \frac{\int_0^R \rho u c_p T 2\pi r dr}{\int_0^R \rho u c_p 2\pi r dr} \tag{2.42}$$

All types of convection are governed by Newton's law of cooling, which is the defining equation for the *heat transfer coefficient, h*:

$$q'' = h\left(T_R - T_b\right) \tag{2.43}$$

where T_R is the fluid temperature at the inner wall, calculable from the temperature profile at $r = R$.

The total heat transfer rate absorbed by the fluid per unit area q'' at any given axial location must be equal to the heat exchanged through conduction at the wall at that location (Fourier's conduction law at $r = R$), so that the following similitude is obtained:

$$h = \frac{k_f\left(\frac{\partial T}{\partial r}\right)_{r=R}}{T_R - T_b} \tag{2.44}$$

where the radial temperature gradient will be derived again from differentiation to r of equation (2.41). When all calculations and substitutions are performed, the heat transfer coefficient for laminar tube flow with constant heat input at the wall results:

$$h = \frac{48}{11}\frac{k_f}{d} \tag{2.45}$$

with d as the inner diameter of the tube. Expressed in terms of the Nusselt number:

$$Nu = \frac{hd}{k_f} = 4.364 \tag{2.46}$$

Constant temperature boundary condition

If a constant wall temperature is taken as boundary condition rather than constant heat flux, the analytical solution for the Nusselt number proves to be $Nu = 3.66$. For turbulent flow we have already seen that the velocity profile is impossible to resolve analytically; in fact, for turbulent heat transfer also only empirical correlations for the Nusselt number can be devised. The most widely used are the Dittus-Boelter correlation for fully turbulent flow ($Re > 10000$):

$$Nu = 0.023\, Re^{0.8}\, Pr^{0.4} \tag{2.47}$$

and the Gnielinski correlation, which may also be used in the transition region ($2300 < Re < 10000$):

$$Nu = \frac{\left(f/8\right)\left(Re-1000\right)Pr}{1+12.7\left(f/8\right)^{1/2}\left(Pr^{2/3}-1\right)} \tag{2.48}$$

where $f = \left(1.82\log\left(Re\right)-1.64\right)^{-2}$. This equation is generally valid for both types of boundary conditions.

Experimental determination of the heat transfer coefficient

If one cares to verify the heat transfer coefficient experimentally, *i.e.* without resorting to the analytic or empiric equations above, whether it be because conditions are not quite ideal, or because one wishes to verify these equations in altered circumstances, or because one hopes to identify any unpredicted phenomena this way, one has to resort to resolving equation (2.43). This means measuring the heat transfer rate, fluid bulk temperature and inside wall temperature.

The global heat absorbed by fluid that flows through a heated channel is by definition:

$$q'' = \frac{\Gamma c_p \Delta T_b}{A_{ht}} \tag{2.49}$$

where A_{ht} is the heat transfer area, for a circular tube equal to $\pi d L_{ht}$. The heat capacity c_p is a known quantity that can be assumed constant under most conditions, Γ is the mass flow, and the bulk fluid temperature rise ΔT_b can be derived from measuring the temperature at the inlet and at the outlet of the channel. The *local* value of the bulk temperature is easily obtained in the case of constant wall heat flux, as the average fluid temperature then increases linearly along the heated length[4]. What remains to be established is the inside wall temperature, T_R. Since, experimentally, it is only possible to measure the *outside* wall temperature – due to the geometry, size and material of the tubes utilised – the local temperature distribution in the wall has to be known to derive the temperature at the fluid interface. This shall be the argument of the next sub-section.

[4] In case of constant wall temperature boundary conditions, the Logarithmic Mean Temperature Difference must be used in equation (2.43). The axial development of the fluid bulk temperature inside the pipe is unknown though, so only an overall evaluation of the heat transfer coefficient can be effectuated.

2.3.2 Conduction – wall temperature distribution

We have already spoken of conduction in the previous sub-section: it is the essential heat transfer mechanism through material contact, and is described by Fourier's conduction law (see footnote 2 of this chapter). Looking at pipe flow, the main conduction problem is to establish the temperature distribution *inside the tube wall*.

The equation for the conservation of energy (2.15), applied to the solid wall without internal heat sources, is:

$$\nabla^2 T = 0 \quad (2.50)$$

In cylindrical co-ordinates, where the conditions are axial-symmetric and temperature changes take place only in radial direction (*i.e.* the tube is suitably long), this becomes:

$$\frac{d^2T}{dr^2} + \frac{1}{r}\frac{dT}{dr} = 0 \quad (2.51)$$

This differential equation is text-book material, and quickly leads to the following solution for the inner wall temperature T_i as a function of the outer wall temperature T_o, the inner diameter of the pipe d, outer diameter D, surface heat flux q'' and wall conductivity k_w (for the derivation, see Appendix I):

$$T_i = T_o - \frac{q''}{2k_w} D \ln\frac{D}{d} \quad (2.52)$$

Cylindrical wall with inner heat sources

If inner heat sources are present, as is the case when a metal tube is heated electrically through Joule effect for example, the differential equation to solve is the following:

$$\frac{d^2T}{dr} + \frac{1}{r}\frac{dT}{dr} + \frac{\rho q_m}{k_w} = 0 \quad (2.53)$$

where the source term of equation (2.15) has been added. The procedure for unravelling this differential equation is slightly more exciting, as the interested reader can verify in Appendix I. Eventually, for a cylindrical wall with uniform heating that is removed only through the inner surface of the tube – a valid assumption given the test section set-up of our experiments, see sub-section 4.2.3 – the inside wall temperature calculates as:

$$T_i = T_o - \frac{q'''D^2}{16k_w}\left[2\,ln\left(\frac{D}{d}\right) + \left(\frac{d}{D}\right)^2 - 1\right] \quad (2.54)$$

Here, q''' is the total heat transfer rate in the heated volume of tube wall, $\frac{\pi}{4}\left(D^2 - d^2\right)L_{ht}$. It is related, for a cylindrical wall, to the heat transfer rate per unit area as: $q''' = q''\frac{4d}{D^2 - d^2}$.

We can now proceed to express the local heat transfer coefficient as a function of measurable quantities only. Since the temperature at the wall-fluid interface must be univocal, the wall and fluid

temperatures at the inner wall (T_R and T_i) must be equal. Thus, we can eliminate T_R from equation (2.42) using equation (2.53). To know the total heat transfer rate in the system, we use equation (2.48). Finally, assembling everything and rearranging, we find the heat transfer coefficient expressed in terms of measurable quantities only, for a tube heated internally and uniformly:

$$h = \left\{ \frac{\pi d L_{ht} \left(T_o - T_b\right)}{\Gamma c_p \Delta T_b} - \frac{D^2 d}{16\left(D^2 - d^2\right) k_w} \left[2\ln\left(\frac{D}{d}\right) + \left(\frac{d}{D}\right)^2 - 1 \right] \right\}^{-1} \tag{2.55}$$

For the sake of being complete, the result of the same procedure for the simpler case of no internal heat sources (*i.e.* with heat put in externally at the outer tube surface and wall temperature profile as in equation (2.52)) is given:

$$h = \left\{ \frac{\pi d L_{ht} \left(T_o - T_b\right)}{\Gamma c_p \Delta T_b} - \frac{d}{2k_w} \ln\left(\frac{D}{d}\right) \right\}^{-1} \tag{2.56}$$

2.3.3 Radiation

Thermal radiation is that electromagnetic radiation that a body emits as a result of its temperature. The total energy emitted per unit time and unit area is proportional to the absolute temperature to the fourth power:

$$q_{rad}'' = \sigma_{S-B} T^4 \tag{2.57}$$

This is called the Stefan-Boltzmann law, and $\sigma_{S\text{-}B}$ is the Stefan-Boltzmann constant: 5.599×10^{-8} W/m^2K^4. From the magnitude of this constant it can be noticed that radiated energy will only assume appreciable strength at very high temperatures, though rapidly so when these are reached due to the fourth-power dependence. The temperatures under consideration for our problem of fluid (usually water) flowing through a heated tube, are quite contained, so it is not expected that radiation will be of much influence. Nevertheless, let us represent the situation schematically and calculate the radiated heat loss from a tube at a certain temperature.

If we assume the channel we are studying (at temperature T_1) to be suitably long and enclosed concentrically by a larger pipe (at temperature T_2) – a situation very close to reality for the experiments carried out, see sub-section 4.2.3 – we can apply the radiation law between two long cylinders, and the exchanged heat between the two bodies is:

$$q_{rad} = \frac{\sigma A_1 \left(T_1^4 - T_2^4\right)}{1/\varepsilon_1 + \left(A_1/A_2\right)\left(1/\varepsilon_2 - 1\right)} \tag{2.58}$$

where A and ε are the radiating area and the emissivity of the two bodies, respectively. For the limiting case in which the convex object is enclosed by a very large concave surface, the area ratio A_1/A_2 approaches zero, and the heat radiated by the internal tube will be:

$$q_{rad} = \sigma \pi D L \varepsilon_1 \left(T_1^4 - T_2^4\right) \tag{2.59}$$

In our case, with T_2 being ambient temperature, the entity of this loss was less than 1% of the maximum viscous heating measured in the channel, increasing to a maximum of 2-3% in the case of heat put in externally, and thus considered negligible under all circumstances.

2.4 Scaling effects

In the previous sections, the generalized conservation equations were introduced, and applied to the particular situation of fluid flowing in a cylindrical pipe, with or without the addition of heat. In these analyses, no restrictions were imposed on the pipe diameter. Basing oneself on the assumptions made to set up the final describing equations (like steady-state flow, constant thermophysical properties *etc.*), no alteration is to be expected in the format of these equations on reducing the diameter. In other words, their validity should remain intact and no change is to be expected in their outcome except for what the quantification of the variables will dictate. However, on downscaling the system it might be that some of the *assumptions* are no longer valid, or that ulterior considerations have to be taken into account that might have been done away with as insignificant in the macro-scale account.

What is it that might change physical conditions reducing the characteristic dimension below a certain limit?

Simple-mindedly, we can immediately gain an idea by looking at the definition of the characteristic dimension in terms of the volume and surface area of the system under consideration:

$$d = \left(\frac{V}{A} \right)_{system}$$

From this relation, it can be concluded that the volume-to-area ratio diminishes with smaller characteristic dimension (the pipe diameter is the obvious characteristic dimension in pipe flow), and with it, the importance of *volume-tied* with respect to *surface-tied* properties. Therefore, the more the system shrinks in size, the less important mass, heat capacity, charge, inertia etc. become in defining system behaviour, with respect to pressure, friction, viscosity, hydrophobicity, contact heat transfer and other such properties tied to surface interactions. The engineer might have to take his simplifications back into consideration…

♪ A system can be described accurately even disregarding certain effects, if they have marginal weight on its behaviour, but on miniaturizing said system these disregarded effects might become influential because the characteristic dimension of the system has become of the same order of magnitude as the scale at which they operate. (By the same principle, some effects can be ignored in microscale because they are significant only at large scale, like gravity.)

This is what is understood as a *scaling effect*, and it is an important concept to keep in mind when one peruses the literature on the recent topic of microchannel flow: many times researchers claim to have unveiled a “new” micro-phenomenon, whereas they probably were thrown off-track because some peripheral effect that was not accounted for, turns out to have been influential in the measurements.

A typical, very practical scaling effect is tied to the method of pressure measurement.
To measure the static pressure in duct flow, a small hole – a pressure tapping – is drilled in the channel wall where the desired quantity has to be known, and a pressure transducer is connected to sense the value. The size of this hole need only be very small, so that in conventionally-sized channels no disturbance of the bulk flow will take place. The hole however, for mechanical reasons, has a minimum size, below which it is impossible either to create or to measure through. Now, if the actual channel inside which one wants to measure the local pressure is of the same order of dimension as this tapping, obviously on a global scale the flow is severely altered. In fact, there is actually no more question of a pipe geometry, strictly speaking. The measured pressure therefore, is not referred to channel flow, but is more indicative of the pressure in, say, a T-junction, and

therefore not representative of the quantity one was aiming to measure. This is a typical scaling effect, which also applies – as can be noted – to very practical, hands-on matters, which nevertheless work through in the ultimate scientific conclusions that are purveyed.

In the following sub-sections, some examples of other scaling effects will be elaborated.

2.4.1 Surface roughness and transition to turbulent flow

A good example of a scaling effect we have already seen in the frictional pressure drop of laminar versus turbulent flow. The laminar velocity profile in a tube is nicely parabolic, the fluid flows in layers that do not mix, and the effect of the wall is "elastic" without being disruptive to the layers. In turbulent flow another characteristic dimension is created: the boundary layer. This is the stratum that has to provide continuity between the still wall and the vigorous mixing in the bulk fluid. It is stretched to the utmost as more flow is pushed through the channel, and can thin out to the same dimension as the roughness peaks on the tube wall: the "continuity" layer is mechanically disrupted and this is felt in the head loss of the flow.

Increasing flow velocity in laminar flow, there will be a point in which the smooth layers are stretched to a point that the "elasticity" is broken and mixing, turbulence, is initiated. This point is called transition, and is shown to depend chiefly on the Reynolds number, although there is a certain stochasticity about the exact place of its occurrence. Generally it is held that transition from laminar to turbulent flow takes place at $Re \approx 2300$, with fully turbulent flow achieved at $Re >$ 10,000, but there is a margin of indetermination in these values (in certain very carefully controlled experiments, laminar flow was maintained up to as much as $Re = 100\ 000$ [11], just as fully turbulent flow can be achieved at $Re \approx 3000$).

A large part of the uncertainty in the occurrence of the transition region is due to the relative roughness of the channel. Studies show that the hydraulic smoothness of the flow depends on the relation between the fluid kinematic viscosity ν ($=\mu/\rho$), the roughness height e and a parameter called the *friction velocity*, u_*, defined as:

$$u_* = \sqrt{\frac{\sigma_R}{\rho}} \tag{2.60}$$

According to Schlichting [12], a hydraulically smooth regime – that is to say laminar flow – is maintained as long as the following inequality is satisfied:

$$0 \le \frac{e u_*}{\nu} \le 5 \tag{2.61}$$

where the upper limit of this parameter (which is a Reynolds number formed with the roughness size and friction velocity) determines the maximum value of the velocity at which laminar flow is possible. Using equations (2.22), (2.25), (2.26) and (2.60) we arrive at the following criterion for the roughness at which transitional effects can be expected to start to occur [13]:

$$\frac{e}{R} = 2\frac{e}{d} = \frac{5}{1.41\sqrt{Re}} \tag{2.62}$$

For $Re \approx 2300$ we find that the roughness boundary up to which a channel may be considered smooth and for which the flow should therefore be perfectly laminar up to that point, is $e/d \approx 4\%$. Preger and Samoilenko, as reported by Idelchik [14] further elaborated the question of roughness effect on laminar-to-turbulent transition. They developed empirical correlations to put the blurry

transition region in a more defined light. The well-known Moody diagram for the determination of the friction factor in turbulent flow was filled in by taking a careful look at the critical region where the Hagen-Poiseuille dependency of the friction factor ($f = 64/Re$) loses validity, see figure 2.3.

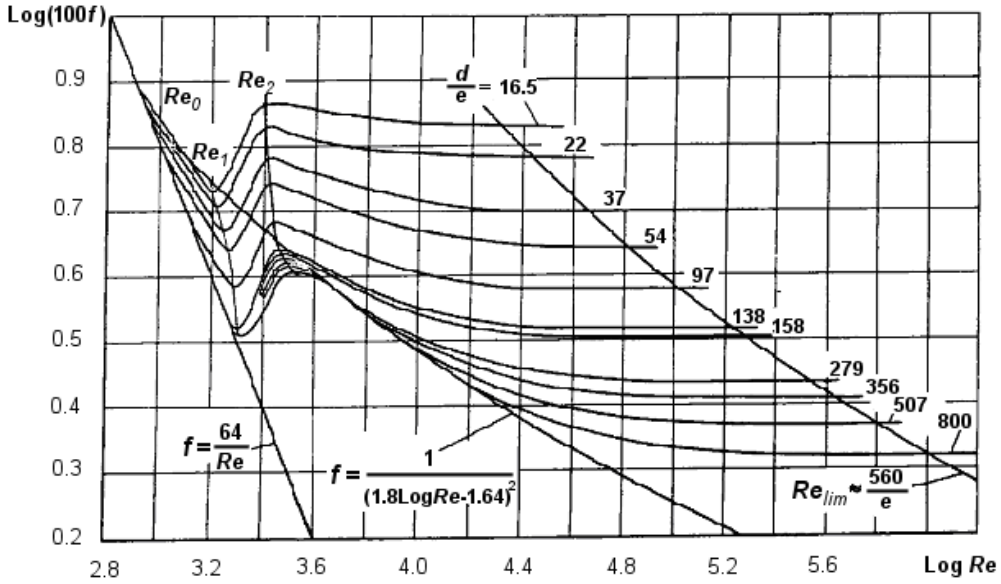

Fig. 2.3: *Moody diagram filled in by Preger and Samoilenko:*
Friction factor vs. Reynolds number with roughness dependency – definition of Re_0, Re_1 *and* Re_2

According to them three distinct points can be discerned in transition from laminar to turbulent flow:

$$Re_0 = 754\, exp\left(\frac{0.0065}{e/d}\right)$$ where deviation from the Hagen-Poiseuille curve occurs; (2.63)

$$Re_1 = 1160\left(\frac{1}{e/d}\right)^{0.11}$$ where the friction factor reaches its minimum value; (2.64)

$$Re_2 = 2090\left(\frac{1}{e/d}\right)^{0.0635}$$ where the friction factor reaches its maximum value. (2.65)

A certain material worked in a certain way will have a more or less constant roughness height e. This means that for all the above relations, reducing the diameter d of a pipe of a certain material worked in a certain way, will eventually bring about a significant influence of the roughness term. This will have an effect on the occurrence of transition from laminar to turbulent flow, but not because of mysterious forces anticipating or delaying turbulence, but because of fixed relations that are always valid – also at macroscale – but that are generally not of significant influence where d is large.

It should be noted that this holds also for the influence of roughness on heat transfer in pipes: the more the asperities are relevant, the more the real wetted perimeter of the channel will be different (larger) than the ideal, smooth perimeter, contributing to an increased heat transfer area.

2.4.2 Slip flow

In the analysis of pipe flow, one of the assumptions was that fluid velocity at the wall be zero, *i.e.* a no-slip boundary condition. Although this widely-accepted boundary condition has been validated experimentally, it remains an assumption that is not strictly based on physical principles. Conditions may arise where the force that keeps fluid molecules in contact with the wall is not strong enough to overcome the shear forces at the wall. This may arise either because the shear rate close to the wall is extremely high, or, conversely, because the attracting force between fluid and solid surface is weakened, or even because the freedom of movement of the fluid molecules is such that no close contact with the wall is enforced. The former two cases arise especially in liquid flows, where the high viscosity and the strong velocity gradient cause high shear stress at the wall, or where the wall is a hydrophobic, non-wettable surface; the latter case is usually tied to gas flows. In all cases, a very narrow passage is required to generate the required conditions in which slip flow might occur.

2.4.2.1 Hydrodynamic slip flow

The occurrence of wall slip in liquid flow has been verified by several researchers, and was even proposed as a possibility by Navier way back in 1823 [15]: if the shear rate at the wall due to the parabolic profile of the velocity becomes high enough, the molecules in contact with the wall might be dragged along with the bulk motion of the fluid. Thus, the boundary condition for the fluid velocity at the wall u_R would be tied to the shear rate $\frac{\partial u}{\partial r}$ at the wall:

$$u_R = \beta \left. \frac{\partial u}{\partial r} \right|_{r=R} \tag{2.66}$$

where β is the so-called *slip length* or slip coefficient and indicates the depth into the wall at which the inferred velocity would go to zero. If $\beta = 0$, the generally assumed no-slip boundary condition is obtained. If β is finite, fluid slip occurs at the wall, but its effect will depend on the length scale of the flow. The velocity profile for laminar fully developed flow with this boundary condition yields (*viz*. equation (2.22)):

$$u = -\frac{R^2}{4\mu}\left(\frac{\partial p}{\partial z}\right)\left[1-\left(\frac{r}{R}\right)^2+\frac{2\beta}{R}\right] \tag{2.67}$$

Thus, for a given frictional pressure drop, the flow through the tube is quicker – or, for a given flow rate, the pressure drop is lower – if slip flow is present. This could be a useful attribute, especially in micro-flows where the head loss is extremely pronounced, because it may allow a significant reduction in the pumping power required to drive the flow. Since β is dependent on shear rate, but can also be significantly affected by the hydrophobicity of the wall, a careful selection of the surface property could bring about appreciable savings this way. The exact dependence of the slip length on contact angle and shear rate is not widely accepted yet, though some studies do deal with the matter [16, 17] (see also in the discussion of results, sub-section 5.1.3).

In attempting to explain the mechanism that causes slip on a hydrophobic surface, the notion has been put forward that a layer of *nanobubbles* is formed on the wall-fluid interface. Tyrrell and Attard [18] managed to achieve striking visualizations of these curious entities, the more so since the putative size of the bubbles is less than the wavelength of light, which rules out optical observation. These images (see figures 2.4a,b) are obtained from Atomic Force Microscopy (AFM)

in the tapping mode, since contact mode imaging destroys or displaces the nanobubbles, which are apparently very delicate.

These images reveal the non-wetting surfaces to be covered with soft domains, apparently nanobubbles, that are close-packed and irregular in cross-section, have a radius of curvature of the order of 100 nm, and a height above the substrate of 20–30 nm. This conclusion is fortified by the large phase shifts represented in figure 2.4a, which indicate that the corresponding features in figure 2.4b are composed of much softer material than the substrate, and that it is not simply surface roughness that is being imaged.

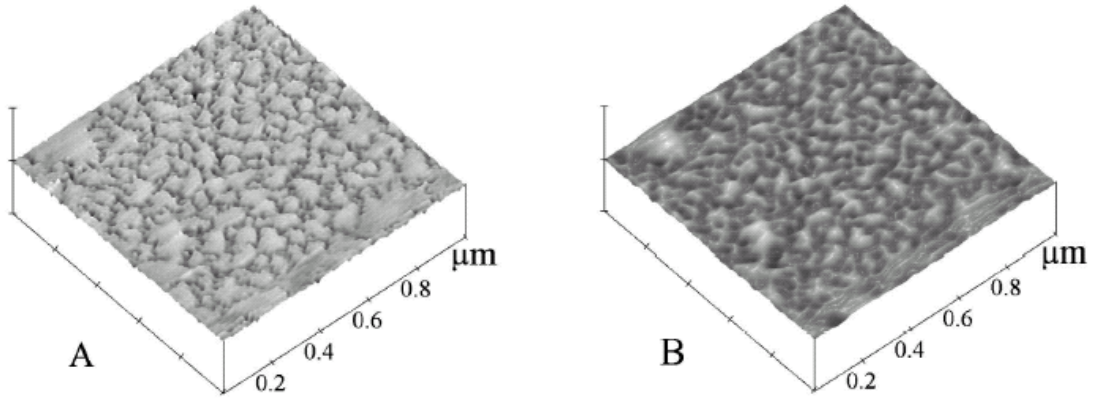

Fig. 2.4a,b: *AFM tapping mode images of a 1µm square of hydrophobic surface in water; peak-to-trough scale in phase image (A): 10° – in height image (B): 30 nm* [18]

It is hard to reconcile the existence and apparent stability of nanobubbles with conventional thermodynamics. They should rapidly dissolve because their high internal gas pressure precludes equilibrium with the atmosphere (the Laplace equation predicts that a 10 nm nanobubble would have a pressure of 140 atm). The images presented here show that this is not the case and that the lateral extent of the nanobubbles is very much greater than their height. In other words, the bubbles are pancake-shaped and rather flat, and the internal gas pressure is therefore much less than previously believed. The irregular and noncircular shape of the nanobubbles indicates that the driving force to minimize the area of the liquid-vapour interface is small compared to the forces that pin the contact line to the substrate. Furthermore, rapid re-emergence of the nanobubbles after they are swept aside suggests that the hydrophobic surface is acting as a nucleation site, pulling dissolved gases out of solution. Thus, the gaseous stratum that is created by the network of nanobubbles practically lifts the liquid off the wall, creating apparent slip flow. In fact, when a two-phase stratified boundary is applied to the fluid-dynamic model, the layer of nanobubbles predicts the slip length measured in experiments rather well [19].

2.4.2.2 Gas-dynamic slip flow

If gas is the working medium, a different mechanism of slip flow may become important on downscaling the fluidic system. The density of gas is orders of magnitude lower than of liquid, so the freedom of movement of the molecules is considerably higher. This is expressed in the *mean free path* of the molecules, λ, which is the average distance a molecule will travel before colliding with another molecule in the system. Intuitively, this quantity will be dependent on temperature and pressure, but also the actual size of the molecule (the *collision diameter* δ) counts; the relation is completed with Boltzmann's constant κ (1.380662×10^{-23} J/K):

$$\lambda = \frac{\kappa T}{\sqrt{2}\pi p \delta^2} \tag{2.68}$$

Again, if the characteristic dimension of the system is reduced to the order of the mean free path of the molecules, there will be no more question of a *bulk* flow – but rather of individual molecules being shot through the flow passage – and fluid-dynamic behaviour can be expected to change radically. The degree of *rarefaction* that takes place of gas flowing in a narrow duct, is expressed by the Knudsen number:

$$Kn = \frac{\lambda}{d} \tag{2.69}$$

where d is the characteristic dimension of the system (the microtube diameter in our case).

In scaling down from continuum flow to fully rarified flow, two intermediate stages are generally classified:

$Kn < 10^{-3}$	*continuum*: conventional Navier-Stokes equations describe the flow;
$10^{-3} < Kn < 10^{-1}$	*slip flow regime*: Navier-Stokes equations can only be employed provided tangential slip-velocity boundary conditions are implemented;
$10^{-1} < Kn < 10$	*transitional regime*: Navier-Stokes equations begin to break down and alternative simulation techniques must be adopted;
$Kn > 10$	*fully rarified* or *free molecular flow*: continuum approach breaks down completely, the flow is of isolated, individual molecules.

The gas that was utilised in the experiments dealt with in this Thesis, was Helium, the molecules of which have a collision diameter of 0.22 nm. At ambient conditions therefore, the mean free path λ of these molecules is around 0.19 μm (equation (2.68)). Channel diameters below 190 μm would thus be small enough to possibly initiate slip flow.

Gas-dynamic slip flow is a rather more developed topic than hydrodynamic slip flow, and several works in the literature address the development of suitable defining equations for the fluid motion. Basically this means coming up with a suitable boundary condition for the slip velocity at the wall (equation (2.66)), which can take on quite complex, high-order forms in some studies [20, 21]. Morini *et al.* [22] elaborated one such model and worked it through to observe directly what the effect of rarefaction is on the global friction factor. Thus, the reduction in the friction factor due to rarefaction effects – calculated by comparing the Poiseuille number (fRe) for an assigned value of the Knudsen number with the value that the Poiseuille number assumes for $Kn = 0$ (i.e., continuum flow) – was found to be:

$$\Phi = \frac{(f\,Re)_{slip}}{(f\,Re)_{cont}} = \frac{1}{1 + \alpha Kn} \tag{2.70}$$

where α is a cross-sectional geometry-related coefficient, equal to 8 for circular channels.

2.4.2.3 Detectability of slip flow effects

What is truly interesting about the previous conclusion, in the light of the nature of this Thesis, is that an evaluation can be made of the sensitivity of an experimental set-up designed to measure any possible slip flow effects [23]. Measurements in a test rig are always subject to uncertainty, tied to

the margin of error of each of its constituent components, such that a certain quantity Y can only be identified within a margin of error e_Y:

$$Y_{meas} \leq Y\left(1+\frac{e_Y}{Y}\right)$$

This means that deviations Δ from the quantity to be verified Y can *not* be evidenced if:

$$Y_{meas} \leq (Y-\Delta)\left(1+\frac{e_Y}{Y}\right) \tag{2.71}$$

Applying this concept to the friction factor reduction in case of slip flow, we obtain the following inequality:

$$(f\,Re)_{cont} \leq (f\,Re)_{slip}\left(1+\frac{e_{f\,Re}}{f\,Re}\right) \tag{2.72}$$

so that applying equation (2.70) gives us a criterion to establish whether slip flow effects will be masked by the experimental uncertainty on the Poiseuille number:

$$\frac{1+\left(\frac{e_{f\,Re}}{f\,Re}\right)}{1+\alpha Kn} \geq 1 \tag{2.73}$$

Thus, the minimum Knudsen number at which evidence of slip flow might be demonstrated is:

$$Kn_{min} = \frac{\left(\frac{e_{f\,Re}}{f\,Re}\right)}{\alpha} \tag{2.74}$$

Calculation of the experimental uncertainty is dealt with in section 4.3.

2.4.3 Viscous dissipation

For a given mass flow through a tube, reducing its diameter causes a squared increase in the fluid velocity. Thus, in microtubes, the fluid velocities achieved can be extremely high. Assuming, conventionally, that there is no slip at the wall, one can vividly imagine how exceptionally stretched-out the parabolic velocity profile must be to satisfy this condition. This very strong viscous deformation of the flow is what causes the exceedingly high pressure drop in a microchannel. From the point of view of the Second Law of Thermodynamics, this huge effort to drive the flow must cause a large irreversible loss somewhere. Indeed, just as a metal bar will heat up as it is drawn or extruded, so the fluid squeezed through a microscopic tube will generate entropy, and therefore heat. This phenomenon is known as viscous heating, or viscous dissipation, and is obviously alien to flow in large-diameter channels, in the sense that the viscous deformation of the velocity profile is quite reduced there, since a large area is available for the flow to pass through.

Consider the equations for conservation of momentum and energy, (2.9) and (2.15). (The following derivation can be obtained in detailed form in [24].) As further simplifications, the flow

will be considered steady-state, incompressible and fully developed throughout a horizontal duct of constant cross-section, with a laminar profile of velocity and no internal heat sources. (This means zero derivatives of the velocity in the direction of flow and zero gravity and source terms.) The mentioned equations reduce to:

$$\begin{cases} \nabla^2 u = -\dfrac{1}{\mu}\dfrac{dp}{dz} \\ k\nabla^2 T + \mu\left[\nabla u \cdot \nabla u\right] = \rho c_p u \dfrac{\partial T}{\partial z} \end{cases} \tag{2.75}$$

Here, the r.h.s. of the energy equation represents convective heat transport and the l.h.s. consists of a conduction term and a viscous dissipation term. Now, reverting through Fourier's law back to a fixed linear heat flux q'_w present at the wall and integrating over the cross-sectional area, the conduction term is described by the fixed linear heat flux q'_w only. The energy equation in (2.75) becomes:

$$\frac{\partial T}{\partial z} = \frac{\partial T_b}{\partial z} = \frac{q'_w + \mu \int_{\Omega} \left[\nabla u \cdot \nabla u\right] d\Omega}{\rho c_p U \Omega} \tag{2.76}$$

where the bulk temperature T_b (equation (2.41)) and the average velocity U have been introduced.

To rewrite the momentum and energy balance equations in dimensionless form, use is made of the following dimensionless parameters:

$$z^* = \frac{z}{L};\ \Omega^* = \frac{\Omega}{d^2};\ \nabla^* = d \cdot \nabla;\ U^* = \frac{u}{U};\ T^* = \frac{\left(T - T_{in}\right)}{\Delta T_{ref}};\ L^* = \frac{L}{d};$$

$$p^* = -\frac{d^2}{\mu U}\frac{dp}{dz};\ Ec = \frac{U^2}{2c_p \Delta T_{ref}};\ \ Pe = \frac{\rho c_p U d}{k} = Re\, Pr;\ q_w{}^* = \frac{q'_w}{k \Delta T_{ref}}.$$

Problem (2.75) is now described in dimensionless form by:

$$\begin{cases} \nabla^{*2} U^* = -p^* \\ \dfrac{\partial T^*{}_b}{\partial z^*} = \dfrac{q_w{}^* L^*}{Pe \Omega^*} + 2\dfrac{Ec L^*}{Re\, \Omega^*} \Phi^* \end{cases} \tag{2.77}$$

where we have defined a dimensionless viscous-energy-dissipation function Φ^*:

$$\Phi^* = \int_{\Omega^*} \left[\nabla^* U^* \cdot \nabla^* U^*\right] d\Omega \tag{2.78}$$

By considering the thermophysical properties as constant, the momentum and energy balances are uncoupled. The momentum conservation equation can then be solved by using the no-slip boundary condition at the wall (which is a reasonable assumption for liquid flow in hydrophilic channels larger than 1 μm hydraulic diameter). From the velocity distribution for laminar flow, it is possible to derive the value assumed by the main flow parameters as a function of the microchannel diameter. In particular, with equation (2.26) and considering carefully the definitions of the dimensionless parameters, it is possible to determine the value of the Poiseuille number using the following relation:

$$f\,Re = -\frac{2}{\Omega^*}\int_{\Omega^*}\nabla^*\cdot\left(\nabla^* U^*\right)d\Omega^* = 2p^* \tag{2.79}$$

It can be demonstrated that the Poiseuille number and the viscous-energy-dissipation function Φ^* are related. Using the properties of the Laplacian operator, integrating over the cross-sectional area and remembering that all velocities are zero at the wall, the momentum equation in (2.77) provides the third equality in the following analogies:

$$\Phi^* = \int_{\Omega^*}\left[\nabla^* U^*\cdot\nabla^* U^*\right]d\Omega = -\int_{\Omega^*} U^*\nabla^{*2}U^* d\Omega = p^*\Omega^* = \tfrac{1}{2} f\,Re\,\Omega^* \tag{2.80}$$

The heat generation due to viscous dissipation in the 1D average model then, can be traced back to friction at the channel walls. Combining equation (2.80) with the energy equation in (2.77), the axial variation of the bulk temperature is thus related to the Poiseuille number:

$$\frac{\partial T^*_b}{\partial z^*} = \frac{q_w^* L^*}{Pe\Omega^*} + \frac{Ec}{Re}\left[f\,Re\,L^*\right] \tag{2.81}$$

Equation (2.81) states that the bulk fluid temperature difference between inlet and outlet of a microtube can be considered as the sum of two terms: the temperature increase related to the heat flux at the wall and the temperature rise due to viscous dissipation in the fluid. In heated or cooled macro-sized channels, the first term is always predominant over the second term, especially in laminar regime. If the channel size is miniaturized enough though, the viscous heating term can become decidedly significant.

> As an example, for a tube with inner diameter (ID) equal to 1 cm, and 1 m long, through which water flows in laminar regime (Re = 1000) the temperature rise due to viscous dissipation is of the order of 10^{-5} K; for an ID equal to 100 μm the temperature rise in same conditions becomes of the order of 10 K and thus significant. This is evidence that viscous heating can be considered a classic *scaling effect* for microchannels.

To analyze the contribution of viscous dissipation alone on the temperature rise, an adiabatic microtube will be considered; so that by integration of equation (2.81) over the length of the channel, where entrance effects are negligible, the value of the dimensionless temperature at the outlet can be calculated as:

$$T^*_b\left(z^*=1\right) = \frac{\Delta T_b}{\Delta T_{ref}} = \frac{Ec}{Re}\left[f\,Re\,L^*\right] \tag{2.82}$$

Hence, the outlet temperature increases if the mean velocity of the fluid increases and if the micropipe diameter decreases; the role of the microchannel geometry is taken into account by means of the term in brackets of equation (2.82). Reverting back to dimensional parameters, the temperature gradient along the microchannel due to viscous heating can now be expressed as follows:

$$\frac{\partial T_b}{\partial z} = \left(\frac{Ec}{Re}\left[f\,Re\right]\right)\frac{\Delta T_{ref}}{d} \tag{2.83}$$

In this equation ΔT_{ref} is a reference temperature rise; this value can be fixed by considering the temperature sensitivity of fluid viscosity; for instance, it could be defined as the temperature rise for which the dynamic viscosity decreases, say, 2-3%. Thus, in order to validly neglect the effects of viscous dissipation in adiabatic flow through microchannels, the temperature rise so induced, between inlet and outlet, shall be less than the reference temperature rise. This enables us to formulate a criterion to establish when viscous dissipation effects cannot be ignored. From equation (2.80) it follows that this is the case if the following condition is satisfied.

$$\frac{Ec}{Re}\left[f\,Re\,L^*\right] \geq 1 \tag{2.84}$$

It is evident that for different fluids the viscous dissipation effect will be different. Considering equation (2.83), the temperature gradient of a fluid c can be rewritten as:

$$\left(\frac{\partial T_b}{\partial z}\right)_c = \frac{[fRe]Re}{2d}\frac{\nu_c{}^2}{c_{p_c}} = K\frac{\nu_c{}^2}{c_{p_c}} \tag{2.85}$$

(for a fixed value of Reynolds number, hydraulic diameter and cross-section geometry), so that for two different fluids, c and d, the temperature gradients are linked to their thermophysical properties as follows:

$$\frac{\left(\frac{\partial T_b}{\partial z}\right)_c}{\left(\frac{\partial T_b}{\partial z}\right)_d} = \left(\frac{\nu_c}{\nu_d}\right)^2\left(\frac{c_{p_d}}{c_{p_c}}\right) \tag{2.86}$$

Finally, it must be noted that equation (2.82) above can be employed to determine the value assumed by the apparent friction factor:

$$f_{app} = \frac{\Delta T_b}{\Delta T_{ref}}\left[\frac{1}{Ec\cdot L^*}\right] \tag{2.87}$$

Equation (2.87) enables us to determine the friction factor without measuring the pressure drop along the microchannel, but by means of temperature and flow rate measurement alone. This can be of considerable advantage at microscale, where pressure tappings and transducers are usually coarse compared to channel dimensions and can be disrupting to the flow. Temperature measurement on the other hand, can be effectuated with comparatively non-invasive means. For large-scale ducts, pressure measurement is far more convenient, as also the temperature effect of viscous dissipation would be negligible in macro-channels, as was indicated earlier.

2.4.4 Axial conduction in the wall

In the discussion on conduction in sub-section 2.3.2, where we obtained the temperature distribution in the tube wall necessary for the determination of the heat transfer coefficient, we assumed the heat flow to take place only in radial direction. Obviously, if a fluid is heated in a pipe with constant heat flux, its temperature *and the wall's* will increase as it flows through the duct. This means that there will be a temperature difference between the outlet and the inlet of the heated tube. Temperature difference means heat conduction: thus, we have generated a potential for heat to flow axially along

the wall (along the fluid is also possible, but as it possesses convective force in the opposite direction, backflow of heat through the working medium is suppressed), and the previous assumption will not hold any more. This superposition of convective and conductive heat fluxes (in perpendicular directions) is known as conjugate heat transfer. It has been studied in the researching past, but its practical importance was generally very limited, since the channel walls in conventionally-sized heat exchanging and fluid flow equipment are usually thin compared to the cross-sectional flow area, so that backflow of heat along the solid walls is always marginal compared to the main transport of heat inside the conduit. It can be felt coming: in microchannels this is not necessarily the case. Due to the exceedingly small diameter of a microtube, combined with the physical necessity of a certain thickness of the capillary for purely practical purposes of production and handling, the proportion of wall thickness and flow area is often inverted. This means that less resistance is put up to the backflow of heat along the walls, and axial conduction can become a competitive mechanism of heat transfer with respect to the internal convection. The consequence is that the wall heat flux cannot stay uniform and that heat accumulates near the entrance of the microchannel, where more heat exchange will take place. Thus, also the bulk fluid temperature rise will not be linear any more, but rather convex (see figure 2.5), so that in the heat transfer equation (2.44), the local value of heat transfer coefficient will be underestimated if nevertheless linear heating is assumed (due to underestimation of T_b).

Unfortunately, an analytical solution to the conjugate problem is generally not possible, and one has to resort to numerical methods for resolving the energy equation, see *e.g.* [25] where simulations were done on a parallel-plate geometry and several fluid temperature profiles along the axial distance x were obtained, according to the influence of axial conduction in the walls (reported in figure 2.5). However, what can be thought up without the aid of computers, is the combination of physical parameters that describe the conjugate effects *qualitatively*. Though in the cited article this dimensionless quantity is claimed to have been invented newly by the authors – under the name of the M number, which is what is given in figure 2.5 – the exact same parameter was proposed by Chiou [26] 23 years before in describing the same situation, just not in a microchannel.

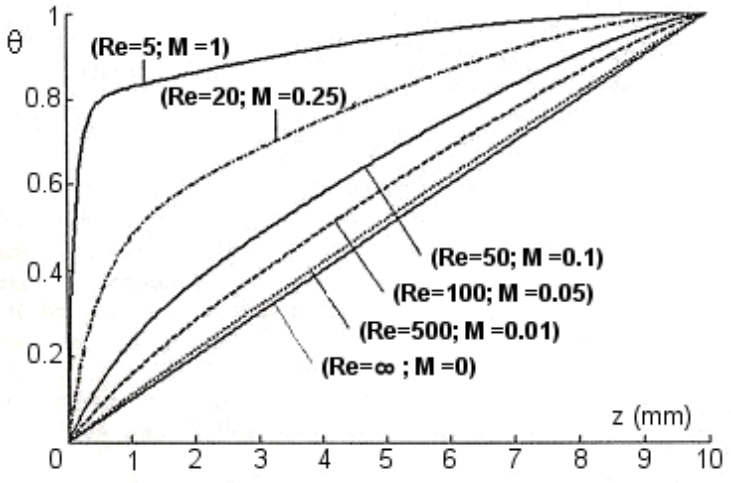

Fig. 2.5: *Normalized bulk temperature* θ *vs. axial location for several Reynolds and conductance numbers* [25]

Intuitively, the importance of axial conduction effects will be tied to: wall conductivity, the ratio of wall and flow passage cross-sectional area, channel length, the convective force and heat capacity of the fluid. Chiou's dimensionless *conductance number* thus is defined as:

$$M = \left(\frac{k_w}{k_f}\right)\left(\frac{D^2 - d^2}{dL}\right)\frac{1}{Re\,Pr} > 10^{-2} \tag{2.88}$$

where the numerical value is the criterion given in [25], above which axial conduction effects in the wall cannot be neglected.

2.4.5 Entrance effects – Thermal entrance length

Laminar flow

When fluid flows from the relatively static inlet plenum into the restrictive channel, it is accelerated and develops its velocity profile. The same goes for its temperature: if the flow enters a heated section of the duct, the temperature profile alters until the steady-state distribution is reached (see figures 2.6 and 2.7 respectively). In these transitory regions we cannot speak of fully-developed flow, so that care should be taken to allow for the entrance region before applying the correlations of the previous sections, which as a rule rely on a steady-state situation.

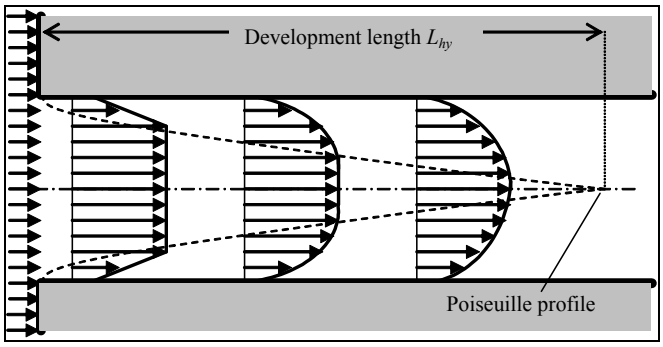

Fig.2.6: *Velocity profile development in the fluid-dynamic entrance length*

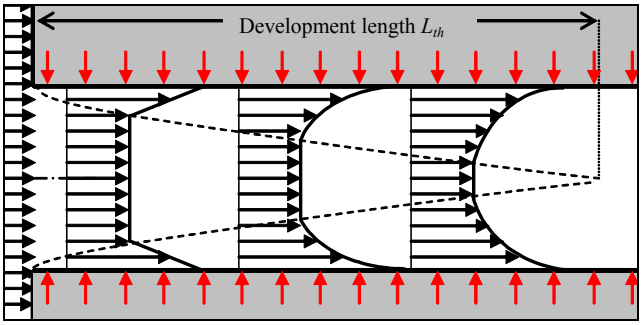

Fig. 2.7: *Temperature profile development in the thermal entrance length*

The hydrodynamic entrance length is calculated from the empirical correlation [27]:

$$L_{hy} = 0.055 \cdot Re \cdot d \tag{2.89}$$

The thermal entrance length is less well-defined. Shah & London [27] give a more or less arbitrary criterion, assuming uniform heat flux at the walls:

$$L_{th} = 0.0430527 \cdot Re \cdot Pr \cdot d \tag{2.90}$$

The entrance regions can become important in microchannel applications when the length of the ducts is chosen short, to save on pressure loss for example. Generally, the thermal entrance length is the more critical one: for a 120 µm tube heated at 50 kW/m^2 and water flowing at Re = 1000 and Pr

= 5.7, the hydrodynamic entrance length is 6.6 mm, whereas the thermal development length is 30 mm.

Obviously, the *bulk* temperature will be increasing continuously as the flow travels through the uniformly heated channel, so thermally fully developed flow must be seen as a steady-state *shape* of the radial temperature distribution rather than *magnitude*. The state of thermal development of the flow can be deduced from the value of the Graetz number:

$$Gz = Re\,Pr\frac{d}{z} \tag{2.91}$$

A thermally fully developed profile is achieved when $Gz < 10$ [28], so the longer the distance z along the channel axis and the less force of convection Re, the more chance there is of obtaining a thermally fully developed profile. The thermal entrance length L_{th} can then be obtained solving for z at $Gz = 10$.

The effect of a thermal entrance region is to *increase the Nusselt number* compared to that of the thermally fully developed region (see also [27]). This can be deduced from the heat transfer law of equation (2.42): before the fluid enters the heated section of tube, its temperature and that of the wall will be equal, so that when the heat flux does arrive, the temperature difference ($T_R - T_b$) will still be close to zero; ergo, the heat transfer coefficient h – and therefore the Nusselt number – will soar, theoretically, to infinity.

The generalized Hausen correlation describes the *mean* Nusselt number (taken over the entire heated length) as the sum of two terms: a fully developed value of Nu, and a term taking into account the effects of the thermal entrance region:

$$< Nu >= Nu_\infty + K_1 \frac{Gz}{\left(1 + K_2 Gz^b\right)} \tag{2.92}$$

Here the Graetz number is taken over the entire heated length of channel, and in the case of constant wall heat flux and fully developed velocity profile, for circular ducts: $K_1 = 0.023$, $K_2 = 0.0012$ and $b = 1$ [29].

Turbulent flow

Entrance effects for turbulent flow in tubes are more complicated than for laminar flow and cannot be expressed in terms of a simple function of the Graetz number. In figure 2.8 numerical computations of the influence of several values of the Reynolds and Prandtl numbers on the local Nusselt number are sketched. In general, the higher Pr and the lower Re, the shorter the entrance length. Thermal entry lengths are much shorter for turbulent flow than for their laminar counterpart.

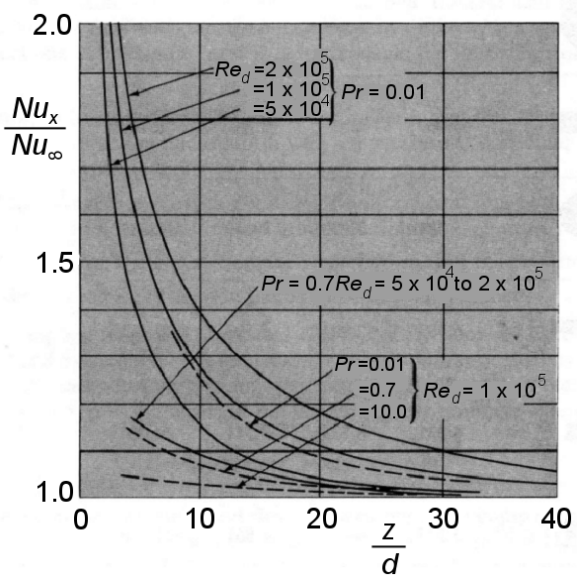

Fig. 2.8: *Turbulent thermal entry Nusselt numbers for circular tubes with constant heat flux* [3]

2.5 Definition of a "micro" channel

After all that has been said and done about the classic descriptions of the physics of (heated) pipe flow and about the traps in the form of scaling effects that lurk in their transposition to microscale systems, where, then, is the boundary at which one leaves the realm of conventional-scale fluid dynamics and enters the Lilliputian kingdom of microfluidics?

The simplest criterion is the literal one: below 1 millimetre, the order of magnitude is measured conveniently in micron: thus, microscale. The difficulties arise as soon as one tries to attach physical significance to the transition from macro- to microscale. In fact, the definitions of a microchannel found in the literature are usually quite random, and the choice of diameter that indicates the advent of microscale characterization is not motivated by any particular physical cause. Mehendale *et al.* [30] call channels "micro" if their diameters fall between 1 and 100 μm, "meso" if they fall between 0.1 and 1 mm and "macro" or "conventional" for diameters larger than 1 mm. Kandlikar [31] maintains that diameters smaller than 200 μm are "micro" and smaller than 3 mm "mini". Larger than that they may be called conventional. Where boiling in microchannels is concerned, the dimension of the bubble provides a convenient basis for the definition of a "micro" regime, so that several criteria have been proposed there too [32, 33, 89, 90].

As the section on scaling effects has shown us, there is no proof that new phenomenology arises when the system is miniaturized, since most "novel" effects that might spring up are coherently predicted by carefully applied conventional theory.

♪ Some assumptions that can be made to characterize a system with large dimensions, are no longer accurate when the object of study is small enough. Thus, the definition of a microchannel becomes more of a *series of criteria* indicating when a negligible effect starts to become important, usually – but only *possibly* – because of diameter reduction. This means that the transition between "macro" and "micro" – if we want to tie these terms to aspects of physical behaviour – depends on the aspect one wishes to study. If one uses the Knudsen number as a criterion, for example, a certain diameter of the system will signal the advent of gas-dynamic slip flow (*for a given gas at given flow conditions*), which we could consider a "micro" effect. If, on the other hand, as a criterion we use the roughness of the pipe at which a given anticipation of laminar-to-turbulent transition occurs, a different diameter value might be found.

The different scales at which certain mechanisms operate become even more apparent when considering two-phase flow: in flow boiling in large ducts, when a bubble nucleates, it grows until the shear force of the flow detaches it from the wall and incorporates it in – at first – a bubbly flow pattern, before further bubble growth and coalescence might change the pattern to slug flow. If the channel diameter is so small that the nucleating bubble is confined by the walls before detaching, bubble growth will continue in axial direction, plugging the flow area. Thus, a different kind of flow regime is created that is tied largely to the system's characteristic dimension, but that is nevertheless a consequence of conventional phenomena and very much related to *flow conditions* as well.

Example of contrasting "micro" effects

Let us take a look at the three scaling effects tied to heat transfer: viscous dissipation, axial conduction in the walls and thermal entrance length. In particular, let us identify the conditions at which each of these mechanisms becomes significant.

From equation (2.81) we can extract a criterion which establishes the significance of viscous dissipation in a microtube heated with linear heat flux q'_w. Reverting back to dimensional parameters and integrating over the channel length, the equation can be written as:

$$\Delta T_b = \frac{q'_w}{\rho c_p U \Omega} L + \frac{\mu U \Phi^*}{\rho c_p \Omega} L = \Delta T_q + \Delta T_v \tag{2.93}$$

which restates that the bulk temperature rise of the fluid is composed of the diabatic term (ΔT_q) and the viscous dissipation term (ΔT_v). If the latter term is marginal compared to the former, viscous heating effects may be neglected in the flow analysis: introducing the Brinkman number $Br = \frac{\mu U^2}{q'_w}$, we can define a criterion χ that states the limit of significance of viscous dissipation:

$$\chi = \frac{\Delta T_v}{\Delta T_q} = Br \Phi^* = \tfrac{1}{2} Br \Omega^* f\, Re \tag{2.94}$$

Putting this limit at a fixed value, say 5%, gives us the conditions for which viscous dissipation effects may be neglected; in other words when the following inequality is satisfied:

$$Br < \frac{2\chi_{lim}}{\Omega^* f\, Re} \tag{2.95}$$

For a circular tube and with the suggested limit, the Brinkman number must be less than 2×10^{-3}.

The mechanism of viscous heating is accentuated, for a given diameter, as the velocity (the Reynolds number) increases. This means that the bulk fluid temperature rises so that *apparently* the heat transfer coefficient rises as well (see equation (2.44)). In reality however, the temperature rise is not due to the wall heat flux but due to viscous dissipation, so that the real heat transfer coefficient (or Nusselt number) will be lower than imagined. In fact, Morini and Spiga [34] show that the net Nusselt number decreases with increasing Brinkman number according to the following relation:

$$Nu_\infty = \frac{Nu_0}{1 + \varpi Br}$$

where Nu_0 is the fully developed Nusselt number for $Br = 0$, and ω is a parameter depending on the geometry of the channel cross-section and morphology of the heated wall.

On the other hand, increasing fluid velocity will push up the effect of the *thermal entrance length* (*viz.* the Graetz number), which is to factually *increment* the Nusselt number (*viz*. equation (2.92)). Thus, the effects of the thermal entrance region and of viscous dissipation enter into direct competition in determining the heat transfer coefficient. Conversely, at low Reynolds numbers, when the previously discussed two effects will not be strong, *axial conduction in the walls* starts to become influential. As mentioned in sub-section 2.4.4, this has the effect that measurements will underestimate the factual Nusselt number, because the heating conditions are distorted from the ideality that was supposed.

Thus, we have 3 different criteria for the Reynolds number which determine whether scaling effects will be important [35]:

- for low Reynolds numbers ($Re<Re_A$) the heat conduction along the solid wall is coupled to the internal convection: this effect tends to reduce the mean Nusselt number;

- entrance effects become important at high values of the Reynolds numbers ($Re>Re_B$) and tend to increase the mean value of the Nusselt number;
- for high Reynolds numbers ($Re>Re_C$) the effects related to viscous dissipation play up, tending to reduce the mean value of the Nusselt number and contrasting the effects of the entrance region.

The value of Re_A can be calculated using equation (2.85), Re_B can be determined from equation (2.91) with $Gz < 10$ and Re_C can be obtained, in an implicit way, by means of equation (2.95), using the limit value of the Brinkman number. Plotting these criteria in a Nusselt number versus Reynolds number plot shows where and how the different scaling effects influence the mean Nusselt number. This is done in figures 2.9a,b which are taken from [35], using rectangular channels and two kinds of fluid.

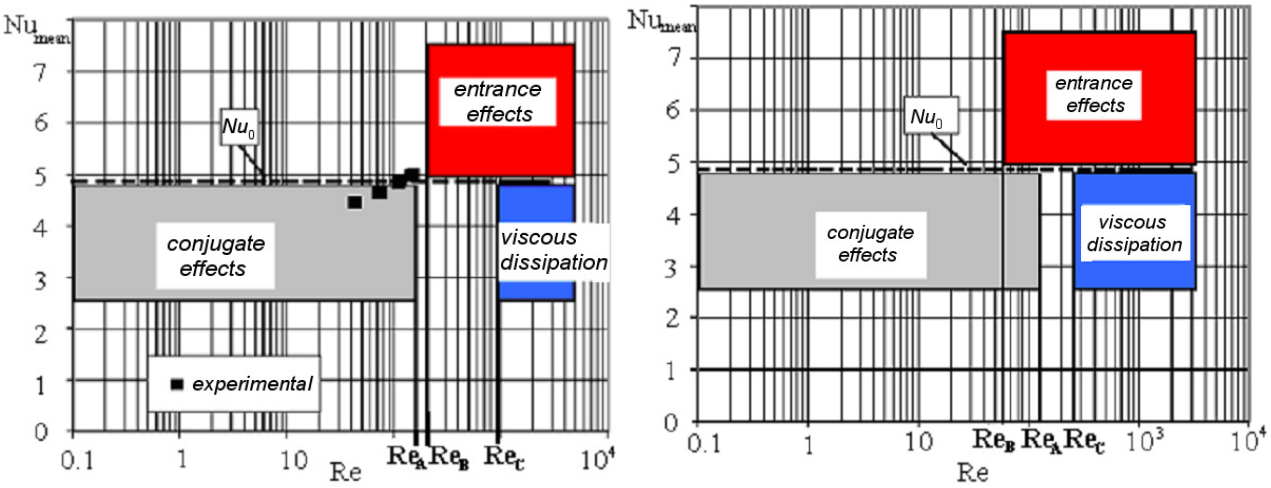

Fig. 2.9a,b: *Scaling effects on the mean value of the Nusselt number for water (a) and isopropanol (b)* [35]

We can see that also *the fluid that is used* determines whether scaling effects will be significant or not: if instead of water (figure 2.9a), isopropanol is used (figure 2.9b) in *identical channels* with the same conditions of heating, different Reynolds numbers mark the rising to importance of conjugate effects (Re_A = 150 vs. 114), thermal entrance effects (Re_B = 200 vs. 54) and viscous dissipation (Re_C = 1000 vs. 256) respectively.

In other words, we are finding difficulty in giving a precise, unequivocal definition of the "micro" scale in terms of size only. One could propose to call microchannels, those channels for which reading glasses of a certain strength have to be donned to see the flow passage at arm's length, at this point…

The circumscription of the domain of microscale therefore, is trivial if a critical dimension is chosen without pertinent motivation; it is equivocal if that motivation is sought in physical terms. Therefore, to prevent further fragmentation and limitation of science through excessive classification, in this Thesis, when is referred to *microgeometries*, simply a scientific-etymological meaning is intended, *i.e. diameters smaller than 1 mm.*

The existence of a "micro regime" in the characterization of transport phenomena *is* justifiable, but implies the occurrence of such scaling effects (one or more) as described in the previous section, which are tied to several process conditions and not just to channel characteristic dimension.

3

STATE OF THE ART

This is not the first study on microchannels. Since the advent of miniaturization in technological appliances a few decades ago, research on the particularities of this regime has been diffusing steadily, in order to better understand and control the performance of all devices microscopic: pumps, heat sinks, actuators, sensors, reactors *etc*. With this expanding research several questions and uncertainties have been unearthed regarding the behaviour of the working fluids used in such circumstances: the properties of flow friction, viscosity, heat transfer, bubble and drop formation and propagation, polarity, diffusivity and others, in sub-millimetre conduits, have they altered manifestations? As many answers – or probably more – have been professed, as the perplexities that have arisen. In this chapter, some of these will be set out and briefly discussed or simply reported. In the first section a survey is given of what can be found in the open literature: in particular on the physical behaviour of single-phase fluid flow and heat transfer in microtubes and -channels. In the second section we will see what answers, in the form of products, the global market can provide us with.

3.1 Literature survey

3.1.1 Fluid flow

The basic aspects of fluid flow in microgeometries that have been studied in the last two dozen years, are the friction factor (or drag coefficient) and the transition from laminar to turbulent flow. Investigation of these characteristics have focused on the influence of channel wall roughness, hydrophobicity, cross-sectional shape and aspect ratio, and of the type of fluid utilised – incompressible or compressible. Some minor works deal with fluid polarity and boundary layer effects like electro-osmosis and local viscosity models, but will not be reviewed here (see for further reference [36-39]).

In the following scheme, the works have been tabulated according to these main points of research. The experimental conditions are listed (channel (hydraulic) diameter, shape and surface; fluid utilised and range of Reynolds number investigated) and the findings are reported regarding the agreement between the experimental and theoretical Poiseuille number (Po/Po_{th}) and the point of transition from laminar to turbulent flow (Re_{tr}). Obviously, the studies that are reported in Table 3.1 are by no means exhaustive: many other works have been published on the matter, but the ones presented are a representative sample.

First of all, it may be noticed that the ground-breaking experiments on laminar flow characterization by Dr. Jean-Louis Poiseuille 170 years ago – from which the Poiseuille profile and the Hagen-Poiseuille law are derived – were done on… microtubes. The validation under certain conditions of a law that was derived exactly for those conditions might seem trivial therefore, but let us say that a periodic reassessment of our knowledge is never amiss. In fact, though the experiments by Poiseuille [6] are remarkable for the care and precision (and time!) with which they were prepared and executed, the means and instruments of the time were decidedly handcrafted, and

it is difficult to imagine that their precision could measure up to that of the sophisticated machines we use nowadays. If it does, that is also valuable information.

In more modern times, the experiments done by Wu and Little [70, 82] were the first to raise interest in the topic. Application in microminiature refrigerators brought them to study gases in trapezoidal microchannels etched in silicon or in glass. They found transition to turbulent flow to be extremely anticipated, and observed a large discrepancy between the experimental and theoretical Poiseuille number. Subsequently, a constantly increasing amount of research has taken place on the possible particularities of microscale flow. This resulted in findings that were often in disagreement or even contradictory to each other. Some institutions maintained to have encountered higher values of the Poiseuille number [43, 48, 49, 56, 57, 60, 61, 62, 66, 69], some lower [40, 52, 63, 65, 73] and some that were comparable to the theoretical dictate.

For rough channels generally a higher friction factor was found, just as for gas flows usually lower friction factors are reported. The dependence on the channel cross-sectional shape is less well defined: both higher and lower values of the Poiseuille number were found whether circular, rectangular or trapezoidal channels were employed. Only one study really compares two different geometries with different experimental conditions (fluids, material, inclination, heat input), and no anomalies were verified there [47].

Sometimes the Poiseuille number was found not to be constant: in most of these cases a positive dependence on the Reynolds number is reported [43, 52, 61, 65, 69], but also an increasing friction constant for smaller diameters has been advocated [48, 69]. In gaseous flows, higher friction factors were found at higher Mach numbers [53, 64], and where truly low experimental values of the Poiseuille number were reported, this was usually in a slip flow regime, at high Knudsen numbers [63, 64, 65].

The values of the Reynolds number at which transition was professed to occur, vary considerably, but anticipated transition is not restricted to rough channels only. According to established theory (see also sub-section 2.4.1), the wall roughness will have an effect on the Reynolds number range wherein transition can be expected. The works where anticipated transition to turbulence was found in smooth channels [44, 58, 67, 68] are slightly suspect therefore. Where an anomalously low critical Reynolds number was found [48, 52, 61, 62, 70] the observations are believed to be erratic, due to incorrect methods of its determination [13].

Microscopic Particle Image Velocimetry (μPIV) was used in two studies to visualize the distortion of the laminar profile due to turbulence [46, 68]. The former study not only validated the conventional transition value, but also confirmed the persistence of the Poiseuille velocity profile for $Re < 1800$ for a wide range of microdiameters.

Kohl *et al*. [9] are the only ones to have observed a dependence of the transition point on the channel length: the shorter the channel (in particular: $L/d < 300$), the higher the critical Reynolds number. They did a comprehensive experimental *and numerical* study on liquid and gas flows with local, axial pressure measurements, which provided many interesting results. Others who have managed to place pressure tappings along the (flat) microchannel were [64]. Turner *et al.* found that at $Kn = 0.15$, the friction factor is reduced by half compared to continuum flow. A first order slip model provided reasonable agreement with the experimental data. No influence of roughness was noticed in rarified and compressible flow. The lower friction factors reported in [73] were explained by gas-dynamic slip flow, but according to the criterion established by Morini (see paragraph 2.4.2.3), no slip should have been detectable with their experimental set-up.

It is evident that many discordant affirmations have been published on the fluid-dynamic characteristics of microchannels in the last 20 years. This is in large amount due to the inexperience there was in the field, especially as regards fabrication and measuring techniques and applications; something that is slowly starting to turn into a kind of competence now. In fact, a tendency can be discerned of the latest publications to consolidate the classic behavioural laws of fluid flow in ducts, as the sensibility of the instruments and those who operate them improve.

Table 3.1: *Experimental research on fluid flow in microchannels*

Study	year	*d* [μm]	shape	*e/d* [%]	fluid	*Re*	Re_{tr}	Note:	Po/Po_{th}	Note:
Poiseuille [6]	1840	14 - 652	○	smooth	H_2O	0.2 - 214	-		1	
Yu *et al.* [40]	1995	19 - 102	○	smooth	H_2O	250 - 20000	2000 - 6000		<1	
Maynes & Webb [41]	1996	700	○	smooth	H_2O	500 - 5000	> 2100		1	
Judy *et al.* [42]	2002	15 - 150	○	smooth	H_2O, CH_3OH	8 - 2300	> 2000		1	
Li *et al.* [43]	2003	80 - 200	○	smooth	H_2O	350 - 2300	1700 - 2000		~1	
Yang *et al.* [44]	2003	173 - 4010	○	smooth	H_2O, R134a, air	150 - 50000	1300 - 2000	*~1/*d	1	
Cui *et al.* [45]	2004	3 - 10	○	smooth	H_2O, C-Cl_4 $(CH_3)2CHOH$	0.1 - 24	-		1	
Sharp & Adrian [46]	2004	50 - 247	○	smooth	H_2O, C_3H_8O $C_3H_8O_3$	50 - 3000	1800 - 2000	*μPIV used*	1	
Celata *et al.* [47]	2006	259 - 1699	○	smooth	H_2O, R134a	100 - 4000	1800 - 3000		1	*also diabatic experiments*
Mala & Li [48]	1999	50 - 254	○	1.4 - 7	H_2O	100 - 2100	< 1000		>1	*~1/*d *(1 for* Re < *500)*
Celata *et al.* [49]	2002	130	○	2.65	R114	100 - 8000	1900 - 2500		1 >1	Re < *900* Re > *900*
Li *et al.* [43]	2003	129 - 180	○	3 - 4	H_2O	350 - 2300	1700		1.15 - 1.37	~Re *for* Re < *1500*
Kandlikar *et al.* [50]	2003	620 - 1070	○	0.32 - 0.71	H_2O	500 - 2600	~2300		~1	
Lelea *et al.* [51]	2004	125 - 500	○	? (steel)	H_2O	50 - 800	-		1	
Choi *et al.* [52]	1991	3 - 81	○	smooth	N_2	30 - 20000	500 - 2000	*2000 for* d > *50μm* *500 for* d < *10μm*	0.8	~Re
Yu *et al.* [40]	1995	19 - 102	○	smooth	N_2	100 - 1500	-		0.6 - 0.9	
Asako *et al.* [53]	2005	150	○	smooth	N_2	?	-		1	~Ma *but 64 for* Ma < *0.1*
Celata *et al.* [54]	2006	30 - 250	○	smooth	He	10 - 1200	-		1	
Morini *et al.* [55]	2006	50 - 751	○	smooth/ rough	N_2	150 - 6000	1800 - 2300		1	
Papautsky *et al.* [56]	1999	44 - 57	□	smooth	H_2O	0.001 - 10	-		1.2	
Pfund *et al.* [57]	2000	128 - 1050	□	smooth	H_2O	60 - 3450	1700 - 2200		1.08 - 1.12	~H
Xu *et al.* [58]	2000	30 - 344	□	smooth	H_2O	20 - 4000	1500		1	
Gao *et al.* [59]	2002	100 - 1000	□	smooth	H_2O	40 - 8000	2200 - 4000		1	
Hrnjak & Tu [60]	2005	70 - 305	□	smooth	R134a	100 - 3000	1600 - 2300		1.02 - 1.08	
Kohl *et al.* [9]	2005	25 - 100	□	smooth	H_2O	5 - 2000	-		1	
Celata *et al.* [47]	2006	259 - 1699	□	smooth	H_2O, R134a	100 - 4000	1800 - 3000		1	*also diabatic experiments*
Peng *et al.* [61]	1994	133 - 367	□	rough	H_2O	50 - 4000	300 - 700		>1	~Re
Peng & Peterson [62]	1996	133 - 367	□	rough	H2O	200 - 4000	300 - 700		>1	
Pfund *et al.* [57]	2000	257	□	0.74 - 5.7	H2O	60 - 3500	1700 - 2000		1.2	

Table 3.1 *(follows from the previous page)*: *Experimental research on fluid flow in microchannels*

Study	year	*d* [μm]	shape	*e/d* [%]	fluid	*Re*	Re_{tr}	Note:	Po/Po_{th}	Note:
Arkilic *et al.* [63]	1994	2.6	□	smooth	He, N_2	0.01 - 0.5	-		0.35 - 0.45	*0.027* < Kn < *0.594*
Turner *et al.* [64]	2004	5 - 96	□	smooth	He, N_2	0.1 - 1000	-		1	*~1*/Kn, ~Ma *Local* p-*measurements*
Hsieh *et al.* [65]	2004	80	□	smooth	N_2	3 - 89	-		0.66	$\sim Re^{-1.02}$ *0.001* < Kn < *0.024*
Kohl *et al.* [9]	2005	25 - 100	□	smooth	Air	7 - 18800	2300 - 6000	~d/L	1	*accounting for dynamic compressibility* *(*Po *not constant)* *Turbulent as in Blasius* *Local* p-*measurements*
Turner *et al.* [64]	2004	5 - 96	□	0.1 - 6%	He, N_2	0.1 - 1000	-		1	*Local* p-*measurements*
Urbanek *et al.* [66]	1993	5 - 25	▽	smooth	$(CH_3)2CHOH$ $C_5H_{11}OH$	?	-		1.05 - 1.35	~T
Wu & Cheng [67]	2003	26 - 291	▽	h-phobic	H_2O	5 - 3000	1500 - 2000		1	
Hao *et al.* [68]	2005	237	▽	smooth	H_2O	50 - 2800	1500 - 1800	*μPIV used*	1	
Qu *et al.* [69]	2000	51 - 169	▽	1.2 - 1.6%	H_2O	1 - 1500	-		1.08 - 1.4	~Re, *~1*/d
Wu & Little [70]	1983	56 - 75	▽	smooth	N_2, H_2, Ar	200 - 10000	400		1 3-4	*1 in silicon channel* *3-4 in glass channel*
Pfahler *et al.* [71]	1991	1.6 - 3.4	▽	smooth	N_2, He, Ar	50 - 300	-		0.95 - 1.05	*slight* ~Re
Harley *et al.* [72]	1995	1 - 36	▽	smooth	N_2, He, Ar	10 - 1000	-		0.92 - 1.08	*slight* ~Re
Araki *et al.* [73]	2002	4 - 10	▽	smooth	N_2, He	0.04 - 4	-		<1	*Slip undetectable* *(Morini Criterion)*

Table 3.2: *Experimental research on single-phase heat transfer in microchannels*

Study	year	*d* [μm]	shape	*e/d* [%]	fluid	*Re*	*Nu/Nu*$_{th}$	Note:
Yu *et al.* [40]	1995	19 - 102	○	smooth	H_2O	250 - 20000	>1	
Adams *et al.* [74]	1998	760 - 1090	○	smooth	H_2O	3200 - 23000	1 - 2.5	$Nu = Nu_{Gn}(1+F)$ *with* $F=7.6.10^{-5}.Re(1-(d/d_0)^2)$
Hetsroni *et al.* [75]	2004	1070	○	smooth	H_2O	10 - 450	<1	~Re: *strong at* Re < *100, tends to* Nu_{th} *at* Re > *400 (axial conduction)*
Owhaib & Palm [76]	2004	800 - 1700	○	smooth	R134a	1000 - 16000	1	$Nu_{turb} = Nu_{Gn}$
Celata *et al.* [77]	2006	120 - 512	○	smooth	H_2O	100 - 3000	<1 1	d < 500μm: ~Re, *peripheral conduction* d > 500μm: *Accounting for thermal development*
Celata *et al.* [49]	2002	130	○	2.65	R114	100 - 8000	>1	T-*boundary condition;* Nu_{lam} ~ Re
Kandlikar *et al.* [50]	2003	620 - 1032	○	0.16 - 0.36	H_2O	500 - 3000	>1	~(e/d) *for* d < *1mm and* e/d > *0.3%*
Lelea *et al.* [51]	2004	125 - 500	○	? (steel)	H_2O	50 - 800	1	~ Re *Thermal development enhances HT, consistent w/ theory*
Grohmann [78]	2005	250 - 500	○	1.07 - 1.2	Ar (l)	400 - 10000	>1	T-*boundary condition;* *introduced real wetted diameter* (d_w) *concept;*
Choi *et al.* [52]	1991	3 - 81	○	smooth	N_2	50 - 20000	>1	~Re, ~Pr *in laminar flow*
Yu *et al.* [40]	1995	19 - 102	○	smooth	N_2	6000 - 20000	>1	
Wang & Peng [79]	1994	747	□	smooth	H_2O, CH_3OH	80 - 4000	<1	~T, ~*1*/d, ~U *Follows Dittus-Boelter relation w/ 0.00805 instead of 0.023*
Harms *et al.* [80]	1999	404 - 1923	□	smooth	H_2O	173 - 12900	<1 >1	*Narrow channel,* Re < *1500* *Wide channel,* Re > *1000* Nu_{lam} ~ Re
Gao *et al.* [59]	2002	100 - 1000	□	smooth	H_2O	40 - 8000	<1 1	H < *0.5mm (0.4 at* H = *0.1mm)* H > *0.5mm* *Inlet (thermal development) effects & transition studied*
Peng & Peterson [62]	1996	133 - 367	□	? (steel)	H_2O	200 - 4000	<1	Nu *depends on geometric parameters;* Nu_{lam} ~ Re, ~ Pr; Nu_{turb} ~ *(Re.Pr.z)*
Rosengarten *et al.* [16]	2006	70	□	h-phobic	H_2O	1 - 100	<1	*Lower* Nu *with higher shear rate and hydrophobicity*
Wu & Little [81]	1984	134 - 164	□	rough	N_2	200 - 20000	>1	~(e/d)
Qu *et al.*[82]	2002	62 - 169	▽	smooth	H_2O	50 - 1500	<1	*Roughness-viscosity model proposed*
Wu & Cheng [83]	2003	68 - 107	▽	h-phobic	H_2O	10 - 900	>1	*decrease of* Nu *with larger hydrophobicity* *large effect of geometric parameters*
Wu & Cheng [83]	2003	68 - 107	▽	0.6 - 1.1	H_2O	10 - 900	>1	~e/d *large effect of geometric parameters;*

3.1.2 Single-phase heat transfer

The high surface-to-volume ratio of microchannels favour all exchanging processes. In this light, especially compact, high heat flux heat exchangers and lab-on-a-chip devices are promising applications where space, time, material and energy can be saved – possibly increasing performance as well. In downscaling a heat exchanger to miniature proportions the trade-off consists mainly in the fabrication costs, pressure requirements and controllability. This last aspect is important because the characteristic residence time in microvolumes is of course minimal, which makes it difficult to handle very dynamic processes, like boiling for example. Though evaporation on the surface is the most effective way of subtracting heat from a heat source (which is why especially microscale flow boiling is the focus of research these days), the dynamics of bubble formation, coagulation and – dangerously – dry-out, will also be accelerated in micropipes where large heat fluxes are absorbed by small quantities of fluid. Thus, for a simpler, more solid system of compact heat exchange, single-phase flow could be preferred.

Research on single-phase heat transfer in microchannels is not very diffused, especially because, as mentioned, specialists have gone straight for phase-changing flows because of their higher performance. The intermediate step between simple adiabatic flow and the intricate world of flow boiling, however, is essential to fully comprehend all possible microscale effects that might be superimposed as the system complexity is increased. In particular, the regular behaviour of the heat transfer coefficient between the wall and the fluid needs to be investigated, in laminar and turbulent flow, and the possible influence of surface conditions.

The heat transfer coefficient is usually expressed as the Nusselt number, and from Table 3.2 we can see again that the conclusions regarding the adherence or no to theoretical prediction seem to be completely disparate in the open literature so far. In reality, the conditions at which the experiments were carried out are rather different as well. In microscale single-phase heat transfer, effects can be expected of roughness, heated length, viscous dissipation, axial conduction through the channel walls and possibly slip flow (see section 2.4). Thus, we find that the studies done on rough channels have generally yielded increased Nusselt numbers with respect to the maintained reference case (Nu = constant) [49, 50, 78, 81, 83], sometimes inducing also a dependence on the degree of roughness.

The actual channel dimensions and proportions are also influential. Here though, the different effects of increased surface area and possible axial conduction in thick walls might well be mixed, which might explain why in [80] a relatively wide channel yields higher Nusselt numbers and in [59] lower values than theory. In [79] a similar inconsistency between actual and presumed experimental conditions could also have thrown off the researchers, tempting them to come up with a modified correlation. In the same way, [74] and [82] preferred using their mathematical imagination to correlate rather than physical interpretation to explain their data.

Frequently a dependence of the Nusselt number on the Reynolds number is perceived, also in laminar flow, as opposed to the constant value predicted by classical theory [75, 49, 52, 80, 62]. Though not always mentioned, a strong argument that can account for this behaviour is that the flow that was studied was in thermal development, which is a plausible event for most microchannel test sections due to their relatively short heated length [77, 51, 59]. The experimental conditions must then not be deemed as “ideal”, and the reasons for Reynolds-dependent heat transfer must be sought in the explanations provided by conventional theory on thermally developing flow.

For sure, wall conduction effects are the most probable reason for low Nusselt numbers especially at low Reynolds numbers [75, 77, 80, 62]. Only recently though, has it been recognised that this conjugation of heat transfer mechanisms is a recognised probability that has to be taken into account when the inner diameter becomes distinctly small compared to the outer diameter of the test section.

The superposition of counterbalancing effects is also the reason why the qualitative behaviour of the Nusselt number in [16] is coherent with the findings regarding hydrophobic channels in [83] (*i.e.* lower *Nu* at higher shear rates and for increasingly non-wetting walls), but quantitatively, values were found respectively lower and higher than theoretical predictions, since the latter studied contemporaneously the effect of channel aspect ratio (which has an incrementing effect on *Nu*).

Thus, also in single-phase heat transfer, amplification of the reserve of data is desired to be able to establish with more security the dependence of the Nusselt number (and therefore the heat transfer coefficient) on the various parameters in microchannel flow. Care has to be taken in this size-area that the actual process conditions conform to what they are assumed to be. To do this, a reduction of the number of variables in the characterization of heat transfer behaviour is recommendable, so that systematic, step-by-step unravelling can take place of what effects are tied to actual size of the flow passage and which ones are just the result of peripheral changes linked to the miniaturization of the test section.

3.2 Business activity

The following section is an attempt to synthesize the level of commercialisation of microtechnological applications. In this short overview purely Research-and-Development institutions have been omitted, as there is a lot of prototype designing activity as regards microscale applications. The mass production and proliferation of these on the consumer market however, is the ultimate evidence of the degree of development of the technology, also, or especially, from a point of view of production costs.

It is stressed that no sponsoring or publicity is involved whatsoever, but that an impartial survey be provided of the availability of off-the-shelf components relating especially to microfluidic set-ups, be they in the nature of scientific research or of specific product development.

3.2.1 Micro heat sinks and exchangers

In the Introduction, it was pointed out how CPU cooling is one of the most promising areas of application of micro heat exchangers. If in 2004 peak heat fluxes of around 160 W/cm^2 were the norm, the level of power generation that has to be removed in the form of heat in 2010 is estimated to reach a maximum of 300 W/cm^2 [91]. It will be impossible for conventional cooling approaches to satisfy this requirement, which is why increased attention is being directed to more efficient, liquid-cooled heat removal units.

At the moment, only coarse solutions are available commercially for this scope: one of the most sought after liquid-cooling solutions on the consumer market is the WaterChill™ solution by Asetek (Brunderslev, Denmark; http://www.asetek.com) which manages to remove 150 W over an unspecified chip area. It is an extremely bulky system however, which presents itself rather clumsily in the context of a high-tech computer (see figure 3.1).

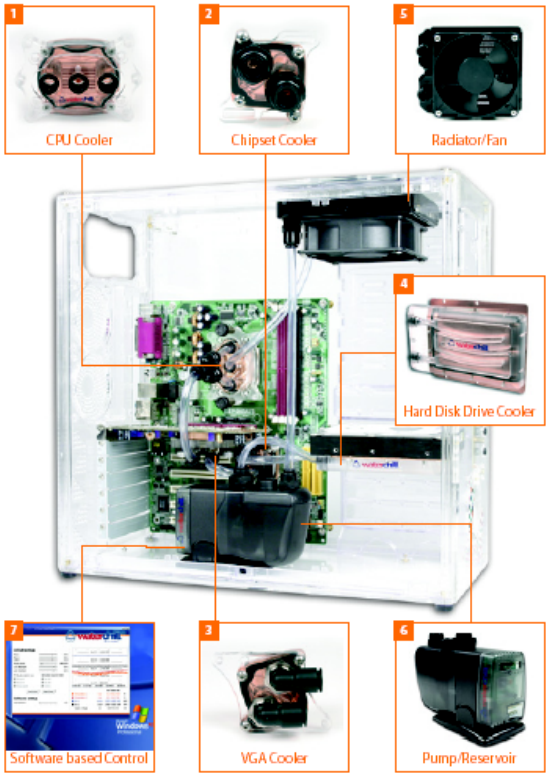

Fig. 3.1: *Liquid cooling in a desktop PC (© Asetek A/S)*

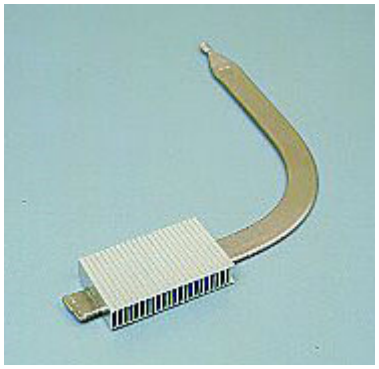

Fig. 3.2: *Example of high-efficiency micro-heat pipe application (heater block dimensions: 5×20×35mm)*

More compact solutions and quite widely utilised, especially in portable computers, are micro heat pipes. These have the great advantage of not necessitating moving parts, as the driving force is provided by capillary action in the wick. They have great potential, especially as near-isothermal heat spreaders. Companies that are cutting edge as far as micro heat pipe technology is concerned are Thermacore (Lancaster (PA), USA; http://www.thermacore.com), Fujikura (Tokyo, Japan; http://www.fujikura.co.jp), Noren Products (Menlo Park (CA), USA; http://www.norenproducts.com) and Furukawa Electric (http://www.furukawa.co.jp/english; Tokyo, Japan). The latter have

developed the micro heat pipe heat sink "HP-HS" as state-of-the-art cooling device (see figure 3.2).

Another company championing a remarkable improvement of heat pipe technology is TS Heatronics (Yokohama, Japan; http://www.tsheatronics.co.jp), who have developed a meandering capillary tube heat pipe, or self-excited oscillation (pulsation) heat pipe (Heatlane™). This technology realizes effective heat transfer (over relatively large temperature differences) conducted not only horizontally but also from top to bottom.

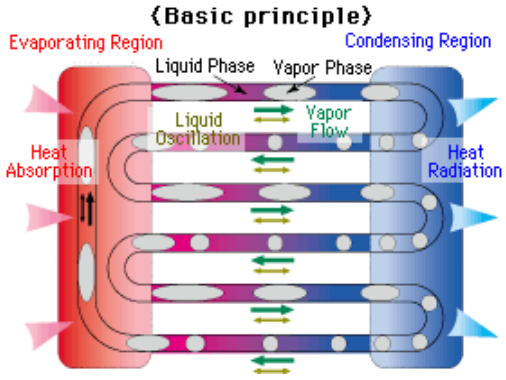

Fig. 3.3: *Operating principle of the micro heat pipe system Heatlane™ (©TS Heatronics)*

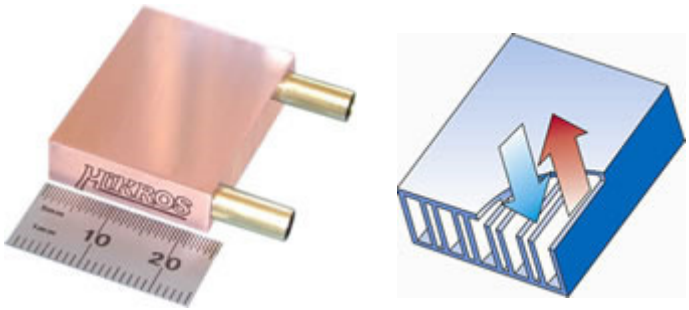

Fig. 3.4: *Normal flow Cold Plate heat exchanger (©Mikros)*

As far as micro heat *exchangers* are concerned, only very few companies have commercialised a model of miniature heat sink based on microchannels as a standard product. (Many Research-and-Development Institutions have prototypes ready and offer custom-made solutions, but very little is found in the way of micro heat exchangers that is a standardized purchasable product.)

Mikros Technologies (Claremont (NH), USA; http://www.mikrostechnologies.com), provider of micro-nozzles for industrial inkjet marking systems, have also developed and now fabricate high performance micro-channel heat exchangers for high-heat-flux electronics cooling applications. Their Normal Flow Cold Plate guides the coolant in the direction normal to the cold plate heat transfer surface (see figure 3.4) and is capable according to them of removing over 1000 W/cm^2 with a low-pressure drop of 2-3 psi.

Yachida (Niigata-ken, Japan; http://www.yacida.co.jp/en/heatex1.html), manufacturer of vacuum devices, with an expertise in diffusion bonding processes and equipment have developed two types of micro heat exchangers, with characteristic channel dimension of 0.2 mm, one of which is shown in figure 3.5a.

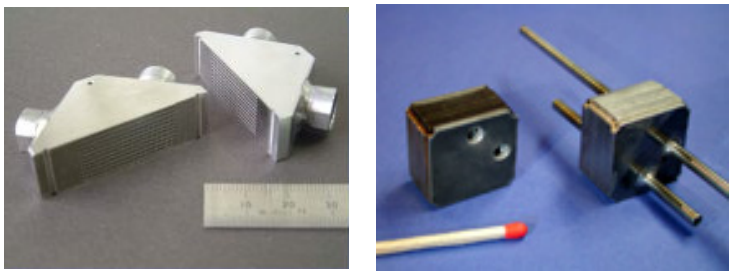

Fig. 3.5a,b: *Two types of market-ready micro-heat exchangers (©Yachida (a) and ©IMM (b))*

In figure 3.5b a market-ready micro-heat exchanger is shown of European manufacture: IMM (Mainz, Germany; http://www.imm-mainz.de) are the producer. Forschungszentrum Karlsruhe (Karlsruhe, Germany; http://www.fzk.de), world-renowned research institute, have developed similar devices.

However, heat transfer improvement through miniaturization does not necessarily mean small applications. The highly effective heat transfer properties of small channels can lead to great savings also in large-scale appliances, simply by multiplying the working component to achieve the desired heat detraction capacity. An example is Printed Circuit Heat Exchangers, of which Heatric (Poole, UK; http://www.heatric.com/compact_heat_exchangers.html) are the most productive exponents. Thus, for an off-shore gas processing unit weighing 108 tons, an equally effective

solution was developed based on microchannels weighing only 20 tons (shown in figure 3.6), thereby also saving $15 million.

Fig. 3.6: *Heat exchanger volume reduction through use of microchannels (©Heatric)*

It should be noted that of the presented heat exchanger systems, none feature flow boiling as a heat transfer mechanism. This mechanism offers the possibility of higher heat fluxes than are achievable with convective single phase processes, or even with pool boiling. There are, however, a number of technical issues to be overcome before flow boiling can be conveniently used for cooling *e.g.* electronic chips:

- it is still a problem achieving reliable and stable boiling in microchannels;
- a choice has to be made of the working fluid that combines optimal heat transfer properties combined with silicon suitability;
- the high pressure drop that results from the restricted flow passage area of the microchannels causes large variations in the saturation temperature and flow pattern;
- how to fill and seal the micro-flow-loop?

As of yet, no-one has demonstrated a complete working system based on flow boiling. Yet, such a system will not only need to be built, but its reliability proven, before acceptance by industry.

3.2.2 Micropumps

Forced convective liquid cooling through microchannel heat sinks is among the more promising technologies that have been proposed for achieving very high heat removal rates. However, the pressure heads encountered in microchannel heat sinks can be very high, requiring the use of a sizeable external pump to drive the flow. Especially for personal computers and mobile electronic devices, conventional rotary pumps are unsuitable due to their large size and power consumption,. In response to this critical need, novel pumping strategies, which have been miniaturized to sub-millimeter dimensions, have been developed in the last two decades. These micropumps offer significant advantages for future electronics cooling applications, as they are much smaller in size than conventional pumps and can be potentially integrated into the microchannels.

Micropumps for microchannel heat sinks used in electronics cooling typically would require both high flow rates to meet the high heat flux needs, as well as large pressure heads to overcome the pressure drop. It is not difficult to imagine that existing micropump designs do not simultaneously meet both these demands. Also, since the various forces affecting fluid flow and pump operation scale at different rates with device size, their relative magnitudes at small scales can be considerably different from those at larger scales.

There are two fundamental ways in which the fluid can be driven at microscale: by applying an external pressure gradient (resulting in the well-known Poiseuille velocity profile in laminar flow), or by applying an external electrical field (in which case only in a very thin region at the wall is there a velocity gradient; the velocity profile in the duct can be considered uniform). The latter method only works with polar fluids, for low head loss and at low flow rates, so that it is not immediately interesting from the point of view of possible application, though the absence of moving parts is a strong point in its favour.

Most business activity focuses on pressure-driving the flows, using micropumps. Micropump

(Vancouver (WA), USA; http://www.micropump.com/) offers complete fluid handling system components and assemblies including pump, motor and controller technologies. Both positive displacement and dynamic pump products are deliverable.

Fig. 3.7: *Micro annular gear pump: 140×45×65mm (©Micropump)*

Debiotech (Lausanne, Switzerland; http://www.debiotech.com) performs research and development on medical devices based on microtechnology, micromechanics and microelectronics, but they also have a catalogue of off-the-shelf products: disposable programmable micropumps, miniaturized infusion pumps, contrast media injectors, as well as drug reconstitution devices, flow regulators and nano delivery systems.

Fig. 3.8: *Nanopump*™ *(©Debiotech)*

Bartels Mikrotechnik (see sub-section 3.2.3 on Lab-on-chips) offer plastic micropumps and microvalves produced in series sold as bought-in products, providing customers with the possibility of quickly and easily integrating microfluidic systems into their own products or systems in a cost-efficient manner.

The true promise of micropumps lies in their potential for integration into microchannel heat sinks. Because an individual micropump may not be able to generate sufficient pressure head and flow rate, a number of micropumps in an array or along the length of a channel may need to be used. The entire microchannel cooling system can then be integrated directly onto the chip. Specifically, the cooling channels could be etched directly onto the backside of the silicon substrate used for active devices. Since the micropump components can be integrated directly into cooling channels, the resulting flow loop would contain only the active silicon device (including integrated micropumps and channels) and an external heat exchanger. This would greatly simplify traditional flow loops characterized by large pumps, heat exchangers and heat sinks, all separate from the active device [84].

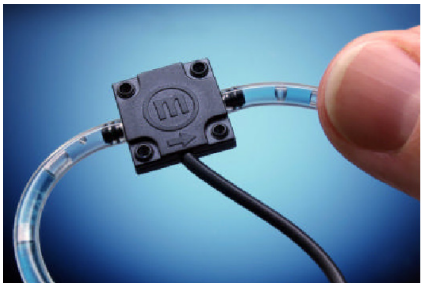

Fig. 3.9: *Membrane Micropump (©Bartels Mikrotechnik)*

3.2.3 Lab-on-chips

Mobile analysis units that can produce rapid results in any location with only tiny sample quantities are increasingly in demand in a world where spaces are reduced, environmental and health regulations are becoming more and more restrictive, polluting and pathogenic emissions are posing risks on sustainable development, and time is running out. Lab-on-a-chip devices are in fact gaining rapid success and are spreading profusely on the market, more so than micro heat exchangers. Obviously, the applications of chemical analysis units are more diverse, and especially more clearly specified, than those of heat removers. Military offence/defence, medicine and process chemistry are major players in the field of elemental analysis and have thereby provided a strong boost to the development of *μTAS*. Thus, also more companies have taken the bull by the horns and have redirected their competences to lab-on-chips.

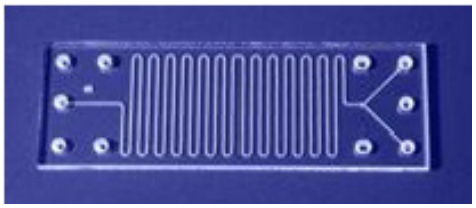

Fig. 3.10: *Microreactor chip (©Micronit Microfluidics)*

Micronit Microfluidics (Enschede, Netherlands; http://www.micronit.com) focuses on lab-on-a-chip design, development and production. They are capable of rapid

prototyping of microfluidic chips and lab-on-a-chip devices, but also manufacture these devices in high volume. They are available in various dimensions, created with several techniques and different materials. The basic material Micronit Microfluidics uses for its products is glass.

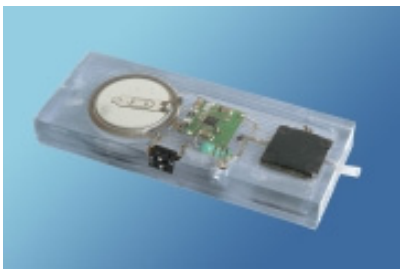

Fig. 3.11: *Physiocheck chip (©Bartels Microtechnik)*

Bartels Mikrotechnik (Dortmund, Germany; http://www.bartels-mikrotechnik.de), in collaboration with partners, have developed a complex plastic chip for analysis of body liquids. The physiocheck-chip (see figure 3.11) integrates microfluidic structures that are as small as 200 x 50 µm. From channel to functional units as spiral mixers, reaction chambers, micro membranes, reservoirs, and detection chambers are combined and parallelized on a single chip. Furthermore, they are competent in high-precision excimerlaser production of microstructures and components specified by the customer.

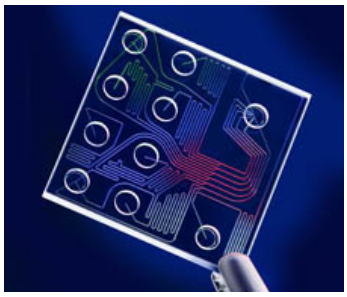

Fig. 3.12: *DNA analysis chip (©Agilent Technologies)*

Agilent (Santa Clara (CA), USA; http://www.chem.agilent.com) provides core electronic and bio-analytical measurement tools to advance the electronics, communications, life science research, environmental and petrochemical industries. Products include mass spectrometers, oscilloscopes, and lab-on-a-chip devices for DNA, RNA and other molecular analyses.

3.2.4 Microfluidic components

Fig. 3.13: *Microfittings for 1/16" tubing (©Upchurch Scientific)*

For the researcher or product developer who wants to assemble his or her own microfluidic system, there are a number of companies who provide the necessary nuts-and-bolts parts.

Upchurch Scientific (situated in Oak Harbor (WA), USA; web-site: http://www.upchurch.com) are a leading manufacturer of fittings, tubing and accessories for the HPLC (High Performance Liquid Chromatography) market and other analytical, biotech, diagnostic and related liquid-transfer instrument markets.

Labsmith (Livermore (CA),USA; http://www.labsmith.com/microfluidickits.html) provides components to build, and re-build, microfluidic setups; inter-compatible and ready to use. Based on the CapTite™ and ChipTite™ components developed by Sandia National Laboratories, these 360 µm (standard capillary OD size) microfluidic products include breadboards, pre-cut capillary tubing, ferrules, tees and crosses, pumps, valves and tools.

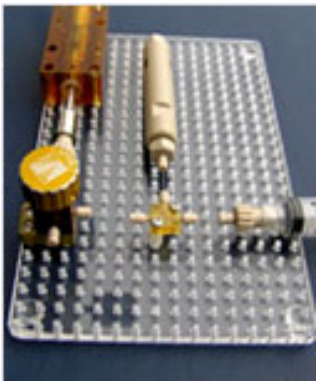

Fig. 3.14: *Microfluidic bread-board, 100×200 mm²* *(©Labsmith)*

Fig. 3.15: *Micro-optic components (©Thinxxs)*

Thinxxs (Zweibrücken, Germany; http://www.thinxxs.com) produces and develops microstructured components and systems. They offer standard microfluidic products (micro diaphragm pumps, microfluidic construction kits, micromixers, fluid splitters, twin pump slides), customization or integration into OEM products, as well as product development and production services. Plastics are at the heart of their solutions, often combined with other materials such as glass, silicon, or metals.

For direct start with microfluidic systems Microfluidic ChipShop (Jena, Germany; www.microfluidic-chipshop.com) offers a catalogue with standard products. This assortment comprises Capillary electrophoresis chips with and without electrodes, micromixers, nanotiterplates, fluidic interfaces and platforms, polymer substrates. Components and systems are realized for applications in analysis and synthesis: lab-on-a-chip systems for diagnostic and bioanalytical applications, mixer and distribution systems for medical technology, micromixers for chemical synthesis, *etc*.

Fig. 3.16: *Micromixers (©Microfluidic Chipshop)*

Fig. 3.17: *Capillaries and tapers (©Polymicro)*

Polymicro Technologies (Phoenix (AZ), USA; http://www.polymicro.com) are a major supplier of fused silica capillary tubing and specialty optical fibres, optical fibre and capillary assemblies, discrete vitreous micro components and quartz optical fibre ferrules.

Sutter (Novato (CA) USA; http://www.sutter.com) specialise in micropipette fabrication, providing both manufacturing service as selling the hardware for in-house production of in particular micron and submicron pipettes and taper fibre optic probes.

Fig. 3.18: *Micropipette puller (©Sutter Instrument)*

Bronkhorst High-Tech (Ruurlo, Netherlands; http://www.bronkhorst.com) are one of the most reliable and successful producers of microflow measuring equipment. They offer a wide product range of thermal mass flow meters and controllers. Flow ranges from 0-1 mln/min up to 1250 ln/min air-equivalent, from 30 mg/h up to 20 kg/h water-equivalent. Also pressure meters and vapour delivery systems are available.

Fig. 3.19: *Microflow meter (©Bronkhorst High-Tech)*

It is clear from the above examples that microtechnology products are still aimed at the top-end market. The required precision of the manufacturing process, the selection of materials and system design lay heavy claims on the production costs, and only in applications where the importance of performance outweighs that of expenditure has the microscale solution gained foothold. Although high-cost-high-efficiency will probably remain a prerogative of miniature applications, this situation provides ample space for improvement of their competitive position.

The most successful application of microfluidic devices so far is probably the lab-on-a-chip: the potential users of miniature total analysis systems cover a wide range of fields, from process industry to medical to military, fulfilling functions varying from forensic investigation to insulin administration.

The widespread use of micro heat exchangers is still latent, though the first prototypes have become consolidated reality and have proved their worth, not only in electronics cooling but also in large-scale industries. It is unlikely that such systems will compete with conventional air-cooling on the basis of cost. Therefore, their introduction would have to be for the top end of the high performance chips, where air cooling is no longer an option. This would allow the opportunity for manufacturing costs to be reduced before these high performance chip capabilities become the expected standard on the market. Another avenue for their introduction is in optoelectronic devices, where their potential to reduce temperature gradients would lead to performance improvements.

Micropumps have many variants, but the most widely used are based on diaphragm operation. These have already found large-scale application in the biomedical field, where precise administration of pharmaceuticals and lubrification of implants are important operations that are necessitated in limitless cases.

In the components industry, the imminent need for microscopic parts has already been appreciated, and many manufacturers and retailers of all kinds of miniature components (capillaries, valves, fittings, meters, controllers, sensors, *etc*.) have offered their products and services on the global market. Some of these components have also been necessary in the building of the experimental set-up used for the gathering of data for this Thesis. The process of its assembly and details of its constituent parts, as well as a description of the methodology of experimentation are the subject of the next chapter.

4

EXPERIMENTAL PROCEDURE

The aim of this study is to put into practice the concepts and empirically validate the hypotheses put forward in chapter 2. To this effect, the design and set-up of the experimental facility will be gone through and described in detail here. Starting with the objects that are of prime interest, the first section will go into the practicalities that yield a reliable, well-characterized microtube for subsequent testing. Fabrication and measurement of such a tube are the processes concerned.

The second section will focus on the insertion of the microtube in a fitting test rig, describing all the apparatus that make up the system of experimentation required for observing the phenomenon under consideration.

In section 4.3, the highly important analysis of experimental accuracy will be set out, serving to put into perspective the difficulty of the experiments to be carried out. An overview of these is summarized and presented in section 4.4.

4.1 The microtubes

This Thesis deals with channels of circular cross-section and sub-millimetre dimensions, and in particular with the conditioning of fluid flow and heat transfer inside these. The circular geometry is useful for the analysis of physical behaviour, because of the simplicity of its co-ordinate system: an axisymmetric problem allows for a 1-dimensional approach in most stationary cases and therefore reduces the margin for error tied to the superposition of a lateral variation in dimensions. This contrasts with the difficulty of *production* of a suitably small, constant, precise channel, which is lower for a rectangular cross-section. Machining or etching a groove and bonding two plates to form a microchannel is an easier and more accessible process than extrusion or drawing and inner surface treatment of capillary tubing (*viz.* sub-section 4.1.1).

The microscopic magnitude of the specimens to be tested puts great demand on the precision of fabrication (instruments used, tolerance margins, production speed) as also on the measurement of their characteristics (diameter, roughness, circularity). These aspects will be dealt with in 4.1.2.

There are ingenious ways of by-passing some measurement constraints tied to the small dimensions of the test section. In 4.1.3 the methodology will be explained that was excogitated to derive the *net* frictional pressure drop along a circular channel that – due to its shape and minitude – does not allow for local *in-situ* pressure measurements.

In sub-section 4.1.4 the modification of the naked capillaries for the enabling of heat input will be shown. A brief word on the fittings connecting the microtube to the test rig is spent in 4.1.5.

4.1.1Tube production

4.1.1.1 Raw tube fabrication

The quality of the microchannel that needs to be studied, and therefore the proper interpretation of flow measurements, is strongly dependent on the material out of which it is fabricated. Two basic types of material are used for the production of capillaries: metallic (in particular stainless steel) and vitreous (quartz or borosilicate). For slightly larger inner diameters polymeric tubes can also be found on the market.

The fundamental difference between metallic and vitreous capillaries lies in the way they are made. Extrusion drawing from a larger tube is the generative process they have in common, but the response of the two materials to plastic deformation in the absence of an inner mandrel is very different. The drawing process is based on heating the mother shape (a large-diameter tube) up to softening point and pulling it with constant velocity through a (conical) die that serves to reduce the cross-sectional area of the tube. The outer diameter of the drawn product is thereby well defined by the die size, whereas the inner radius of the emerging tube is not directly controlled by tooling. The final thickness of the tube is then a dependent parameter, influenced by the dimensions of the mother tube, the drawing stress, the length of the land of the die, the back tension and the friction between tube and die. In the case of drawing vitreous material this only means there is a relative uncertainty on the *dimension* of the inner radius; the *circularity* and *smoothness* of the inside cross-section is however maintained because the amorphous structure of glass has no preferential orientation. Metal, on the other hand, has a crystalline structure that persists unless it is physically deformed or heat-treated. For large inner diameter tubes a *mandrel* is therefore utilised, that exerts a size determination on wall thickness and inner diameter, as well as providing a smooth finish inside the tube. In the case of capillary tubing, the miniscule dimensions required for the mandrel make it impossible to achieve this, and simple drawing is necessary. The result is exemplified by figures 4.1a,b, that show the respective cross-sections of a glass and steel microtube of similar dimensions. It is clear that the inner surface of the metal capillary is extremely difficult to characterize: how to establish the inner diameter? the roughness? the circularity? For the vitreous tube these parameters are relatively precise and straightforward.

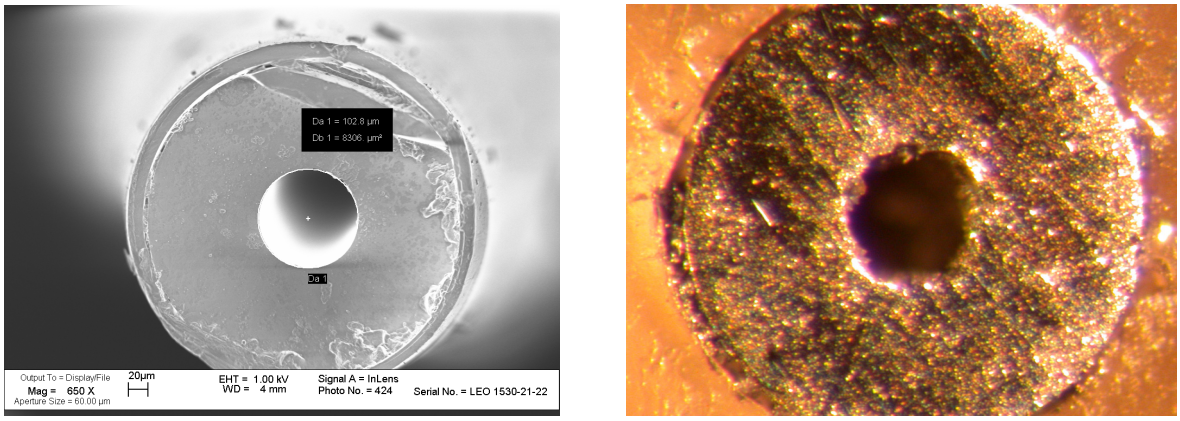

Fig. 4.1a,b: *Similar diameter Fused Silica (a) and Stainless Steel (b) capillaries cross-sections: ~0.1 mm ID, drawn without inner mandrel*

4.1.1.2 Smooth vitreous tubes

For the benefit of reliable and simple channel characterization therefore, glass tubes were opted for, at least for adiabatic experiments and the study of fluid flow behaviour. Two types of vitreous capillary have been used in the experiments reported here: Fused Silica and Borosilicate tubing. The former is manufactured by Polymicro Technology and is commercially available from Upchurch Scientific (see also section 3.2). Fused Silica tubing is highly precise in shape and diameter (see figure 4.1a) and comes with a coating of Polyimide which provides protection and a large amount of flexibility to the otherwise extremely fragile capillary – see the schematic representation of figure 4.2. For constant outer diameter, several inner diameters are available.

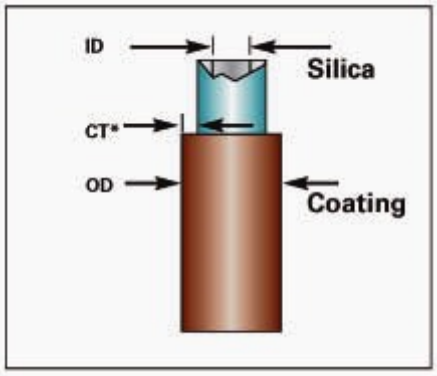

Fig. 4.2: *Schematic example of a Fused Silica tube (©Polymicro Technology)*

The Borosilicate (hereafter to be referred to simply as *glass*) capillaries were manufactured in-house with a custom-made tube puller, where the drawing velocity determines the final dimensions of the product. Thus, a large range of diameters are achievable and – importantly, considering the trying fragility of a glass microtube – in large quantities.

Both types of vitreous tubing are conventionally used as columns in gas chromatography, where the inner surface is coated with the stationary phase that separates the sample compounds.

4.1.1.3 Rough tubes

As mentioned in section 2.4, surface roughness is likely to become an important parameter in channels where the characteristic dimension is reduced considerably. The average value of asperities on the surface is tied to the material and to the way that it is worked. Given these, reducing the dimensions of the channel will cause the size of this roughness to noticeably influence the idealised geometry of the duct. To evaluate this effect, it was attempted to create an artificial roughness inside the otherwise smooth glass tubes (for the measurement of surface roughness, see sub-section 4.1.2). To this purpose, a mixture was used of fine-grain abrasive powder and fluid silicon oil, in a weight ratio of between 1:1 and 1.5:1. This mixture was introduced in the capillary tube with a fine steel thread, and in a to-and-fro motion of about 30 cycles, the entire length of the capillary tube (about 15cm) was 'filed', roughening the inner surface practically without altering the inner diameter.

From figure 4.3 it can be observed that the roughness that is obtained is clearly distinguishable from the untreated, smooth surface of a virgin glass tube (example in figure 4.4b).

For a more immediate achievement of roughened tubes, stainless steel capillaries as described in 4.1.1.1 can be used, although these are of considerably more distorted inner surface quality, rendering a precise, reliable characterization of the roughness difficult.

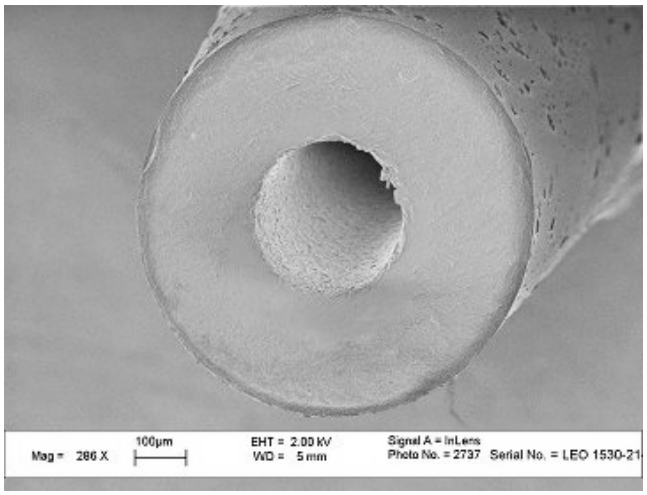

Fig. 4.3: *SEM image of a roughened glass tube; the inner surface can clearly be seen to have a uniform roughness*

4.1.1.4 Hydrophobic tubes

As the fluid-wall interface becomes important with respect to the bulk fluid volume in microducts, the hydrophobicity of the contact surface could start to influence flow characteristics. A non-wetting surface could then give rise to water molecules not adhering to the wall and provoke hydrodynamic slip flow (see paragraph 2.4.2.1). This could conceivably diminish the pressure loss due to friction at the channel wall, thereby improving the power consumption of pumping apparatus – a heavy-weighing aspect in microfluidics. Therefore, a selection of smooth glass tubes was coated on the inside with a hydrophobic substance, in order to verify any slip flow effects while using water in pressure drop experiments. To this effect, capillary tubing about 50 cm in length was treated with a 250:25 volume ratio reactant of Hexamethyldisilazane (HMDS): Divinyltetramethyl-disilazane. Absorbing between 5 and 7 cm of reactant through capillary effect, this plug is then caused to travel along the entire length of tubing and sealed in by fusing the extremities, ensuring a vacuum is kept inside of around 30 mmHg. Static coating then takes place heating the capillaries to 330ºC for about 20 hours. For a better adherence of the non-wetting layer, a subsequent reactant was used to further coat the inside wall (51mg of polymeric Methylsilicone dissolved in 5 ml of 1:1 *n*-pentane/dichloromethane mixture; Dicumylperoxide was added in proportion of 1.5% of the Methylsilicone). Heating the capillaries from 160ºC to 200ºC at 0.3 K /min, the polymer was then immobilized by radicalic reaction through the thermal decomposition of the Dicumylperoxide.

Subsequently the treated, siliconated capillaries could be used directly for experiments.

4.1.2 Tube characterization

Having the tubes in possession is only half the job done. To be able to sensibly interpret the data obtained in experiments, an accurate characterization of the test section is mandatory. This entails measurement of surface roughness, cross-section circularity and constancy, but above all an as precise as possible measurement of the diameter. As was shown in sub-section 2.2.1, the close estimation of this parameter is extremely important, especially in pressure drop analysis, as errors herein weigh heavily on the elaboration of taken data.

4.1.2.1 Measuring tube diameter

There are a number of ways of determining the diameter of a tube, divided principally in:

- indirect measurement of an average diameter based on a volumetric analysis of the capillary,
- direct measurement of a local, cross-sectional diameter.

Indirect measurement methods

These function by taking a length of the capillary to be characterized, and measuring a length-averaged property like weight or fluid-dynamic friction. Here, the longer the piece of tube that is taken into consideration, the less margin for measurement error is realised; but at the same time the less one knows about the lengthwise variation of the cross-section. A classic example is weighing the capillary tube having measured the length and (average) outer diameter. With the density of the tube material known, an estimate can be made of the inner diameter. Similarly, one can choose to weigh the tube before and after filling it with, say, distilled water, and using the density of the liquid to determine the average inner diameter.

Another indirect measuring method is based on measuring the pressure drop of a known fluid in laminar flow. According to the equations of sub-section 2.2.1 it is then possible to derive the average channel diameter. Obviously, if the objective of the experiments to be carried out – as is the case here – is to validate those same equations, one cannot use those equations *a priori*, in the determination of such an important parameter as the inner diameter.

Direct measuring methods

Cross-sectioning the tube and measuring the size of the hole inside – using a magnifying device in the case of microtubes – is a direct measurement. The intrinsic limitation in this case is that the measurement is localized, but by cross-sectioning at several locations a good idea can be got about the variance of the inner diameter. The actual sectioning is a difficulty to be handled carefully. In the case of elastic materials, like metal or PTFE for example, slicing the tube will cause a certain deformation of the cross-section to be measured. The brittleness of glass has the one advantage that with a single incision on the outer surface the cross-sectional cut breaks clear cleanly. The difference can be observed in figures 4.4a,b.

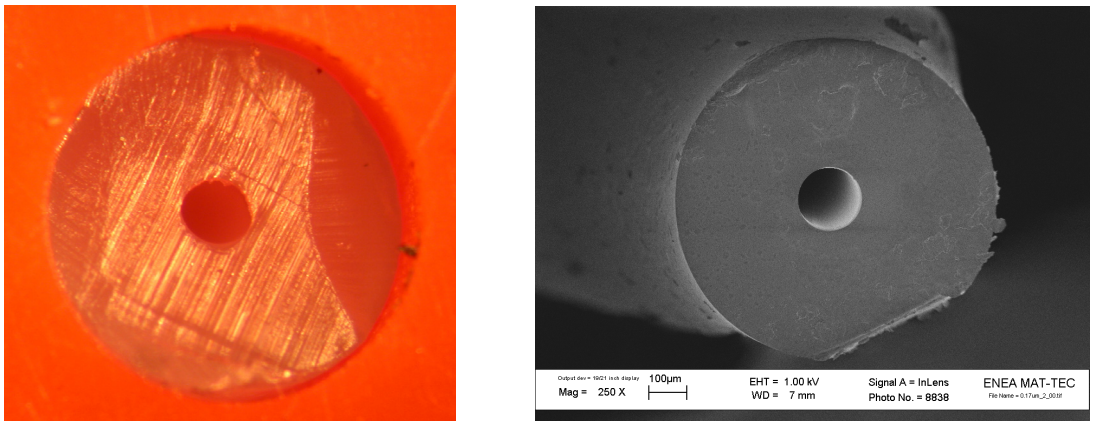

Fig. 4.4a,b: *Cross-sectioned PTFE tube (a) and glass tube (b) for diameter measurement*

Once the cross-section is prepared, the question is how to measure the diameter. Obviously, material measurement devices are unfit for the dimensions dealt with here, so that one has to resort to visual techniques. One method is to project the enlarged image of the cross-section and measure

the latter; knowing the magnification, the real diameter can then be deduced. This entire process can also be done electronically, using a Scanning Electron Microscope (SEM, a Gemini LEO 1530 in our case) for magnification and digitally analysing the image.

Consider the close-up of the inner diameter of the 120 μm siliconated glass tube, figure 4.5a. To determine its magnitude, two methods are possible: i) superimpose a virtual circle on the image, trying to achieve a best-fit, as is done in the figure (the corresponding value of the diameter can be read in the insert); ii) digitally analyse the area and apply pixel count, the result of which can be seen in figure 4.5b.

The processing of the original SEM image is not straightforward. Sometimes, upon magnification, the hole will not be well defined: slight deviations of the cross-section from the plane of focus can cause a fuzzy contour, and specks of extraneous nature that happen to intrude upon the image will distort the pixel count of the inner area. Therefore, the former method was the one generally applied: taking several samples of the same capillary and averaging the estimated diameters of each, a satisfactory definition of the average diameter was found.

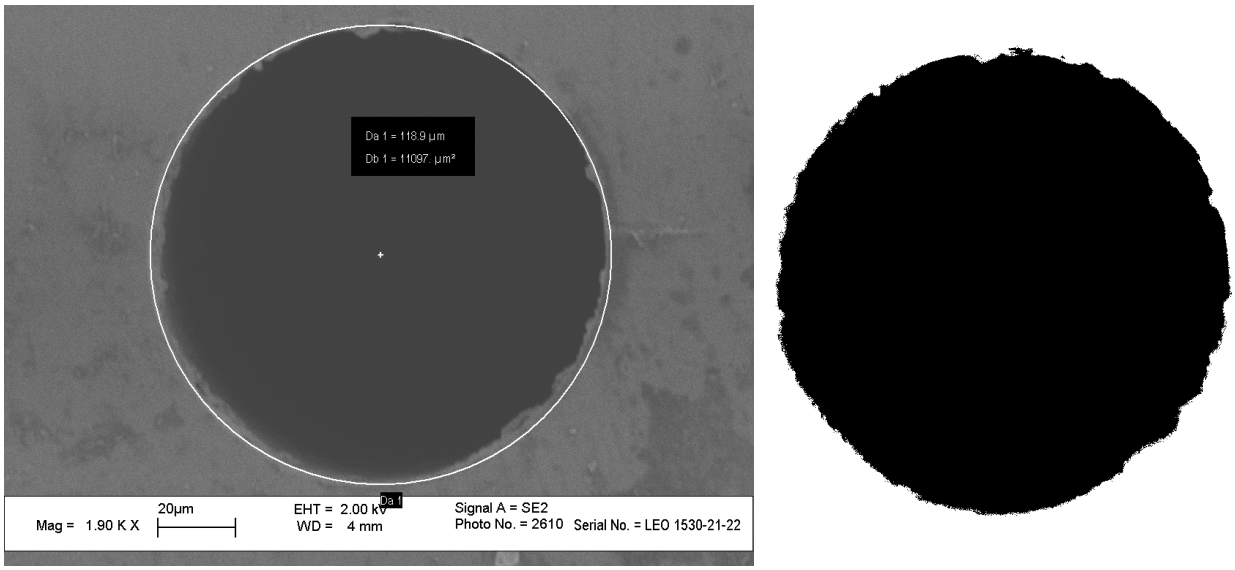

Fig. 4.5a,b: *SEM image of 120μm siliconated glass tube with superimposed virtual circle for diameter evaluation (a); digitally processed black-white rendition of same cross-section (b)*

4.1.2.2 Measuring tube roughness

In order to be able to evaluate an eventual influence of roughness, a quantification of this parameter is required. In the case of the enclosed, concave surface of a microtube, this is not a trivial operation. To expose the surface of interest to be characterized, the tube has to be cut transversally more or less along the axis. In the case of glass, this is done by simply breaking the capillary, bluntly with a solid object, until a suitable shard of tube results. For metal tubes, the operation is more sophisticated, and requires a high-speed micro-mill to remove a lengthwise half of the capillary, taking extreme care not to plastically deform the resulting sample of tube.

Once the surface to be characterized is visible, one can proceed to measure the rugosity.

A schematic representation of such a surface is shown in figure 4.6 above. A surface can be characterized according to the following concepts:

- *Actual profile*: the effective surface profile
- *Ideal profile*: the surface profile as it is represented on paper
- *Technical or waviness profile*: the surface profile as would be obtained from conventional 25 mm styli profilometers

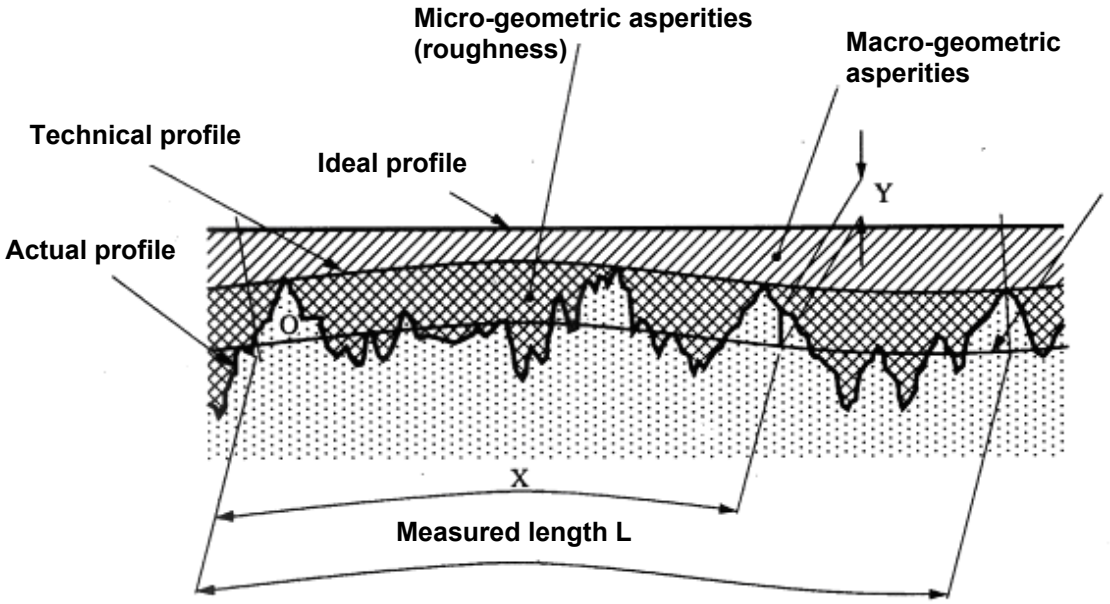

Fig. 4.6: *Schematic example of surface roughness*

The averaged profile is drawn parallel to the technical profile, and compensates for the actual profile curve within the analysed section L. If y is the orthogonal deviation of the actual profile from the averaged profile at a position x along the latter, this line is defined by:

$$\int_0^L y dx = 0 \tag{4.1}$$

The definition of roughness adopted in this Thesis, the value *Ra*, is then given by the arithmetic mean of the absolute value of y along the averaged line, and is expressed in microns:

$$Ra = \frac{1}{L}\int_0^L |y| dx \tag{4.2}$$

The *measured profile* ideally should approach the actual surface profile. Due to the scale of the asperities, mechanical measurement devices like styli will always introduce a tolerance error, as well as potentially alter the analysed surface.

For this reason an optical interferometric profilometer is preferred (for the rugosity measurements in this Thesis, a ZYGO NewView 5000 was used). This instrument functions by emitting a single light beam, part of which is reflected on the surface to be measured and the other is deviated to reflect on a reference surface. When the separated reflected light beams recombine, the interference pattern of phase and amplitude provides the information on the height of the analysed point on the sample. This method is very precise (a resolution of 10 nm on the height is achievable) but works reliably only on reflecting surfaces, especially metals. Scanning the sample in this way yields a topographical map of the surface – an example of the profilometer output is shown in figure 4.7. To establish the true roughness of the curved inner surface, the cylinder shape is removed from the isometric data (figure 4.8), yielding the correct *Ra* value.

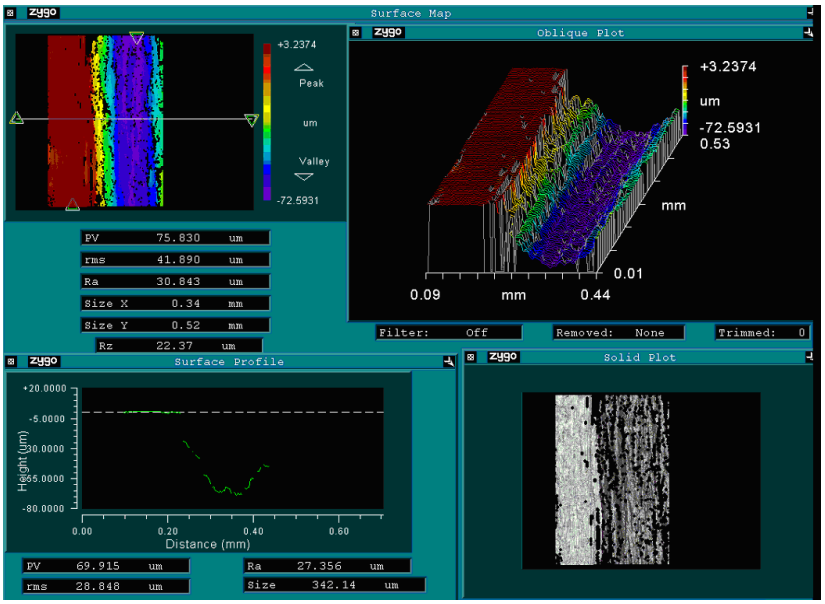

Fig. 4.7: *Scan output of the optical interferometric profilometer for the evaluation of tube roughness (raw) – Ra=30.843µm*

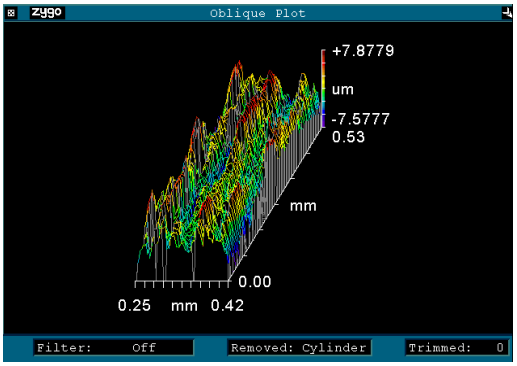

Fig. 4.8: *Scan output for the evaluation of tube roughness (Cylinder-corrected) – Ra = 1.999 µm (same tube as in figure 4.7)*

4.1.3 The "tube-cutting" method

When the restrictions of microtube dimensions prevent direct measurement of the flow conditions due to the excessive coarseness of the sensors, approximations or methodological solutions have to be found. Pressure measurement in ducts of microscopic dimensions is extremely problematic because the minimum size of pressure tappings is of the same order of magnitude as the channel. This means that the conditions of flow with respect to the untouched passage would be severely altered, and therefore not representative of the flow one is intending to characterize. Furthermore, the use of glass as tube material augments the practical difficulty of drilling tappings in the channel passage. At the end of the line, this means that the fluid pressure has to be measured in plenums situated just before the microtube inlet and just after the outlet, and that the resulting pressure difference is not only the *frictional* pressure drop – which gives us a clean analysis of flow behaviour in that particular channel – but is inclusive of *concentrated* pressure losses (due to contractions, expansions, flow separation etc.) that are tied to the test section fittings and are difficult to quantify.

4.1.3.1 Incompressible flow

Thus, one has to resort to approximations or, preferably, to an ingenious solution to bypass the problem of direct static pressure measurement. This is found in the so-called "tube-cutting" method, which for incompressible flow works as follows. See figure 4.9.

For each type of capillary studied, two lengths are cut. The tubes are then equal in all respects except their lengths; the method of fitting the test section in the rig will be identical as well. For incompressible flow this means that at equal mass flow rates the *concentrated* pressure losses at the inlet and outlet (ΔP_{in} and ΔP_{out}) must also be equal. Therefore, by subtracting the *total* pressure drop along the shorter tube from that measured by the transducers for the longer tube, the concentrated losses are eliminated and the difference yields the net *frictional* pressure drop over the extra length of capillary ($\Delta P_f / \Delta L$). As the fluid is considered incompressible, this value can be extrapolated indefinitely and will be valid for any length of tube of that diameter. This way also the friction factor can be established univocally – see equation 2.27.

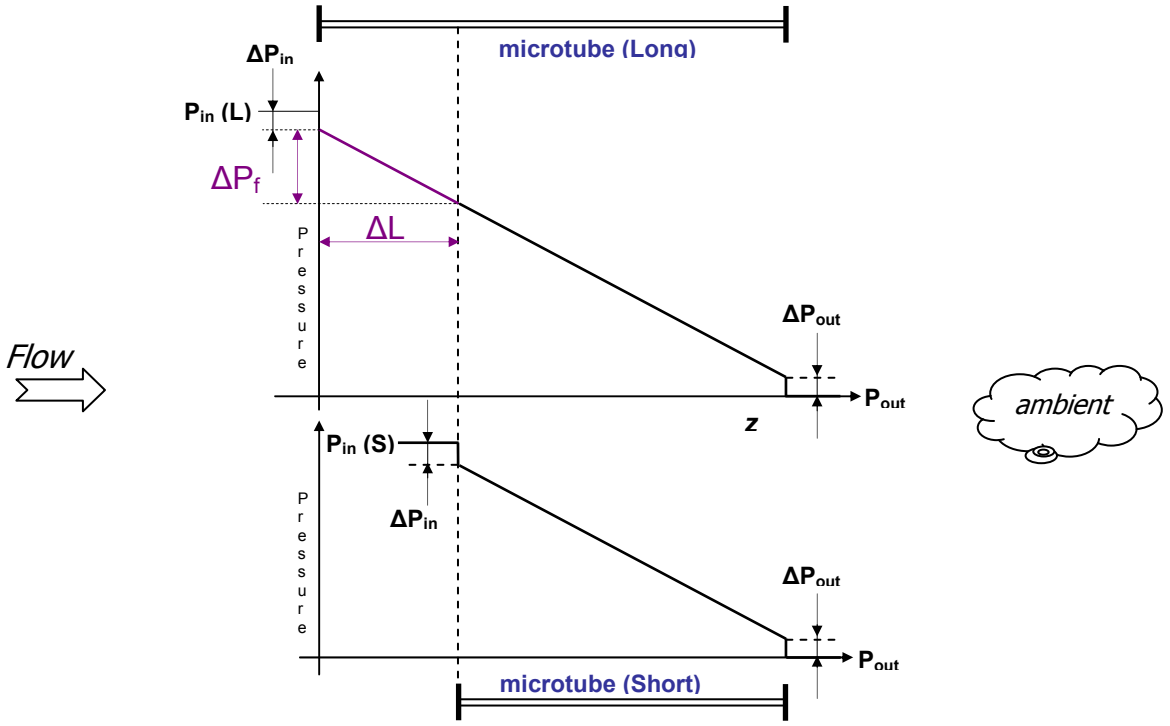

Fig. 4.9: *Pressure drop vs. axial distance at a given* incompressible *mass flow in a long and short microtube*

4.1.3.2 Compressible flow

In the case of a compressible fluid, *i.e.* with density dependent on pressure (see sub-section 2.1.4), the velocity is forced to change along the channel due to the frictional pressure loss. The acceleration of the fluid in turn affects the local frictional pressure loss, so that applicability of the tube-cutting method as above for *compressible* flow has to be justified. A qualitative representation of the axial pressure drop profile for compressible flow in a tube is given in figure 4.10.

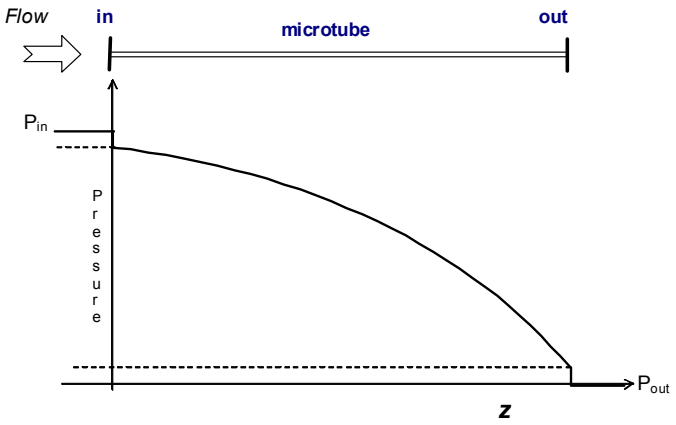

Fig. 4.10: *Schematic of pressure drop vs. axial distance at given* compressible *mass flow*

Again, the difference between the measured values of the pressures at the inlet (P_{in}) and outlet (P_{out}) of the tube does not correspond to the actual *frictional* head loss (between the dashed lines) because it contains concentrated losses due to geometry effects at the test section fittings. The same mass flow passing through a *shorter* tube with the same exit pressure (ambient) will have an identical profile to the one in figure 4.10 – they overlap in other words – from the outlet backwards, with the inlet step occurring at a lower pressure than P_{in}. Assuming this step – which represents a concentration of all inlet effects – of the same size as for the long tube (which is acceptable for a relatively short ΔL), subtraction of the two measured *gross* pressure differences will still yield the *net* frictional head loss in the high-pressure section of the long tube, see figure 4.11.

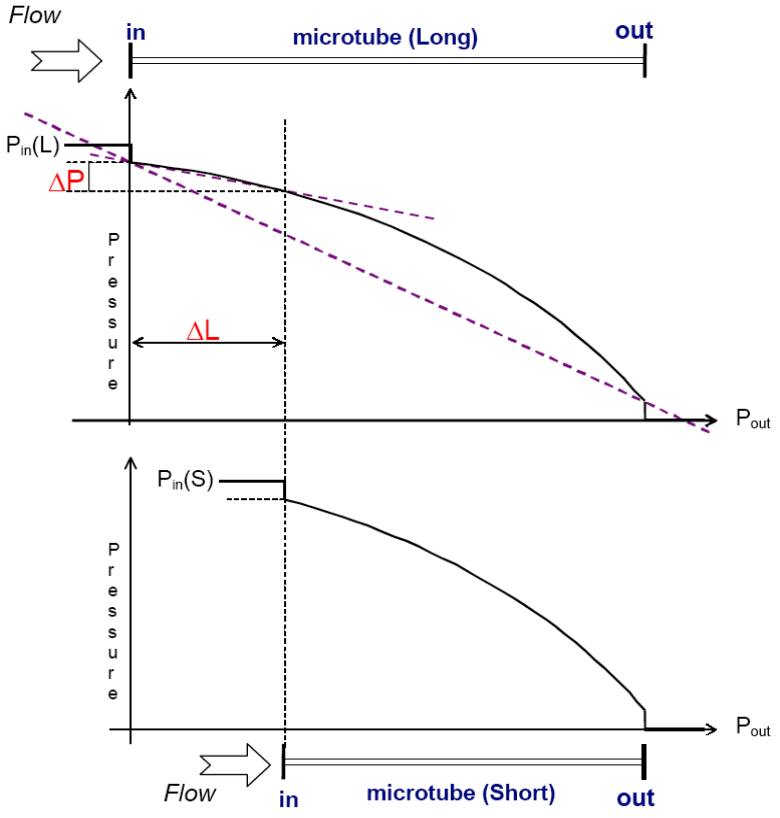

Fig. 4.11: *Pressure drop vs. axial distance, compressible flow: determination of the local and global friction factor*

The friction factor being equivalent to the slope of the pressure profile, an experimental approximation should be more accurate with the above method than by considering one length of

tube alone, as the tangential (dashed) lines in figure 4.11 indicate. Increasing the length of tube to diminish the weight of the concentrated losses on the total pressure drop would not improve precision because the non-linearity of the head loss would be more accentuated.

The experimental linearized local friction factor is taken directly from the Darcy equation (2.29):

$$f = \frac{\pi^2}{8}\frac{\Delta p}{\Delta L}\frac{\rho d^5}{\Gamma^2} \tag{2.29}$$

where ΔP and ΔL are as defined in figure 4.11 for the *differential* friction factor calculation. We shall refer to this also as the *local* friction factor, so that it is clear that this value refers to a particular *section* of the axial distance. For the *global* friction factor (taken over the entire length of the longer tube, L) the gross difference between $P_{in(L)}$ and P_{out} (therefore inclusive of concentrated head losses) is used:

$$f_{glob} = \frac{\pi^2 \rho (P_{in}(L) - P_{out}) d^5}{8\Gamma^2 L} \tag{4.3}$$

It should be mentioned that the value of the density ρ here is variable, as it changes with the static pressure of the flow in the tube (for more on this, see sub-section 2.2.2). Therefore, an average value has to be found to fill into the equation. Considering only the differential tract ΔL, the value of the average pressure will in any case be *lower* than the inlet pressure for the long tube, $P_{in(L)}$, and *higher* than the *net* inlet pressure of the short tube (referring to figure 4.11, the size of the inlet pressure step of the short tube is unknown). For simplicity, the *gross*, measured, inlet pressure of the short tube was used as value. The uncertainty analysis (see sub-section 4.3.1) will determine whether this assumption is acceptable or whether this value is too influential to approximate in this fashion. The linear average value between $P_{in(L)}$ and P_{out} is used for the calculation of ρ in the global evaluation, as also the average temperature between inlet and outlet (which are practically isothermal). Γ is the measured mass flow.

The objective of experimentation with compressible fluids will be to determine the difference between the local and the global analysis: the larger this is found to be, i.e. the further the dashed violet lines in figure 4.11 diverge, the greater the non-linearity of the axial pressure profile can be said to be.

4.1.4 Applying heat input

Heating microtubes can take place in direct or indirect fashion. An example of indirect heating is to let steam condensate as it passes across the outer wall of the test section. Such a configuration, with 6 parallel microtubes heated inside a vertical steam conduit, is shown in figure 4.12 [49].

The vapour is produced in a separate boiler and flows through the central conduit at known pressure so that the condensation temperature – and therefore the outside wall temperature of the microtubes – is given. This configuration allows indirect measurement of the external microtube wall temperature without placing a thermocouple on the microtube surface. In this way wall temperature is not influenced by the presence of thermocouples on the microtubes, which are so small that a contact with any external body may sensibly affect the temperature measurement and the fluid temperature (this phenomenon is particularly dangerous in microsystems characterized by very small dimensions and fluid mass flow rate, as it will appear). The wall temperature of the microtubes is assumed constant at the value of the saturation temperature of water. If the

experiments are carried out at atmospheric pressure, this temperature is 100°C. The defect of this system is that it can only yield an estimate of the *global* heat transfer coefficient inside the microtubes, as the temperature profile of the heated fluid in the test sections is unknown. Furthermore, the condensation film is not perfectly static, and instils doubts as to the value of the heat transfer coefficient at the outer wall.

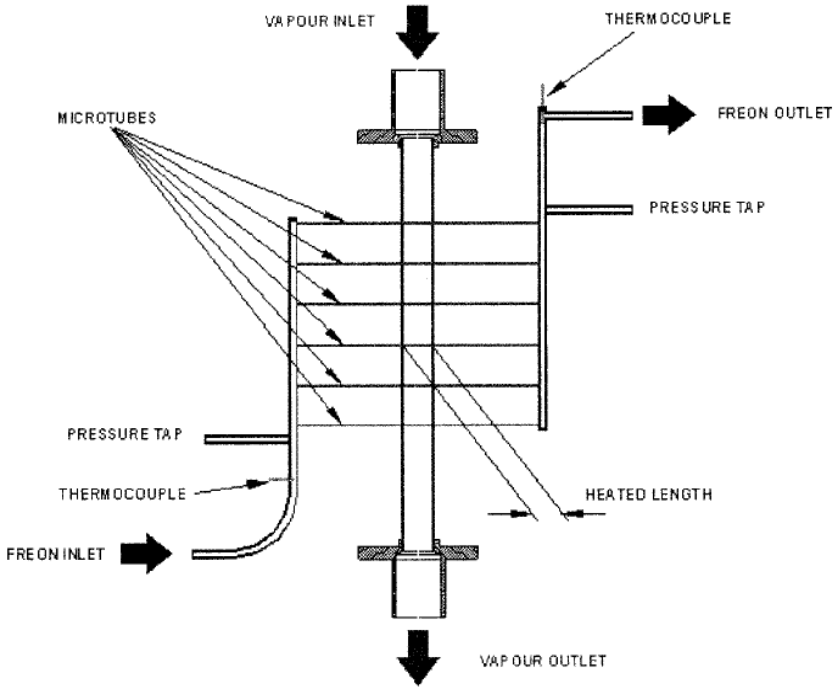

Fig. 4.12: *Example of indirect heating: set-up for diabatic experiments with 6 parallel microtubes heated by condensing steam*

A better way to apply heat would be direct heating of the channel wall through Joule effect. This ensures a uniform heat flux at the wall (in the case of uniform wall properties), so that the fluid temperature rise can be assumed as linear in the heated tract (in the case of uniform fluid properties). However, to know the wall temperature, direct measurement through the placement of thermocouples is necessary, which can induce the losses indicated above. The convective heat loss from the outer surface can be estimated as occurring through natural convection, or – in our case, as we shall see presently – neglected if the tube is placed in a vacuum environment.

Therefore, to be able to do diabatic experiments with the glass tubes, they were coated with a 100 nm layer of Chromium-Molybdenum through sputtering, effectuated by Nanonics Ltd., Israel (www.nanonics.co.il). Subsequently the treated tubes were instrumented with fine-wire thermocouples (50 μm, Type K) placed on the outer wall with cyanacrylic adhesive at first and subsequently fixing them with a non-conductive epoxy resin. This ensures in addition to a quick and reliable response, that there is no electrical conductance to disturb the temperature measurement, and minimizes heat conduction away from the test section. See figure 4.13.

In figure 4.14 a schematization is shown of the test section for the mapping of the heat transfer behaviour along the axial distance z, showing pressure tappings at the inlet and outlet, inlet thermocouple before the fitting, outlet thermocouple inside the fitting, power supply and wall thermocouple positioning for localized determination of the heat transfer coefficient, with the definition of the heated length L_{ht}.

When stainless steel tubes are used obviously no coating is necessary, as direct application of electrical current to the wall will provide the Joule effect heat input. If the wall can be considered acceptably uniform, so will the heat flux be to the fluid.

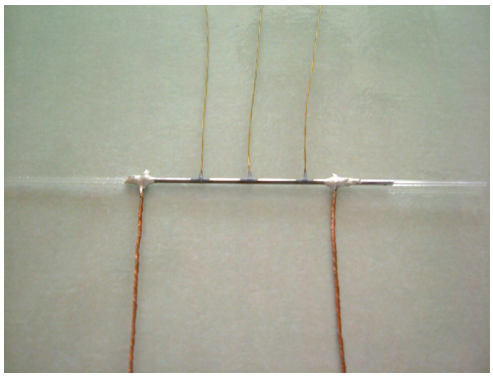

Fig. 4.13: *Glass capillary with 100 nm Cr-Mo coating, 2 feeding wires and 3 externally placed thermocouples*

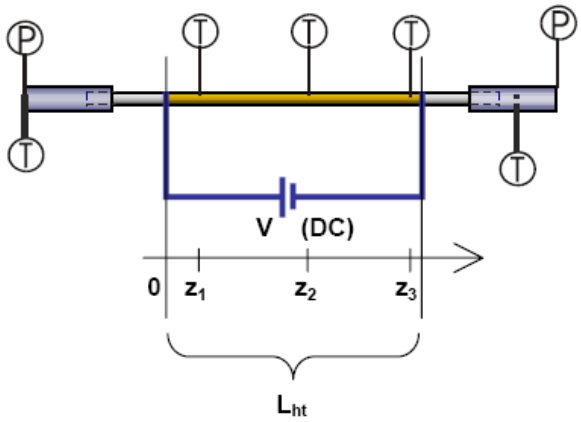

Fig. 4.14: *Schematization of instrumented microtube for heat transfer experiments*

4.1.5 Tube fittings

Once the micropipe to be tested is prepared, it is important that the insertion into the experimental set-up is precise – in the sense that no pronounced discontinuities result at the connections – and straightforward – intending ease of placement and replacement. This is achieved with the specific high-pressure fittings supplied by Upchurch Scientific. Originally made for Gas Chromatography applications, these fittings are made of Peek and resist to extremely high pressures (600 bar) and moderately high temperatures (125 °C), providing nevertheless a highly accurate flow environment.

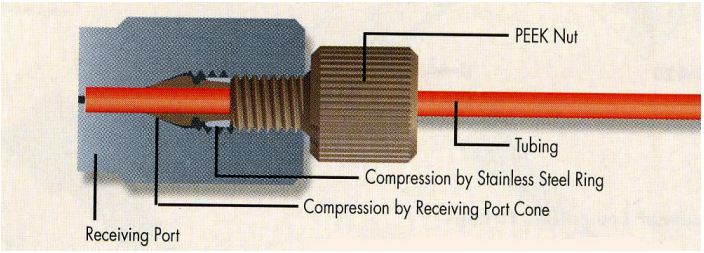

Fig. 4.15: *Working principle of microtube fittings (©Upchurch Scientific)*

The working principle is based on a conax closure of the tube, as shown in figure 4.15 above, combined with a near-zero dead volume that unites the two ends (microtube and test loop). This design ensures a leak-free connection, minimal abruptness disturbing flow conditions and facility of manoeuvring.

4.2 The test rig

The manufactured and prepared capillary tubes subsequently have to be mounted into a test loop. This section describes the experimental facility in its entirety, which was developed for simple fluid flow measurements (sub-section 4.2.1), and modified for gas flow measurements (4.2.2) and heat transfer experiments (4.2.3).

4.2.1 For liquid flow measurements

The scheme of the set-up is shown in figure 4.16. Experiments are carried out using demineralised water, which is degassed by passing through it a very small, but continuous quantity of Helium. Being insoluble in water, an atmosphere of only Helium is created above the liquid level, so that all dissolved gases are driven out by their respective partial pressures in the water. After being filtered of solid impurities through a filter, the water passes through a gear pump or a piston pump with damper.

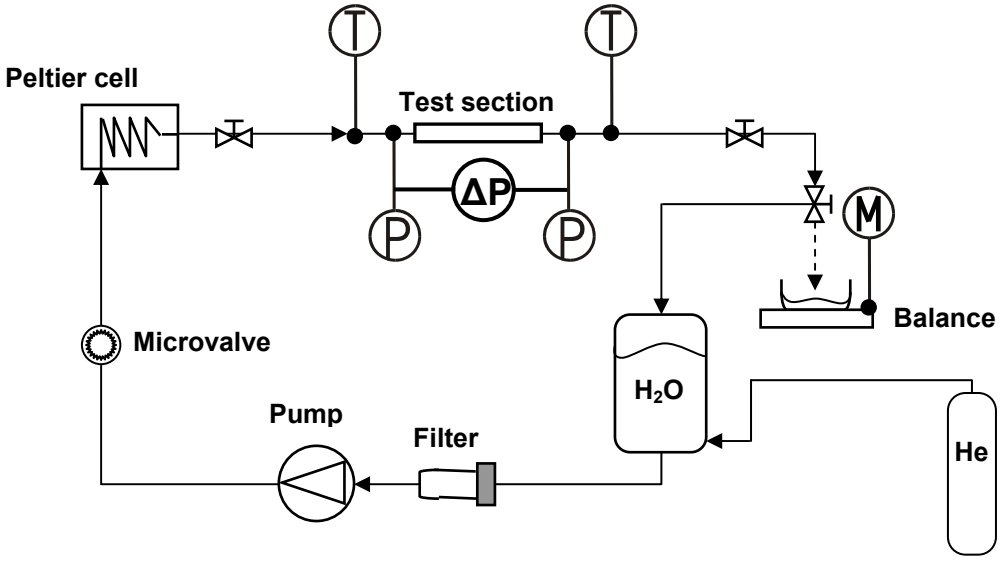

Fig. 4.16: *Test rig for liquid flow measurements*

- The gear pump (Ismatec MCP-Z) is based on a rotating mechanism that draws in the fluid through volume expansion on one side and drives it out of the chambers on the other side, where the head is conquered by the power of rotation. It produces a smooth feed of the flow and is durable and reliable in operation. The indicated volumetric flow rate is not as reliable however, as a calibration test showed, especially at higher head losses. Also, at very high flow rates, cavitation can occur if the upstream pressure is not high enough. These restrictions commend the use of this pump for flow rates above 5 ml/min but for heads up to about 6 bars. The maximum flow rate before cavitation was about 100 ml/min.
- On the other hand, the piston pump (Gilson 305) is a fixed volume pump, that operates through alternate suction and expulsion of the fluid in a single cylinder. This allows for the production of extremely high heads, but obviously also imposes a discontinuous flow, as the actual feeding of the liquid into the system is interrupted in the refilling phase. It is possible to set this refill time to a minimum of 125 ms but again attention has to be paid that no cavitation occurs during piston retraction. The refill time also imposes

conditions on the flow rate: to be able to manage high flow rates the refill time has to be as short as possible, thereby increasing the risk of cavitation. The characteristic is given in figure 4.17.

- To regularize the supplied pressure to the system, a pressure peak damper (Gilson Manometric Module 806) is placed downstream of the pump. The damper performs best at a certain operating pressure, as can be seen from the characteristic in figure 4.18. With the piston pump head model 25SC, it can be seen that for the pulsation to be less than 4% of the system pressure, the damping module has to operate at more than 3 MPa (30 bars). The combination of piston pump and damper was used when high head loss was present (up to 120 bars for a 30 μm tube) at low flow rates (below 25 ml/min).

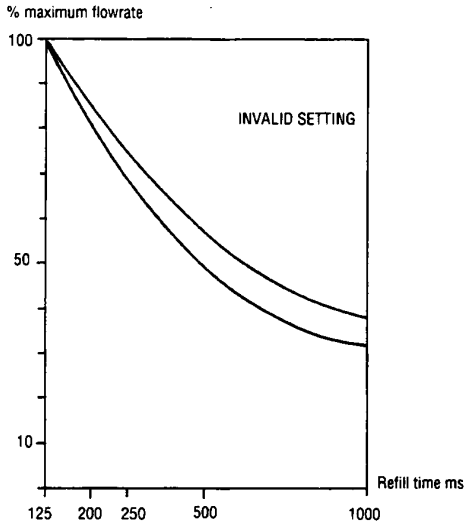

Fig. 4.17: *Gilson 305 piston pump refill characteristic: achievable flow rate as a function of piston refill time*

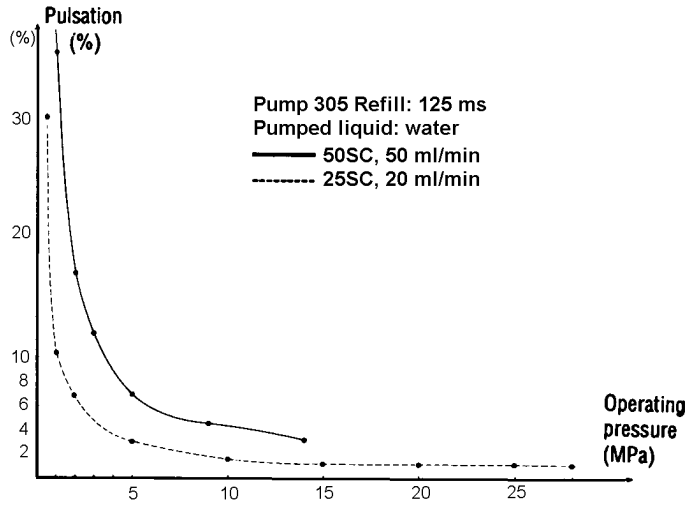

Fig. 4.18: *Gilson Manometric Module 806 dampening performance: degree of pulsation as a function of operating pressure at 125 ms refill time, 20 ml/min*

The water is then, if desired, brought to a certain controlled temperature level with a Peltier cell type pre-heater. This can be convenient to reduce water viscosity and thus head loss.
A 250 μm K-type thermocouple verifies the actual fluid temperature on entrance into the test section, and pressure transducers (Transamerica 0-160 bar; Druck PTX 110 0-35 bar) on either side of the microtube investigated allow the pressure drop over the channel to be established. In parallel, and for low pressure differences, a differential manometer (Rosemount 1151 Dp, 0-6.85 bar) is placed, which has higher accuracy in its operating range. The mass flow rate is measured by weighing the expelled water in a given time with a high precision scale (Gibertini Europe 500).

4.2.2 For gas flow measurements

To be able to handle gas as the working fluid, the experimental set-up described in the previous sub-section had to be slightly modified. First of all, as Helium was chosen as the working fluid, special attention had to be paid to the hermetic closure of the circuit. Helium has a strong propensity to escape through any aperture, the molecule being extremely small (only Hydrogen is smaller). Connections that are leak-tight for *water* thus can prove not to be efficient in containing *gas* particles. To ensure that no loss of mass occurs, especially in the tract between the mass flow measurement device and the test section, a strict leak detection is required after each modification or adjustment of the experimental set-up. This was effectuated by the use of a so-called Sniffer (Balzers FrigoSniff), a picture of which is shown in figure 4.19.

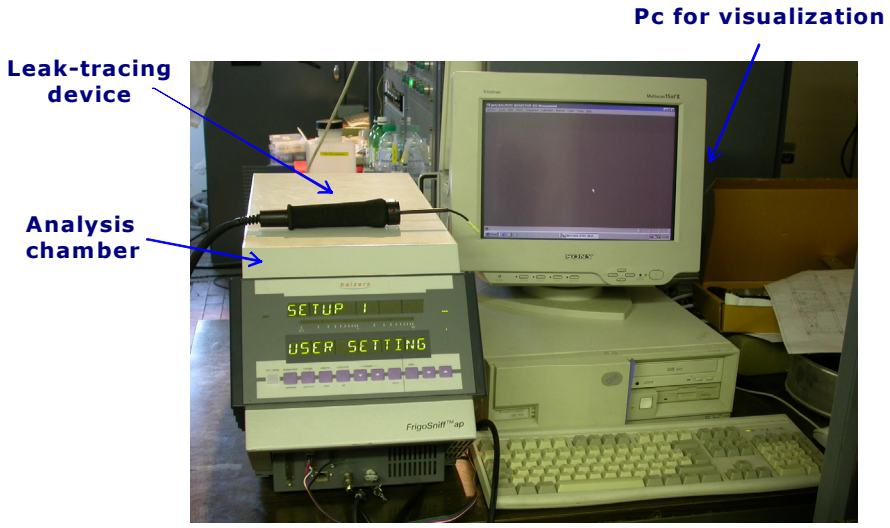

Fig. 4.19: *Sniffer leak detector*

- The Sniffer consists of a tracing device – the "nose" shall we say – which samples the air at the tested location and an analysis chamber which operates in high vacuum (~10^{-5} mbar, generated by an internal turbomolecular pump). The analysis of the sampled air is based on mass spectrometry: the flow seized by the detector is ionised by electron bombardment at 70 eV – this ensures that all molecules are relieved of (one of) their outer electrons and renders them positively charged; subsequently the flow is accelerated and focalised through an electrostatic lens towards 4 parallel aligned steel rods; the rods are excited at an imposed radiofrequency and cause the concentrated ionized molecules to oscillate; the frequency of the oscillation of each molecule is dependent on its mass: those that oscillate in-phase with the rods' reverberations pass through the bars unimpeded, whereas all molecules of different mass will impact on the rods, which act as an earth and neutralize the ions' charge, preventing them to reach the Faraday cage. This is the final detection stage, where the filtered ions are converted to an ionic current that is measured and quantified to indicate the concentration of the element to be detected.
- The output of the Sniffer is visualised on a computer, making use of dedicated software, allowing for a large-scale mapping of the leak detection history, as in figure 4.20.

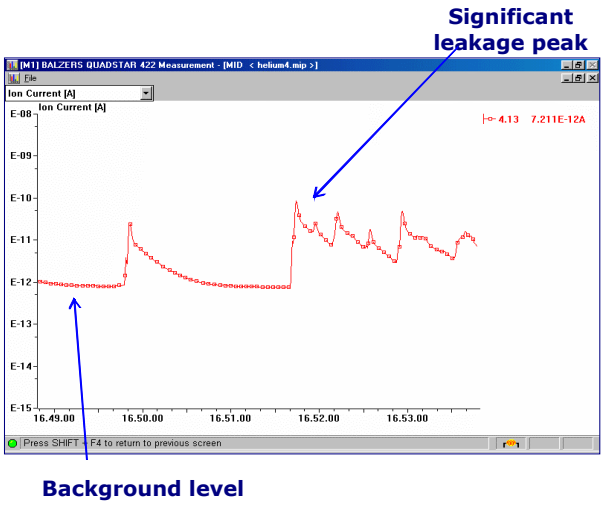

Fig. 4.20: *Output screen of a Sniffer leak detection test – Ionic current vs. time*

Having ensured a leak-free circuit, the constituent elements can be set out, see figure 4.21. The Helium flow is supplied to the test loop by a pressurized cylinder, controlled through a two-stage pressure reduction regulator, and is relieved of particulate matter through a 0.5 μm filter. The fine-tuning of the inlet pressure is done with a microvalve regulator. Pressure measurements are made just before the inlet and just after the outlet of the test section by absolute pressure transducers (Druck PTX110 0-35 bar) and in parallel by a differential manometer (Rosemount 1151DP, 0-6.85 bar). Thermocouples are inserted in the plenums for determination of the state of the gas flowing in and out of the microtube.

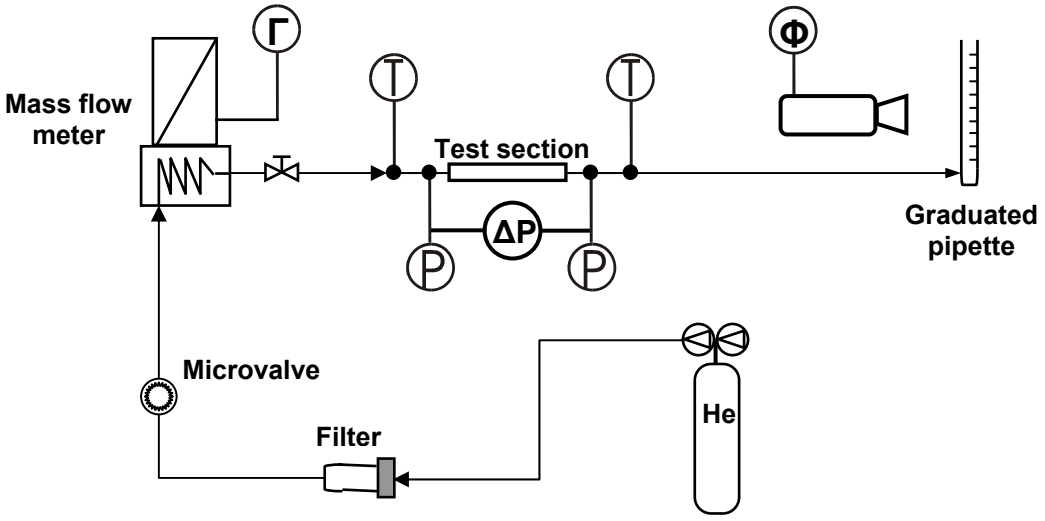

Fig. 4.21: *Test rig for gas flow measurements*

- For measuring the mass flow, two methods were applied. At relatively high mass flow rates ($\Gamma > 5$ mg/min) the Helium upon exit from the test section was passed through a pipette of known diameter carrying up with it a thin film of soapy water. The velocity at which the meniscus travelled through the pipette was recorded with a high-speed camera (SpeedCam+512) and elaborated from measured volumetric flow to mass flow. This is a simple and reliable method for gas flow measurement, but in the experimental error analysis the precision of the pipette diameter weighs almost as heavily as the test section diameter – see paragraph 4.3.1.2 on the uncertainty analysis. For smaller mass fluxes, this method yielded unpredictable, scattered results.
- Therefore, a dedicated, high-precision thermal mass flow meter (Bronkhorst EL-Flow, 0-5 ml/min) was implemented for the experiments on the smallest diameters. This mass flow meter operates on a heat absorption principle, where the temperature rise is sensed along a heated section of an internal capillary tube. Part of the total flow is forced through the capillary by means of a laminar flow device in the main stream. Flow conditions in both the capillary and bulk flow are kept comparable, resulting in proportional flow rates through the meter. The temperature rise sensed by the upstream and downstream temperature sensors on the capillary depends on the amount of heat absorbed by the gas flow. The transfer function between gas mass flow Γ and the output signal V_{signal} can then be described by the following equation.

$$V_{signal} = K \cdot c_p \cdot \Gamma \tag{4.4}$$

where c_p is the gas specific heat and K is a constant factor.

The gas is then expelled to the open air.

4.2.3 For viscous dissipation and heat transfer measurements

For measurements on viscous dissipation and heat transfer, the test loop as described in 4.2.1 was taken as basis. Water is still the working fluid, so only the aspects regarding heat input and minimization of heat loss are to be added to the basic scheme for liquid flow measurements.

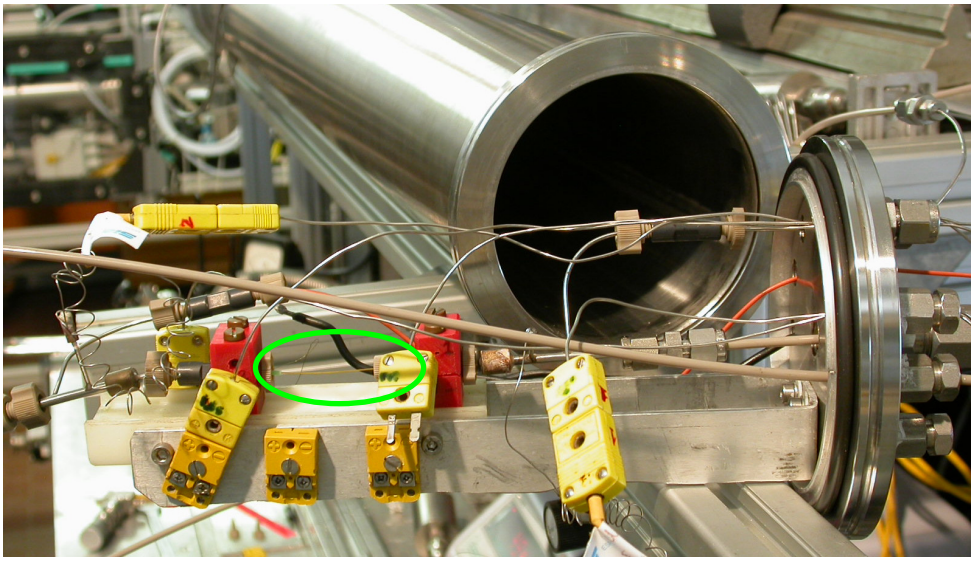

Fig. 4.22: *Vacuum chamber and flange with mounted test section (circled), thermocouples and pressure ducts*

First of all, for experiments involving heating and temperature differences, it is essential to close the energy balance as much as possible within quantities that can be measured. Thus, difficultly quantifiable losses like conduction, free convection and radiation must be avoided or minimized, in order to be able to accept taken data as representative of the phenomenon under investigation. In the case of microtubes intended for diabatic characterization, one aims especially to eliminate convective loss to the surroundings, so that one can conclude that all the heat applied to the outside of the tube will be absorbed by the fluid. To this effect the test section was placed inside a vacuum chamber, a stainless steel capsule (visible in figure 4.22) which is vacated by a turbo-molecular vacuum pump (Alcatel ATS-100) to create an environment free of natural convection. To this effect, the level of vacuum must be less than 10^{-3} mbar. The level measured in our set-up is 2×10^{-4} mbar (Edwards Penning Gauge Model 6), so that we can consider the heat loss to the surroundings through convection inexistent.

The heat loss due to radiation is evaluated by considering the formula for two concentric cylindrical surfaces as given in sub-section 2.3.3, simplified for the limiting case where the surface of the internal body is much smaller (OD of the test section is < 1 mm) than the external, concave surface (ID of the vacuum chamber is 100 mm), see equation (2.59). The entity of this loss is of the order of 1% of the maximum viscous heating measured, and can increase to 2 or 3% in the case of heat put in externally, and thus considered negligible.

To further improve the accuracy of the measured heated fluid temperature, and thereby the energy balance, the thermocouple that was placed in the outlet plenum for simple liquid flow experiments was made to be inserted inside the actual near-zero dead volume of the channel fitting (slightly enlarged for the purpose), immediately at the outlet of the microtube as shown in figure 4.23 below.

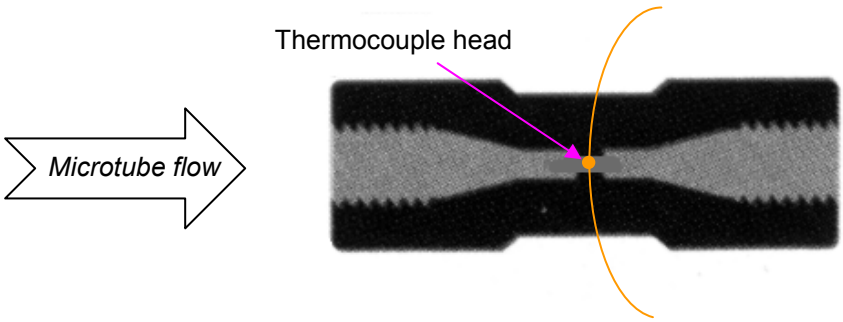

Fig. 4.23: *Thermocouple positioning inside outlet fitting*

The main connections of the microtube to the remainder of the fluid circuit (the fittings) are of polymeric material with very poor conductivity and should insulate the former from the latter as far as *conduction* is concerned. The peripheral attachments to the test section (thermocouples and power supply wires mainly) constitute a heat sink of unknown importance, but are neglected by default.

The direct current for test tube heating is supplied by a Pulsar 50V/5A power supply for the glass Molybdenum-coated tubes, and by an M.B.H. 50V/1200A for the stainless steel tubes.

The scheme of the complete test rig is then as depicted in figure 4.24.

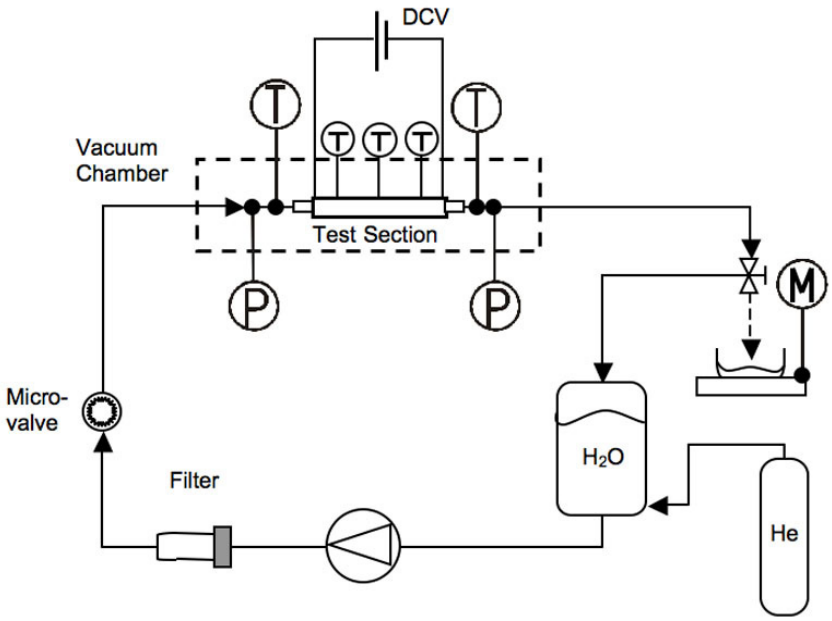

Fig. 4.24: *Test rig for heat transfer experiments*

4.3 Uncertainty analysis

It is not necessary to go into Heisenberg's Uncertainty Principle[5] to realize that it is impossible to know to perfection the physical state of an object of observance. To get to know this state the observer cannot avoid intrusive action by way of measurement. Empirical study will therefore always maintain a degree of uncertainty in its conclusions, but it is the experimentalist's challenge to reduce or balance out the errors as much as possible and evince the point of view that adequately characterizes the phenomenon under consideration through reduction to the smallest number of dominating principles. In any case, to be able to weigh one's findings with the correct amount of modesty is a general virtue.

The objective of experimentation is to obtain information on a quantity that usually cannot be measured directly, but is deduced from the experimental parameters that can be acquired. In order to understand the influence of the latter on its determination, it is convenient to perform an uncertainty analysis of the quantity of interest. This exercise not only provides one with a value of the reliability of the carried out experiment as a whole, but also specifies the weight of each acquired variable in determining the total uncertainty. Knowing this improves the efficacy of data analysis, as one can evaluate to which variables the obtained results are more sensitive, and are therefore in need of higher precision, or in any case of careful interpretation. Similarly, knowing that the contribution to the total experimental error of an error in, say, a temperature measurement is less than 1%, saves one from resorting to complex technical wizardry to further improve the precision of that particular thermocouple read-out.

(The procedure for determination of the experimental uncertainty is classical theory, and is set out in detail in [85, 86], for example.) To obtain an estimate of the uncertainty e_Y of a quantity Y = Y(x_1, x_2, ..., x_n) which is a function of n independent, directly measurable variables, the relative uncertainties e_{x_i} of each of these need to be taken into account:

$$e_Y = \sqrt{\left(\frac{\partial(Y)}{\partial x_1} e_{x_1}\right)^2 + \left(\frac{\partial(Y)}{\partial x_2} e_{x_2}\right)^2 + \ldots\ldots\ldots + \left(\frac{\partial(Y)}{\partial x_n} e_{x_n}\right)^2} \tag{4.6}$$

4.3.1 Friction factor uncertainty

4.3.1.1 Incompressible flow

For example, if one wishes to determine the uncertainty on the liquid friction factor e_f, one applies the above relation to equation (2.29), which expresses f in terms of directly measurable quantities only. The relative uncertainty then is obtained by proportioning with the actual magnitude of the analysed quantity:

$$\frac{e_f}{f} = \sqrt{\left(5\frac{e_d}{d}\right)^2 + \left(\frac{e_\rho}{\rho}\right)^2 + \left(2\frac{e_\Gamma}{\Gamma}\right)^2 + \left(\frac{e_{\Delta L}}{\Delta L}\right)^2 + \left(\frac{e_{\Delta P}}{\Delta P}\right)^2} \tag{4.7}$$

[5] It might be interesting to remark that the subject of Heisenberg's PhD Thesis in 1923 was the – indeterminate, exactly – transition from laminar to turbulent flow. See for a highly abridged discussion of the topic, sub-section 2.4.1.

Thus, for every experimental condition a corresponding relative uncertainty can be calculated. By taking a reference working condition, *i.e.* inserting representative values in equation (4.7), we can choose to plot the total relative error as a function of one of the parameters which is kept as variable. The term $(5e_d/d)^2$ plays an important role in the uncertainty of the friction factor due to the presence of the factor 5 and the small value of channel diameter in the denominator. Let us see how the relative error changes with the absolute value of the inner diameter d by choosing the following working condition, with corresponding uncertainty values:

Water density ρ:	998 kg/m^3	e_ρ = 4 kg/m^3
Mass flow Γ:	100 mg/s	e_Γ = 2 mg/s
Length difference:	25 mm	$e_{\Delta L}$= 0.2 mm

The pressure drop read-out uncertainty is taken from the transducer characteristics, and is given directly in percent: $e_{\Delta P}/\Delta P$ = 2%. If we take the uncertainty on the diameter – measured directly according to the methods described in paragraph 4.1.2.1 – fixed at e_d = 2 µm, the dependence of the experimental error in determining the friction factor on the assumed magnitude of the tube diameter looks like the dashed line in figure 4.25. As can be seen, the experimental uncertainty on the friction factor – at the given working condition – increases rapidly for very small diameters: from 11% at 100 µm to 40% at 25 µm ID.

By taking the terms on the right hand side of equation (4.7) individually, and proportioning them with the (squared) left hand side, the contribution of the several uncertainties to the total relative error on the friction factor (e_f/f) can be obtained. These are shown in percentage figures, also in figure 4.25, for variable diameter.

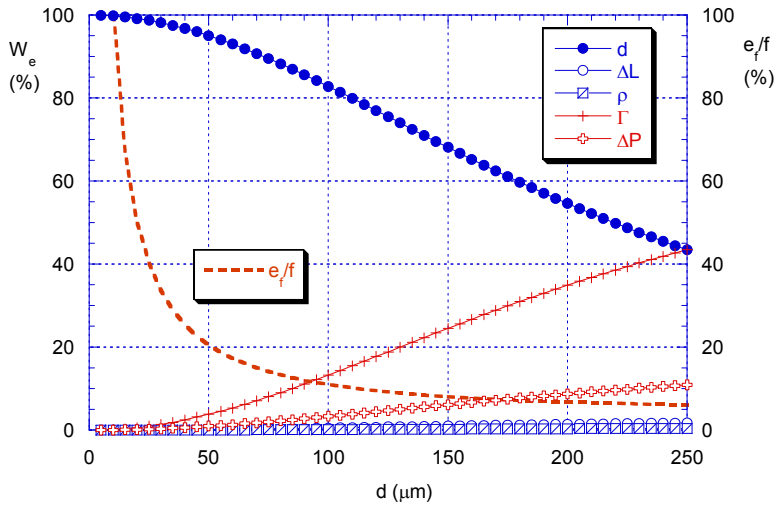

Fig. 4.25: *Weight of variables' uncertainties on total relative error* e_f/f *as a function of diameter - incompressible flow*

For given conditions, at diameters lower than 100 µm (along the x-axis), the error on the diameter measurement e_d/d constitutes more than 80% of the total relative error e_f/f. Furthermore, we can see that errors on fluid density and tube length practically have no influence on the friction factor uncertainty, and that errors on pressure drop and mass flow measurements start to become relatively important only at larger diameters.

4.3.1.2 Compressible flow

The same operation as above can be repeated for the experiments with gas as working fluid. In this case, equation (2.29) is still used, but the density will not be univocal any more and the description of mass flow will differ according to the method used for measurement.

- The mass flow was either measured by a volumetric visualization method or through a dedicated mass flow meter. The former method implied the measurement of the speed of a bubble meniscus pushed by the gas flow through a glass pipette of known inner diameter. To this effect, a high-speed camera recorded the travelling of the bubble film against a graduated background; elaboration of the images knowing the shutter frequency allowed determination of its velocity, u_{pip}, and thereby of the volumetric gas flow rate. A thermocouple placed inside the pipette to measure the temperature there, T_{pip}, consented to convert this value to mass flow. To express the mass flow Γ in measurable quantities only therefore, the following relation is required:

$$\Gamma = \rho_{pip} \cdot u_{pip} \cdot \frac{\pi d_{pip}^{\,2}}{4} \tag{4.8}$$

where

$$\rho_{pip} = \frac{P_{out}}{T_{pip}} \frac{M_{He}}{R} \tag{4.9}$$

according to the ideal gas description of density, (see sub-section 2.1.4). P_{out} is the outlet pressure of the test rig (ambient).

Finally, for the test rig with pipette volume flow measurement, the friction factor can be expressed in terms of measurable quantities only:

$$f = 2 \frac{R}{M_{He}} \frac{\Delta P}{\Delta L} \frac{P d^5 T_{pip}^{\,2}}{P_{out}^{\,2} u_{pip}^{\,2} d_{pip}^{\,4} T} \tag{4.10}$$

and the expression for the relative error on the friction factor becomes:

$$\frac{e_f}{f} = \sqrt{\left(5\frac{e_d}{d}\right)^2 + \left(\frac{e_P}{P}\right)^2 + \left(2\frac{e_{T\_pip}}{T_{pip}}\right)^2 + \left(\frac{e_{\Delta L}}{\Delta L}\right)^2 + \left(\frac{e_{\Delta P}}{\Delta P}\right)^2 + \left(2\frac{e_{P\_out}}{P_{out}}\right)^2 + \left(2\frac{e_{u\_pip}}{u_{pip}}\right)^2 + \left(4\frac{e_{d\_pip}}{d_{pip}}\right)^2 + \left(\frac{e_T}{T}\right)^2} \tag{4.11}$$

P and T are to be taken as average values of the pressure and temperature in the length of tube analysed: for *local* analysis, the measured inlet pressure and temperature of the short tube are taken as representative (see paragraph 4.1.3.2); for global analysis, the linear average between measured inlet and outlet conditions of the long tube.

Now, the uncertainty and its weight distribution can be plotted, see figure 4.26. The reference working conditions are:

Pipette velocity u_{pip}: 100 mm/s $\quad e_{u\_pip} = 0.1$ mm/s
Pipette diameter d_{pip}: 4.04 mm $\quad e_{d\_pip} = 0.1$ mm

Length difference: 25 mm $e_{\Delta L}$= 0.2 mm

The certified relative errors of the Pressure transducers are 2% (e_P/P, e_{P_out}/P_{out}), of the differential manometer 1% ($e_{\Delta P}/\Delta P$). The temperature of the system is taken as 20°C ± 0.2 K.

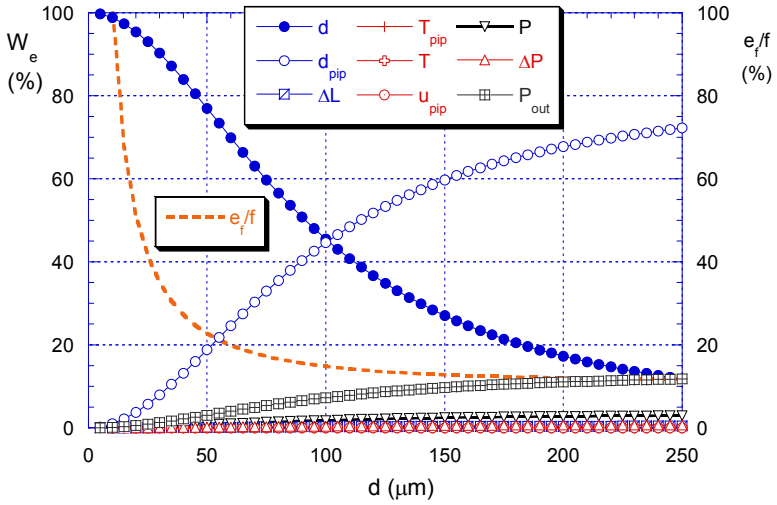

Fig. 4.26: *Weight of variables' uncertainties on total relative error* e_f/f *as a function of diameter - compressible flow, pipette volumetric flow measurement method*

Again, the measured value of the inner diameter of the test section is the most influential parameter at small values of the latter. Note however, that the second-most critical variable for experimental accuracy is the *pipette* diameter! This is due to the factor 4 in equation (4.11), but also due to the high uncertainty adopted for the pipette diameter measurement (0.1 mm). This relatively large error margin was the result of measurements done on the pipette, which revealed a non-constant geometry along the axis. The pipette is relatively long to maximize accuracy of the velocity estimation (length over time) of the film front, but thus induces however, a larger variance in the estimated "constant" diameter.

As to the correctness of the assumption regarding the average pressure in the tube segment, P (see paragraph 4.1.3.2), the incurred error can be seen to be quite uninfluential compared to the former two errors. The assumption is therefore justified.

- If the dedicated mass flow meter is used, the uncertainty on the measurement is given by the certified accuracy of the instrument. Thus, the *pipette* terms in equation (4.11) are replaced by e_Γ/Γ, certified at maximum 2%:

$$\frac{e_f}{f} = \sqrt{\left(5\frac{e_d}{d}\right)^2 + \left(\frac{e_P}{P}\right)^2 + \left(\frac{e_\Gamma}{\Gamma}\right)^2 + \left(\frac{e_{\Delta L}}{\Delta L}\right)^2 + \left(\frac{e_{\Delta P}}{\Delta P}\right)^2 + \left(2\frac{e_{P\_out}}{P_{out}}\right)^2 + \left(\frac{e_T}{T}\right)^2} \qquad (4.12)$$

The other relative errors are equivalent to the ones mentioned above. Their weight distribution is shown as a function of the assumed diameter in figure 4.27.

The *pipette* terms have vanished, but now the precision of the mass flow meter has come forward. The meter used in this set-up was calibrated however for extremely small flow rates, so that experiments could only be done with this instrument on the test section of smallest diameter, $d \leq$ 50 μm. At that value we can see that the error on the microtube diameter value is by far the most influential (> 80%).

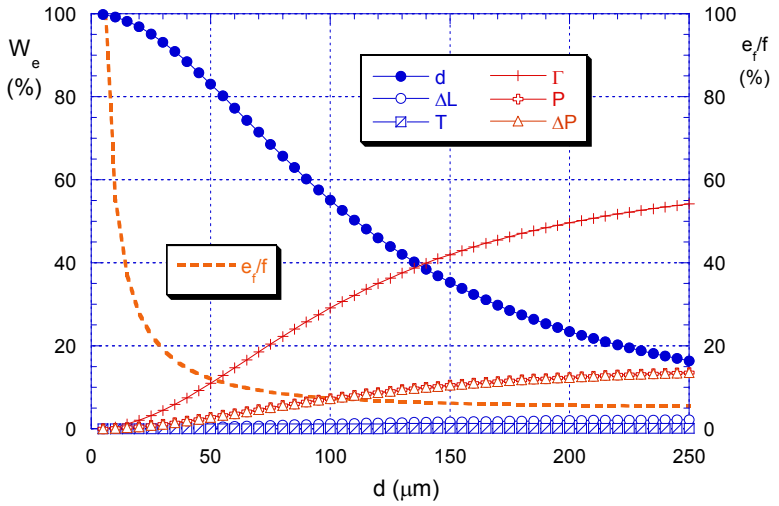

Fig. 4.27: *Weight of variables' uncertainties on total relative error* e_f/f *as a function of diameter - compressible flow, direct mass flow measurement method*

In an overall comparison of the two measurement methods it can be seen how the direct measuring of mass flow has higher experimental accuracy. The operative range of the mass flow meter however, restricted its use to the smallest diameter tubes ($\leq$ 50 μm ID); for larger tubes and therefore larger flows, the pipette volumetric flow measurement method had to be used.

4.3.1.3 Flow characterized by viscous dissipation

The expression for the friction factor based upon the viscous heating of a liquid that undergoes a strong pressure gradient in a narrow passage, was derived in sub-section 2.4.3. With the assumption of zero heat loss from the channel, we can rewrite equation (2.87) in terms of measurable quantities only, yielding:

$$f = \frac{\pi^2}{8}\frac{\rho^2 c_p d^5}{\Gamma^2 L}\Delta T_b \tag{4.13}$$

This means that the uncertainty on the friction factor measured through viscous heating is:

$$\frac{e_f}{f} = \sqrt{\left(\frac{2e_\rho}{\rho}\right)^2 + \left(\frac{e_{c_p}}{c_p}\right)^2 + \left(5\frac{e_d}{d}\right)^2 + \left(\frac{e_{\Delta T_b}}{\Delta T_b}\right)^2 + \left(2\frac{e_\Gamma}{\Gamma}\right)^2 + \left(\frac{e_L}{L}\right)^2} \tag{4.14}$$

With the certified errors on the various parameters in equation (4.14) and an error on the measurement of the channel diameter of 1 μm, this uncertainty becomes dependent mainly on the diameter of the tube under consideration, d (here in μm), and the viscous heating, ΔT_b:

$$\frac{e_f}{f} = \sqrt{0.027 + \left(\frac{5}{d}\right)^2 + \left(\frac{e_{\Delta T_b}}{\Delta T_b}\right)} \tag{4.15}$$

Therefore, as expected, with a constant error of ±0.1 K on the sum of thermocouple read-outs, the larger the viscous heating obtained, the more precise the measurement will be. The fundamental

cause for erroneous conclusions at microscale, however, is always the small diameter, with relatively large uncertainty, see also the weight distribution of the errors in figure 4.28.

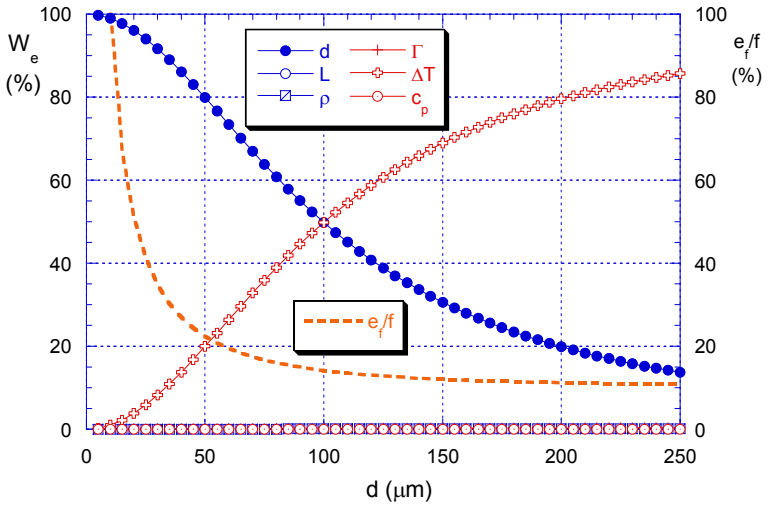

Fig. 4.28: *Weight of variables' uncertainties on total relative error* e_f/f *as a function of diameter – characterization through viscous heating*

4.3.2 Heat transfer coefficient uncertainty

The variable that is sought in the heat transfer experimental campaign is the inner wall heat transfer coefficient, h, locally along the axis z, as it is defined by equations (2.55) and (2.56):

$$h(z)=\left[\frac{\pi d L_{ht}\left(T_w(z)-T_f(z)\right)}{\Gamma c_p \Delta T_f}-\Lambda\right]^{-1} \tag{4.16}$$

where Λ depends on the manner of heat input: in our case through direct Joule heating either of the entire wall of the stainless steel microtubes or of the metallic film deposited on the glass tubes.

Due to the complex nature of the differentiated form, it is not reported here (see Appendix II). Taking two representative examples of heat transfer experiments and elaborating the contribution of the various parameters' errors to the total uncertainty on the heat transfer coefficient, we can make a comparison of the effect of the two methods of applying heat. In Table 4.1 the conditions and the calculated local heat transfer coefficient are reported for a 120 μm ID glass tube and for a 146 μm ID stainless steel tube. The temperatures are taken at similar axial locations (see also figure 4.14).

Table 4.1: *Comparison of a glass and a stainless steel microtube in similar diabatic conditions*

Tube	<Re>	$T_w(z_2)$	$T_f(z_2)$	ΔT_f	h	e_h/h
Glass	1002	60.8°C	29.8°C	10.0 K	16200 W/m^{2}K	9.7%
St.Steel	963	35.3°C	28.3°C	10.8 K	25260 W/m^{2}K	6.5%

The total experimental error in the last column is made up of the relative weights of each of the parameters in equation (4.16), where the following values were taken for the uncertainty on each of these (error on the diameter given in Table 5.4, see chapter 5): e_T = 0.1 K; $e_{\Delta T}$ = 0.2 K; e_{L_ht} = 0.2 mm; e_Γ/Γ = 5%; e_{k_w} = 0.04 W/mK; e_{c_p} = 20 J/kgK.

If, for the working point under consideration, we plot these weights (the sum of which will always be 100, which corresponds to the total experimental error e_h/h) as a function of the variance

in the wall conductivity k_w – since that is the chief difference between the two working conditions – we can get an idea of the contribution of each variable to the total experimental uncertainty. In figure 4.29 this is done for the glass tube as given in Table 4.1. If we compare this plot with the graph for the stainless steel tube in similar conditions (figure 4.30), we notice a clear difference. Observe the graphs at the respective working values of the conductivity parameter k_w (1.18 W/mK for glass, 16.3 W/mK for stainless steel). First of all, it can be noted how the weight of k_w to the total experimental error is higher in the case of the glass tube (35% compared to 0.6%). Furthermore, for the stainless steel tube there is a practically stable distribution of the variables' weights around the working value of the wall thermal conductivity. This means that the sensitivity of the total error to variations is much lower. Therefore, if the effective wall resistance to heat conduction is not well known, this will create a larger margin for error more quickly in the case of the glass test sections. As we shall see in the discussion of the results, this is an important realization to keep in mind in the explanation of the data.

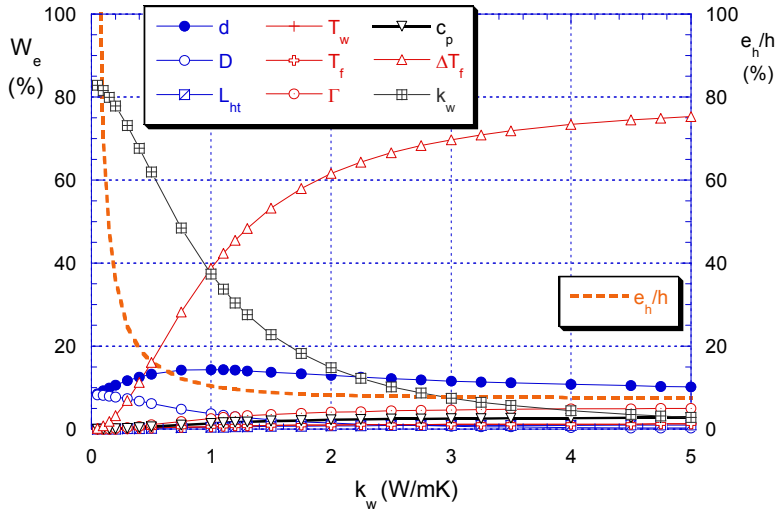

Fig. 4.29: *Weight of variables' uncertainties on total relative error* e_h/h *as a function of wall conductivity – glass tube of Table 4.1*

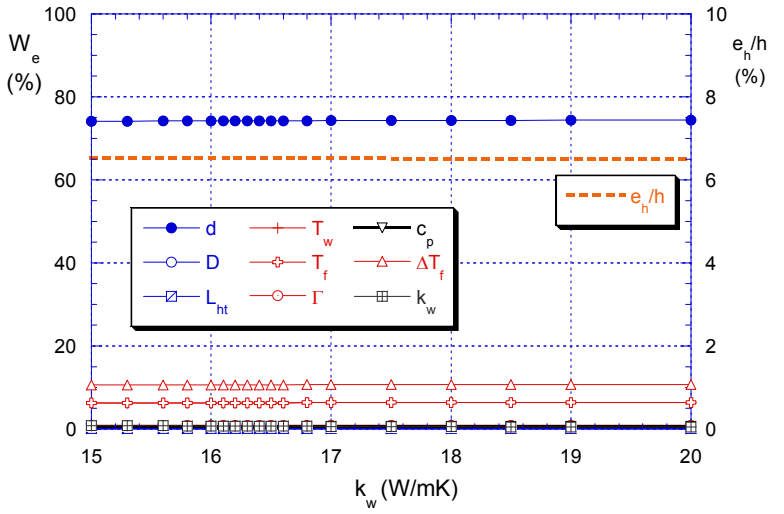

Fig. 4.30: *Weight of variables' uncertainties on total relative error* e_h/h *as a function of wall conductivity – stainless steel tube of Table 4.1*

Furthermore, we can see that the measurement of the *outer* diameter D has crept into the equation, by virtue of the radial conduction of heat across the wall thickness. In the plot for the stainless steel tube experiment the weight of this variable is practically zero, whereas we can notice

a significant contribution of the outer diameter – and therefore wall thickness – measurement to heat transfer coefficient accuracy in the glass tube plot.

As we have already seen from these examples, the uncertainty analysis is of vital importance in experimental research. For further elaboration and an example where this exercise can explain highly unexpected results, see Appendix III.

4.4 Overview of experiments

Eventually, the design, preparation, assembly and optimisation of the experimental material has to come to fruition in the way of a comprehensive and coherent set of data, that is representative of the conditions one aims to characterize and generalize. Achieving this is a constant searching for compromise between accuracy, repeatability and time and resources management. The fundamental objectives of each experimental campaign have to be kept in mind without losing the eye for detail; the flexibility to adapt to unforeseen circumstances and findings is essential, maintaining observance as much as possible of a meticulous experimental procedure.

The programme of experiments carried out with this in mind is presented in this section, divided into the main arguments of the objective of this research: liquid flow, gas flow, viscous dissipation and heat transfer in microtubes.

4.4.1 Liquid flow campaign

The objectives of the experiments on liquid flow are to:

- Verify whether anomalies occur in the friction factor for laminar flow in smooth circular tubes of extremely small diameter with respect to the behaviour predicted for conventionally-sized tubes (equation (2.29));
- Verify whether the increased relative roughness value in microtubes has an effect on same friction factor behaviour;
- Verify whether a hydrophobic contact surface in a microscopic circular duct can induce so-called slip flow, that has an attenuating effect on same friction factor.

Table 4.2: *Programme of experiments – liquid flow*

Tube classification	Tube material	diameter (µm)	error (µm)	Ra (µm)	Lengths[6] (mm)	
					long	short
Smooth	Glass	259	±8.2	~0.05	98.2	49.2
	Fused Silica	101	±2.5	~0.05	100.2	50.4
	Fused Silica	50	±2.6	~0.05	70.0	49.7
	Fused Silica	30	±0.82	~0.05	46.0	31.1
Rough	Glass	299	±6.4	~0.22	91.2	58.9
	Glass	126	±6.5	~0.22	72.3	51.9
Hydrophobic, non-wetting	Glass	326	±1.8	-	79.7	51.0
	PTFE	304	±19	-	82.7	54.1
	Glass	116	±1.7	-	75.5	55.8
	Glass	70	±0.9	-	75.5 | 66.5	57.5 | 49.7[7]

The matrix of experiments that results is given in Table 4.2. Three categories of microtubes are aimed to address these objectives, each divided in a range of diameters. The regular, untreated smooth tubes (see 4.1.1.2) were Fused Silica capillaries for the smallest diameters, Borosilicate for the larger, 259 µm section. The latter type of tubing was also used in the treatment of the surface condition – 2 diameters were roughened abrasively, a treatment which was only physically possible

[6] According to the tube-cutting method, see sub-section 4.1.3
[7] 4 different lengths studied

down to a lower limit of 126 μm ID (see 4.1.1.3), and 4 pipes covering a wide range of radial size were coated on the inside with non-wettable material for experiments on hydrophobicity effects (see 4.1.1.4). The diameters were measured according to the techniques explained in paragraph 4.1.2.1. The reported errors are mainly caused by size and shape variance of the various samples of measured cross-sections, rather than an inaccuracy in the microscope image. The roughness of the tubes was measured on the profilometer (see paragraph 4.1.2.2), though this is a difficult operation because vitreous materials do not reflect the optic beam that scans the sample well. Out-of-focus images result, so the measured roughness (*Ra* value) must be taken as an estimate, representative of the order of magnitude though.

4.4.2 Gas flow campaign

The objectives of the experiments on compressible flow are to:

- Establish to what degree the large drop in pressure along a microchannel – and associated density change – affects the overall flow behaviour;
- Verify whether the friction factor for laminar compressible flow in microtubes can be validly approximated by the equations for incompressible or quasi-compressible flow (equations (2.28), (2.36) and (2.38)).

It is important to underline that these observations are relevant to flow that is amply sub-sonic, with Mach numbers below 0.3: at this value *dynamic* compressibility becomes a factor to take into account. In our case, we are interested to verify whether *static* compressibility – the fact that gas density will decrease with decreasing static pressure – will also have an effect on flow characteristics.

The experiments were carried out on untreated, smooth tubes, and are tabulated below.

Table 4.3: *Programme of experiments – gas flow*

Tube material	diameter (μm)	error (μm)	Lengths (mm)[8]	
			long	short
Fused Silica	254	±8.8	89.7	74.7
Fused Silica	101	±2.5	84.8	60.5
Fused Silica	50	±2.6	91.7 | 63.1	50.3 | 48.8[9]
Fused Silica	30	±0.82	72.0	55.6

Due to the low density of gas the flow regime will remain decidedly laminar, so no transition-to-turbulence effects are expected.

4.4.3 Viscous dissipation campaign

The objectives of the experiments on viscous dissipation are to:

- Individuate and quantify the heat produced by the strong viscous deformation of flow through extremely narrow passages;
- Validate the analogy proposed by Morini [24] that correlates this viscous heating with the friction factor of the channel, equation (2.87).

[8] According to the tube-cutting method, see sub-section 4.1.3
[9] 4 different lengths of tube studied

Again, the test sections were smooth, untreated tubes, placed in a vacuum environment to minimize heat losses, and fitted with accurately placed thermocouples to obtain temperature measurements as precise as possible, see sub-section 4.2.3.

Table 4.4: *Programme of experiments – viscous dissipation*

Tube material	diameter (µm)	error (µm)	Length (mm)
Fused Silica	101	±2.5	109.2
Glass	70	±0.9	77.5 | 93.0 | 103.5[10]
Fused Silica	50	±2.6	63.4

4.4.4 Heat transfer campaign

The objectives of the experiments on single-phase heat transfer are to:

- Characterize the diabatic behaviour of uniformly heated liquid water flow in microtubes by determination of local heat transfer coefficients;
- Study this behaviour both in laminar as in turbulent flow, in smooth and rough tubes;
- Verify whether anomalies occur or whether the correlations valid for conventionally-sized tubes in similar conditions hold in a downscaled system (equations (2.46), (2.48)).

Table 4.5: *Programme of experiments – heat transfer*

Tube classification	Tube material	d (µm)	D (µm)	e_d (µm)	Ra (µm)	L (mm)	L_{ht} (mm)
~ ½ mm	Glass	528	859	±3.9	~0.05	79.0	36.8
	St. Steel	440	708	±14	2.7	133.0	92.9
~ ¼ mm	Glass	259	951	±4.4	~0.05	82.1	36.4
	St. Steel	280	500	±4.2	2.0	141.9	88.8
~ ⅛ mm	Glass	120	804	±2.4	~0.05	65.4	35.4
	St. Steel	146	470	±8.2	0.6	107.0	52.8

Adding heat input to the set-up of experiments brings with it a substantial multiplication of parameters to manage and take into account. Due to the thermal development length, no linear profiles can be assumed as in the adiabatic liquid flow experiments; furthermore, the laws of conduction superimpose a radial component on the heated length as well, so the thickness of the tubes will also have to be taken into consideration.

Table 4.6: *Test section characteristics for heat transfer experiments*

Tube classification	Tube material	d (µm)	L_{ht} (L_{ht}/d)	TC1 (z_1/d)	TC2 (z_2/d)	TC3 (z_3/d)
~ ½ mm	Glass	528	70	14	33	63
	St. Steel	440	211	36	134	200
~ ¼ mm	Glass	259	141	36	75	123
	St. Steel	280	317	16	230	301
~ ⅛ mm	Glass	120	295	79	161	266
	St. Steel	146	361	74	176	334

[10] Three different lengths of tube studied

The preparation of the tubes to effectuate the necessary measurements is described in sub-section 4.1.4, the adapted test rig in 4.2.3. The programme of experiments carried out is given in Table 4.5; in Table 4.6 the axial locations of the wall thermocouples as defined in figure 4.13 are indicated.

In the following chapter the data, evinced from the experimental campaigns described above, will be presented, analysing the results obtained in reply to the stated objectives. Proving whether the experimental procedure was sufficiently well prepared; and putting into evidence the key parameters of flow in (heated) microtubes.

5

RESULTS & DISCUSSION

The running of tests is an organic process that entails creating an affinity with the set-ups as described in the previous chapter, optimizing experimental procedures, and feeding observations both scientific and practical back into the programme of experiments to be carried out. In the meanwhile, perforce, data are gathered, thousands of data, and according to their precision and reliability – closely connected to the organic process mentioned – these are selected, elaborated, tabulated and will now be presented.

The experimental effort has been divided into four campaigns, as they are listed in section 4.4. First, the behaviour of liquid incompressible flow in microtubes will be discussed, in relation to the classic laws set up for laminar flow in circular channels. In section 5.2, the large degree of compressibility of gaseous flows in micropipes will be examined. In both these campaigns, the parameter that has been used for verification of the flow characteristics is the Darcy friction factor, as a function of the Reynolds number.

The friction factor is viewed from a different angle in section 5.3, where the heating of the flow due to viscous dissipation is used as an indication thereof, as opposed to pressure measurements. It will be verified under what conditions this may prove a valid alternative.

Finally, heat input will be introduced in the discussion on microtube flow behaviour in section 5.4. In particular, the value of the (localized) heat transfer coefficient will be considered and its dependence on the Reynolds number – laminar and turbulent – and tube morphology.

5.1 Liquid flow campaign

The simplest case of internal flow to analyse and translate into idealized concepts, is laminar flow in a tube – see also section 2.2 of Chapter 2. The axial-symmetric geometry and the ordered nature of the flow allow for a streamlining of the problem to its bare essentials, and is therefore a good basis for further development of experimental conditions.

The programme of experiments for this campaign was already presented in sub-section 4.4.1. In Table 5.1 this overview is supplemented with some basic parameter ranges of the experiments on each test section. Also, the tube lengths are transcribed in multiples of the diameter, so that it can be seen clearly that the axial distances in the experiments are always sufficient to consider the tubes *long*, *i.e.* that the flow always achieves full development.

First of all, the case of smooth untreated tubes will be discussed, where the friction factor is determined as a function of the Reynolds number using equation (2.29), while only varying the microtube inner diameter (ID).

Table 5.1: *Experiment parameters – liquid flow campaign*

Tube classification	Tube material	diameter (µm)	error (µm)	Ra (µm)	Ra/d (%)	Lengths[11] (*L/d*)		Reynolds number
						long	short	
Smooth	Glass	259	±8.2	~0.05	0.02	379	190	440 - 3160
	F. Silica	101	±2.5	~0.05	0.05	992	498	220 - 2150
	F. Silica	50	±2.6	~0.05	0.1	1400	994	40 - 770
	F. Silica	30	±0.82	~0.05	0.17	1484	1000	60 - 1080
Rough	Glass	299	±6.4	~0.22	0.07	305	197	310 - 3300
	Glass	126	±6.5	~0.22	0.17	574	412	310 - 2980
Hydrophobic, non-wetting	Glass	326	±1.8	-	-	244	156	680 - 2960
	PTFE	304	±19	-	-	272	178	230 - 4030
	Glass	116	±1.7	-	-	651	481	530 - 2820
	Glass	70	±0.9	-	-	950	710	620 - 2490

5.1.1 Smooth tubes

To fulfil a complete set of measurements on each of the diameters discussed below, as explained in sub-section 4.1.3 on the tube-cutting method, pressure measurements were taken for a long section and a short section of the tube at comparable mass flow rates. Being fitted into the test rig in an identical fashion, the different head losses measured are a result of the difference in length between the two sections only. This pressure difference was used in the determination of the friction factor, so that for each data point that is plotted in the following graphs, two experimental runs had to be carried out.

Thus, two pressure drop curves are obtained from the measurements, as is shown in the following graph, figure 5.1.

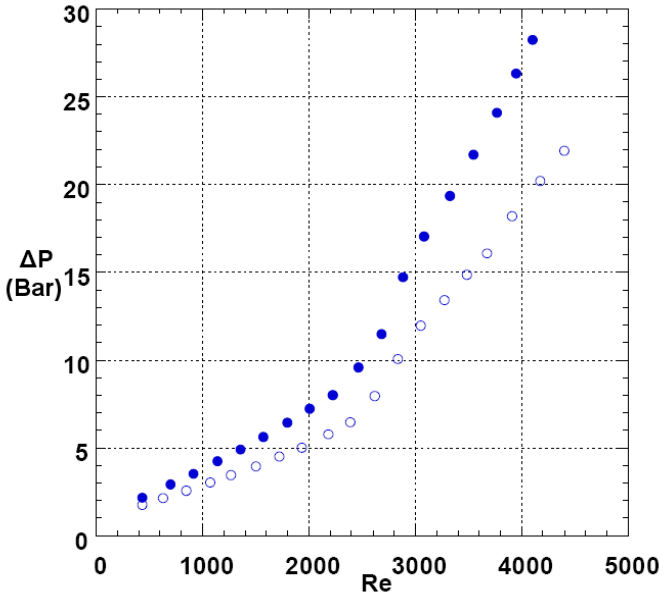

Fig. 5.1: *Representative experiment curves: pressure drop vs. Reynolds number – long tube (closed symbols) and short tube (open symbols)*

[11] According to the tube-cutting method, see sub-section 4.1.3

The long tube (closed symbols) has the higher pressure drop naturally. Now, since the data points will rarely coincide exactly as far as the value for the mass flow is concerned, an interpolation polynome is applied to the curve for the shorter tube. Thus, for each value of the measured mass flow in the long tube, the corresponding (interpolated) pressure drop in the short tube can be found, and the "exact" difference in head loss computed. The Δp thus found applied to the difference in length ΔL yields the friction factor as in equation (2.29).

259 µm

The first capillary to be studied was a 259 µm ID glass tube. The measured friction factor vs. Reynolds number is plotted in figure 5.2a. Zooming in on the Poiseuille number (defined as $Po = fRe$, equal to 64 for circular tubes) a very detailed evaluation of the friction behaviour with respect to an ideal tube can be gained; this is evident from figure 5.2b. The Reynolds number was varied from 440 to well into the transition region, $Re = 3160$. Shortly before transition, the profile of the datapoints just dips below the boundary of the experimental error margin around the reference value described by the Hagen-Poiseuille law ($f = 64/Re$). At low Reynolds numbers this curve is adhered to more closely. Transition to turbulent flow can be clearly viewed at $Re \approx 2200$, where the friction factor experiences some turmoil as the fluid layers break up and start to mix and whirl.

All in all, considering this to be the *very first experiment* carried out, the fluid-dynamic behaviour at this diameter does not present excessive peculiarities compared to macroscale flow; reducing the diameter further will determine if any genuinely unconventional trends come about.

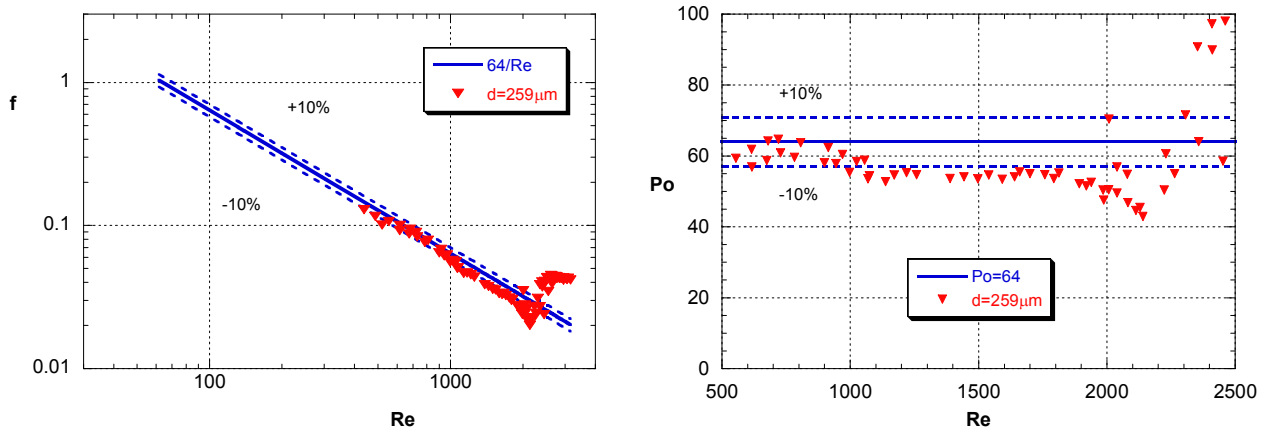

Fig. 5.2a,b: *Friction factor vs. Reynolds number (a) Poiseuille vs. Reynolds number(b) – 259 µm smooth glass tube*

101 µm

Changing to the Polymicro® fused silica tubes, of the same order of smoothness as the glass 259 µm tube, the 101 µm ID capillary shows a near perfect laminar behaviour for all Reynolds numbers studied – see figure 5.3a,b. The measured friction factor lies practically on top of the $64/Re$ curve and even the Poiseuille number on a linear scale shows proof of a very neat laminar flow up to the first evidences of transition at $Re \approx 2100$. Due to the much smaller diameter of the tube, pressure drop is very much higher, and the flow could not be pushed all the way into transition to turbulent flow with the adopted pump hardware.

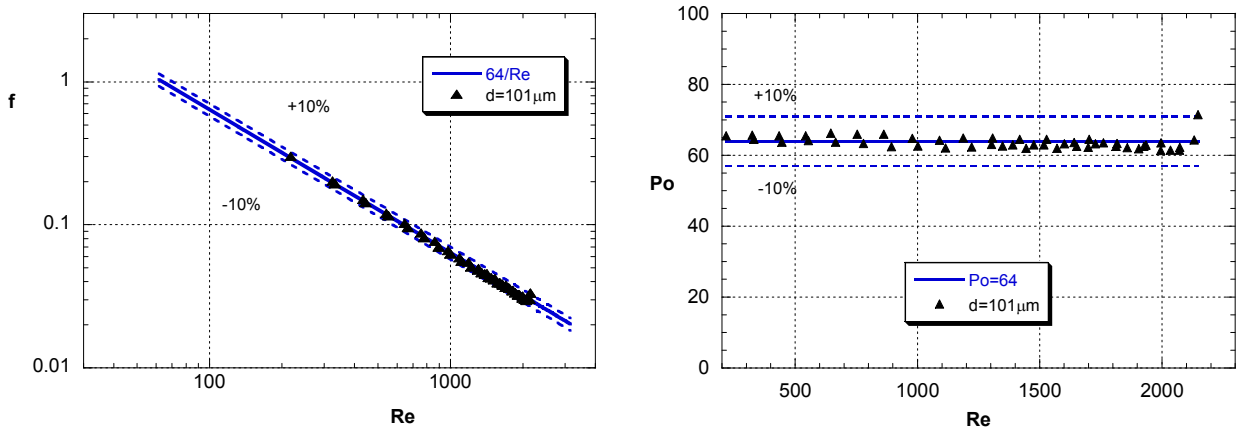

Fig. 5.3a,b: *Friction factor vs. Reynolds number(a) Poiseuille vs. Reynolds number(b) – 101µm smooth fused silica tube*

50 µm

If we reduce the diameter again by half, increasing the pressure drop 16-fold compared to the 101 µm tube for the same mass flow rate, the friction factor still measures up well to the values predicted by the Hagen-Poiseuille law for laminar flow in a tube. Even though there is a slight divaricating tendency at higher Reynolds numbers, representing two different trains of experiments, practically all points converge around the classical curve within the margin for experimental error.

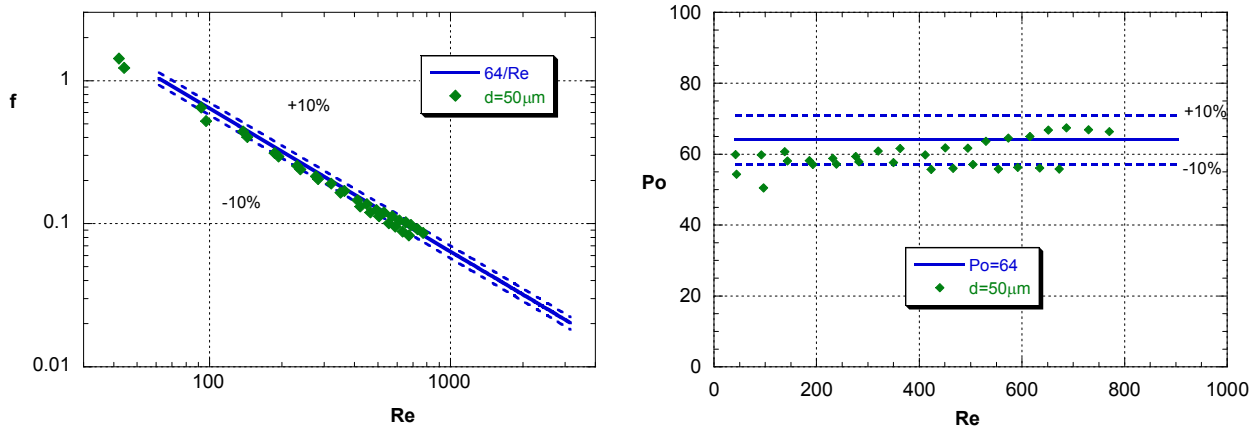

Fig. 5.4a,b: *Friction factor vs. Reynolds number (a) Poiseuille vs. Reynolds number (b) – 50µm smooth fused silica tube*

30 µm

The experimental error of the test rig starts to become influential as the diameter is reduced further (see figure 4.24 on the total relative error at a given working condition), so that the error bands in the friction factor and Poiseuille number plots have to be widened. The extremely high pressure drop (up to 4 bar/mm!) in this microtube make the range of experimentation necessarily narrow, so that the data taken are mainly at low mass fluxes. However, at the minuscule flows involved, the error on the mass measurement starts to play up as well, so that a larger dispersion in the points results at the lowest Reynolds numbers. The plots for the friction factor and Poiseuille number are given in figure 5.5a,b above. The data do stay within the band of uncertainty, but tend consistently towards a level which is on the verge of this margin as Reynolds numbers increase.

With caution it might be maintained that at a certain shear rate[12] (which reaches the 10^6 s^{-1} mark at Re = 225, becoming 4.4×10^6 s^{-1} at Re = 1000) the liquid in contact with the wall starts to slip, reducing frictional loss. However, given the experimental uncertainty, the hypothesis of conventional laminar flow behaviour cannot be refuted with these data.

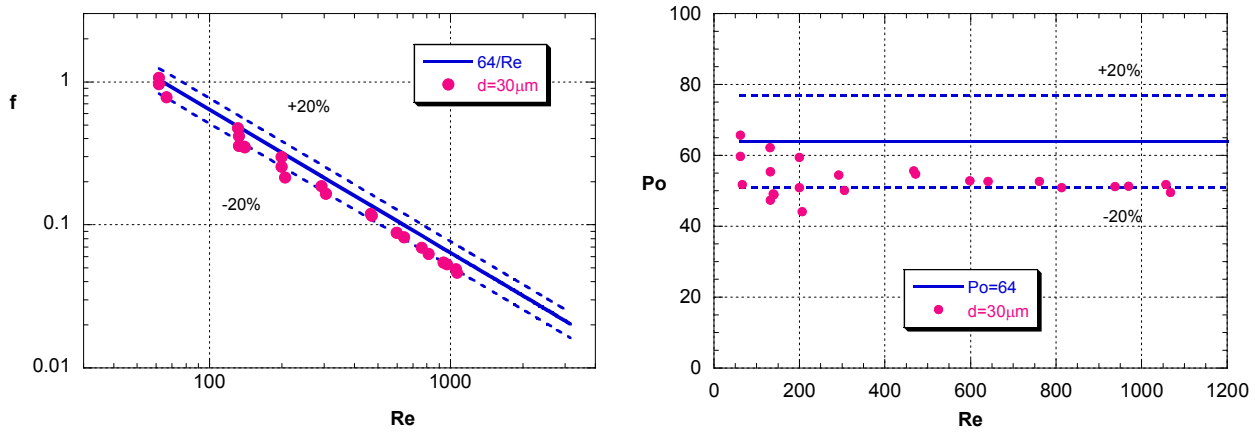

Fig. 5.5a,b: *Friction factor vs. Reynolds number (a) Poiseuille vs. Reynolds number (b) – 30μm smooth fused silica tube*

5.1.2 Rough tubes

Two diameters of glass tubes were roughened on the inside to establish whether perhaps an accentuated effect of the rugosity could be observed on liquid flow in microtubes. To render glass rough is not an easy task (see paragraph 4.1.1.3), but it was sought to maintain the surface material equal to the untreated smooth tubes discussed in the previous sub-section, to be able to exclude possible effects due to polarity or hydrophobicity. The roughness obtained, unfortunately, was not very elevated, as can be seen from the *Ra/d* values reported in Table 5.1. Based on these values, these should be considered smooth tubes, but it is remembered that the measurement of roughness on non-reflecting surfaces, like glass, is imprecise (see paragraph 4.1.2.2). Also, since the different state of the roughened inner surface is very apparent (compare figures 4.3 and 4.4b or 4.1a) the experiments were pursued anyway to verify whether the increased *absolute* roughness might have an effect on the friction factor as compared with untreated, perfectly smooth glass tubes.

299 μm

The largest roughened micropipe presented no significant alterations in the friction factor with respect to what was observed for smooth tubes. There is a degree of scatter in the disposition of the data, but overall the tendency confirms the Hagen-Poiseuille law.
Also, no anticipated transition to turbulence is encountered as has been referred in some articles [48, 57, 62]: the jump in friction factor takes place for $Re > 2000$.

[12] Or: the velocity gradient at the wall; obtainable by differentiating equation (2.22) to r and using equation (2.25) for the axial pressure gradient. The equation that results is evaluated at $r = R$.

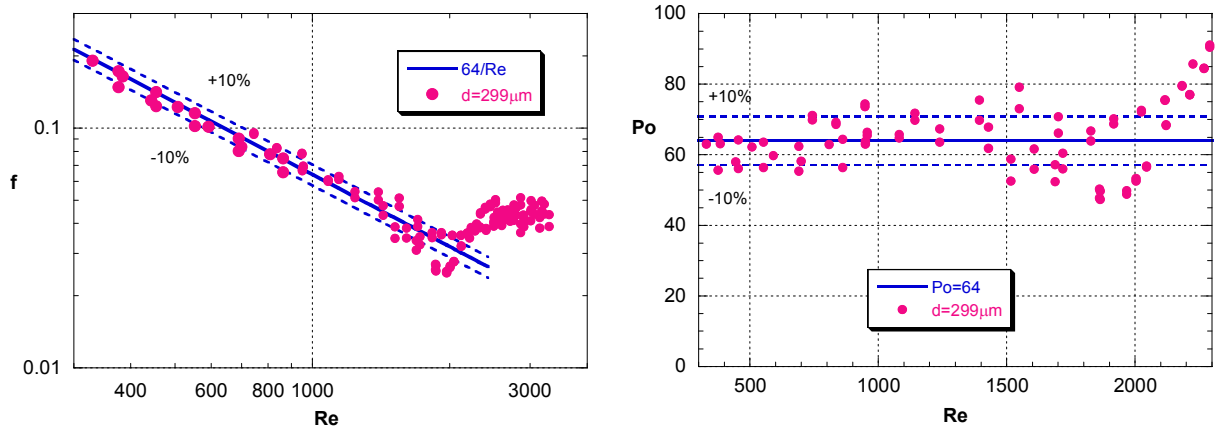

Fig. 5.6a,b: *Friction factor vs. Reynolds number (a) Poiseuille vs. Reynolds number (b) – 299 μm rough glass tube*

126 μm

The tests on the roughened tube of 126 μm ID were slightly erratic: only few measurements could be taken due to the extreme fragility of the test section. Possibly the surface treatment that the capillary received had created one or more microscopic cracks that undermined the structure's usual solidity. Also a particular, unexpected effect of the tube-cutting method arose, which can be evidenced in the following plots.

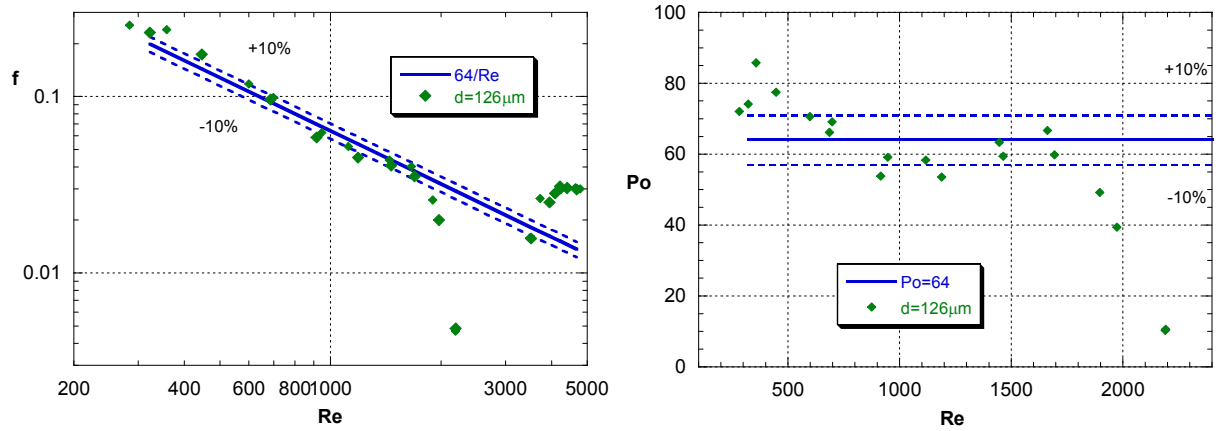

Fig. 5.7a,b: *Friction factor vs. Reynolds number (a) Poiseuille vs. Reynolds number (b) – 126 μm rough glass tube*

The few data points in the laminar regime are reasonably acceptable as oscillating around the reference curve. For $1800 < Re < 3500$ though, there is a strange collapse of the friction factor values. This is explained as follows. In the plot of the pressure drop curves presented in figure 5.1, the transition to turbulence can be noted in the change in gradient of the two curves at $Re \approx 2400$. As is known from classical theory though, transition to turbulence is somewhat stochastic in nature: it is a grey area in which laminar flow is broken up and transversal mixing starts to take hold more or less quickly of the flow pattern (see also sub-section 2.4.1). Thus, the point of transition may occur in slightly different conditions or with differing dynamics between the long and the short test sections. This is manifested in the respective pressure drop curves, see figure 5.8.

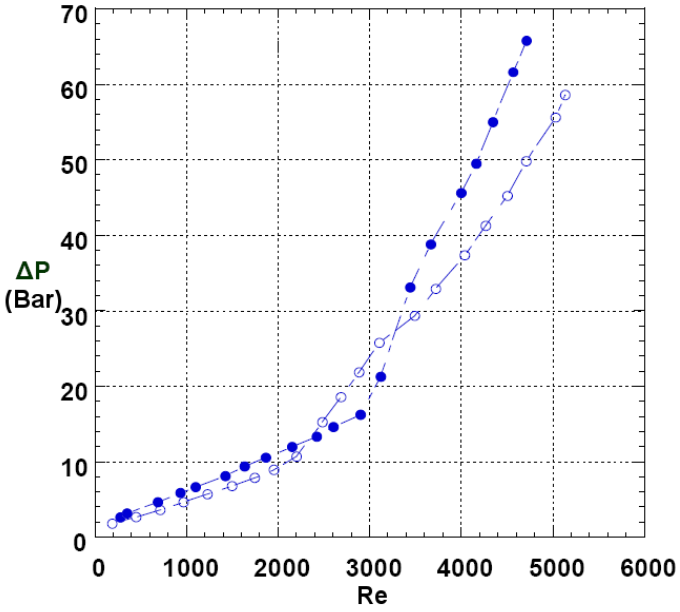

Fig. 5.8: *Example of different dynamics in transition to turbulence between long tube (closed symbols) and short tube (open symbols) – Pressure drop vs. Reynolds number curves, 126 µm rough glass tube*

Transition in the long tube (closed symbols) takes place only at $Re \approx 3000$, whereas in the short tube it has occurred already at $Re \approx 2200$, initiating higher pressure drop due to the creation of vortices and eddies. The contradictory situation arises, between these Reynolds number values, that for the same mass flow there is a *lower pressure drop in the long tube than in the short tube*. The difference in head loss between the two lengths becomes negative and so does the friction factor that results, becoming physically void of significance. Therefore, the region around these transitional effects must be disregarded in the graphs for this diameter, and only the strictly laminar or fully turbulent regime taken into consideration. Nevertheless, the conception of physically meaningless results based on actual, measured behaviour is an occurrence that needs to be appreciated for its proper value, and in this case it helps to underline the indeterminate nature of laminar-to-turbulent flow transition.

5.1.3 Hydrophobic tubes

To investigate whether slip flow can be detected in capillaries with non-wetting inner surface, glass microtubes with 3 different diameters were coated with a silicon film in the manner described in paragraph 4.1.1.4. Also a PTFE tube was studied. As with the previous experiments, *degassed* distilled water was used as the working fluid, which has a contact angle on silicone and PTFE of 110°, as opposed to 14° on regular glass surfaces.

326 µm

Again, no distinct deviation from the reference curves are observed for the entire range of Reynolds numbers inspected, see figure 5.9a,b. The shear rate at the wall varies from 11×10^3 s^{-1} at $Re = 700$ to 34×10^3 s^{-1} at $Re = 2000$. According to [16], this should already be in the region where apparent slip flow can be implied from pressure and flow rate measurements, for which a critical shear rate of 10×10^3 s^{-1} is given. In [17], this shear rate is said to be critical only at surface roughness values of about 6 *nanometres* – which is at least an order of magnitude lower than the apparent roughness of glass – so only for ultra-smooth surfaces.

Transition to turbulent flow can be observed at *Re* = 2300, which is in keeping with conventional behaviour of pipe flow in smooth tubes.

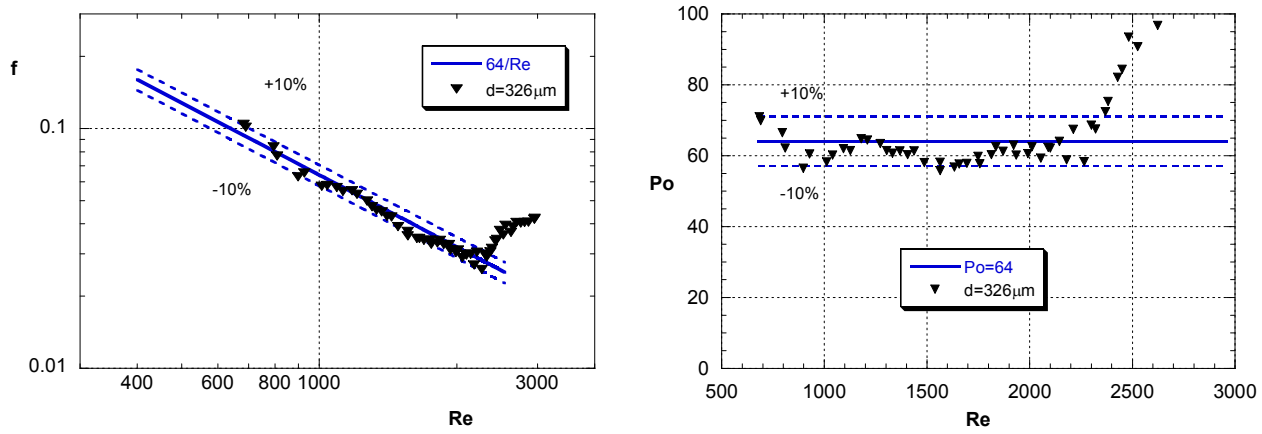

Fig. 5.9a,b: *Friction factor vs. Reynolds number (a) Poiseuille vs. Reynolds number (b) – 326 µm siliconated glass tube*

304 µm

Even though the diameter measurements of the PTFE tube were rather disparate in their results (the standard deviation amounting to 19 µm, see Table 5.1), the pressure drop data were quite well ordered, so they are reported anyway in figure 5.10a,b, in the form of friction factor and Poiseuille number vs. Reynolds number graphs. Within a rather large error band, a typical smooth tube behaviour was found, with the friction factor observing the 64/*Re* dependence and transition to turbulent flow initiating at *Re* = 2350. Furthermore, we can see from the flattening out of the points representing the highest velocities that fully developed turbulent flow was reached even before *Re* = 3000.

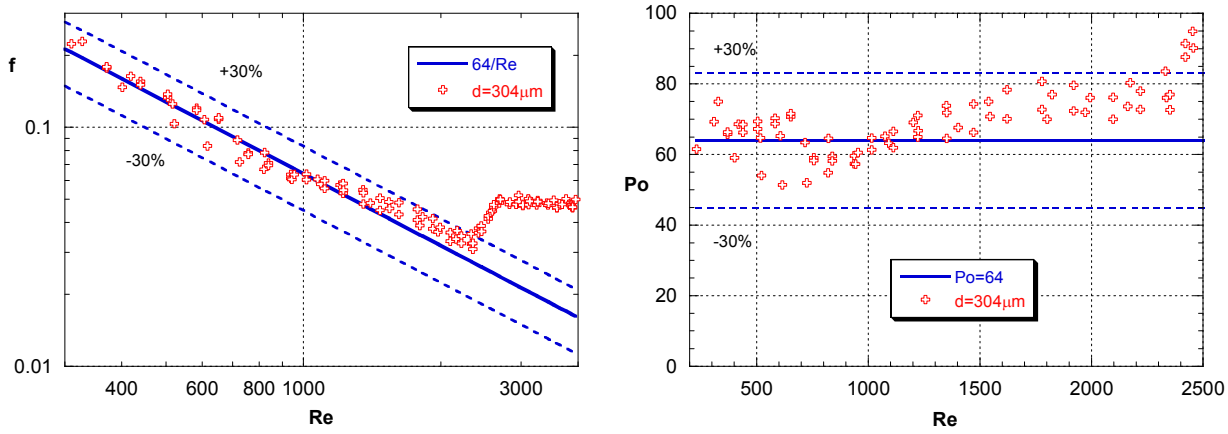

Fig. 5.10a,b: *Friction factor vs. Reynolds number (a) Poiseuille vs. Reynolds number (b) – 304 µm PTFE tube*

116 µm

The experimental error band for the 116 µm siliconated tube is uniformly filled with data points, giving a good impression of the random uncertainty that exists in measurement. From *Re* = 500 to *Re* = 2200, where transition can be seen to occur, 51% of data points fall within the 10% error band; for a 15% margin, already 81% of data are acceptable. Apart from the very slight dip in the Poiseuille number values just before transition – an area which is always subject to the inversion of pressure drops between long and short tube described for the 126 µm rough tube – no

indication can be found of reduced flow resistance. The shear rates at this diameter vary from 110×10^3 s^{-1} to 339×10^3 s^{-1} in the range of Reynolds number studied. This is already an order of magnitude above the critical shear rate given by [16], but from these data it is only clear that no clear conclusions can be drawn as to the appearance or not of slip flow effects.

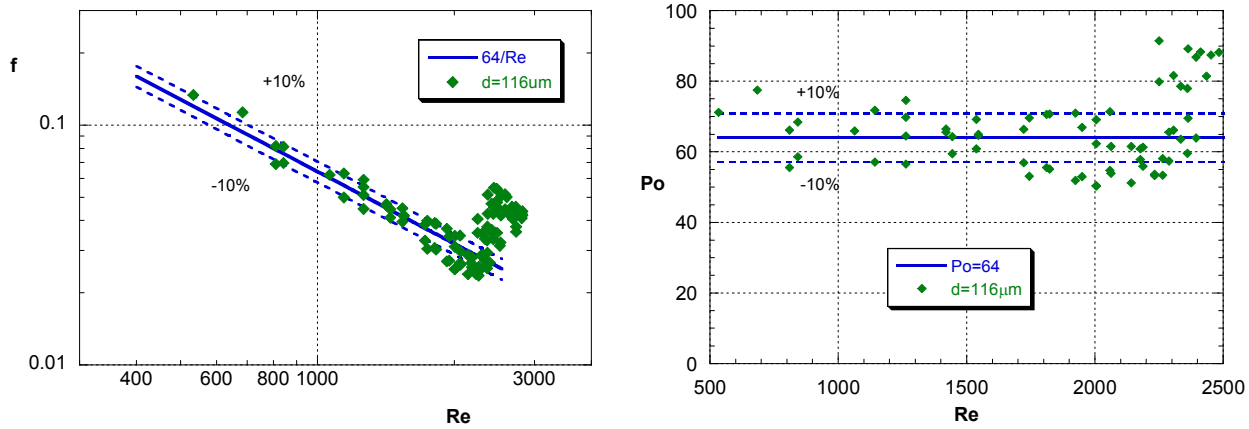

Fig. 5.11a,b: *Friction factor vs. Reynolds number (a) Poiseuille vs. Reynolds number (b)– 116μm siliconated glass tube*

70 μm

For the lowest diameter pipe some systematic reduction in the values of the friction factor can be observed. However, the experimental error margin around the reference curve is never quite abandoned, so no strong conclusion can be drawn to the effect that the shear rate is such as to induce slip at the tube wall, and therefore a reduction in the friction factor. The shear rates involved grow from 0.49×10^6 s^{-1} at Re = 600 to 1.63×10^6 s^{-1} at Re = 2000, which is around the same value at which a slight diminution of friction was observed in the 30 μm untreated smooth tube. Unfortunately no smaller diameters tubes were available for siliconation to elaborate the occurrence of critical shear rate as a function of wall wettability.

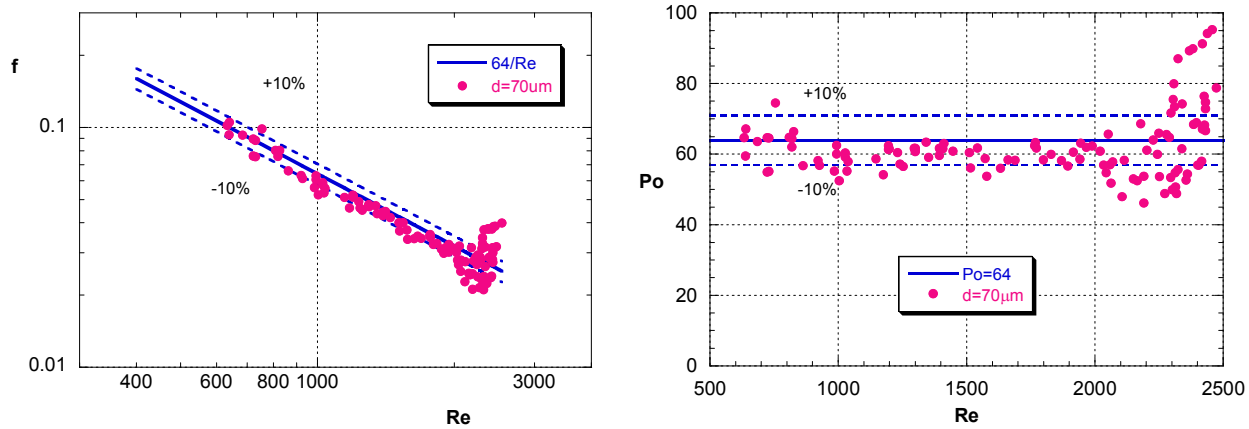

Fig. 5.12a,b: *Friction factor vs. Reynolds number (a) Poiseuille vs. Reynolds number (b) – 70 μm siliconated glass tube*

The absence of a clear slip flow effect on the friction factor, even though some experimental studies have witnessed this at lower shear rates than those in the tests discussed here [83, 16, 17] provides strong evidence that slip flow on hydrophobic surfaces is especially induced by the *desorption of nanobubbles on the tube surface*. This phenomenon was explained in paragraph 2.4.2.1, and occurs when dissolved gases in the fluid nucleate on the non-wetting surface. This creates a stratum of closely packed "cushions" (of the height of a few nanometres) over which the

liquid can run without being restricted by the solid wall. Since, in these experiments, *degassed* water is used, no possibility exists for this phenomenon to take place. And, in fact, anticipation of slip flow due to hydrophobicity of the channel wall is not seen to occur.

As for the rest, turbulent flow is seen to initiate – with the usual dip that indicates a difference in the dynamics of turbulence incipience between the long and short tube – at Re = 2250, which is in agreement with what is usually found in conventionally-sized channels.

5.1.4 Summary liquid flow campaign

The results on the measurement of the Darcy friction factor presented in the previous paragraphs indicate above all that the restrictions of experimental accuracy are quite strong at these diameters. This means that the data obtained remain to a certain degree "out of focus", and therefore it is difficult to pinpoint exactly their placement. Nevertheless, in the same way as short-sightedness goes by degrees, the outlines of our object of study can still be determined if looked at closely enough, with the light of reason.

As regards the *smooth untreated tubes*, a clear adherence to the Hagen-Poiseuille law can be deduced from the flow behaviour in pipes down to 50 µm ID. The variously dispersed data points of the 259 µm tube tests are put down to inexperience in experimentation. At 30 µm ID, the experimental uncertainty blows up rather rapidly, so that it is only very tentatively that the statement is put forward that at a shear rate of over 10^6 s^{-1} in laminar flow on smooth glass surfaces, hydrodynamic slip could take place.

Transition to turbulence, where this was achieved, proved to occur in the usual area around Re = 2300. The results of the experiments on smooth microtubes are summarized in the friction factor versus Reynolds number plot below, figure 5.13.

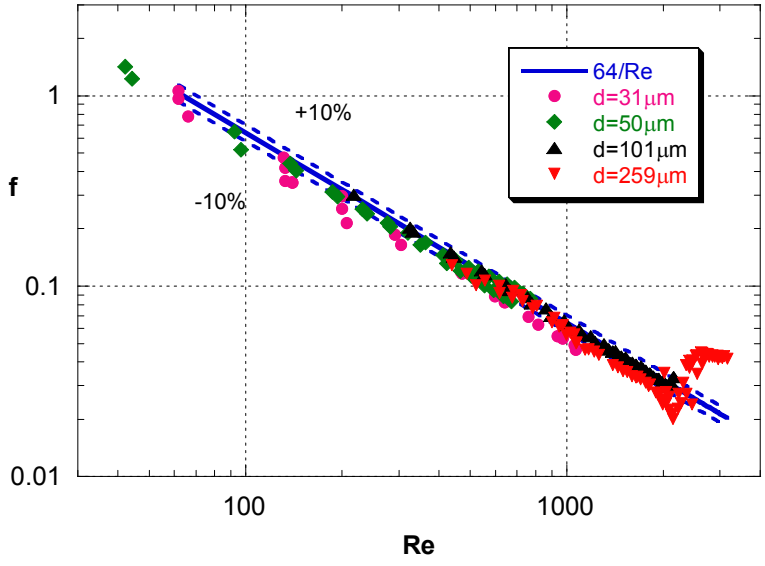

Fig. 5.13: *Friction factor vs. Reynolds number for smooth, untreated vitreous tubes*

Rough microtubes. Certainly, the slight roughness applied to the glass microtubes of 299 µm and 126 µm ID did not affect visibly the magnitude of the friction factor in laminar flow, see figure 5.14. The tests on the smallest, 126 µm ID tube did bring out a curious effect: due to a delayed incipience of turbulence in the long tube with respect to the short tube, a situation is created where

the pressure drop in the latter becomes higher than in the former, due to the higher head loss of turbulent flow. Due to the method of their calculation, this causes the collapse in the values of the friction factor around the point of transition for this particular tube, and should not be taken into consideration.

Within the range of experimental conditions, and in particular with the degree of roughness applied – which, according to the tentative optical measurements, was always below 1% of the inner diameter – no altered effect could be witnessed with respect to the hydrodynamics of flow through smooth microtubes.

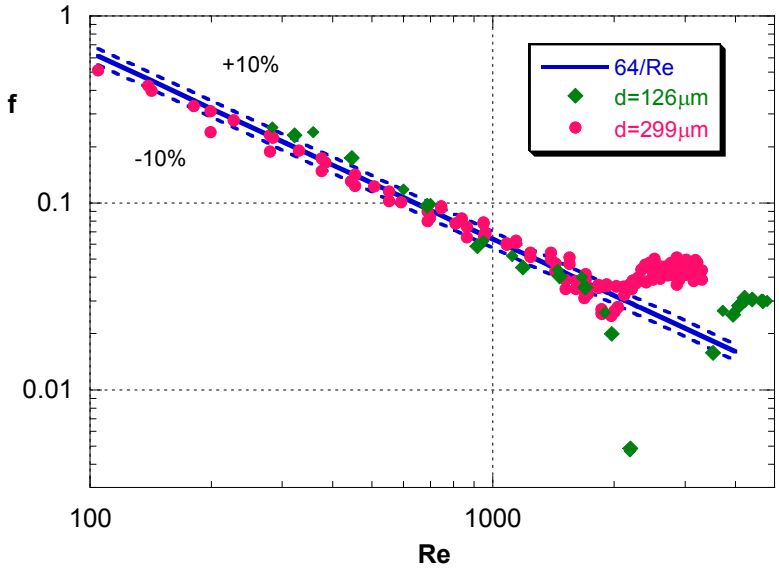

Fig. 5.14: *Friction factor vs. Reynolds number for roughened glass tubes*

Finally, as regards *hydrophobic microtubes*, no anomalous behaviour was observed both in the friction factor as in the point of transition to turbulent flow. For all diameters studied, incipience of turbulence occurred around Re = 2300. In laminar flow, the friction factor obeyed the Hagen-Poiseuille law, allowing for a certain margin of experimental error. The data are plotted in summarized form in figure 5.15.

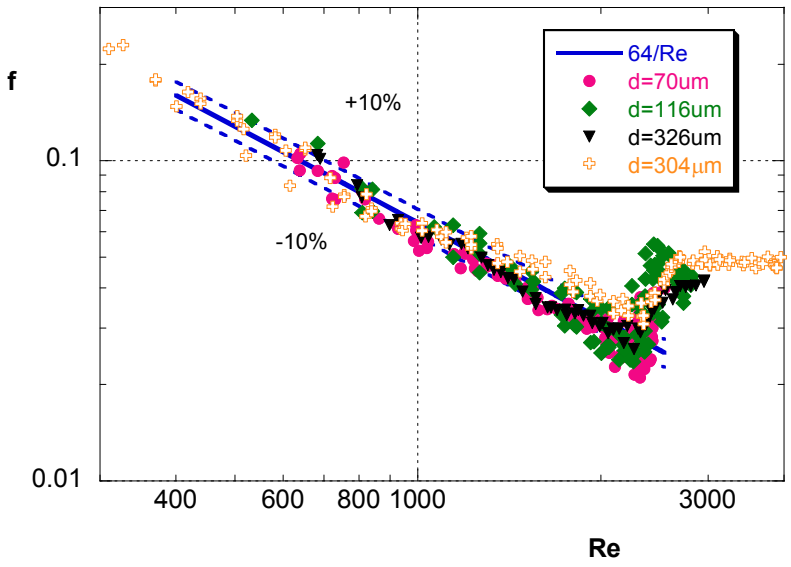

Fig. 5.15: *Friction factor vs. Reynolds number for hydrophobic tubes*

Observations in the literature indicating the advent of slip flow effects (pressure drop reduction) at shear rates of 10^5 s^{-1} when hydrophobic surfaces are employed, are negated by the measurements obtained in these experiments. The most probable explanation lies in the fact that – as opposed to the studies referred to – *degassed* water was used in the tests. This means that the phenomenon which causes the non-adherence of fluid flowing over a non-wetting surface – *i.e.* the desorption of dissolved gases into close-packed nanobubbles on the wall – is inhibited, and thus the conditions for hydrophobicity-induced slip remain absent.

5.2 Gas flow campaign

Due to the large frictional head loss per unit length in microchannels, sharp pressure drops can take place over short distances. Accordingly, due to the (linear) dependence of density on pressure in gaseous fluids, strong accelerations will take place in order for the mass flow to remain constant. This might cause an increase in flow resistance with respect to incompressible flow, where instead the density can be considered constant. Furthermore, as the speed of the gas increases along the channel, the pressure gradient will become steeper as well – according to equation (2.26) – so that a linear pressure drop between inlet and outlet cannot be assumed *a priori*.

The following series of experiments were aimed at locating any effects resulting from these different conditions of flow. This was done by measuring a linearized friction factor over a section of tube according to the tube-cutting method described in paragraph 4.1.3.2, and by comparing this with the values predicted by quasi-compressible correlations for the friction factor as derived in sub-section 2.2.2. These localized values were also compared with their corresponding globalized values, *i.e.* using the same calculations but applied to the *entire length* of tube under consideration (see, again, paragraph 4.1.3.2). The confrontation of a local value of the friction factor with the global length-average, will indicate to what degree the flow resistance varies along the axis, as fluid density is reduced and the flow accelerated. It is important to underline that these observations are relevant to flow that is amply sub-sonic, with Mach numbers below 0.3.

Helium was used as the working fluid, and smooth tubes were investigated of increasingly small diameter, down to 30 µm ID. The experimental parameters are given in Table 5.2.

Table 5.2: *Experimental parameters – gas flow campaign*

Tube material	diameter (µm)	error (µm)	Lengths (L/d)[13]		Reynolds number	Knudsen number x10^3	Pressure Ratio[14]
			long	short			
Fused Silica	254	±8.8	360	300	30 - 500	0.4 - 0.8	1.1 - 2.2
Fused Silica	101	±2.5	840	599	5 - 250	0.4 - 1.9	1.1 - 5.0
Fused Silica	50	±2.6	1834	976	5 - 100	0.5 - 4.7	2.4 - 9.2
Fused Silica	30	±0.82	2400	1853	0.8 - 13	0.3 - 6.4	2.2 - 10

It may be noted that the flow regime is decidedly laminar, almost viscous for the smallest diameter tube, so no transition effects are to be observed. Also, the value of the Knudsen number hovers around the upper limit of continuum flow (10^{-3}) – see paragraph 2.4.2.2 – so it should be taken into account that gas-dynamic slip flow might initiate, especially at the two smaller diameters. However, the analysis of the detectability of slip flow effects, expounded in paragraph 2.4.2.3, teaches us that, for an average of 15% uncertainty on the Poiseuille number, the minimum value of the Knudsen number at which anything might be perceived of these effects, is one order higher:

$$Kn_{min} = \frac{\left(\frac{e_{f\,Re}}{f\,Re}\right)}{\alpha} = \frac{0.15}{8} = 0.019 \qquad (5.1)$$

[13] According to the tube-cutting method, see sub-section 4.1.3

[14] Ratio of pressure between test section inlet and outlet

Thus, if any reduction in flow friction occurs due to the rarefaction of the gas in the microtubes, this can not be detected with this experimental set-up in these experimental conditions. It will therefore not be discussed in the following paragraphs.

The other important thing to notice is that the ratio of pressure between the inlet and the outlet of the test sections always reaches values which *compel* us to consider the flow as compressible, with the gas density diminishing up to an order of magnitude for the largest flow in the 30 µm pipe.

254 µm

First of all, comparing the two equations (2.36) and (2.38) for the friction factor, valid for isothermal or adiabatic conditions respectively, it should be stated that in (continuum) microscale *gas* flow, viscous heating effects are negligible. This means that in ambient conditions both isothermal and adiabatic approximations are valid. The difference in value between the two never reached 1% in these experiments, both in global as in local characterization. For reasons of clarity therefore, only the isothermal approximation is presented in the graphs (as the quasi-compressible expression), but the adiabatic values can be considered as overlaying.

The results for the largest capillary, d = 254 µm, are presented in figure 5.16a,b. Transition to turbulence was not reached because of the upper limit of functionality of the pipette volume flow measuring system. There is a large amount of dispersion in the data, especially in the differential (ΔL) analysis. This is due to the relatively short tubes studied and the small difference in length between the two sections: only 60 diameters (see Table 5.2). Coupled with the large diameter, this resulted in measured pressure (difference) values that were extremely small and therefore subject to high relative uncertainties. At low flow rates this effect is accentuated. This shows that the difference in length between the 2 tubes, though it should be as small as possible for an accurate derivation of the pressure slope (see figure 4.10), should also not be so little that measurement inaccuracy and flow oscillations interfere notably.

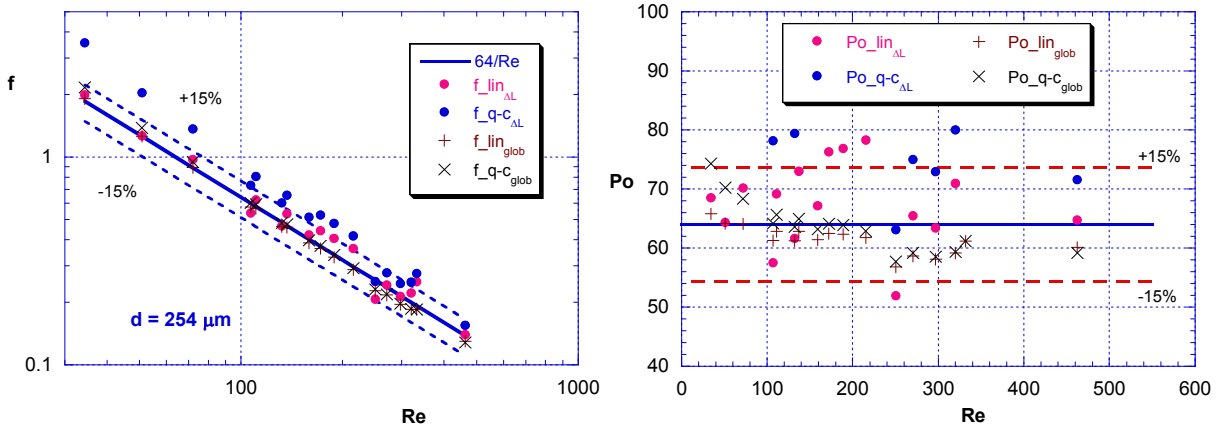

Fig. 5.16a,b: *Friction factor vs. Reynolds number (a) and Poiseuille vs. Reynolds number (b) – 254 µm tube; linearized (lin) and quasi-compressible (q-c) approximations, local (ΔL) and global (glob) values*

The global analysis allows for a less precarious measurement, although it omits elimination of concentrated pressure losses, and is a lot more stable, so that we can conclude that incompressible flow (Po = 64) is approximated quite neatly up to a Reynolds number of about 500, with a corresponding pressure ratio of 2.15 between inlet and outlet, and an outlet Mach number of 0.22.

The slightly larger scatter of the quasi-compressible compared to the linearized analysis is related to the relatively higher inaccuracy of the absolute pressure transducers (especially at low

pressures) compared to the differential manometer. The latter value can be used in equation (2.29), but quasi-compressible equation (2.36) requires absolute pressure measurements.

101 µm

In figure 5.17a,b the assessment of experiments on the 101 µm diameter tube is represented. Data points are well-situated around the reference line of the theoretical Poiseuille number for incompressible flow (*Po* = 64). The linearized and quasi-compressible analyses give similar results demonstrating behaviour that is equivalent to incompressible flow. It can be seen that the linear approximation of the *global* friction factor (f_lin_{glob}) is equally consistent as the theoretically more accurate correlations (2.36) and (2.38), also at higher values of the Reynolds number and therefore larger pressure ratios. The maximum Mach number was 0.23 at the channel outlet (*Re* = 255). Data dispersion is more pronounced in the *differential* analysis, due to the summing of measurement errors for the two lengths of capillary. The *global* elaboration is consistent with incompressible theory, with a very slight bias to lower *Po* values.

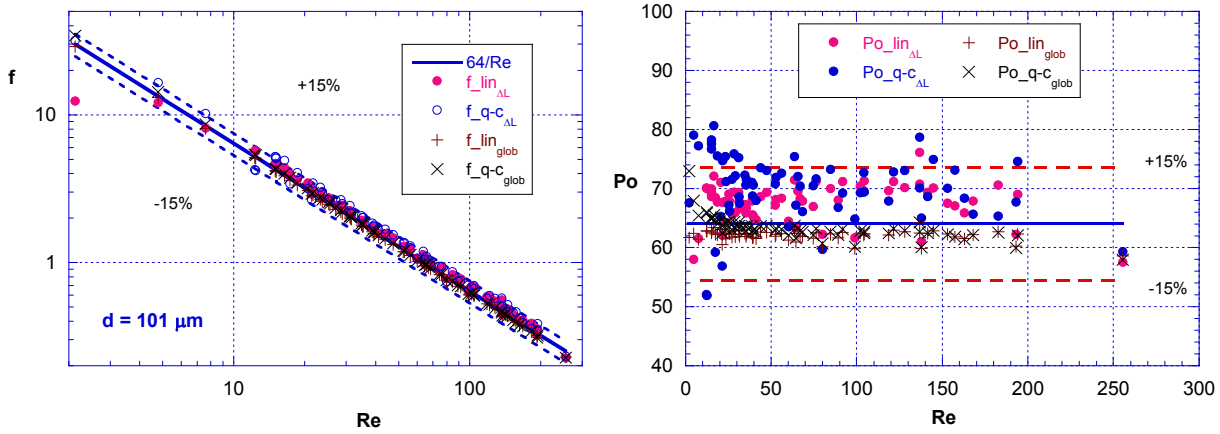

Fig. 5.17a,b: *Friction factor vs. Reynolds number (a) and Poiseuille vs. Reynolds number (b) – 101 µm tube; linearized (lin) and quasi-compressible (q-c) approximations, local (ΔL) and global (glob) values*

50 µm

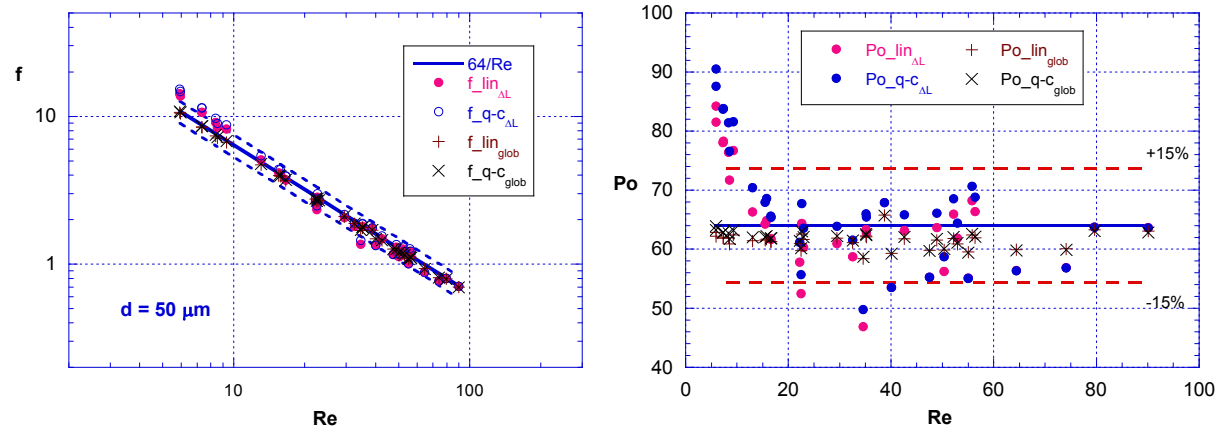

Fig. 5.18a,b: *Friction factor vs. Reynolds number (a) and Poiseuille vs. Reynolds number (b) – 50 µm tube; linearized (lin) and quasi-compressible (q-c) approximations, local (ΔL) and global (glob) values*

In the case of the 50 µm diameter micropipe, see figure 5.18a,b, it is remarkable to note that even at quite large pressure ratios (R_P = 9.2, *Re* = 75, *Ma* = 0.19), therefore where the density

variation in the tube is considerable, the *global* linearized determination (Po_lin_{glob}) still follows the more elaborate approximation of compressible flow behaviour ($Po\_q\text{-}c_{glob}$) almost perfectly. The differential evaluations ($Po\_lin_{\Delta L}$ and $Po\_q\text{-}c_{\Delta L}$) maintain a larger dispersion, but also converge closely around the reference line, which, it is remembered, is valid for completely incompressible flow.

30 µm

The smallest channel in this study has a diameter of 30 µm. The elaborated data for the various interpretations of the friction factor and Poiseuille number are shown in figure 5.19a,b. It is clear then, that compressibility effects are negligible as regards the fluid-dynamic behaviour on the scale of a long tube (where the *L/d* value is very large), because the *global* correlations (both linearized and quasi-compressible) give perfectly coherent results with the incompressible solution for tubes, $fRe = 64$.

The *local* Poiseuille number however, apart from the increased uncertainty of mass flow measurements at low Reynolds numbers, demonstrates a slight increment with respect to its global counterpart, especially in the linear approximation. This would go to indicate that the pressure derivative along the axis is steeper in the region after the inlet than the linear interpolation of figure 4.10. This would indicate a profile there that is convex rather than concave, which might reflect extended inlet effects, which are then "laminarized" along the channel.

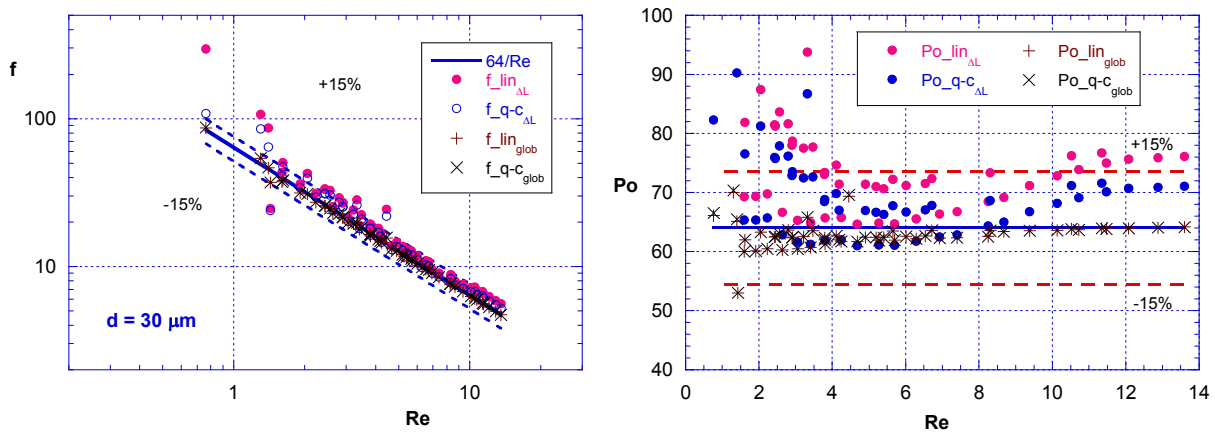

Fig. 5.19a,b: *Friction factor vs. Reynolds number (a) and Poiseuille vs. Reynolds number (b) – 30 µm tube; linearized (lin) and quasi-compressible (q-c) approximations, local (ΔL) and global (glob) values*

This stabilization of the flow must also be what explains the absence of any appreciable effects of compressibility. These effects – in particular, increased friction due to density-change-induced acceleration – were expected to become relevant when high head loss takes place over short distances like in microchannels. Instead we find that the layers in the flow are not affected by the change in fluid velocity profile in an irreversible way, in other words with very little extra entropy gain. This is confirmed by the measured temperature rise which was always extremely reduced, and the fact that both the isothermal and adiabatic equations for the friction factor (equations (2.36) and (2.38)) yielded always almost equal solutions. This also implies that no "anomalous" energy conversion takes place with respect to incompressible flow in the low sub-sonic region ($Ma < 0.3$). Thus it can be stated that the pressure profile as sketched in figure 4.10, is quite exaggerated, and that there is certainly therefore such a thing as a fully developed "self-similar" velocity profile [87], which – although it is changed in magnitude along the direction of flow – yields locally stable frictional resistance. After all, this is what is defined in the Reynolds number, where the bulk mass flow compensates for both the density and the velocity:

$$Re = \frac{\rho U d}{\mu} = \frac{4\Gamma}{\pi \mu d} \tag{5.2}$$

for circular cross-sections. Therefore, within the range of accuracy, it is licit to confirm not only the validity of the "quasi-compressible" equations for the friction factor ((2.36) and (2.38)), but also of the actual incompressible description given in equation (2.29). And that the value of this factor is inversely proportional to the Reynolds number, with Poiseuille constant equal to 64.

♪ This validity can be expressed in terms of *experimental parameters* by considering the following limitation, based on equation (2.29), using the same principle as was employed for the detectability of slip flow effects in paragraph 2.4.2.3:

$$f\left(1+\frac{e_f}{f}\right) \geq \frac{\pi^2 \rho (R_P - 1) P_{out} d^5}{8\Gamma^2 L} \tag{5.3}$$

where the pressure drop over the capillary Δp is rewritten in terms of the pressure ratio, R_P, and the experimental uncertainty $\frac{e_f}{f}$ defines the range of accuracy of the equality. Inserting the incompressible solution for f, $64/Re$, yields the limit of the pressure ratio that allows such an approximation for compressible fluids:

$$R_P \leq 1 + \frac{128\left(1+\frac{e_f}{f}\right)\mu L \Gamma}{\pi d^4 \rho P_{out}} \tag{5.4}$$

The effects of inlet and outlet can be considered of minor importance. A tube cutting method was utilised to eliminate these but this objective was evidently nullified by the extremely limited magnitude of these effects. The increase in measurement uncertainty with this method therefore proved more distorting to measurements than the concentrated losses included in the global analyses. The latter type of evaluation consistently yielded a tight adherence to the theoretical Poiseuille number, so that the concentrated losses can be deemed insignificant within the limits of experimental detection.

5.3 Viscous dissipation campaign

Many experimental works on forced convection through microchannels have evidenced deviations from conventional theory in fluid-dynamic and diabatic behaviour. Whereas often these anomalies were ascribed to "new" micro-effects, it can usually be shown that the explanations for different behaviour at microscale are hidden in the conventional theory. It is a *scaling effect* that causes certain phenomena that are negligible at macro-scale to become influential when channel geometry is reduced below a certain limit. Such an effect also pertains to viscous dissipation, which becomes important especially in liquid microchannel flows, as is explained in sub-section 2.4.3.

The table of experimental parameters in the campaign to qualify and quantify the viscous heating of a fluid flowing adiabatically through a microscopic tube, is shown below.

Table 5.3: *Experimental parameters – viscous dissipation campaign*

Tube material	diameter (μm)	error (μm)	Length (*L/d*)	Reynolds number	Viscous heating (K)
Fused Silica	101	±2.5	1081	458 - 2300	0.2 - 2.6
Glass	70	±0.9	1107 | 1400 | 1479[15]	87 - 1019	0.1 - 1.4
Fused Silica	50	±2.6	1268	40 - 685	0.1 - 2.2

Since no heating is applied to the channels, the values of the bulk temperature rise in the last column of Table 5.3 are due to viscous dissipation alone, minus losses incurred by radiation from the microtube surface and by conduction through peripheral attachments to the test section. The larger values reported for the 101 μm tube are mainly due to the higher Reynolds number of the flow, as we shall see in the following paragraphs.

The results of the experiments are given as graphs that plot the viscous heating per unit length, together with the reference curve which is described by equation (2.83), with the reference temperature rise set to 1 K, and *fRe* equal to 64 according to classical theory for laminar pipe flow. In these graphs, also the correlation by Xu *et al.* [88] for the viscous heating is given for comparison. Their empirical correlation to describe the viscotic temperature rise is:

$$\Delta T_v = \frac{93.419 \cdot Vi\ Pr^{-0.1}}{5.2086 + Vi\ Pr^{-0.1}} \tag{5.5}$$

Here, Vi is a dimensionless parameter the authors call the Viscous number, defined as the ratio of viscous energy dissipation and total thermal energy of the flow:

$$Vi = \frac{\mu U^2 L}{\rho U c_p \Delta T_{ref} d^2} \tag{5.6}$$

Thus, it can be verified whether the empirical fit of equation (5.5) or the relation (2.83) based on a careful study of the classic Navier-Stokes equations is more accurate in predicting the viscous heating in arbitrary conditions.

Next to the graphs that indicate the viscous heating of the flow in the tubes under consideration, also the correlated *friction factor* will be plotted, obtained through the analytical deduction described in sub-section 2.4.3 and expressed in equation (2.87). The friction factor obtained,

[15] Three different lengths of tube studied

conventionally, through pressure drop measurements (equation (2.28)) will be given simultaneously, so that an evaluation of the innovative method can take place.

101 μm

In figure 5.20a,b the results of the experiments on the 101 μm ID microtube are reported. The viscous dissipation effect will be least manifest here because the viscous deformation of the velocity profile is least accentuated. Furthermore, because of the high heat capacity of water, a given quantity of heat input or heat generation is reflected in relatively little temperature rise, so that detection of viscous heating becomes more difficult. At the lowest flow rates, the increase in temperature is of the same order as the accuracy of the thermocouple read-outs, so that a large margin for error is expected at those conditions; see also the uncertainty analysis in paragraph 4.3.1.3. The function for the error band is given by equation (4.15).

The predicted heating of the fluid is approached more closely by the measured values as they increase in magnitude – for the reference curve by Morini. It can be seen from figure 5.20a that the correlation by Xu *et al.* underpredicts the temperature rise per unit length, especially at higher fluid velocities. If we consider Morini's analytical equation (2.83) for viscous dissipation, we find that – since the Reynolds number is eliminated by multiplication in the expression – the Eckert number is dominant. It is defined as:

$$Ec = \frac{U^2}{2c_p \Delta T_{ref}}$$

where ΔT_{ref} is a reference temperature rise, for which the dynamic viscosity changes by about 2-3%. For water it is taken as 1 K. We see that the fluid velocity has a quadratic influence on the Eckert number, and therefore on the viscous heating of the flow in the microtube. This means that measurements should be more precise at higher flow rates and should therefore agree better with correlations that propose to predict the entity of this temperature rise.

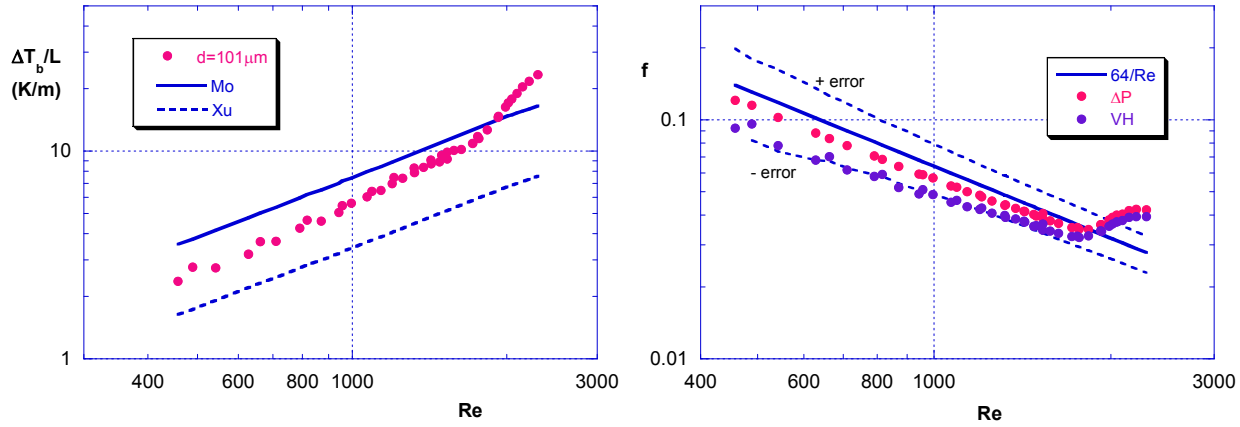

Fig. 5.20a,b: *Viscous heating vs. Reynolds number – reference lines by Morini and Xu* et al. *(a) and friction factor vs. Reynolds number – pressure drop (ΔP) and viscous heating (VH) analyses (b); 101 μm tube*

The dependence of viscous heating on flow rate also means that at low velocities, the error margin on the friction factor approximation increases, as predicted by the uncertainty analysis synthesized in equation (4.15) and depicted by the dashed lines in figure 5.20b. Nevertheless, the data are maintained within this region, and converge to the reference curve of $f = 64/Re$. Utilising pressure drop measurements at these conditions proves more accurate, as the ΔP data in the same

figure go to show. However, the point of transition from laminar to turbulent flow (at *Re* = 1800) is clearly defined and consistent for both description methods.

70 µm

Three different lengths of 70 µm capillary were studied, primarily to verify the influence of the channel length on the measurement of the viscous heating, but also to have extended proof of the tube-cutting method in determining the friction factor. (This diameter was not dealt with in the section on liquid flow pressure drop measurements, section 5.1.)

It can be seen from figure 5.21a that the experimental data approach the reference curve by Morini closer than for the 101 µm tube. Evidently the increased viscous heating (at a given Reynolds number $\Delta T_b/L$ is distinctly higher for the smaller diameter) facilitates temperature measurements, and the analytical prediction proves to be a valid asymptote for the data obtained. The empirical correlation by Xu and coworkers is increasingly inaccurate according to these experiments.

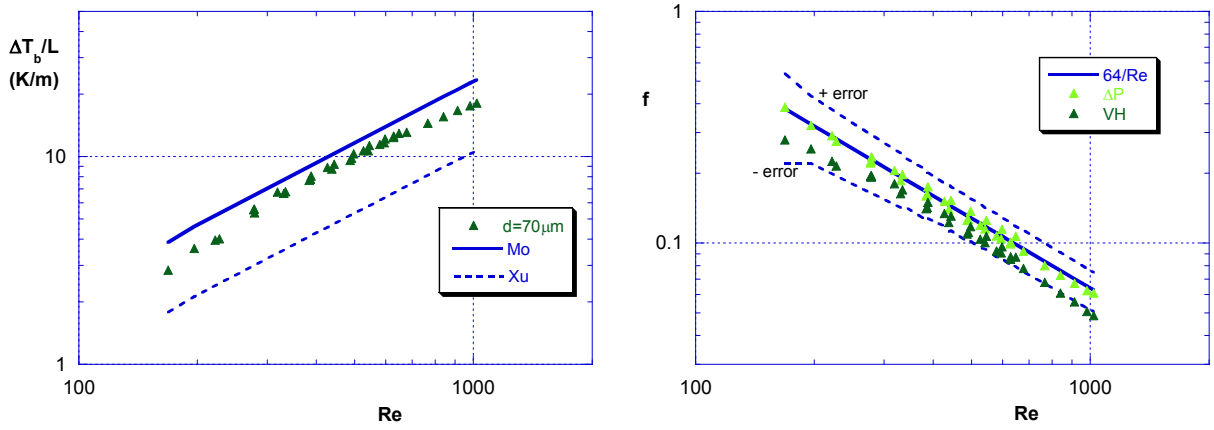

Fig. 5.21a,b: *Viscous heating vs. Reynolds number – reference lines by Morini and Xu* et al. *(a) and friction factor vs. Reynolds number – pressure drop (ΔP) and viscous heating (VH) analyses (b); 70 µm tube*

Thus, also the approximation of the friction factor using the bulk temperature rise of the fluid is more accurate. Especially in the middle range of the Reynolds number a close agreement is found between the values obtained from viscous heating measurements and pressure drop measurements. The latter prove to be a reliable verification of the analytical curve of Hagen-Poiseuille over the entire range studied.

The influence of the length of tube can be noticed in the measurements at higher Reynolds number: these were taken with the shortest test section to be able to contain the high head loss. The points for *Re* > 700 maintain a slightly larger distance from the solid reference lines in figures 5.21a,b due to the lower accuracy in measuring the lower temperature rise: even though the flow rate is large, the short distance does not allow the fluid to gain enough heat as it squeezes through the tube. Nevertheless, the corresponding error margin is indicative of a good correspondence between the viscous heating analysis and the pressure drop formulation of the friction factor: at *Re* = 1019 the datapoint straddles the negative error margin at -19.3% from the 64/*Re* reference line.

50 µm

With the smallest diameter tube we achieve a definitive validation of the concept of viscous dissipation in a microchannel. It can be noticed from figure 5.22a that the measured bulk temperature rise in the length of capillary studied is very close to the theoretical heating expressed by equation (2.83), derived from Morini's analysis in [24]. The residual difference that remains is

probably due to the marginal heat losses due to radiation and conduction along the test section and fittings. Also, the high heat capacity of water still is the cause that the temperature rise remains limited, so that a certain margin of tolerance has to be allowed for in its measurement. Using a refrigerant for example, which has much lower heat capacity and comparable viscosity, would cause the viscous heating to be much more highlighted and therefore easier to detect. This is also manifested in the graphs comparing scaling effects for two different fluids (water and isopropanol) exhibited in section 2.5, figure 2.9a,b. The correlation of Xu *et al.* can definitely be refuted at this point.

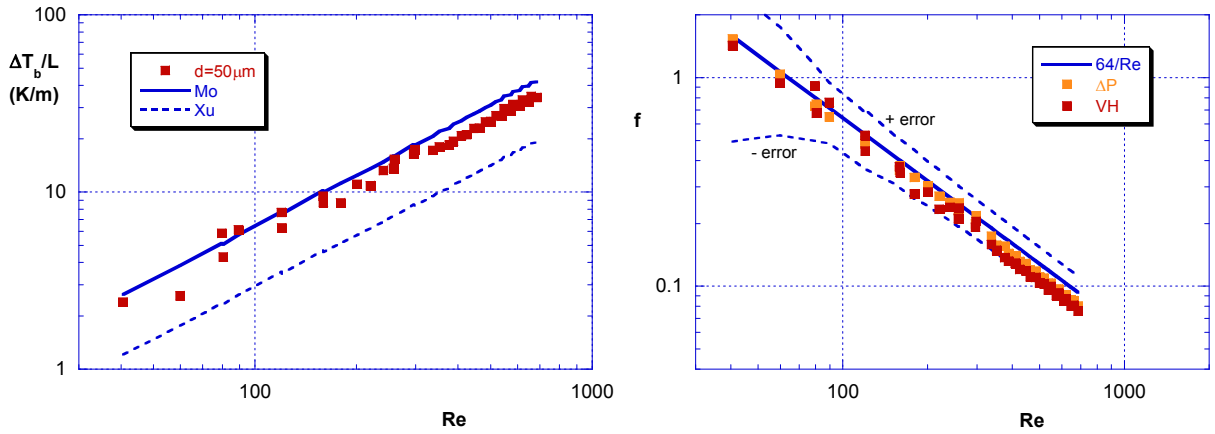

Fig. 5.22a,b: *Viscous heating vs. Reynolds number – reference lines by Morini and Xu* et al. *(a) and friction factor vs. Reynolds number (b) – pressure drop (ΔP) and viscous heating (VH) analyses (b); 50 μm tube*

In figure 5.22b, the friction factor is seen to be accurately predicted both by the viscous heating approximation of equation (2.87) as by the classic description in terms of pressure loss. Thus, we have obtained a valid alternative method for characterizing the frictional loss in a microchannel. If we wish to know the friction factor of a microfluidic system, this method allows us to bypass the cumbersome practicalities of measuring pressure in microscopic conduits – an operation which has to combine coarse pressure tappings and pressure sensors with fragile flow passages and minuscule flow rates – and resort to the finer, less intrusive measurement of fluid temperature. The smaller the characteristic dimension of the system, the more accurate this method will be.

As an overview of the effect of tube diameter on viscous dissipation, figure 5.23 exposes the viscous heating per unit length for all three capillaries studied.

It is clear that viscous dissipation is a typical scaling effect, a phenomenon that has to be taken increasingly into account as the system characteristic dimension decreases *ceteris paribus*. Thus, for a given fluid, flow rate and channel length, viscous heating of the flow will become more pronounced as the channel diameter is reduced. In figure 5.23, for a given Reynolds number, we can see that the bulk temperature rise as a function of length (in adiabatic conditions it is remembered) is *steeper* for *smaller* tubes.

This effect was predicted, analysed and described accurately by Morini in [24], who provided the analytical solution to the energy and momentum balance in terms of the viscous dissipation in frictional flow, and which has been successfully validated by the experimental data presented. The correlation suggested by Xu *et al.* is to be considered not generally applicable.

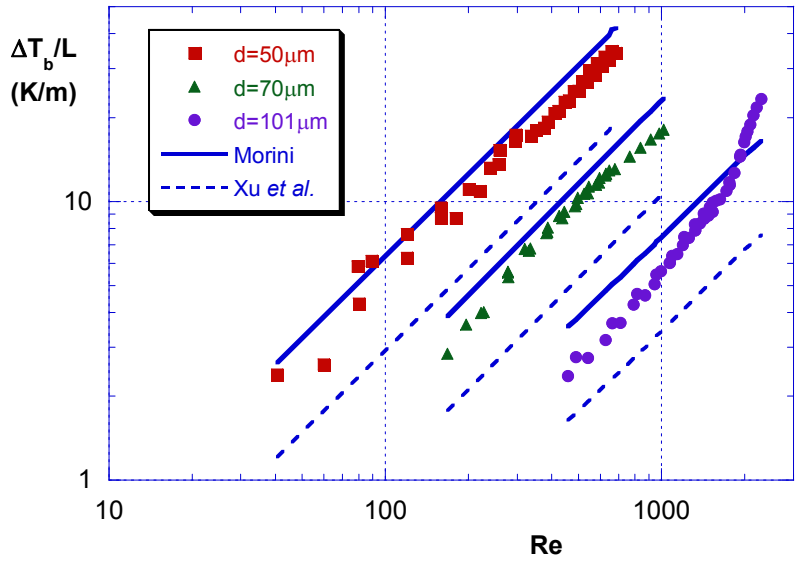

Fig. 5.23: *Viscous heating vs. Reynolds number for 3 different diameters, validated against predictions by Morini* [24] *and Xu* et al. [88] – *fluid: water*

The results on the approximation of the friction factor are united in figure 5.24. Viscous dissipation is caused by wall friction, so that the viscous heating of a flow is representative of the degree of friction it undergoes. This conversion of friction to heat is only measurable when the proportion of viscous deformation of the velocity profile to flow rate heat capacity is high enough, as it can be in microchannels. Thus, in the case of water as a working fluid, the friction factor can be accurately established with *temperature measurements alone*, at diameters smaller than 100 µm. Also the transition from laminar to turbulent flow can easily be deduced from the value of the viscous temperature rise, which increases sharply as the flow layers start to be disrupted by eddies and vortices. The error bands refer to the Viscous Heating analysis.

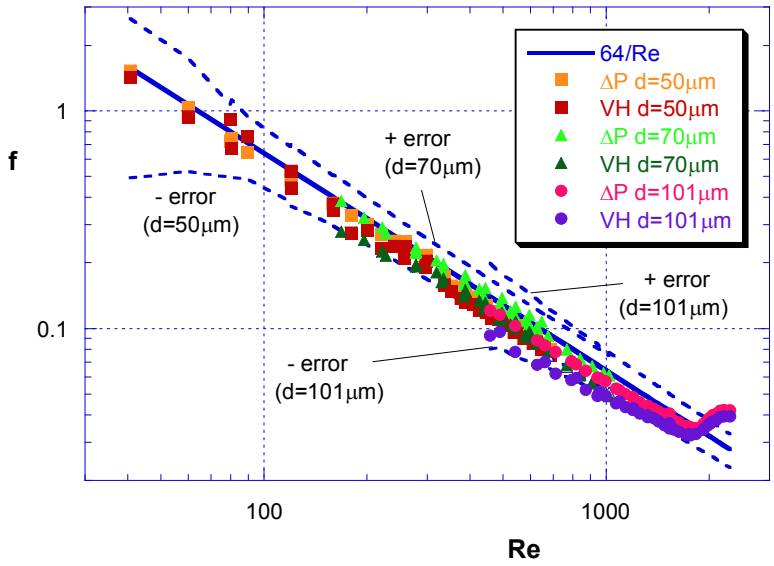

Fig. 5.24: *Friction factor vs. Reynolds number for 3 diameters; pressure drop (ΔP) and viscous heating (VH) analyses*

5.4 Heat transfer campaign

One of the most promising applications of microscale flow is miniature, high-efficiency heat transfer. In this context, the most simple and immediate solution to the problem of concentrated heat exchange is the use of small diameter channels with single-phase water flow, but there is paucity of publicised knowledge of these conditions (see sub-section 3.1.2). Furthermore, the possible intrusion of scaling effects in the thermal behaviour of a typical microchannel, makes characterization more complex (see in particular sub-sections 2.4.3, 2.4.4 and 2.4.5).

To attempt a systematic confrontation of this problem, the following train of experiments was carried out (Table 5.4). The aim of these experiments was to map the internal heat transfer coefficients at 3 axial locations in a uniformly heated microtube, considering variations in inner diameter, surface condition and flow regime (laminar/turbulent). Apart from a single reference test with a 1 mm ID specimen, microtubes of glass and stainless steel of comparable diameter were utilised (considered smooth and rough, respectively), both heated by Joule effect: the former through a thin metal film deposited on the outside surface, the latter through direct application of DC voltage to the tube wall. As was the case with the fluid-dynamic experiments on roughened glass tubes (see sub-section 5.1.2), the inner surface of the test specimens is technically considered "smooth", except for the smallest stainless steel tube which has more than 5% relative roughness. It is extremely difficult to apply an increased, uniform roughness on top of a finished surface. Therefore, again, it is the *absolute* increase of roughness that justifies the investigation: to verify whether the distinctly coarser wall of the stainless steel tubes (compared to the glass tubes) gives rise to noticeable effects in laminar or turbulent heat transfer.

Table 5.4: *Experimental parameters – heat transfer campaign*

Tube classification	Tube material	d (μm)	D (μm)	e_d (μm)	Ra (μm)	Ra/d (%)	L (*L/d*)	<Re>	<Gz>	M x10^6
1 mm	St.Steel	1004	1598	±2	1.2	0.12	100	1750- 7565	-	28 - 120
~ ½ mm	Glass	528	859	±3.9	~0.05	0.01	150	50 - 2775	9 - 233	3 - 70
	St.Steel	440	708	±14	2.7	0.61	302	354 - 4979	8 - 111	9 - 58
~ ¼ mm	Glass	259	951	±4.4	~0.05	0.02	317	105 - 2576	3 - 103	12 - 330
	St.Steel	280	500	±4.2	2.0	0.71	507	307 - 5775	6 - 90	6 - 94
~ ⅛ mm	Glass	120	804	±2.4	~0.05	0.04	545	279 - 3138	6 - 58	17 - 170
	St.Steel	146	470	±8.2	0.6	5.62	733	323 - 7025	5 - 50	36 - 377

The average Graetz values in Table 5.4 show us that the flow is usually in thermal development, which is above all the consequence of the short heated length (given later in Table 5.5). However, the heated section of the tube was placed at such a distance from the inlet of the channel, that hydrodynamically the flow was always fully developed upon heating. This way the heat transfer behaviour in the thermal entrance length can be studied, which is the probable regime of operation in microchannels.

The conductance number, *M* (definition in sub-section 2.4.4) is always well below the criterion given in the defining equation (2.88), which states the limit above which significant conjugate effects can be expected in the tube wall. Though conduction in axial direction in the wall is then unlikely to be discerned, we shall see that a different kind of conduction – equally disturbing and even more evanescent – will unsettle the heat input conditions and distort the results, especially in the glass tubes.

Turbulent flow is studied particularly in the steel microtubes, as any anomalous effects are expected especially in rough surface conditions. The Reynolds numbers achieved with the glass test sections were enough to initiate transition.

Table 5.5 is a copy of Table 4.6, indicating the axial locations of the wall thermocouples as defined in figure 4.13.

Table 5.5: *Test section characteristics for heat transfer experiments*

Tube classification	Tube material	d (μm)	L_{ht} (L_{ht}/d)	TC1 (z_1/d)	TC2 (z_2/d)	TC3 (z_3/d)
1 mm	St.Steel	1004	52	14	28	41
~ ½ mm	Glass	528	70	14	33	63
	St.Steel	440	211	36	134	200
~ ¼ mm	Glass	259	141	36	75	123
	St.Steel	280	317	16	230	301
~ ⅛ mm	Glass	120	295	79	161	266
	St.Steel	146	361	74	176	334

The experimental results for *laminar flow* (sub-section 5.4.1) will be displayed as graphs showing the measured local Nusselt numbers at the 3 axial locations given in Table 5.5 versus the Reynolds number. Thus, for each diameter class, the dependence of the heat transfer coefficient will be revealed on flow rate, axial distance and the type of microtube.

The experimental error is visualized in the form of error bars on each datapoint. Utilising the expressions for the uncertainty on the heat transfer coefficient given in Appendix II, a *median error* was taken, calculated at Re = 1000 for the middle thermocouple position, at an average heat flux, and applied to all datapoints in the laminar regime. The divergence of the *true error* from this median is negligible for the stainless steel tubes; but for the glass tubes the actual uncertainty increases sharply for larger Reynolds numbers (up to double the error at Re_{tr}). The reason for this difference is that the maximum allowed outside wall temperature (<100°C to avoid any local sub-cooled flow boiling) is reached sooner by the glass tube, due to its much higher thermal resistance – see also Table 4.1 in chapter 4. Thus, at large flow rates, only a small fluid temperature rise can be achieved. This gives rise to the high influence on the total uncertainty of the *bulk temperature rise* measurement (see the graph in figure 4.29) since the error on the thermocouple read-out is kept at a constant 0.1 K (thus for the temperature difference between outlet and inlet 2×0.1 = 0.2 K).

As for the results on *turbulent flow* (sub-section 5.4.2), due to the more complex behaviour of the heat transfer number in this flow regime, the results are displayed as a convergence of the measured local Nusselt number to the predicted value according to the Gnielinski correlation, so that any anomalies can be recognised more readily. The error bars show the median error at Re = 4000, which is representative for the data-range where fully turbulent flow can be seen to have set in, generally for Re > 3500. Experimentation was carried out on the stainless steel tubes only.

In all the experiments the heat input was also varied ($20 < q'' < 400$ kW/m^2), but was found to influence the Nusselt number very little in laminar flow, and not at all in turbulent flow.

5.4.1 Laminar flow

½ mm

To begin with the largest class of diameter, the results depicted in figure 5.25 are clearly indicative of thermally developing flow. There is a considerable axial dependence of the heat transfer coefficient, especially for the glass tube, with higher Nusselt numbers nearer to the channel inlet over the entire range of Reynolds number. In fact, as is known from classical theory, the less thermal development, the stronger the drive for heat exchange (see sub-section 2.4.5). As we can see from the table of experimental conditions, at 528 μm ID (due to the relatively short length of

heated tube) the flow is nearly always in thermal development (Gz > 10). Therefore only nearest to the exit and at low Reynolds numbers do we approach the thermally developed state corresponding to the constant value for the Nusselt number, 4.36.

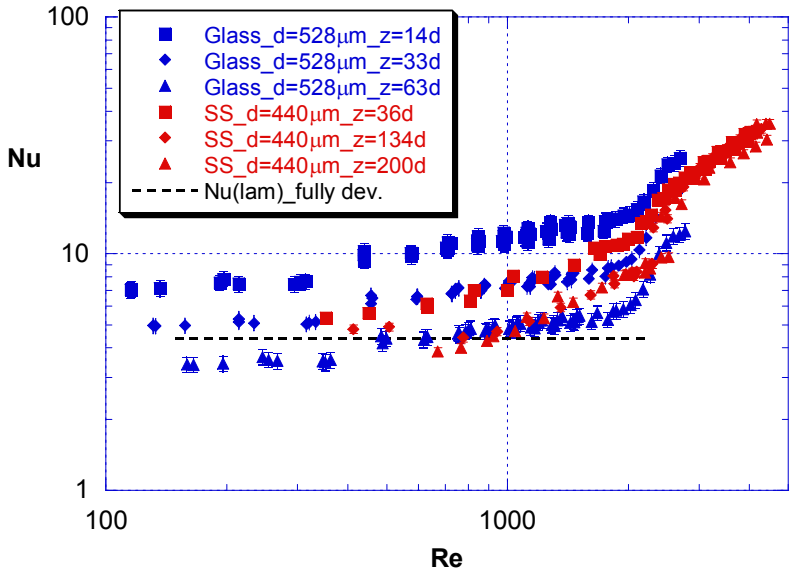

Fig. 5.25: *Glass vs. Stainless Steel tubes (~ ½ mm ID) – Local Nusselt vs. Reynolds numbers at 3 axial locations*

It is interesting to note that the local temperature measurements at the corresponding axial location of z ≈ 35 diameters, show a behaviour of the Nusselt number which is practically identical for both the glass (smooth) and the stainless steel (rough) pipe, confirming the lack of influence of increased roughness in the latter type of tube. For the 2 axial locations on the steel microtube further downstream (z = 134*d* and z = 200*d*), the development effects can be seen to have disappeared, as the Nusselt numbers are overlaying for all Reynolds numbers, and tending to the fully developed value, as is also the case for the glass tube (though with a slight undershoot).

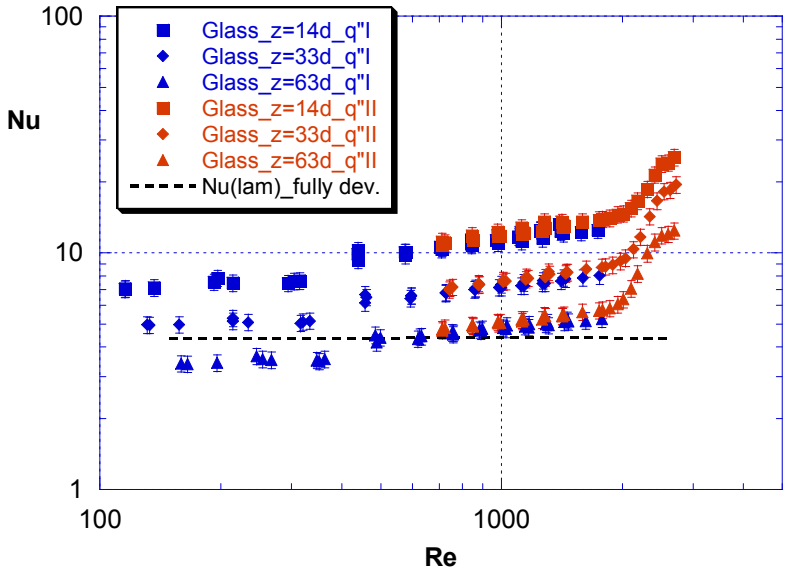

Fig. 5.26: *Glass tube (*d = *528 μm) – Local Nusselt vs. Reynolds numbers at 3 axial locations, 2 levels of heat input*

The advent of turbulence and its increased heat transfer efficiency can be individuated where the curves turn sharply upwards at *Re* ≈ 2000.

The numerical values of the heat transfer coefficient vary between a minimum of h = 4078 W/m^{2}K at z = 63d of the glass tube at Re = 169, and a maximum of h = 16 868 W/m^{2}K at Re = 2009 for the glass tube at z = 14d. (The values for the stainless steel tubes are situated within this range.)

To point out the extremely limited influence of the heat input, the data for the glass tube in the figure above are segregated in the following figure 5.26 into values with 2 ranges of heat input:

40 < q"I < 100 kW/m^2 ;

120 < q"II < 180 kW/m^2 .

Upon close inspection, a very slight increase in the Nusselt number at equal Reynolds numbers can be discerned, but it is not sufficient to justify separate mapping of the heat input.

¼ mm

In figure 5.27 above, the experimental data of the ~ ¼ mm ID tubes can be seen. We notice with respect to the larger diameter duct a *decrease* of the local Nusselt numbers for the smooth glass tube, whereas the steel channel manifests comparable behaviour. The thermocouple closest to the inlet of the latter channel yields distinctly higher heat transfer values because of its extreme proximity to the start of the heated section (z = 16d), and therefore in full stage of thermal development. The other two axial locations indicate coherence with the fully developed Nusselt number for Re < 700. In fact, the corresponding global Graetz number drops below 10 there (see sub-section 2.4.5). The numerical values of the heat transfer coefficient vary between h = 9695 W/m^{2}K at z = 301d at Re = 647, and h = 27 496 W/m^{2}K at Re = 2000 at z = 16d.

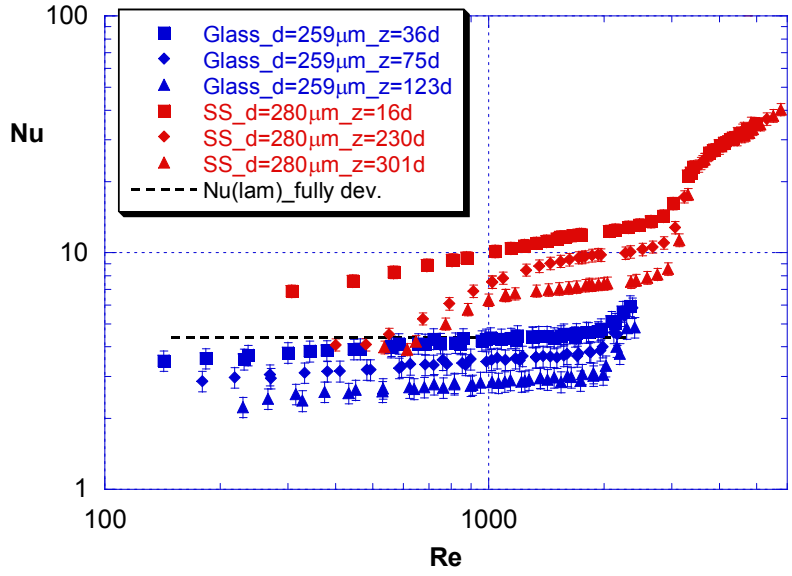

Fig. 5.27: *Glass vs. Stainless Steel tubes (~ ¼ mm ID) – Local Nusselt vs. Reynolds numbers at 3 axial locations*

For the glass channels the axial dependence is reduced (more fully developed heat transfer due to the relatively longer heated length) but especially the considerable decrease of the Nusselt numbers – to below the theoretical fully developed value in laminar regime – catches the eye. The heat transfer coefficients are practically halved with respect to the steel tubes at equal Re.

Before attempting to explain this behaviour, let us take a look at the data for the smallest class of conduits.

⅛ mm

The values of the heat transfer coefficient for the steel capillary vary between h = 15 565 W/m^{2}K at Re = 680 and h = 53 013 W/m^{2}K at Re = 2011, with scarce axial dependence. For the glass tubes the heat transfer coefficients at the corresponding Reynolds numbers are h = 15 470 W/m^{2}K and h = 24 951 W/m^{2}K, respectively. The transition to increased heat transfer efficiency in turbulent flow can be seen to be smoother in the metallic channels (see figure 5.28). This might be an effect of the much coarser inner surface in the steel microtube of this diameter.

The trend that was already observed for the glass pipes is continued for the 120 µm tube as regards the *lowering* of the local Nusselt numbers and the decrease in axial dependence. In fact, at this diameter the heated length is relatively much larger so that the flow reaches thermal development well inside the test section and no more axial dependence is expected. We can see from Table 5.4 that the Graetz number is still mainly above 10, but compared to the larger tubes the order of magnitude is distinctly lower.

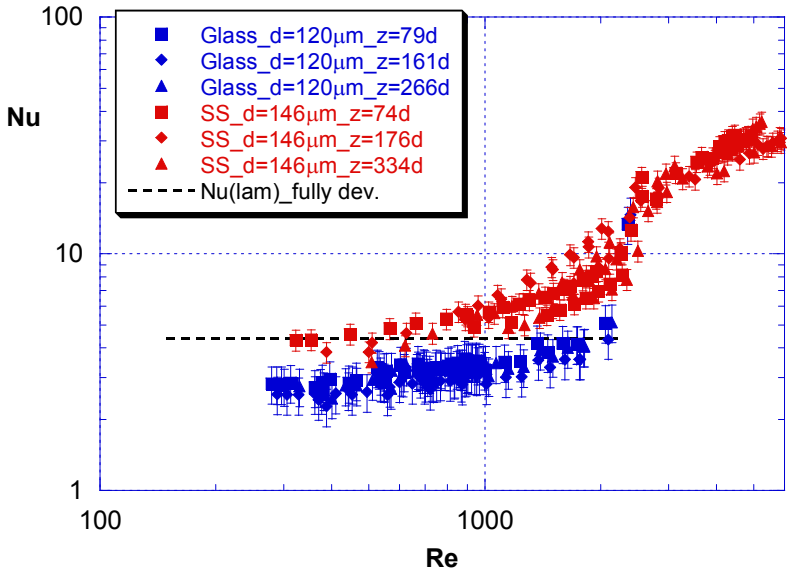

Fig. 5.28: *Glass vs. Stainless Steel tubes (~ ⅛ mm ID) – Local Nusselt vs. Reynolds numbers at 3 axial locations*

There is still a distinct dependence on Reynolds number present, however. This could be due – at this small proportion of inner to outer diameter – to an incipience of the phenomenon of conduction along the walls and in the other materials attached to the test section. At very small diameters, the mass flow of fluid becomes itself extremely reduced compared to the mass, for example, of connected auxiliaries. Thus, in bringing the entire system to a stable, steady-state temperature, a large dispersion of the heat put in takes place, since only very little heat is absorbed by the convective force of the fluid, so that large losses and long settling times are the consequence. The lower the flow rate (the Reynolds number), the more accentuated this effect will be.

If we look at the criterion given for the heat conductance number (equation (2.88)), we find that the values of this number for all experiments carried out here (see Table 5.4) are well below the limit suggested for the occurrence of significant axial conduction. This fact seems to point to an explanation that, yes, asserts heat maldistribution, but attributes it rather to disturbances (heat sinks) that lie outside the system boundary of the channel strictly, like *e.g.* thermocouples, feeding wires, fittings and connected tubing.

This conclusion is fortified by observing the behaviour of the stainless steel tube of similar inner diameter, but *smaller outer diameter* (and therefore thinner wall). This channel maintains the general level of Nusselt numbers as was observed for the larger tubes of the same material: with an

improving heat transfer at high (laminar) Reynolds numbers, but, importantly, tending to the fully developed value at lower *Re*, without dropping below.

Evidently, for the steel tubes, the heat put in electrically is absorbed more efficiently by the water flow, both because of the thinner wall with better conductivity, and because of the fact that the *entire wall thickness* is heated as opposed to only a thin layer deposited on the tube outer surface. Therefore, it is not so much a question of increased *axial* conduction in the thick glass wall that distorts the heat transfer coefficient measurements (in fact, the conductance number *M* is lower than for the stainless steel tubes, see Table 5.4), but rather a question of inhibited *radial* conduction, causing the heat put in to disperse more easily to peripheral mass.

The outer wall temperature measurements are true in both types of capillary, but the generated heat that causes these temperatures on the external surface is *underestimated* in the case of the thick-walled glass tubes: only part of the heat is absorbed by the fluid, while a significant amount goes lost before the flow passage is reached. Thus, the enthalpy rise of the water ($\Gamma c_p \Delta T_b$) is deficient because the fluid bulk outlet temperature is lower than it would be if all the heat were absorbed. Since the *local* fluid temperature along the axis is *also* determined from the fluid bulk outlet temperature (assuming a linear profile between inlet and outlet), this value will also be underestimated.

Let us try to describe the situation mathematically.

In the following figure 5.29 the hypothetical temperature profiles of a typical experiment are sketched, assuming there is a significant amount of the heat applied at the wall that is not absorbed by the fluid. Thus, the temperature profile of the wall (T_{wall}) is given – assuming for now that the wall is uniform – and the temperature of the fluid is divided into the actual *measured* value (T_{f_meas}) and the *ideal* value it would acquire if no dispersion took place (T_{f_ideal}).

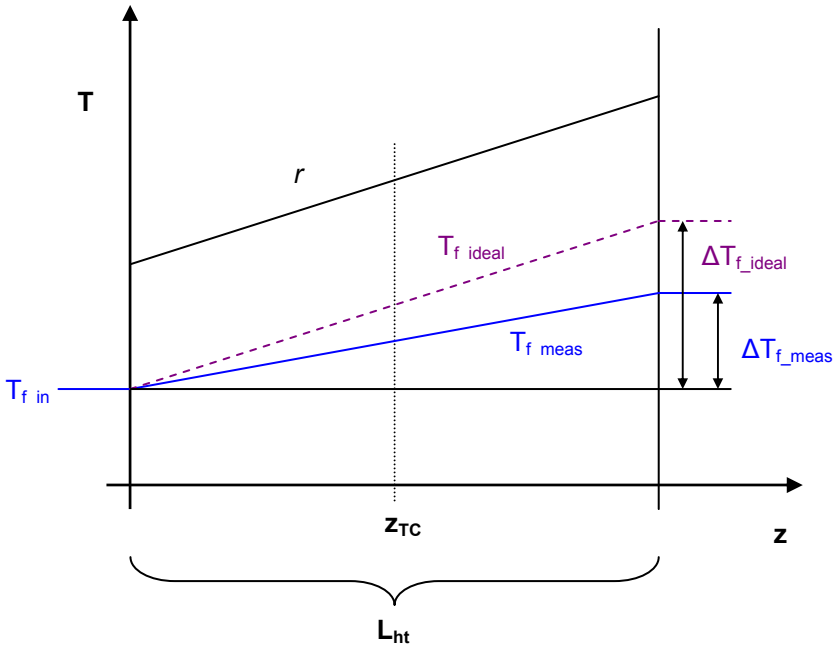

Fig. 5.29: *Schematic of the axial temperature profiles in a heat transfer test where significant peripheral heat dispersion takes place (*e.g. *in a thick-walled glass capillary)*

Now, the heat transfer equations are derived from (2.43) and (2.49):

$$\begin{cases} q_{ideal} = \Gamma c_p \Delta T_{f\_ideal} = h_{ideal}\left(T_{wall} - T_{f\_ideal}\right)A_{ht} \\ q_{meas} = \Gamma c_p \Delta T_{f\_meas} = h_{meas}\left(T_{wall} - T_{f\_meas}\right)A_{ht} \end{cases} \tag{5.7}$$

We want to find out what the effect on the measured heat transfer coefficient is (compared to the ideal value) of an underestimation of the exit bulk fluid temperature, as depicted in figure 5.29.

Let us define an underestimation factor a on the ideal fluid temperature rise ($0 < a < 1$). Thus, $\Delta T_{f\_meas} = a\Delta T_{f\_ideal}$. Also, let us scale all temperatures with the fluid inlet temperature (which equates to stating $T_{f\_in} = 0$) since we are only interested in a qualitative analysis of the temperature differences between the wall and the fluid. This means that at each point z_{TC} along the microtube – since the assumed profile is linear between inlet and outlet – the measured fluid temperature is underestimated by the same factor: $T_{f\_meas} = aT_{f\_ideal}$.

Inserting these corrections in the second of equations (5.7):

$$h_{meas} = \frac{\Gamma c_p a \Delta T_{f\_ideal}}{A_{ht}\left(T_{wall} - aT_{f\_ideal}\right)} \tag{5.8}$$

The effect on the heat transfer coefficient is strengthened therefore: if a is reduced (or: a larger error is made on the fluid temperature rise) the numerator decreases *and* the denominator increases. The underestimation of the heat transfer coefficient is therefore even larger.

This translates in lower Nusselt numbers, and the effect is stronger as the convective force ($\sim Re$) of the fluid diminishes, because the relative contribution of *conductive losses to peripheral mass* will increase (in the example above, this would correspond to a smaller value of a).

5.4.2 Turbulent flow

For heat transfer in turbulent flow, the Gnielinski correlation – equation (2.48) – provides the standard of reference. This correlation has proved to be the most reliable in a wide range of flow conditions at macro-scale, although it lacks the simplicity in computation of the more intuitive Dittus-Boelter correlation. However, since computation is the one thing that is made easy nowadays and accessible to everyone, we shall maintain the more precise, though less streamlined, Gnielinski expression as the icon of comparison for the turbulent heat transfer measurements presented in the following paragraphs.

The influence of roughness, if any, should be to increase heat transfer performance with respect to smooth tubes due to increased contact between wall and fluid. Therefore, turbulence experiments were carried out first on the rough, stainless steel tubes, assuming – in the case of adherence to the unmodified Gnielinski correlation – that for smooth tubes the same behaviour would hold. This decision was underpinned by the very limited degree of fluid heating that could be achieved with the glass tubes at high flow rates, as was explained in the introduction to this section, 5.4.

1 mm

To verify the validity of the experimental set-up and to establish a reference case for subsequent tests, a preliminary investigation of the turbulent heat transfer behaviour in a 1 mm pipe was effectuated. The local Nusselt numbers as a function of the (local) Reynolds number is given in figure 5.30 for 3 different temperature levels. The inlet temperature of the water was varied from 20°C to 45°C to be able to reach higher Reynolds numbers (thanks to the lower viscosity of water at higher temperature).

The variation in the Nusselt numbers for the 3 temperature levels is related to the change in Reynolds number which is tied to the viscosity. Therefore, to get a better idea of whether the behaviour of the flow in the tube is coherent with predictions, it is more useful to normalize the experimental Nusselt numbers with the theoretical values, in this case those calculated from the Gnielinski correlation, equation (2.48). This is done in figure 5.31, where it can be seen that the measured values (for $Re > 3000$) converge rather well within a range from -5% to +15% with what Gnielinski determined. The convergence seems to improve at higher Reynolds numbers and for higher inlet temperature. It should be noted that the mass flow measurement is more erratic at the high mass fluxes in such a "large" diameter pipe, since the liquid level in the mass scale (see figure 4.23) increases rapidly and beyond the optimal range of precision.

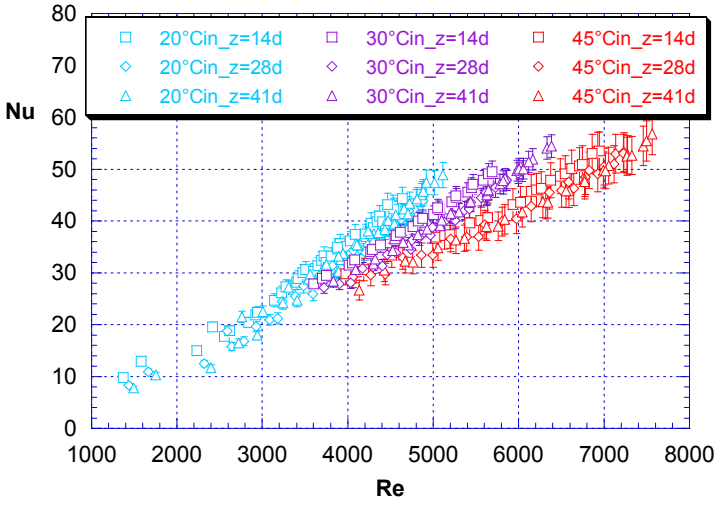

Fig. 5.30: *Stainless steel 1 mm tube – experimental local Nusselt vs. Reynolds numbers at 3 axial locations for 3 levels of fluid inlet temperature*

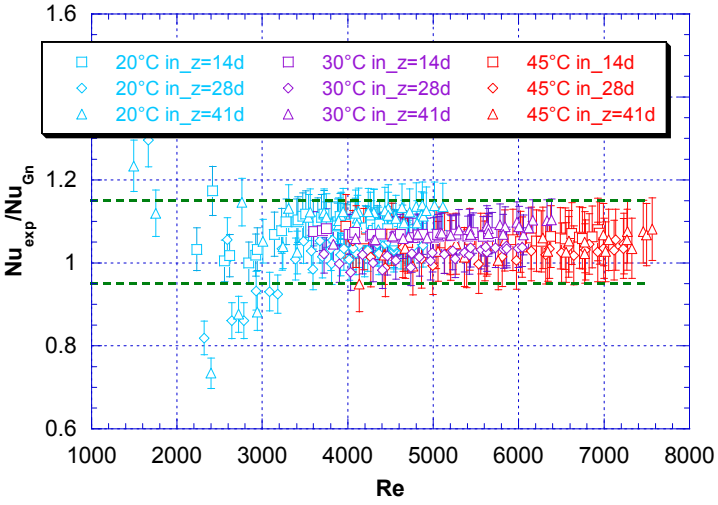

Fig. 5.31. *Stainless steel 1 mm tube – normalized Nusselt (experimental over Gnielinski) vs. Reynolds numbers at 3 axial locations for 3 fluid inlet temperature levels.*
The measured and predicted Nusselt numbers can be seen to fit between -5% and +15% accuracy

Overall, the test rig performs well and replicates the established correlation within acceptability. We shall now observe turbulent heat transfer behaviour in genuine microtubes.

½ mm

The convergence of the experimental Nusselt number to the Nusselt number according to Gnielinski's correlation is plotted in figure 5.32.

It is evident that up to *Re* = 3500 the flow is not yet fully turbulent, so that the Gnielinski approximation is not yet applicable. After a relatively stable profile of turbulence is reached, the experimental values coincide quite well with the correlation's predictions. The heat transfer coefficients in the fully turbulent regime vary from h = 27 190 W/m^{2}K to h = 52 400 W/m^{2}K at the maximum achieved Reynolds number of 5000.

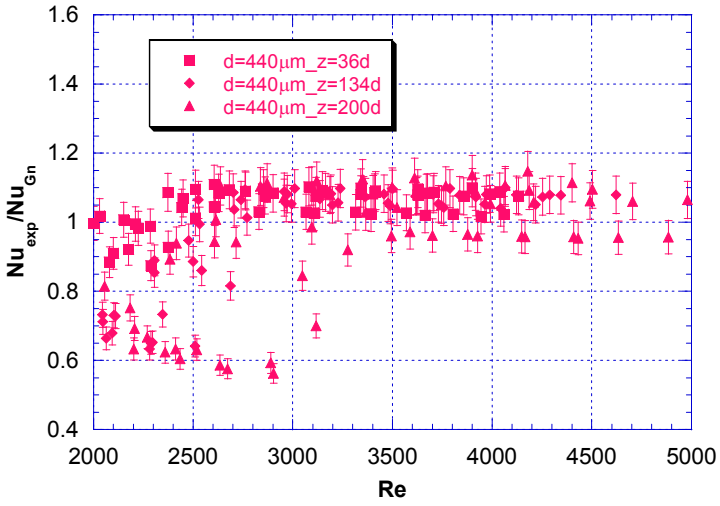

Fig. 5.32: *Stainless steel tube (*d = *440 μm) – normalized Nusselt (experimental over Gnielinski) vs. Reynolds numbers at 3 axial locations*

¼ mm

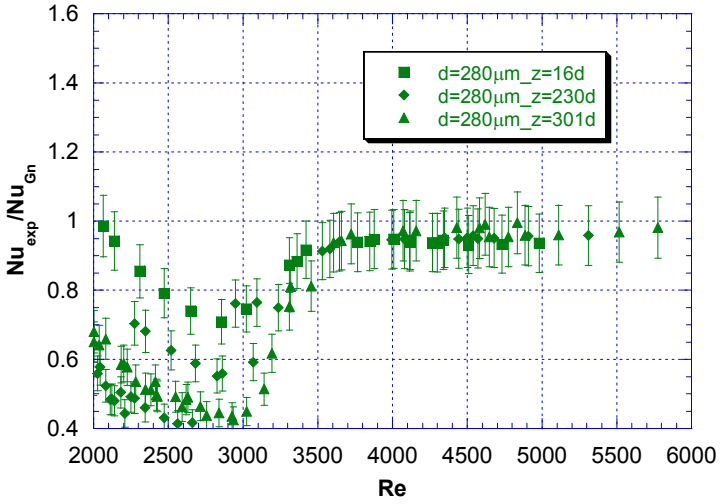

Fig. 5.33: *Stainless steel tube (*d = *280 μm) – normalized Nusselt (experimental over Gnielinski) vs. Reynolds numbers at 3 axial locations*

Reducing the inner diameter to ~ ¼ mm an even flatter curve is obtained around the value of perfect coincidence between the experimental and theoretical heat transfer coefficient. Again, stable turbulent flow is achieved at *Re* = 3500 (h = 51 000 W/m^{2}K), after which the Nusselt values converge, showing no axial variation and in any case respecting the behaviour predicted by the

Gnielinski correlation. A maximum Reynolds number was achieved of 5775, where the heat transfer coefficient amounts to h = 89 755 W/m^{2}K. See figure 5.33 below.

⅛ mm

Finally, the smallest tube can be taken into consideration (d = 146 μm), see figure 5.34. We can see more scatter in the data this time, though the convergence of the experimental and theoretical values takes place slightly earlier, at Re = 3000 (h = 96 840 W/m^{2}K). After Re = 5000 (h = 123 000 W/m^{2}K) there appears to initiate a descent of the ratio, but it should not be assumed that this will proceed at higher Reynolds numbers. A flattening of the trend above the 0.8 value could be just as plausible from the disposition of the data. Also, it should be noted that the data are rather sharply segregated according to their axial location. The points above Re = 6000 all pertain to the thermocouple placed furthest away from the inlet (at Re = 7000, h = 145 000 W/m^{2}K). Likewise, for 5000 < Re < 6000, nearly only measurements of the middle thermocouple are visible. We can notice a stronger axial differentiation therefore, which is explained by the larger intermediate distance between the thermocouples (see Table 5.5), but above all by the large difference in fluid viscosity along the channel, since very high temperature differences were obtained for this channel to keep the absorbed heat as high as possible.

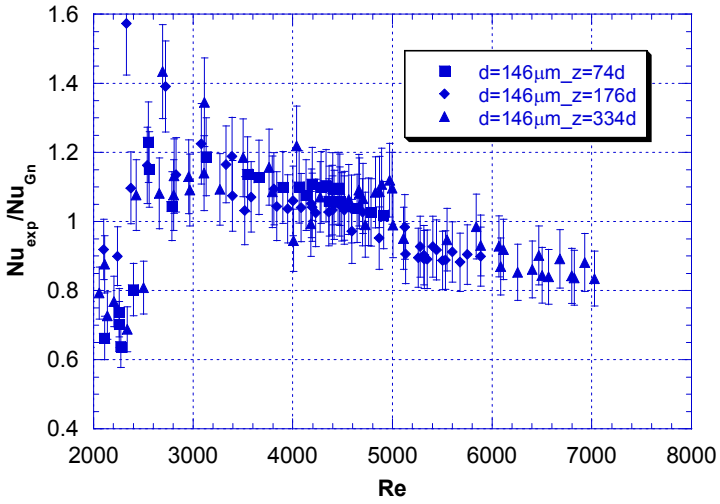

Fig. 5.34: *Stainless steel tube (*d = *146 μm) – normalized Nusselt (experimental over Gnielinski) vs. Reynolds numbers at 3 axial locations*

Due to the exceedingly high pressure drop that is incurred at these flow rates, no higher Reynolds numbers could be investigated. But all in all no evidence has been discovered to refute the validity of the Gnielinski correlation for turbulent flow (3000 < Re < 7000) even at very small diameters, down to d = 146 μm.

This is exemplified once more by combining the findings for the 3 microdiameters studied, as is done in figure 5.35.

Thus, we have discovered that also the *thermal* behaviour of microtubes does not, on the whole, unsheathe improbable new phenomena, but adheres to the classic laws and widely accepted correlations that are valid for conventional size ducts. However, unexpected manifestations may still arise.

Surprises in mechanics are generally due either to an error of method or to numerical mistakes. The latter are of casual nature, however, careful checking of the numbers can reduce the event to a minimum. An example of an error of method was already apparent in the discussion of the

phenomenon of viscous dissipation. This phenomenon is of very marginal influence in conventionally-sized flow equipment, where it can be validly ignored, but its occurrence must not be forgotten about when the applications are downscaled!

The quantities that are of influence on a system are always manifold, whereas its function, its definition, is usually assessed according to a single aspect only. In the case of microtubes, this aspect is considered to be the inner diameter, which is in fact what defines the system as such. The error of method that can be committed is to overlook the other properties of the system that perhaps do not undergo the same amount of downscaling and thereby increase their effect on its behaviour. These properties can be tied to the fluid (so that different influences of a given diameter reduction can be seen according to the type of fluid used) or to the hardware. The experiments that have been carried out on single-phase heat transfer have evidenced how important such a parameter as the *outer* diameter can become. This dimension is not reduced as easily as the inner diameter, because of the necessity of a certain structural solidity (and visibility) of the microfluidic system. Also such auxiliary attachments as feeding wires and temperature and pressure sensors have a limitation on their minimum size for proper functioning. The distorting effect, when aiming to heat a micropipe uniformly, can be considerable, due to the relatively large unwanted heat sinks that have thus been created.

Then again, this effect is also tied to the channel wall *material* and to the *flow rate*, so that only for a certain combination of all these parameters, will the unexpected – though explicable – behaviour come out. Thus, for turbulent flow at the conditions studied, no unusual effects were observed. Also for laminar flow in the thin-walled steel tubes no severe anomalies were encountered. Upon departure from these specific conditions though, the assumptions regarding certain system interactions can become invalid, as was the assumption of a uniform heat input in the case of the small ID glass tubes. This obviously has an effect on the heat transfer coefficient that results, as was seen in the previous sub-section.

So yes, size matters. But so do many other qualities, and reliable performance depends upon mastering the combination of *all* their effects.

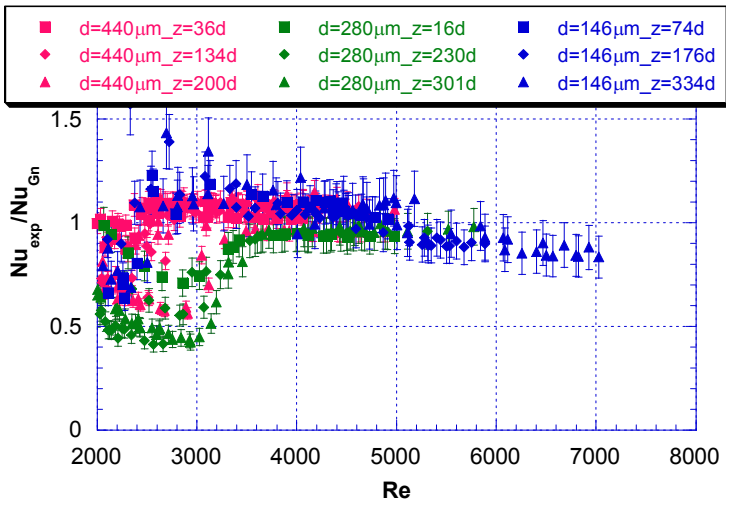

Fig. 5.35: *Normalized Nusselt vs. Reynolds number for 3 different diameters at 3 axial locations*

6

SUMMARY & CONCLUSIONS

Experimental investigation is a diversified process that combines theoretical insight in the subject of research with very menial skills to extract the physical evidence supporting or refuting a preset hypothesis. In the previous chapters these aspects have all been discussed: a sound base of theory was put up, from which a survey was made of the current degree of scientific refinement and practical application of the specialized topic; the assembly was illustrated of an as reliable as possible test rig and finally the retrieved data were validated against previously established criteria. It is now time to condense the observations that were made and interpret the results to formulate our new hypotheses.

The behaviour of fluid flow and heat transfer in microtubes – without considering phase-changing phenomena – was studied through measurement of the friction factor and the heat transfer coefficient, respectively. In the liquid flow and gas flow campaigns, summarized in section 6.1, pressure measurements were used to obtain the frictional resistance in microtubes down to 30 μm inner diameter, considering in the former case also the effect of different surface conditions (smooth, rough or hydrophobic). No significant deviation from classical theory was found.

The high frictional loss in microscopic ducts leads to a non-negligible heating of the fluid: this phenomenon – known as viscous dissipation – can be used to deduce the friction factor by alternative means than pressure measurements, as is reiterated in section 6.2.

The positive effect of the thermal entrance length and the complications in correct interpretation of diabatic data due to non-uniform downscaling of the test section are explained in section 6.3, as a result of the heat transfer coefficient measurements done on stainless steel and glass microtubes in both laminar and turbulent flow.

6.1 Findings regarding the friction factor in microtubes

6.1.1 Incompressible flow

Smooth tubes

Using the "tube-cutting" method – where the net frictional pressure drop in a tube is determined by subtracting the total pressure drop measured in a shorter tube from that of a longer one – a fairly precise evaluation was effectuated of the friction factor in microtubes down to 30 μm inner diameter. The base case of an incompressible fluid (distilled, degassed water) flowing in a smooth capillary pipe yielded no evident deviations from theory regarding conventionally-sized tubes in this respect: the Darcy friction factor is correlated to the Reynolds number only, with Poiseuille constant equal to 64 ($f = 64/Re$), see figure 6.1.

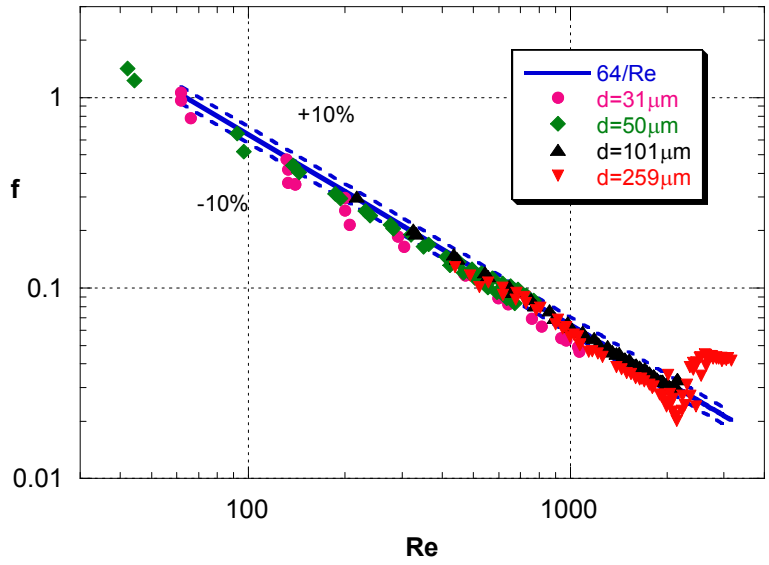

Fig. 6.1: *Friction factor vs. Reynolds number for water flow in smooth, untreated vitreous tubes*

It is evident that down to 50 μm inner diameter the reference line that expresses the law of Hagen-Poiseuille for laminar flow correlates the data points very well, within a ±10% error margin. The data for the smallest tube drop below this line; however, it must be stated that the calculated experimental uncertainty at this diameter is larger (±19%) before attempting to clarify this slight deviation. An explanation can be put forward though: assuming the fluid has zero velocity at the channel wall (no-slip boundary condition) means that the velocity *gradient* there is extremely high, because the flow has to be squeezed through an extremely narrow passageway. At a certain point, it can well be imagined, the shear rate on the fluid molecules attached to the wall can become so strong as to conquer the adhering force of the molecules of the solid surface, inducing slip flow. This will cause a reduction in the friction factor, and might be what is observed in the disposition of the data-points of the 30 μm microtube. The margin of error however, caused by the weight of uncertainties particularly on the values of the tube diameter and the fluid mass flow, prohibit a confident statement as to the occurrence or no of this effect here.

Rough tubes

No influence of wall roughness is predicted by classical theory on the friction factor in laminar flow. There are studies of the 20th century that specify an effect on the *point* where transition to turbulent flow takes place, however. To verify the extent to which these statements are true for microchannels, a couple of smooth glass tubes were roughened on the inside and tests were run similar to those for the smooth, untreated tubes to determine the behaviour of the laminar friction factor and point of transition. The results are synthesized in figure 6.2.

First of all, behaviour in the laminar regime can be seen to be closely adherent to the unmodified relation for the friction factor in smooth tubes. So it is “business as usual” in that respect. The strange collapse in friction factor values of the 126 μm tube around transition to turbulence is actually a confirmation of the stochastic nature of the point of incipience of turbulent flow. The explanation of this phenomenon is set out in sub-section 5.1.2, with the aid of figure 5.8.

The points of transition of both the long and the short tube fall within the range suggested by Preger and Samoilenko (as reported by Idelchik [14]), so that the conclusion to be drawn is that there is a fundamental indeterminacy about the precise moment of turbulence initiation within this range. (It should be noted that the respective lengths of the investigated tubes were always long enough to be able to assume fully developed flow without protracted inlet effects.)

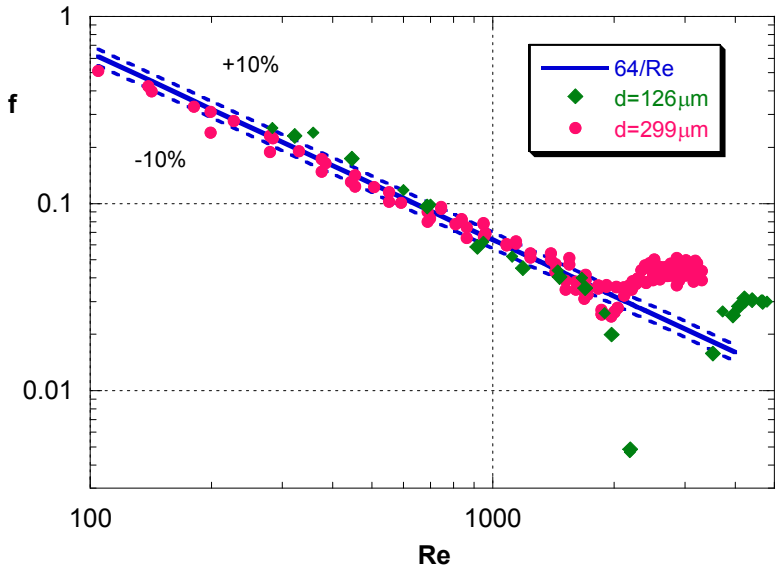

Fig. 6.2: *Friction factor vs. Reynolds number for water flow in roughened glass tubes*

Hydrophobic tubes

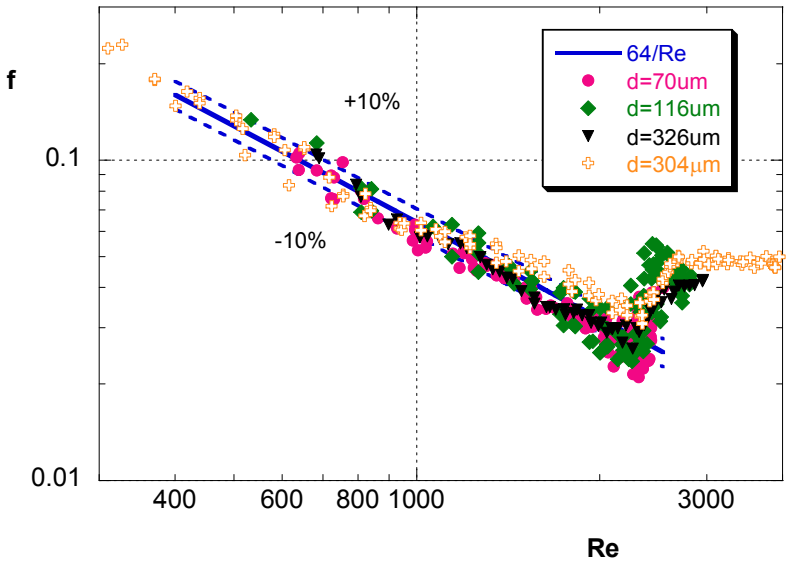

Fig. 6.3: *Friction factor vs. Reynolds number for water flow in hydrophobic tubes*

Since a non-wetting or hydrophobic wall has a stronger propensity to liquid repulsion, slip flow might be anticipated in microtubes where there is also a strong shear rate. This was investigated by coating 3 diameters of smooth glass tubes on the inside with a silicon-based layer. Also a PTFE pipe was tested, even though its cross-section was observed to be variable in shape and size.

The results on the elaborated friction factor behaviour are presented in the figure 6.3 above. Here, all diameters studied show a perfectly regular correlation between friction factor and Reynolds number, as though the walls were simply smooth and untreated. Even at 70 µm no indication of reduced friction due to slip flow is present. Though it is not a widely studied effect, in the literature its occurrence has been demonstrated however, and the utilisation of a non-zero slip velocity boundary condition in the defining equations proves to describe the measured behaviour

quite well generally. There is disagreement on the exact entity of this velocity though. In a study by Tyrrell and Attard [18] the mechanism of slip is shown to be tied to the presence of nanobubbles on the hydrophobic surface, over which the liquid may flow as in a two-phase system (validated by Trethaway *et al*. [19]). The nanobubbles are created by desorption of dissolved gases in the liquid, and this is probably the reason why no effect was observed in the experiments presented here: the working fluid is *degassed* before entering the test loop. The hypothesis put forward by Tyrrell and Attard can therefore be said to have been supported with these experiments, but for confirmation hereof an identical campaign would be required using regular, gas-containing demineralized water.

6.1.2 Compressible flow

If the working fluid is compressible, the considerable frictional pressure loss in microchannels will have an effect on the dynamics of flow, even at low speeds ($Ma < 0.3$). Since the density of a gas is dependent on the static pressure, to maintain conservation of mass the flow will accelerate as it loses pressure due to friction in the narrow duct. The objective of the campaign on gas flow was to verify whether any effects of these altering dynamics could be discerned in the friction factor.

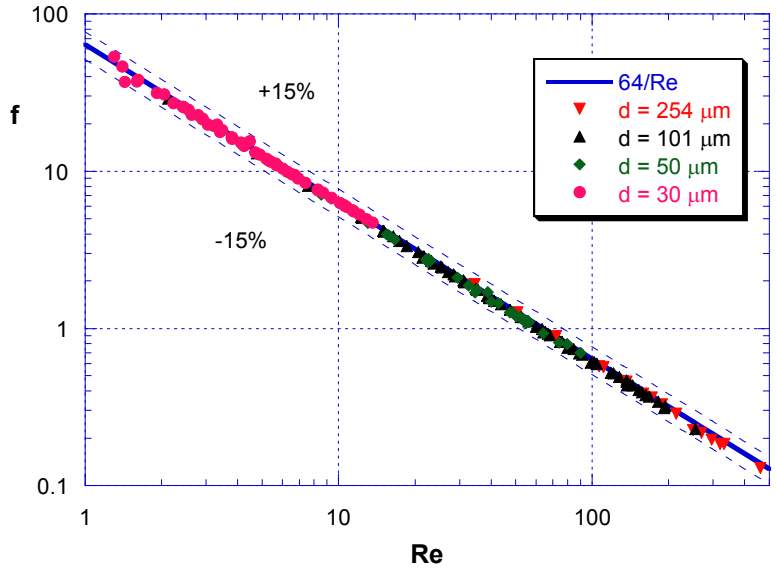

Fig. 6.4: *Friction factor vs. Reynolds number for Helium flow in smooth vitreous tubes*

The experimental results of the measurement of the overall friction factor in 4 differently sized tubes are shown in figure 6.4. The data plotted in the figure were obtained by considering the pressure drop over an entire length of tube, without considering concentrated losses inside the test section fittings. The tube-cutting method was applied as well, to attempt to eliminate inlet and outlet effects, as well as to evaluate the friction factor in a *localized* section of tube compared to the *global* approximation, but the results were not significantly different (apart from an increased random error due to the superposition of two measurements for each data-point). This indicates that the pressure profile along the axis of the channel is practically linear, especially towards the inlet of the channel, which was the section that was analysed locally.

As can be seen from figure 6.4, the disposition of the friction factor values converges closely around the relation valid for *incompressible* flow in smooth tubes ($f = 64/Re$), as if the density-change-induced acceleration were a reversible process (this means no irreversible entropy is produced in the process of expansion). The head loss already due to *friction* at the walls, therefore,

does not increase further. This is at least remarkable, since pressure ratios were obtained between inlet and outlet of up to 10, in the case of the smallest tube, signifying a ten-fold increase in velocity along the tested channel.

Comparing the incompressible approximations of the friction factor with quasi-compressible correlations for the friction factor equally did not show significant differences, so that a criterion can be established for the pressure ratio, below which the flow can be considered acceptably to behave as *incompressible*:

$$R_P \leq 1 + \frac{128\left(1 + \frac{e_f}{f}\right)\mu L \Gamma}{\pi d^4 \rho P_{out}}$$

In very small flow passages, where the characteristic dimension is of the same order of magnitude of the free molecular path of the gas, rarefaction effects may occur. In the experimental conditions of this study however, the degree of rarefaction was too low to detect any modifications in flow behaviour – lower pressure or smaller ducts would be required to put these into evidence.

6.2 Findings regarding viscous dissipation in microtubes

Another effect of the unusually small flow area that characterizes microchannels, is the rising to significance of viscous dissipation. This is the conversion to heat of the strong viscous deformation of the fluid in the conduit, caused by the high shear rate. This heating of the fluid can be traced back to friction at the walls and provides therefore an alternative means to determining the friction factor. The possibility of establishing this value through temperature rise rather than pressure drop measurement is promising since the former can be effected with considerably less disturbing intrusion to the flow. Through careful analysis of the conservation equations and the adoption of conventional assumptions regarding the dynamics of flow (no slip, fully developed incompressible laminar flow and no heat source terms), the temperature rise per unit length due to viscous dissipation can be deduced (work first done by Morini [24]):

$$\frac{\partial T_b}{\partial z} = \left(\frac{Ec}{Re} [f\ Re] \right) \frac{\Delta T_{ref}}{d}$$

An experimental validation of this equation was carried out, thereby also making a comparison with the correlation proposed by Xu and coworkers [88]. The result is shown in figure 6.5.

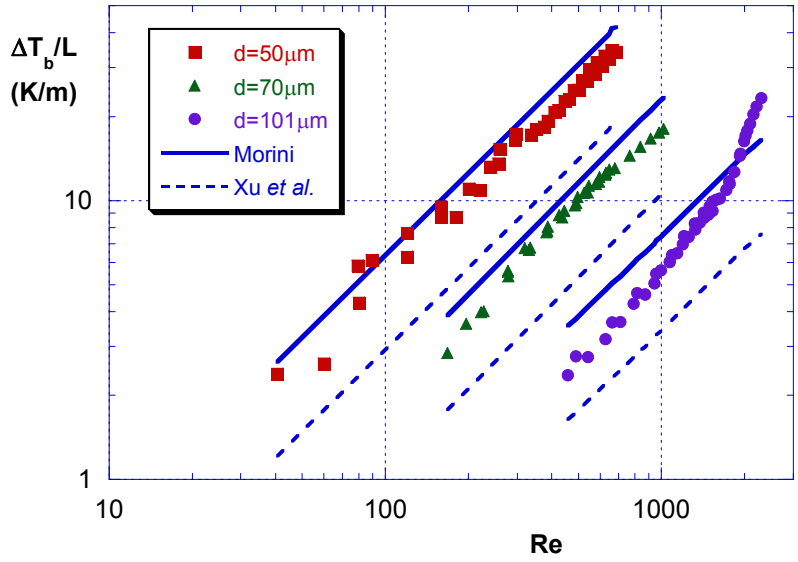

Fig. 6.5: *Viscous heating vs. Reynolds number for 3 different diameters, validated against predictions by Morini* [24] *and Xu* et al. [88] – *fluid: water*

The closer adherence of the data-points to the model of Morini as the tube diameter is decreased, is evidence of viscous heating being a typical *scaling effect*. Here, it means that for a given mass flow, the bulk temperature rise over a given length is more marked – and therefore more precisely measurable – the smaller the channel diameter. Indeed, for the 70 and 50 μm micropipes the prediction is excellent, with a slight overestimation due to unavoidable minimal heat losses from the test section during experiments. At 101 μm the disposition of the points is approximated well enough, and transition to turbulence can be clearly identified where the sharp increase in fluid heating takes place due to the incipience of eddies and vortices in the flow.

As can be seen from the equation reported above, the friction factor is explicitly defined for a given experimental condition (T_{ref} is a reference temperature rise for which the fluid viscosity

decreases by, say, 2-3%; this is 1 K in the case of water). Elaborated in terms of measurable quantities it is expressed as:

$$f = \frac{\Delta T_b}{\Delta T_{ref}} \left[\frac{d}{Ec \cdot L} \right]$$

The confrontation of this definition of the friction factor with the conventional pressure drop approximation yields a good agreement – again, especially at the smaller diameters. Figure 6.6 groups the data according to the two methods, within the experimental error margins of the former.

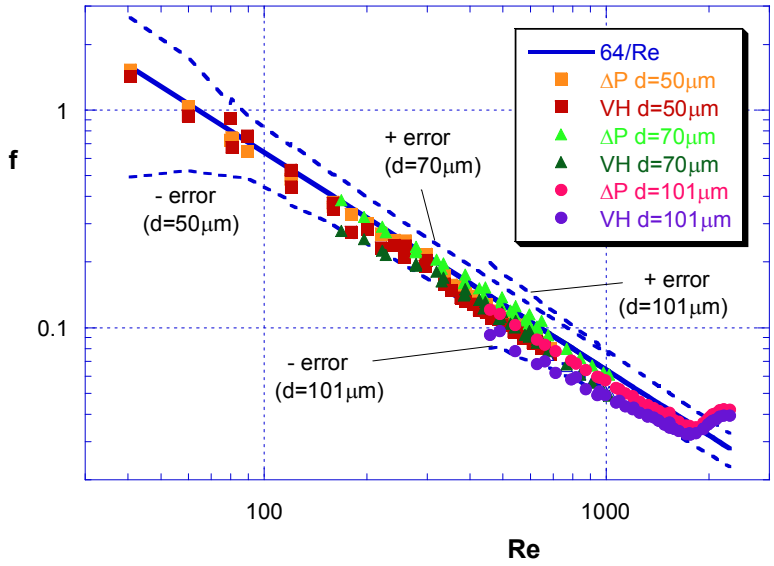

Fig. 6.6: *Friction factor vs. Reynolds number for 3 diameters; pressure drop (ΔP) and viscous heating (VH) analyses*

6.3 Findings regarding heat transfer in microtubes

An experimental mapping of the local inside wall heat transfer coefficient was attempted for three classes of diameter and two types of tube material with different surface conditions. Looking at 3 axial locations, through measurement of the outside wall temperature and the overall heat absorption by the working fluid (water), an evaluation was made of the efficiency of heat transfer in laminar and turbulent flow, comparing the results with predictions from conventional (empiric) theory.

The experimental conditions that were envisioned were of uniform heat input along a section of capillary where the flow would be hydrodynamically fully developed. The test section was placed in a vacuum environment to be able to disregard heat loss through natural convection; the radiative losses were calculated to be marginal. Thus, it was assumed that all the heat put in would be absorbed by the fluid inside the microtube under consideration.

In the following figure 6.7a,b, the local Nusselt versus Reynolds numbers are compared of two diameter classes of smooth glass tubes and rough stainless steel tubes (~½ mm and ~⅛ mm ID). A reference line is plotted which is the analytical, constant value of the Nusselt number for single-phase heat transfer in tubes with uniform heat input ($Nu = 4.36$).

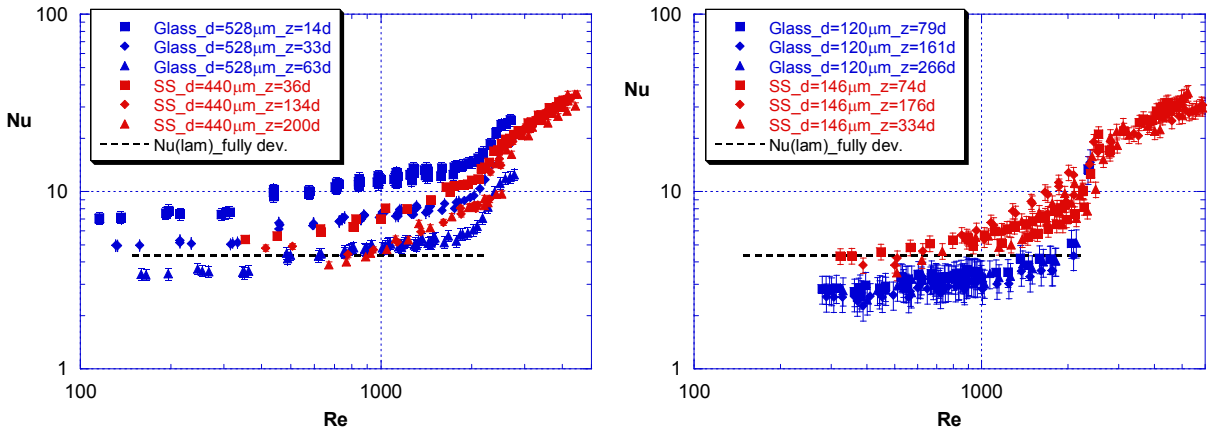

Fig. 6.7a,b: *Single-phase laminar heat transfer in glass vs. stainless steel tubes – Local Nusselt vs. Reynolds numbers at 3 axial locations; ~½ mm ID (a) and ~⅛ mm ID (b)*

Focusing on the laminar flow regime, the graph on the left (~½ mm ID) shows clear indications of incremental heat transfer due to thermal development of the flow. The heated length being relatively short in relation to the inner diameter means that the flow does not obtain a steady-state thermal profile. The drive for heat transfer in this region is therefore greater, as equilibrium is sought. This is evidenced by the higher Nusselt numbers for the axial locations (indicated by the z variable) closer to the inlet. This effect is in keeping with conventional theory for thermally developing flow, and provides a strong recommendation for the use of short microtubes in (single-phase) cooling applications, as this combines *increased heat transfer* with *reduced pressure drop* – a crucial benefit at this scale.

If we take a look at the graph for the smaller class of tubes (~⅛ mm ID), we notice that the relatively longer flow path attenuates the thermal entrance effects: there is no axial segregation of the Nusselt numbers, which tend towards the uniform value for fully developed laminar flow – *in the case of the steel tube*. What sticks out above all though, is that the glass microtube shows a distinctly poor performance. This was shown to be due to the excessive thermal resistance of the tube wall for this material: a larger wall thickness combined with much lower conductivity compared to the stainless steel microtube of comparable inner dimensions. Also, the method of heat input relied on the electric warming of a thin metal film deposited on the outside wall rather than

direct heating of the entire tube as was the case with the stainless steel pipes. Firstly, this meant that the maximum allowable wall temperature (<100°C) was reached for low heat inputs, creating large relative errors on the temperature rise of the fluid, which remains low, especially at high flow rates. Secondly, this excessive thermal resistance of the glass microtubes inhibits the radial flow of heat to the fluid-wall interface. Thus, preferential paths are selected, like the peripheral attachments to the test section, and in particular the feeding wires made of copper. These heat losses are not easily quantifiable, but prove to be of considerable influence, so that the assumed hypothesis of zero heat loss to the surroundings and uniform heat absorption by the fluid cannot be considered valid in the case of these glass microtubes. Thus, also the error on the inner wall temperature estimation is increased.

The individuation of this problem does not mean however, that it can be solved. The outside diameter of the glass microtubes needs to be of a minimum size to maintain strength and manageability of the capillary, especially in view of the instrumentation that has to be applied to it for measurement. Unfortunately, glass is also the only material that can guarantee a smooth and precise inner geometry of the capillary. This highlights the fundamental importance – easily overlooked – of proper scaling, and of distinguishing *all* the variables that have an effect on the property that is studied with a correct estimation of their importance. For what can be neglected in one case, is not necessarily unimportant in another, apparently similar case. Before this operation is successfully fulfilled, no bold premises should be advocated from premature data, and no over-hasty simplifications should be applied *a priori*.

From the disposition of the Nusselt values for the steel microtubes, finally, no influence can be determined of the increased roughness in laminar heat transfer.

The experiments on turbulent flow were performed on the stainless steel tubes only. Since no notable deviations were observed of the Nusselt number behaviour with respect to the behaviour predicted by the Gnielinski correlation (coined originally for macro-tubes, and widely accepted as being the most reliable and precise), further testing of smooth glass tubes was omitted, especially in view of the difficulties mentioned earlier. The graph that collects the experimental data of the three diameters studied – normalized with the corresponding value predicted by Gnielinski – is shown again in figure 6.8.

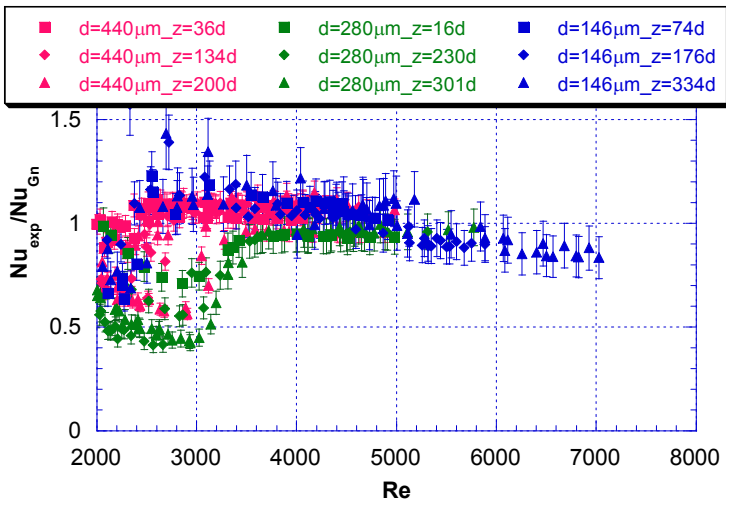

Fig. 6.8: *Single-phase turbulent heat transfer in stainless steel tubes – Normalized Nusselt vs. Reynolds number for 3 different diameters at 3 axial locations*

Regarding the recommendation of careful analysis of all the variables that may have an effect on experimental conditions, it must be added that even if such an estimation could be exhaustive and precise, not always can all variables be adapted subsequently to conform to ideal conditions.

This is the case with the degree of roughness inside the channels, for example. The relative roughness of the two larger stainless steel micropipes (see Table 5.4) is technically considered as "smooth" ($e/d < 5\%$) , even though their asperities are considerably coarser than the surface of the glass tubes. There is no feasible way of creating a given degree of roughness inside a steel microtube – for the glass microtubes also an attempt was made but proved of limited effect, see sub-section 5.1.2. One is left with limited means and has to make up for it with scientific acumen, making the best of hypothesis, inference and deduction to mould a presentable investigation that can carry the responsibility of its name, and offers the best possible foundations for further research.

6.4 Recommendations for future work

Research always raises new questions. This is why the activity of the researcher will always be of relevance, yet can never call itself completed or fulfilled. In bringing to conclusion this study, many queries were left untreated and many uncertainties remain. Can liquid slip at the walls occur at a certain shear rate? does the dissolution of gases in water promote the formation of a slipping layer on a hydrophobic surface? are compressibility effects really only related to Mach number regardless of the pressure drop? can a closed energy balance be obtained for the characterization of uniformly heated smooth glass microtubes? what is the exact degree of roughness at which altered behaviour in heat transfer and pressure drop will manifest itself, and will this degree still warrant the assumption of a circular geometry (in the case of microtubes)?

These are the main questions that spring to mind after studying carefully the results that are reported in this Thesis. Suggestions for the tackling of these problems left open – though the term for putting them into practice, as regards this present particular context, has expired – can be offered:

- A balance of forces set up for a liquid molecule attached to a channel wall should provide insight into the order of magnitude at which imposed shear will overpower attractive forces of the wall;
- Tests done with gasified water in hydrophobic microtubes should emphasize a possible effect of nano-bubble desorption;
- If a method can be found to render a surface uniformly rough by increasing degrees inside a microtube, a threshold of the effect of roughness can be investigated;
- In compressible flow, applying the differential analysis to the latter section of the long tube, *i.e.* maintaining the inlet pressure constant for the long and the short tube while varying the outlet pressure, will roughly characterize the pressure drop profile in the part of the tube where most acceleration takes place (towards the outlet); also, increasing further the length of the test sections until very high pressure ratios are obtained should trigger a more noticeable compressibility effect;
- If it were possible to coat glass microtubes on the *inside* with a thin metal film for heating, efficient heat transfer to the fluid would be ensured; also the outside wall temperature would be less high, and therefore less subject to losses; however, there would remain the problem of attaching the feeding wires;
- Studies of single-phase heat transfer with gaseous fluids or considering slip flow are still very scarce.

As regards possible application of the knowledge acquired to a cooling device, the recommendation is to design a heat exchanger with short, parallel channels, in order to stimulate heat detraction and reduce head loss (and viscous dissipation), and that utilizes thin, highly conductive walls with a high heat capacity fluid to reduce temperature rise.

APPENDIX I

Conduction equations in a cylindrical wall

Consider the following cylindrical wall that exchanges heat only across the inner surface (figure A.1).

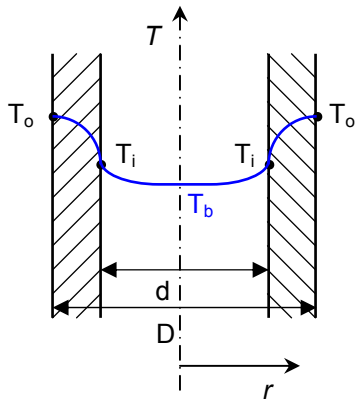

Fig. A.1: *Heat transfer across a uniform cylindrical wall*

In order to establish the inner heat transfer coefficient, first of all we need to determine the inner wall temperature T_i. Since the measured temperature is the outer wall temperature T_o, the temperature profile in the wall will have to be known to obtain the former quantity.

The energy equation for the tube wall with external heat input at the outer surface is given by equation (2.51). The solution to this differential equation is postulated as:

$$T(r) = A \ln r + B \tag{A.1}$$

which gives, with the boundary conditions given in figure A.1, at the two wall surfaces:

$$\begin{cases} T_i = A \ln r_i + B \\ T_o = A \ln r_o + B \end{cases} \tag{A.2}$$

where r_i and r_o are the values of the inner and outer radii respectively. Subtracting the two equations and solving for A:

$$T_o - T_i = A \ln\left(\frac{r_o}{r_i}\right) \qquad \Rightarrow \qquad A = \frac{(T_o - T_i)}{\ln\left(\frac{r_o}{r_i}\right)} \tag{A.3}$$

Re-inserting this value in one of the equations (A.2), gives B:

$$B = T_o - \frac{(T_o - T_i)}{ln\left(\frac{r_o}{r_i}\right)} ln\, r_o \tag{A.4}$$

so that the solution to the temperature profile becomes:

$$T(r) = \frac{(T_o - T_i)}{ln\left(\frac{r_o}{r_i}\right)} ln\left(\frac{r}{r_o}\right) + T_o \tag{A.5}$$

From Fourier's law of conduction (see footnote 2 in Chapter 2) and differentiation of the above temperature profile, the heat flux can be calculated:

$$q = -k_w \frac{dT}{dr} A_{ht} = k_w \cdot 2\pi r \cdot L_{ht} \frac{(T_o - T_i)}{r\, ln\left(\frac{r_o}{r_i}\right)} \tag{A.6}$$

where the direction of the heat flux is chosen in the direction of decreasing temperature, so against the direction of the radius variable. This heat flux is assumed to be exchanged totally at the fluid-wall interface, where Newton's law of cooling states (see equation (2.43)):

$$q = h \cdot 2\pi r_i \cdot L_{ht} (T_i - T_b) \tag{A.7}$$

Evaluating the equality of these equations at the inner surface, rearranging and using diameter rather than radius values, we obtain:

$$\begin{cases} T_o - T_i = \dfrac{q\, ln\left(\frac{D}{d}\right)}{k_w \cdot 2\pi \cdot L_{ht}} \\ T_i - T_b = \dfrac{q}{h \cdot \pi d \cdot L_{ht}} \end{cases} \quad \Rightarrow \quad T_o - T_b = \frac{q}{\pi L_{ht}} \left(\frac{ln\left(\frac{D}{d}\right)}{2k_w} + \frac{1}{h \cdot d} \right) \tag{A.8}$$

In the experiments, the heat flow q is calculated by measuring the enthalpic temperature rise of the fluid, as given by equation (2.49). Thus, we can describe the heat transfer coefficient at the inner wall h, for *heat put in externally at the outer tube surface*, in terms of measurable quantities only:

$$h = \left\{ \frac{\pi d L_{ht} (T_o - T_b)}{\dot{m} c_p \Delta T_b} - \frac{d}{2k_w} \ln\left(\frac{D}{d}\right) \right\}^{-1} \tag{2.56}$$

In the case of *heat generated inside the tube wall*, the solution is a little more complex. The boundary conditions are as follows:

at $r = r_i$, $\quad \left(\frac{dT}{dr}\right)_{r=r_i} = \frac{q_i''}{k_w} = \frac{h(T_i - T_b)}{k_w}$

at $r = r_o$, $\quad \left(\frac{dT}{dr}\right)_{r=r_o} = 0$

The energy equation describing this situation, equation (2.53), substituting θ for $\frac{dT}{dr}$, can be expressed as follows:

$$rd\theta + \theta dr + \frac{q'''}{k_w} rdr = 0 \tag{A.9}$$

where q''' is the applied heat flux distributed over the volume of the heated length of tube, $\frac{4q}{\pi\left(D^2 - d^2\right)L_{ht}}$. Integrated, with subsequent re-insertion of the original variable, equation (A.9) becomes:

$$\theta + \frac{q'''r}{2k_w} = \frac{C_1}{r} = \frac{dT}{dr} + \frac{q'''r}{2k_w} \tag{A.10}$$

Using the second boundary condition, C_1 can be deduced:

$$C_1 = \frac{q'''{r_o}^2}{2k_w} \tag{A.11}$$

Integrating equation (A.10) a second time, the temperature profile is described:

$$T(r) = \frac{q'''{r_o}^2}{2k_w}\ln r - \frac{q'''r^2}{4k_w} + C_2 \tag{A.12}$$

where we need to find C_2. Taking into account the first boundary condition, the inner wall temperature can be written as:

$$T_i = \frac{k_w}{h}\left(\frac{dT}{dr}\right)_{r=r_i} + T_b = \frac{k_w}{h}\left(\frac{q'''{r_o}^2}{2k_w r_i} - \frac{q'''r_i}{2k_w}\right) + T_b \tag{A.13}$$

Equating this expression with (A.12) evaluated at the inner wall yields the value of the constant:

$$C_2 = \frac{k_w}{h}\left(\frac{q'''{r_o}^2}{2k_w r_i} - \frac{q'''r_i}{2k_w}\right) + T_b + \frac{q'''{r_i}^2}{4k_w} - \frac{q'''{r_o}^2}{2k_w}\ln r_i = T_b + \frac{q'''r_i}{2h}\left[\left(\frac{r_o}{r_i}\right)^2 - 1\right] + \frac{q'''{r_o}^2}{4k_w}\left[\left(\frac{r_i}{r_o}\right)^2 - 2\ln r_i\right] \tag{A.14}$$

so that the temperature profile is given by:

$$T(r) = T_b + \frac{q'''r_i}{2h}\left[\left(\frac{r_o}{r_i}\right)^2 - 1\right] + \frac{q'''{r_o}^2}{4k_w}\left[2ln\left(\frac{r}{r_i}\right) + \left(\frac{r_i}{r_o}\right)^2 - \left(\frac{r}{r_o}\right)^2\right] \tag{A.15}$$

Evaluating the temperature at the inner and outer surfaces and subtracting the one from the other, yields equation (2.54):

$$T_o - T_i = \frac{q'''{r_o}^2}{4k_w}\left[2ln\left(\frac{r_o}{r_i}\right) + \left(\frac{r_i}{r_o}\right)^2 - \left(\frac{r_o}{r_o}\right)^2\right] = \frac{q'''D^2}{16k_w}\left[2ln\left(\frac{D}{d}\right) + \left(\frac{d}{D}\right)^2 - 1\right] \tag{2..54}$$

Using this expression for the first equation in set (A.8), and describing the heat flux in terms of the enthalpic temperature rise of the fluid, ultimately resolves to the heat transfer coefficient as given by equation (2.55).

APPENDIX II

The uncertainty on the heat transfer coefficient

The description of the internal heat transfer coefficient in terms of measurable quantities only, is given by equation (2.56):

$$h = \left\{ \frac{\pi d L_{ht} \left(T_o - T_b\right)}{\Gamma c_p \Delta T_b} - \frac{d}{2k_w} \ln\left(\frac{D}{d}\right) \right\}^{-1} \tag{2.56}$$

According to the definition of the error on this variable, equation (4.6), the predicted experimental error will be:

$$\begin{aligned} e_h{}^2 = &\left(\frac{\partial h}{\partial d} e_d\right)^2 + \left(\frac{\partial h}{\partial L_{ht}} e_{L_{ht}}\right)^2 + \left(\frac{\partial h}{\partial T_o} e_{T_o}\right)^2 + \left(\frac{\partial h}{\partial T_b} e_{T_b}\right)^2 + \left(\frac{\partial h}{\partial \Gamma} e_\Gamma\right)^2 + \\ &+ \left(\frac{\partial h}{\partial c_p} e_{c_p}\right)^2 + \left(\frac{\partial h}{\partial \Delta T_b} e_{\Delta T_b}\right)^2 + \left(\frac{\partial h}{\partial k_w} e_{k_w}\right)^2 + \left(\frac{\partial h}{\partial D} e_D\right)^2 \end{aligned} \tag{A.16}$$

Thus, one has to proceed to determine each of the above partial derivatives. They are given by:

$$\frac{\partial h}{\partial d} = \frac{J - 1/(2k_w) - A/d}{(J \cdot d - A)^2} \quad \text{with } A = \frac{d \ln\left(\frac{D}{d}\right)}{2k_w} \text{ and } J = \frac{\pi L_{ht}\left(T_o - T_b\right)}{\Gamma c_p \Delta T_b}$$

$$\frac{\partial h}{\partial L_{ht}} = \frac{-B}{(B \cdot d - A)^2} \quad \text{with } B = \frac{\pi d\left(T_o - T_b\right)}{\Gamma c_p \Delta T_b}$$

$$\frac{\partial h}{\partial T_o} = \frac{-C}{\left(C\left(T_o - T_b\right) \cdot d - A\right)^2} \quad \text{with } C = \frac{\pi d L_{ht}}{\Gamma c_p \Delta T_b}$$

$$\frac{\partial h}{\partial T_b} = \frac{C}{\left(C\left(T_o - T_b\right) \cdot d - A\right)^2}$$

$$\frac{\partial h}{\partial \Gamma} = \frac{K/\Gamma^2}{\left(K/\Gamma - A\right)^2} \quad \text{with } K = \frac{\pi d L_{ht}\left(T_o - T_b\right)}{c_p \Delta T_b}$$

$$\frac{\partial h}{\partial c_p} = \frac{E/c_p{}^2}{\left(E/c_p - A\right)^2} \quad \text{with } E = \frac{\pi d L_{ht}\left(T_o - T_b\right)}{\Gamma \Delta T_b}$$

$$\frac{\partial h}{\partial \Delta T_b} = \frac{F/\Delta T_b{}^2}{\left(F/\Delta T_b - A\right)^2} \quad \text{with } F = \frac{\pi d L_{ht}\left(T_o - T_b\right)}{\Gamma c_p}$$

$$\frac{\partial h}{\partial k_w} = \frac{A/k_w}{(B \cdot L_{ht} - A)^2}$$

$$\frac{\partial h}{\partial D} = \frac{d/(2k_w D)}{(B \cdot L_{ht} - A)^2}$$

Summing these terms and dividing by the original function (2.55) squared, gives us the squared relative error on the quantity under investigation. Assembling, simplifying and taking the square root results in the following expression for the relative uncertainty on the inner heat transfer coefficient in the case of heat put in externally at the outer surface of the tube:

$$\frac{e_h}{h} = \sqrt{\left(\frac{A/d - J - 1/(2k_w)}{J \cdot d - A} e_d\right)^2 + \left(\frac{B}{B \cdot L_{ht} - A} e_{L_{ht}}\right)^2 + \left(\frac{C}{C(T_o - T_b) - A}\right)^2 \left(e_{T_o}{}^2 + e_{T_b}{}^2\right) + \left(\frac{K/\Gamma^2}{K/\Gamma - A} e_\Gamma\right)^2 + \left(\frac{E/c_p{}^2}{E/c_p - A} e_{c_p}\right)^2 + \left(\frac{F/\Delta T_b{}^2}{F/\Delta T_b} e_{\Delta T_b}\right)^2 + \left(\frac{A/k_w}{B \cdot L_{ht} - A} e_{k_w}\right)^2 + \left(\frac{d/(2k_w D)}{B \cdot L_{ht} - A} e_D\right)^2} \tag{A.17}$$

For the steel tube with inner heat generation, the expression for the heat transfer coefficient to undergo the above operation is equation (2.55):

$$h = \left\{ \frac{\pi d L_{ht}(T_o - T_b)}{\Gamma c_p \Delta T_b} - \frac{D^2 d}{16(D^2 - d^2)k_w}\left[2\ln\left(\frac{D}{d}\right) + \left(\frac{d}{D}\right)^2 - 1\right]\right\}^{-1} \tag{2.55}$$

The significant variables are the same as for the glass tube, so that the definition of the experimental error is identical to equation (A.16), but the differentiation of the above expression is slightly more involved, though structurally equivalent. Only the partial derivatives to *d* and *D* change; the result of the operation is:

$$\frac{e_h}{h} = \sqrt{\left(\frac{A/d - J - d^2/(2k_w D)}{J \cdot d - A} e_d\right)^2 + \left(\frac{B}{B \cdot L_{ht} - A} e_{L_{ht}}\right)^2 + \left(\frac{C}{C(T_o - T_b) - A}\right)^2 \left(e_{T_o}{}^2 + e_{T_b}{}^2\right) + \left(\frac{K/\Gamma^2}{K/\Gamma - A} e_\Gamma\right)^2 + \left(\frac{E/c_p{}^2}{E/c_p - A} e_{c_p}\right)^2 + \left(\frac{F/\Delta T_b{}^2}{F/\Delta T_b} e_{\Delta T_b}\right)^2 + \left(\frac{A/k_w}{B \cdot L_{ht} - A} e_{k_w}\right)^2 + \left(\frac{d^2/(2k_w D)}{B \cdot L_{ht} - A} e_D\right)^2} \tag{A.18}$$

where the definitions of *A, J, B, C, K, E* and *F* are equal to those given above.

APPENDIX III

Error analysis of a diabatic experiment on a 50 µm tube

It is interesting to show the experimental manifestation of the singularity that can arise from equation (4.16). The smallest capillary tested was a fused silica tube of 50 µm inner diameter and an outer diameter of around 363 µm. The results of the single-phase heat transfer experiments are shown in figure A.2. For this tube, it was possible to study only two axial locations, but a third range of heat input was applied.

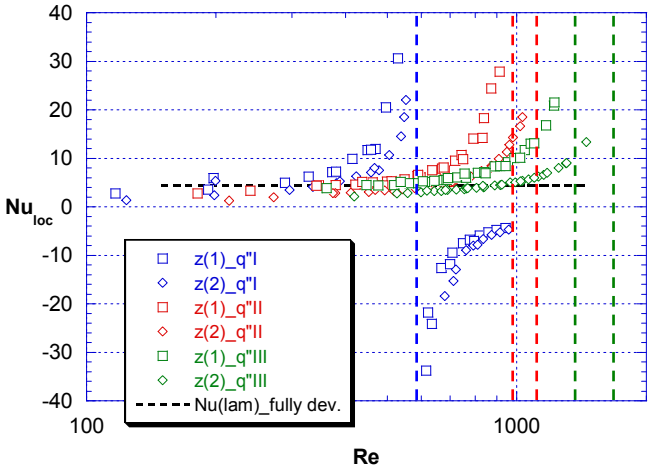

Fig. A.2: *Local Nusselt vs. Reynolds numbers at 2 axial locations; 3 ranges of heat input*

The anomaly is immediately apparent. A vertical asymptote can be observed for certain definite values of the Reynolds number, each corresponding to a different level of heat input or axial location. This is of course physically non-sense, but it shows very clearly how the experimental error can be of sudden extreme influence. At the various experimental conditions indicated by the asymptotes, the quantities of the conduction and convection term in equation (4.16) become equal and it is impossible to determine the conditions of heat transfer precisely (with the instruments available).

If we analyse the uncertainty more in detail around one of these experimental points, we can take into consideration the 9 variables in equation (4.16) and plot their influence on the total experimental error at these conditions. For example, around Reynolds number 700, heat input q"I (just after the asymptote), one of the datapoints has the following conditions:

$d = 50$ µm; $D = 363$ µm; $L_{ht} = 34.2$ mm; $T_w = 31.26$°C; $T_f = 29.27$°C; $\Gamma = 0.023$ g/s; $\Delta T_f = 3.18$ K.

With constant values for c_p and k_w (4180 J/kgK and 1.38 W/mK respectively) the local Nusselt number calculates as -8.98, and the total experimental error shoots up from around 10% at more stable conditions to 80% with the above quantities for the variables plus their certified uncertainties (0.1 K on the thermocouple values, *etc.*).

Let us observe the *fluid temperature rise*: by varying this value where the other parameters remain constant we get an idea of the instability of this experimental condition – see figure A.3.

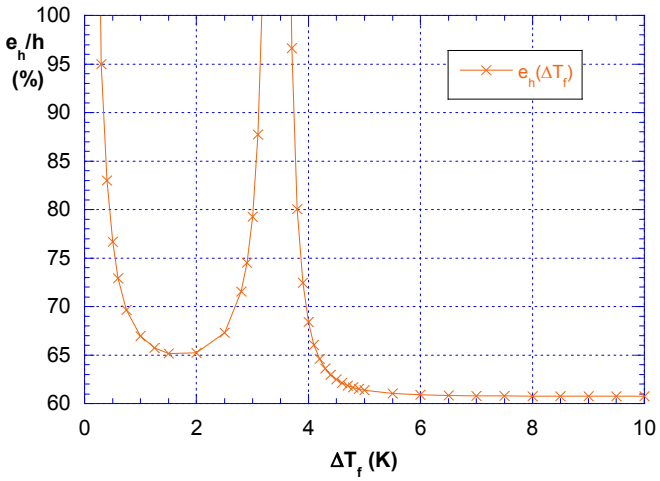

Fig. A.3: *Total experimental error at 1 condition as a function of the fluid temperature rise along the test section*

As we can see from the graph, there is a sharp peak in the total error on the heat transfer coefficient, just around the conditions we are working at (ΔT_f = 3.18 K). The same effect is visible for each of the other variables analysed around this particular set of conditions.

The relative contribution to the total experimental error of each of the variables at this condition (still with ΔT_f as the parameter that is varied) also shows this – purely conceptual – singularity, see figure A.4.

It can be concluded that the experimental test rig is unfit to do experiments on this size of tube in its current configuration and with the available level of precision. This also illustrates the importance of carrying out a thorough error analysis *before* embarking on an extended program of laboratory effort.

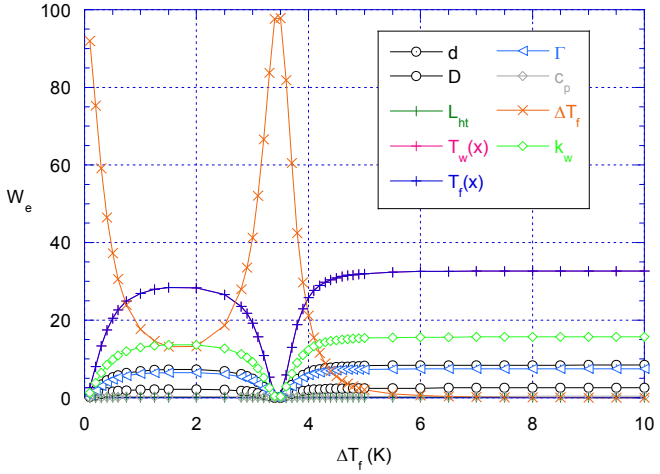

Fig. A.4: *Weight of variables' uncertainties on total relative error for the 50 μm tube at the specified condition as a function of the value of the fluid temperature rise along the test section (ΔT_f)*

LIST OF SYMBOLS

A	surface area	m^2
a	underestimation factor in equation (5.8)	-
b	shape-dependent exponent in equation (2.92)	-
Br	Brinkman number $\frac{\mu U^2}{q'_w}$	-
c	speed of sound	m/s
c_p	constant-pressure specific heat	J/kg.K
c_V	constant-volume specific heat	J/m^3.K
D	outer diameter	m
d	inner diameter	m
E	energy	J
e	roughness height	m
e_Y	error on variable Y	$[Y]$
Ec	Eckert number $\frac{U^2}{2c_p \cdot \Delta T_{ref}}$	-
F	force	N
f	friction factor	-
G	mass flux	kg/m^2.s
g	acceleration of gravity	m^2/s
Gz	Graetz number $Re \cdot Pr \cdot \frac{d}{z}$	-
H	height	m
h	heat transfer coefficient	W/m^2.K
I	linear momentum	kg.m/s
K	form coefficient in equation (2.92)	-
k	thermal conductivity	W/m.K
Kn	Knudsen number $\frac{\lambda}{d}$	-
L	length	m
L^*	dimensionless length $\frac{L}{d}$	-
M	thermal conductance number $\left(\frac{k_w}{k_f}\right)\left(\frac{D^2-d^2}{d \cdot L}\right)\frac{1}{Re \cdot Pr}$	-
m	mass	kg
M_{mol}	molar mass	kg/mol
Ma	Mach number $\frac{u}{c}$	-
$\vec{n}$	normal vector	-
Nu	Nusselt number $\frac{h \cdot d}{k_f}$	-
P	pressure (value)	Pa
p	pressure (variable)	Pa
p^*	dimensionless pressure $-\frac{d^2}{\mu \cdot U}\frac{\partial p}{\partial z}$	-

Pe	Péclet number $\frac{\rho \cdot c_p \cdot U \cdot d}{k}$ (= *Re.Pr)*	-
Pr	Prandtl number $\frac{c_p \cdot \mu}{k_f}$	-
q	heat flow	W
q'	linear heat flux	W/m
q''	area-specific heat flux	W/m^2
q'''	volume-specific heat flux	W/m^3
q_w^*	dimensionless wall linear heat flux $\frac{q'_w}{k\Delta T_{ref}}$	-
R	universal gas constant = 8.314	J/mol.K
R	radius value	m
r	radius variable	m
R_P	pressure ratio between inlet and outlet	-
Ra	average roughness value as defined in equation (4.2)	m
Re	Reynolds number $\frac{\rho \cdot U \cdot d}{\mu}$	-
T	temperature	K
t	time	s
T^*	dimensionless temperature $\frac{(T - T_{in})}{\Delta T_{ref}}$	-
U	average velocity	m/s
U^*	dimensionless velocity $\frac{u}{U}$	-
u	velocity (variable)	m/s
u_*	friction velocity as defined in equation (2.60)	m/s
V	volume	m^3
$\dot{V}$	volume flow rate	m^3/s
Vi	viscous number $\frac{\mu \cdot U^2 \cdot L}{\rho \cdot U \cdot c_p \cdot \Delta T_{ref} \cdot d^2}$	-
W	weight of variable error on total experimental error	-
w	work rate	W
x, y, z	Cartesian co-ordinates	m
Z	compressibility factor	-
z^*	dimensionless axial co-ordinate $\frac{z}{L}$	-

Greek symbols

α	form coefficient in equation (2.70)	-
β	slip length	m
Γ	mass flow rate	kg/s
γ	ratio of specific heats $= \frac{c_p}{c_V}$	-
δ	collision diameter	m
ε	emissivity	-
θ	normalized bulk temperature $\frac{T(z) - T(0)}{T(L) - T(0)}$	-
κ	Boltzmann constant = 1.380662×10^{-23}	J/K

Λ	conductance term in the definition of the heat transfer coefficient	$K.m^2/W$
λ	free molecular path	m
μ	dynamic viscosity	Pa.s
ν	kinematic viscosity = $\frac{\mu}{\rho}$	m^2/s
Π	wetted perimeter	m
ρ	density	kg/m^3
σ	shear stress	N/m^2
$\sigma_{S\text{-}B}$	Stefan-Boltzmann constant = 5.599×10^{-8}	$W/m^2.K^4$
τ_{ij}	tensor of surface tensions	N/m^2
Φ^*	viscous energy dissipation function as defined in equation (2.78)	-
χ	criterion as defined in equation (2.94)	-
Ω	cross-sectional area	m^2
Ω^*	dimensionless cross-sectional area $\frac{\Omega}{d^2}$	-
ω	unspecified cross-sectional form coefficient	-

Sub-scripts

b	bulk
c	centreline
cont	pertaining to continuum flow
f	fluid
ht	heated
hy	hydrodynamic
i	inner
in	inlet
lim	limit
M	pertaining to the molar mass
m	mass-specific
meas	measured
o	outer
out	outlet
q	pertaining to the heat input
R	at the inner wall ($r = R$)
rad	radiative
ref	reference
slip	pertaining to slip flow
th	thermal
V	volume-specific
v	pertaining to viscous dissipation
w	wall

REFERENCES

[1] J.R.E. Christy, K. Sefiane, Global Market Report for Development of Microelectronic Cooling Based on Boiling Heat Transfer – *Market Survey conducted on behalf of Scottish Enterprise*, p. 11, 2002.

[2] R.W. Fox, A.T. McDonald, Introduction to Fluid Mechanics, 4th ed., John Wiley & Sons, 1994.

[3] J.P. Holman, Heat Transfer, 7th ed., McGraw-Hill, 1992.

[4] J.M. Smith, H.C. Van Ness, M.M. Abbot, Introduction to Chemical Engineering Thermodynamics, 5th ed., McGraw-Hill, 1996.

[5] O.H. Bosgra, Mathematical Modelling of Dynamical Engineering Systems, TU Delft publishing, 1998.

[6] J.P. Poiseuille, Recherches Expérimentales sur le Mouvement des Liquides dans les Tubes de Très-Petits Diametres, Académie des Sciences, Paris, Imprimerie Royal, 1844, p.87 (128).

[7] R.H. Perry, D.W. Green, Perry's Chemical Engineers' Handbook, McGraw-Hill, p. 6-92, 1999.

[8] S.F. Choquette, M. Faghri, E.J. Kenyon, B. Sunden, Compressible Fluid Flow in Micron Sized Channels – *HTD Vol. 327, Proc. National Heat Transfer Conference,* vol. 5, pp. 25-32, 1996.

[9] M.J. Kohl, S.I. Abdel-Khalik, S.M. Jeter, D.L. Sadowski, An Experimental Investigation of Microchannel Flow with Internal Pressure Measurements – *Int. J. Heat Mass Transfer*, vol. 48, pp. 1518-1533, 2005.

[10] V. Isachenko, V. Osipova, A. Sukomel, Heat Transfer, 2nd Edition, MIR Publishers, Moscow, pp.92-97, 1974.

[11] W. Pfenniger, Boundary Layer and Flow Control, G. V. Lachman (Ed.), Pergamon, Oxford, pp. 970–980, 1961.

[12] H. Schlichting, Boundary-Layer Theory, McGraw-Hill, 7th Edition, pp. 615-617, 1979.

[13] G. Hetsroni, A. Mosyak, E. Pogrebnyak, L.P. Yarin, Fluid flow in microchannels – *Int. J. Heat Mass Transfer*, vol. 48, pp. 1982-1998, 2005.

[14] I.E. Idelchick, Handbook of Hydraulic Resistance, Hemisphere Publishing Corporation, 2nd Edition, 1986.

[15] C.L.M.H. Navier, Memoirs de l'Académie Royale des Sciences de l'Institut de France, vol.1, pp. 414-416, 1823.

[16] G. Rosengarten, J. Cooper-White, G. Metcalfe, Experimental and Analytical Study of the Effect of Contact Angle on Liquid Convective Heat Transfer in Microchannels – *Int. J. Heat Mass Transfer*, vol. 49, pp. 4161-4170, 2006.

[17] Y. Zhu and S. Granick, Limits of the Hydrodynamic No-Slip Boundary Condition – *Physical Review Letters*, vol. 88 (10), pp. 106102-1-4, 2002.

[18] J.W.G. Tyrrell and P. Attard, Images of Nanobubbles on Hydrophobic Surfaces and their Interactions – *Physical Review Letters,* vol. 87 (17), pp. 176104/1-4, 2001

[19] D.C. Trethaway, X. Liu, C.D. Meinhart, Analysis of Slip Flow in Microchannels – *Proc. 11th Int. Symp. On Applications of Laser Techniques to Fluid Mechanics*, Lisbon, 8-11 July 2002.

[20] Y. Sun, WK Chan, N Liu, A Slip Model with Molecular Dynamics – *J. Micromechanics Microengineering,* vol.12, 316-322, 2002

[21] C. Aubert, S. Colin, High-Order Boundary Conditions for Gaseous Flows in Rectangular Microducts – *Microscale Thermophysical Engineering,* vol. 5, pp. 43-77, 2001.

[22] G.L. Morini, M. Spiga, P. Tartarini, Rarefaction Effects in Microchannels and Friction Factor Reduction – *Proc. of Microscale Heat Transfer 2 (75th Eurotherm Seminar),* Reims, France, pp. 143-145, 8-10 July 2003.

[23] G.L. Morini, A Criterion for Experimental Validation of Slip-Flow Models for Incompressible Rarefied Gases through Microchannels – *Microfluidics and Nanofluidics*, vol. 1 (2), pp. 190-196, 2005.

[24] G.L. Morini, Viscous Heating in Liquid Flows in Microchannels – *Int. J. Heat Mass Transfer*, vol. 48, pp. 3637-3647, 2005.

[25] G. Maranzana, I. Perry, D. Maillet, Mini- and Micro-channels: Influence of Axial Conduction in the Walls – *Int. J. Heat and Mass Transfer,* vol. 47, pp. 3993-4004, 2004.

[26] J.P. Chiou, The Advancement of Compact Heat Exchanger Theory Considering the Effects of Longitudinal Heat Conduction and Flow Non-Uniformity – *Symposium on Compact Heat Exchangers*, ASME HTD vol. 10, pp. 101-121, 1980.

[27] R.K.Shah, A.L.London, Laminar Flow Forced Convection in Ducts – in: T.F. Irvine, J.P. Hartnett (Ed.), *Advances in Heat Transfer*, pp. 50-52, 124-128, Academic Press, New York, 1978.

[28] http://www.energy.kth.se/Courses/4A1602/HEAT%20TRANSFER%20Rep%20Course.pdf; p.57

[29] W.M. Rohsenow, H.Y.Choi – *Heat, Mass and Momentum Transfer*, PrenticeHall Eds., 1961.

[30] S. S. Mehendale, A. M. Jacobi, and R. K. Shah, Fluid Flow and Heat Transfer at Micro- and Meso-scales with Application to Heat Exchanger Design – *Applied Mechanics Reviews*, vol. 53 (7), pp. 175-193, 2000.

[31] S.G. Kandlikar, Fundemental Issues Related to Flow Boiling in Minichannels and Microchannels – *Experimental Thermal and Fluid Science*, vol. 26 (2), pp. 389-407, 2002.

[32] K. Cornwell, and P.A. Kew, Boiling in Small Parallel Channels – in: P.A. Pilavachi (Ed.) *Energy Efficiency in Process Technology*, Elsevier Science, 1993.

[33] E. Brauner, Verbal communication at the 44th European Two-Phase Flow Group Meeting, 7-9 June 2006.

[34] G.L. Morini, M. Spiga, Nusselt numbers in rectangular ducts with viscous dissipation – *Trans. ASME J. Heat Transfer*, vol. 121, pp. 1083-1087, 1999

[35] G.L. Morini, Viscous Dissipation as Scaling Effect for Liquid Flows in Microchannels – *Proc. 3rd Int. Conf. on Micro and Minichannels*, Toronto, Ontario, Canada, 13-15 June 2005.

[36] L. Ren, W. Qu, D. Li, Interfacial Electrokinetic Effects on Liquid Flow in Microchannels – *Int. J. Heat Mass Transfer*, vol. 44, pp. 3125-3134, 2001.

[37] R.J. Lang, L.M. Fu, Y.C. Lin, Electroosmotic Flow in Microchannels – *J. Colloid Interface Science*, vol. 239, pp. 98-105, 2001.

[38] G.M. Whitesides, A.D. Stroock, Flexible Methods for Microfluidics – *Physics Today,* vol. 6, pp. 42–48, 2001.

[39] D. Brutin, L. Tadrist, Experimental Friction Factor of a Liquid Flow in Microtubes – *Physics of Fluids*, vol. 15 (3), pp. 653-661, 2003.

[40] D. Yu, R. Warrington, R. Barron, T. Ameel, Experimental and Theoretical Investigation of Friction Factor and Heat Transfer in Microtubes – *ASME/JSME Thermal Engineering Conf.,* pp. 523-553, Maui, Hawaii, March 1995.

[41] D. Maynes, A.R. Webb, Velocity profile characterization in sub-diameter microtubes using molecular tagging velocimetry – *Experiments in Fluids,* vol. 32, pp. 3-15, 1996.

[42] J. Judy, D. Maynes, B.W. Webb, Characterization of Frictional Pressure Drop for Liquid Flows through Microchannels – *Int. J. Heat Mass Transfer*, vol. 45, pp. 3477-3489, 2002.

[43] Z.X. Li, D.X. Du, Z.Y. Guo, Experimental Study of Flow Characteristics in Circular Microtubes – *Microscale Thermophysical Engineering,* vol. 7, pp. 253-265, 2003.

[44] C.Y. Yang, J.C. Wu, H.T. Chien, S.R. Lu, Friction Characteristcs of Water, R-134a, and Air in Small Tubes – *Microscale Thermophysical Engineering,* vol. 7, pp. 335-348, 2003.

[45] H. Cui, Z. Silber-Li, S. Zhu, Flow Characteristics of Liquid in Microtubes Driven by High Pressure – *Physics of Fluids*, vol. 16 (5), pp. 1803-1810, 2004.

[46] K.V. Sharp and R.J. Adrian, Transition from Laminar to Turbulent Flow in Liquid Filled Microtubes – *Experiments in Fluids*, vol. 36, pp. 741-747, 2004.

[47] G.P. Celata, K. Chmiel, R. Kulenovic, C. Martín-Callizo, S. McPhail, R. Mertz, W. Owhaib, B. Palm, E. Sobierska, G. Zummo, Frictional Pressure Drop in Single-Phase Flow in Narrow Channels – *Proc. 4th Int. Conf. on Nano Micro & Minichannels*, Limerick, Ireland, 19-21 June 2006.

[48] G.M. Mala, D. Li, Flow characteristics of water in microtubes – *Int. J. Heat Fluid Flow*, vol. 20, pp. 142-148, 1999.

[49] G.P. Celata, M. Cumo, M. Guglielmi, G. Zummo, Experimental Investigation of Hydraulic & Single-Phase Heat Transfer in 0.13 mm Capillary Tube – *Microscale Thermophysical Engineering*, vol. 6, pp. 85-97, 2002.

[50] S.G. Kandlikar, S. Joshi, S. Tian, Effect of Surface Roughness on Heat Transfer and Fluid Flow Characteristics at Low Reynolds Number in Small Diameter Tubes – *Heat Transfer Engineering,* vol. 24 (3), pp. 4-16, 2003.

[51] D. Lelea, S. Nishio, K. Takano, The Experimental Research on Microtube Heat Transfer and Fluid Flow of Distilled Water – *Int. J. Heat Mass Transfer*, vol. 47, pp. 2817-2830, 2004.

[52] S.B. Choi, R.F. Barron, R.O. Warrington, Fluid Flow & Heat Transfer in Microtubes – *Micromechanical Sensors, Actuators & Systems*, vol. 32, pp. 123-134, 1991.

[53] Y. Asako, K. Nakayama, T. Shinozuka, Effect of Compressibility on Gaseous Flows in a Micro-tube – *Int. J. Heat Mass Transfer*, vol. 48, pp. 4985-4994, 2005.

[54] G.P. Celata, M. Cumo, S.J. McPhail, L. Tesfagabir, G. Zummo, Experimental Study on Compressible Flow in Microtubes – *Int. J. Heat Fluid Flow*, in press, corrected proof, available on-line 9 August 2006.

[55] G.L. Morini, S. Colin, S. Geoffroy, M. Lorenzini, Experimental Investigation of the Compressibility Effects on the Friction Factor of Gas Flows in Microtubes – *Proc. 4th Int. Conf. Nano Micro & Minichannels*, Limerick, Ireland, 19-21 June 2006.

[56] I. Papautsky, J. Brazzle, T. Ameel, A. Bruno Frazier, Laminar Fluid Behaviour in Microchannels using Micro-Polar Fluid Theory – *Sensors & Actuators*, vol. 73, pp. 101-108, 1999.

[57] D. Pfund, D. Rector, A. Shekarriz, A. Popesku, J. Welty, Pressure Drop Measurements in a Microchannel – *AIChE J.,* vol. 46, pp. 1496-1507, 2000.

[58] B. Xu, K.T. Ooi, T.N. Wong, W.K. Choi, Experimental Investigation of Flow Friction for Liquid Flow in Microchannels – *Int. Comm. Heat Mass Transfer*, vol. 27 (8), pp. 1165-1176, 2000.

[59] P. Gao, S. Le Person, M. Favre-Marinet, Scale Effect on Hydrodynamics and Heat Transfer in Two-Dimensional Mini and Microchannels – *Int. J. Thermal Sciences*, vol. 41, pp.1017-1027, 2000.

[60] P.S. Hrnjak and X. Tu, Single-Phase Pressure Drop in Microchannels – *Proc. ECI Conf. Heat Transfer & Fluid Flow in Microscale*, Castelvecchio Pascoli, Italy, 25-30 September 2005.

[61] X.F. Peng, G.P. Peterson, B.X. Wang, Frictional Flow Characteristics of Water Flowing through Microchannels – *Experimental Heat Transfer,* vol. 7, pp. 249-264, 1994.

[62] X.F. Peng and G.P. Peterson, Convective Heat Transfer & Friction for Water Flow in Micro-Channel Structures – *Int. J. Heat Mass Transfer*, vol. 39, 2599-2608, 1996.

[63] E.R. Arkilic, K.S. Breuer, M.A. Schmidt, Gaseous flow in microchannels – *ASME Applications Microfabrication Fluid Mechanics*, vol. FED-197, pp. 57-66, 1994.

[64] S.E. Turner, L.C. Lam, M. Faghri, O.J. Gregory, Experimental Investigation of Gas Flow in Microchannels – *J. of Heat Transfer*, vol. 126, pp. 753-763, 2004.

[65] S.S. Hsieh, H.H. Tsai, C.Y. Lin, C.F. Huang, C.M. Chien, Gas Flow in a Long Microchannel – *Int. J. Heat Mass Transfer*, vol. 47, pp. 3877-3887, 2004.

[66] W. Urbanek, J.N. Zemel, H.H. Bau, An Investigation of the Temperature Dependence of Poiseuille Numbers in Microchannel Flow – *J. Micromechanics Microengineering*, vol. 3, pp. 206-208, 1993.

[67] H.Y. Wu, P. Cheng, Friction Factors in Smooth Trapezoidal Silicon Microchannels with Different Aspect Ratios – *Int. J. Heat Mass Transfer*, vol. 46, pp. 2519-2525, 2003.

[68] P.F. Hao, F. He, K.Q. Zhu, Flow Characteristics in a Trapezoidal Silicon Microchannel – *J. Micromechanics Microengineering*, vol. 15, pp. 1362-1368, 2005.

[69] W. Qu, G.M. Mala, D. Li, Pressure Driven Water Flows in Trapezoidal Silicon Microchannels – *Int. J. Heat Mass Transfer*, vol. 43, pp. 353-364, 2000.

[70] P. Wu, W.A. Little, Measurement of Friction Factors for the Flow of Gases in Very Fine Channels Used for Microminiature Joule-Thompson Refrigerators – *Cryogenics,* vol. 23, pp. 273-277, 1983.

[71] J. Pfahler, J. Harley, H. Bau, J.N. Zemel, Gas and Liquid Flow in Small Channels – *Micromechanical Sensors Actuators Systems*, vol. 32, pp. 49-60, 1991.

[72] J. Harley, Y. Huang, H. Bau, J.N. Zemel, Gas Flows in Microchannels – *J. Fluid Mechanics*, vol. 284, pp. 257-274, 1995.

[73] T. Araki, M.S. Kim, H. Iwai, K. Suzuki, An Experimental Investigation of Gaseous Flow Characteristics in Microchannels – *Microscale Thermophysical Engineering*, vol. 6, pp. 117-130, 2002.

[74] T.M. Adams, S.I. Abdel-Khalik, S.M. Jeter, Z.H. Qureshi, An Experimental Investigation of Single-Phase Forced Convection in Microchannels – *Int. J. Heat Mass Transfer*, vol. 41, pp. 851-857, 1998.

[75] G. Hetsroni, M. Gurevich, A. Mosyak, R. Rozenblit, Drag Reduction and Heat Transfer of Surfactants Flowing in a Capillary Tube – *Int. J. Heat Mass Transfer*, vol. 47, pp. 3797-3809, 2004.

[76] W. Owhaib, B. Palm, Experimental Investigation of Single-Phase Convective Heat Transfer in Circular Microchannels – *Experimental Thermal Fluid Science*, vol. 28, pp. 105-110, 2004.

[77] G.P. Celata, M. Cumo, V. Marconi, S.J. McPhail, G. Zummo, Microtube Liquid Single-Phase Heat Transfer in Laminar Flow – *Int. J. Heat Mass Transfer*, vol. 49, pp. 3538-3546, 2006.

[78] S. Grohmann, Measurement and Modeling of Single-Phase and Flow Boiling Heat Transfer in Microtubes – *Int. J. Heat Mass Transfer*, vol. 48, pp. 4073-4089, 2005.

[79] B.X. Wang, X.F. Peng, Experimental Investigation on Liquid Forced Convection Heat Transfer through Microchannels – *Int. J. Heat Mass Transfer*, vol. 37, 1994.

[80] T.M. Harms, M.J. Kasmierczak, F.M. Gerner, Developing Convective Heat Transfer in Deep Rectangular Microchannels – *Int. J. Heat Fluid Flow*, vol. 20, pp. 149-157, 1999.

[81] P. Wu, W.A. Little, Measurement of the Heat Transfer Characteristics of Gas Flow in Fine Channel Heat Exchangers used for Microminiature Refrigerators – *Cryogenics*, vol. 24, pp. 415-420, 1984.

[82] W. Qu, G.M. Mala, D. Li, Heat Transfer for Water Flow in Trapezoidal Silicon Microchannels – *Int. J. Heat Mass Transfer*, vol. 43, pp. 3925-3936, 2002.

[83] H.Y. Wu, P. Cheng, An Experimental Study of Convective Heat Transfer in Silicon Microchannels with Different Surface Conditions – *Int. J. Heat Mass Transfer*, vol. 46, pp. 2547-2556, 2003.

[84] B. D. Iverson and S. V. Garimella, Micropumping Technologies for Electronics Cooling – *Electronics Cooling Magazine*, vol. 12 (2), 2006.

[85] J.P. Holman, Experimental Methods for Engineers, McGraw-Hill, 1978.

[86] R.J. Moffat, Describing the Uncertainties in Experimental Results – *Experimental Thermal Fluid Science*, vol. 1, pp. 3-17, 1988.

[87] R.H. Van der Berg, C.A. Seldam, P.S. Van der Gulik, Compressible Laminar Flow in a Capillary – *J. Fluid Mechanics*, vol. 246, p. 1020, 1993.

[88] B. Xu, K.T. Ooi, C. Mavriplis, M.E. Zaghloul, Viscous Dissipation Effects for Liquid Flow in Microchannels – *5th Int. Conf. Modeling and Simulation of Microsystems*, San Juan, Puerto Rico, 22-25 April 2002.

[89] J.R. Thome, M. Groll, R. Mertz, Heat Transfer and Fluid Flow in Microchannels: Boiling and Evaporation – in: G.F. Hewitt (Ed.), *Heat Exchanger Design Handbook – Update Journal*, vol. 9, pp. 2.13.4-1-4, Begell House, 2002.

[90] H. Chen, M. Groll, S. Roesler, Micro Heat Pipes: Experimental Investigation and Theoretical Modeling – *Proc. 8th Int. Heat Pipe Conference*, Beijing, China, October 1992.

[91] J.R. Thome, Verbal communication at the Short Course on Fundamentals of Microscale Heat Transfer: Boiling, Condensation, Single- and Two-Phase Flows, J.R. Thome, A. Jacobi, I. Zun, G.P. Celata (lecturers), Lausanne, Switzerland, 12-16 June 2006.